

# Implementation of Functional Microfluidic Dispensing Tools Enabling Enhanced Control in Extrusion Bioprinting

Thèse N° 9281

Présentée le 22 février 2019

à la Faculté des sciences et techniques de l'ingénieur  
Laboratoire de microsystemes 4  
Programme doctoral en microsystemes et microélectronique

pour l'obtention du grade de Docteur ès Sciences

par

**Ludovic SEREX**

Acceptée sur proposition du jury

Prof. H. Shea, président du jury  
Prof. Ph. Renaud, Prof. T. M. Braschler, directeurs de thèse  
Prof. M. Zenobi-Wong, rapporteuse  
Prof. A. Van den Berg, rapporteur  
Prof. J. McKinney, rapporteur

2019





Some men see things as they are and say, why;  
I dream things that never were and say, why not.  
— Robert F. Kennedy

To Jurassic Park...





# Abstract

Inspired from additive manufacturing's success, the structuring of biocompatible materials through bioprinting has become a growing field of research in the past fifteen years. It opened the door to a plethora of applications ranging from the fabrication of tissue models for research, for drug discovery or even for regenerative medicine. This field of research has mainly been tackled from a biological view point to study the culture of cells and their behavior "*ex-vivo*" as well as through a materials science lens as to synthesize the best possible extracellular matrices. *Per contra*, the tools currently used for bioprinting do not allow advanced manipulations that are needed to reproduce the complex structures found in tissues. This sets strict limitations on what can be achieved by bioprinting. This thesis proposes an engineering perspective on bioprinting by providing new tools which improve the level of control over deposited biomaterials through extrusion bioprinting. The advancements in microfluidic technology are leveraged to micromanufacture extrusion tools serving as printing heads for bioprinters.

Successful implementation of a microfluidic mixer combined with a heating element and temperature sensor in an extrusion tool, enabled the printing of cryogels. These macroporous materials display remarkable properties, such as high pore interconnection, large surface to volume ratio and high mechanical stability. A collagen coating that is covalently bonded to the cryogel has been developed to enable the culture of adherent cells such as fibroblasts within the printed scaffold. Using the heating element, the pores' size of the printed cryogel can be controlled during printing. It allows to select the position of the seeded cells, making relevant the use of matrices that require post-printing cell seeding in tissue modeling applications.

A cell concentrator capable of working on a moving printing head, at relevant flow rates for bioprinting was designed and implemented. The ability to concentrate cells just before printing presents remarkable advantages such as reduced risk of cell lysis in tubings and reduced cell losses in dead volumes of bioprinters. As evidence of the beneficial effects of printing at a high cell concentration were found, such tools provide the opportunity to work at high cellular concentrations without the complications usually associated with it. The implementation of a herringbone microfluidic mixer downstream of the cell concentrator enables the addition of extracellular matrix, providing a complete platform for tissue printing at high cell concentration. Using this

tool, NOR-10 fibroblast cells were printed at high concentration in a collagen matrix. Cells cultured at high concentration showed better spreading and rapidly expanded to confluency. Moreover, using the concentrator, primary uroepithelial cells were printed in a basement membrane extract. The control over the cellular concentration allowed for the optimization of the amount of printed cells which has been demonstrated to have a major impact on bladder organoid formation.

Finally, as many extracellular matrices take several minutes to crosslink, multi-layer 3D printing of these materials can be challenging. Hence solutions for the printing of liquid materials are explored through the creation of a composite biomaterial containing collagen and alginate, co-printing of rigid support materials and liquid materials using a dedicated extrusion head and the printing of liquid materials within a supporting gel. These printing techniques allowed to cope with the long curing time of certain bio-inks and to shape them in 3D.

The tools developed in this work set the ground for the development of a new generation of bioprinters providing more freedom for the design and printing of functional tissues through enhanced control over the printed materials.

**Keywords:** Bioprinting, Additive manufacturing, Tissue engineering, Microfluidics, Cryogels, Collagen Coating, Cell concentration, Organoid.

# Résumé

Inspirée par le succès de la fabrication additive, la structuration de matériaux biocompatibles via des procédés de bio-impression est devenue un domaine de recherche qui n'a eu cesse de croître durant ces quinze dernières années. Ce domaine de recherche a ouvert la porte à une multitude d'applications comme la fabrication de modèles de tissus à des fins de recherche, la découverte de nouveaux médicaments ou même la médecine régénérative. Le sujet a principalement été abordé d'un point de vue biologique pour étudier la culture de cellules et leur comportement "*ex vivo*", ainsi que via la science des matériaux afin de synthétiser les meilleures matrices extracellulaires possibles. A l'inverse, les outils usuellement utilisés pour la bio-impression restent primitifs et ne permettent pas la réalisation de structures complexes présentes dans les tissus. Cela impose des limites strictes à ce qui peut être réalisé par bioprinting. Cette thèse propose une approche d'ingénierie à la bio-impression, en fournissant de nouveaux outils de dispense permettant d'améliorer le niveau de contrôle sur les biomatériaux et cellules déposés par le biais de la bio-impression par extrusion. Les progrès réalisés dans le domaine de la micro-fluidique ont été exploités afin de micro-fabriquer des outils d'extrusion qui serviront de tête d'impression pour les imprimantes cellulaires.

Les cryogels sont des matériaux macroporeux présentant des propriétés remarquables, telles qu'une interconnexion des pores élevée, un rapport surface sur volume élevé ainsi qu'une grande stabilité mécanique. L'intégration, dans une tête d'impression, d'un mixer micro-fluidique, associé à un élément chauffant et à un capteur de température a permis d'imprimer, en 3D, ces cryogels. La culture de cellules adhérentes telles que des fibroblastes, dans les structures imprimées, a été rendue possible grâce à un revêtement de collagène attaché de manière covalente au cryogel. De plus, en utilisant l'élément chauffant de la tête d'impression, la taille des pores du cryogel imprimé a pu être contrôlée durant l'impression. Grâce à cela, la position des cellules ensemencées peut être déterminée par exclusion de taille, rendant pertinente l'utilisation de matrices nécessitant un ensemencement post-impression de cellules pour des applications de modélisation tissulaire.

Un concentrateur de cellules, capable d'opérer sur une tête d'impression mobile, à des débits pertinents pour la bio-impression, a été conçu et mis en œuvre. La possibilité de concentrer des cellules juste avant l'impression présente des avantages remarquables,

tels que la réduction du risque de lyse cellulaire dans les tubes et la réduction des pertes de cellules dans les volumes morts des imprimantes cellulaires. Comme des preuves d'un effet bénéfique pour les cellules d'une impression à concentration cellulaire élevée ont été trouvées, l'utilisation de cet outil permet donc de travailler de hautes concentrations, ce sans les complications qui y sont habituellement associées. L'addition d'un mélangeur micro-fluidique en aval du concentrateur de cellules permet le mélange de matrice extracellulaire aux cellules concentrées, créant une plate-forme complète pour l'impression de tissus à haute concentration cellulaire. En utilisant cet outil, des fibroblastes NOR-10 ont été imprimés à une concentration élevée dans une matrice de collagène. Les cellules cultivées à concentration élevée ont montré un bon élongation et se sont rapidement développées jusqu'à confluence. De plus, en utilisant le concentrateur, des cellules uro-épithéliales primaires ont été imprimées dans de l'extrait de membrane basale. Le contrôle sur la concentration cellulaire a permis d'optimiser la quantité de cellules imprimées, ce qui a eu un impact majeur sur la formation d'organoides de la vessie.

Enfin, comme de nombreuses matrices extracellulaires prennent plusieurs minutes pour réticuler et durcir, l'impression en 3D, multicouches, de ces matériaux peut s'avérer difficile. Par conséquent, de multiples solutions pour l'impression de matériaux liquides ont été explorées. Premièrement, un biomatériau composite contenant du collagène, pour la culture des cellules, et de l'alginate, fournissant une réticulation rapide, a été créé. Ensuite, la séparation du matériel de support et de la matrice extracellulaire a été explorée via la co-impression de supports rigides et de matériaux liquides à l'aide d'une tête d'extrusion spécifique et via l'impression de matériaux liquides dans un gel de support. Ces techniques d'impression ont permis de contourner le long temps de durcissement de certains biomatériaux afin de les façonner en 3D.

Les outils développés dans ce travail ouvrent la voie au développement d'une nouvelle génération d'imprimantes cellulaires offrant plus de liberté pour la conception et l'impression de tissus fonctionnels grâce à un contrôle amélioré sur les matériaux imprimés.

# Zusammenfassung

Die Strukturierung von biokompatiblen Materialien durch Biodrucken hat sich, inspiriert vom Erfolg der additiven Fertigung, in den letzten 15 Jahren zu einem wachsenden Forschungsfeld entwickelt. Das hat die Tür geöffnet zu einer Fülle von Anwendungen, wie der Herstellung von Gewebemodellen für die Forschung, der Wirkstoffforschung oder der regenerativen Medizin. Dieses Forschungsfeld wurde hauptsächlich aus biologischer Sicht angegangen, um die Kultur von Zellen und ihr Verhalten "*ex vivo*" zu untersuchen. Zudem wurde das Forschungsfeld von materialwissenschaftlicher Seite angegangen, um die bestmöglichen extrazellulären Matrizen zu synthetisieren. Demgegenüber erlauben die Werkzeuge, die für das Biodrucken benutzt werden, keine fortgeschrittenen Manipulationen, die erforderlich wären, um komplexe Strukturen in Geweben zu reproduzieren. Das setzt der Anwendung des Biodruckens strikte Limiten.

Diese Doktorarbeit unterbreitet eine technische Perspektive für das Biodrucken durch neue Werkzeuge, welche die Kontrolle über die aufgetragenen Biomaterialien durch Extrusionsbiodrucken verbessert. Die Fortschritte in der Mikrofluidik-Technologie werden für die Mikrofabrikation von Extrusionswerkzeugen benutzt, die als Druckköpfe für Biodrucker dienen.

Der erfolgreiche Einbau eines Mikrofluidikmischers in Kombination mit einem Heizelement und einem Temperatursensor in einem Druckkopf ermöglicht es, Kryogele in 3D zu drucken. Diese makroporösen Materialien zeigen bemerkenswerte Eigenschaften wie einen hohen Porenzusammenhalt, ein großes Oberfläche/Volumen Verhältnis und eine hohe mechanische Stabilität. Die Kultur von adhären Zellen, wie Fibroblasten, innerhalb der gedruckten Strukturen wurde ermöglicht dank einer Kollagenbeschichtung, die kovalent an das Kryogel gebunden ist. Zudem kann dank des Heizelements die Größe der Poren des gedruckten Kryogels während des Druckens kontrolliert werden. Dank diesem Element kann die Positionierung der gesäten applizierten Zellen durch Grössenausschluss festgelegt werden, was die Verwendung von Matrizen erfordert, die eine Nachdrucker-Zellsaat ermöglichen, wie sie für die Gewebemodellierung notwendig ist.

Es wurde ein Zellkonzentrator entwickelt, der in der Lage ist, an einem sich bewegenden Druckkopf mit Flussraten für den Biodruck zu arbeiten. Die Fähigkeit, unmittelbar vor

dem Drucken Zellen zu konzentrieren, hat bemerkenswerte Vorteile, wie das verringerte Risiko der Zellyse in Röhrchen und die verringerten Zellverluste in Totvolumen von Biodruckern. Da substanzielle Vorteile nachgewiesen werden konnten für die vorteilhaften Auswirkungen des Druckens bei einer hohen Zellkonzentration, erlauben es solche Werkzeuge, bei hohen Zellkonzentrationen ohne die üblicherweise damit verbundenen Komplikationen zu arbeiten. Der Einbau eines Mikrofluidik-Mischers hinter dem Zellkonzentrator ermöglicht das Zumischen von extrazellulärer Matrix zum Zellkonzentrat, wodurch eine vollständige Plattform für den Gewebedruck bei hoher Zellkonzentration entsteht. Mit diesem Werkzeug wurden Fibroblasten NOR-10 in hoher Konzentration in eine Kollagenmatrix gedruckt. Bei hoher Konzentration kultivierte Zellen zeigen eine gute Spreizung und vervielfachen sich rasch bis zur Konfluenz. Mit der Anwendung des Konzentrators war es möglich urothelial Primärzellen in einen Basismembranextrakt zu drucken. Die Kontrolle der Zellkonzentration ermöglichte die Optimierung der Menge an gedruckten Zellen, was einen entscheidenden Einfluss auf die Bildung von Blasenorganoiden hat.

Weil viele extrazelluläre Matrizen mehrere Minuten zum Vernetzen und Aushärten benötigen, stellt der mehrschichtige 3D-Druck dieser Materialien eine Herausforderung dar. Daher wurden zahlreiche Lösungen für das Bedrucken von flüssigen Materialien untersucht. Erstens ein Biomaterial-Verbundwerkstoff, der einerseits Kollagen für die Zellkultur enthält und andererseits Alginat, das für eine schnelle Vernetzung sorgt. Anschliessend wurde die Trennung von Trägermaterial und extrazellulärer Matrix untersucht durch gleichzeitiges Aufbringen von starren Trägermaterialien und flüssigen Materialien. Das gelang mit Hilfe eines speziellen Druckkopfes und Druck von flüssigem Material in ein Trägergel. Diese Drucktechniken ermöglichten, die lange Aushärtezeit bestimmter Biomaterialien zu umgehen und dieses Material in 3D zu formen.

Die Werkzeuge die aus dieser Arbeit resultieren, öffnen den Weg für die Entwicklung einer neuen Generation von Biodruckern, die durch eine verbesserte Kontrolle der bedruckten Materialien, mehr Freiheit für den Druck von Funktionszellgewebe bieten.



# Acknowledgements

I would like to take the opportunity, in this chapter, to express my deepest gratitude to the people who helped me during this work. Producing a thesis has been an enormous endeavor and it wouldn't have been possible without their help.

I would like first to thank Prof. Philippe Renaud for giving me the opportunity to work on a PhD at the microsystems laboratory 4. It is often said that *"If you're the smartest person in the room, you're in the wrong room"*. Thanks to him, I had the opportunity to meet and discuss with astounding people that allowed me to learn a lot and develop myself. The freedom he gave me coupled with the subtle guidance he provided throughout my thesis really made him the best mentor possible. I am truly grateful for the trust he put in me, for the challenge he proposed and for all his guidance.

I would like to thank Prof. Thomas Braschler for all his advice as well as for the hours long discussions we had. He is fueled by his passion for research and always keen to share his knowledge on any topic. It has been enlightening to work with him and I am grateful for his supervision on this thesis.

I would like to thank all jury members, Prof. Marcy Zenobi-Wong, Prof. John McKinney and Prof. Albert Van den Berg for their constructive feedback and for bringing their knowledge to the discussion over this work. I would like to thank Prof. Herbert Shea as well for taking the time to preside this jury and for being available since the beginning of the project as he was also part of the jury for the candidacy examination.

I would like to particularly thank Dr. Arnaud Bertsch for all his help. As a senior scientist his help was extremely valuable especially as he is an expert in chemistry and 3D printing. Sometimes one needs to destroy to better rebuild. That is why I am also grateful for all his (destructive) corrections and (constructive) feedback over my texts. Sorry for the red pencils. I also want to thank Pia Grieder and Carina Schey for their corrections as well.

I would like to acknowledge Harald van Lintel, Sylvie Clavel, Christine Vuichoud and Lucie Auberson for their help on all the tasks that need to be done in order for the laboratory and the doctoral school to work smoothly.

It has been my privilege to share the office with multiple mates. The order brought by Guillaume and the chaos from Stefano made an intriguing mix I enjoyed particularly. I also had the opportunity to share the office with Martina for a short period of time, Joan who brought a fresh girly touch to the office and Clémentine that I could convince to go climbing. We all had great discussions and they all made my time in BM 3.119 a delight.

## Acknowledgements

I would like to acknowledge every member of the LMIS4 group. Clarisse, Fethemeh and Margaux for their help on cell culture, Benoît for never backing down as well as the new PhD candidates, Jiande and Nicolas, which I don't see very often as I am secluded in my office for writing purposes as well as Jonathan. There is a great startup culture in the laboratory and the members are very helpful and motivated. A big thanks to Marc, David and David as well as George for the discussion we had on entrepreneurship and their advises that were priceless as I envision making a startup after my PhD. I also want to acknowledge Tengfei, Ivan, Victor and Julian as they beautifully contributed to this work through their projects under my supervision. A special thank you to Kunal who helped me a lot with organoids, sharing his know how and helping with experiments I could not have conducted by myself.

Many platforms are available at EPFL and I had the opportunity to work with some of them throughout my thesis. A big thank you to the bioimaging and optics platform and especially to Romain for his help with FIJI as well as Luigi for his help on microscopes. The histology facility, the interdisciplinary center for electron microscopy as well as the atelier de fabrication additive provided outstanding services and I am extremely grateful to their staff members. I also abundantly used the cleanrooms of the center of micro-nano technology to do the micro-manufacturing processes. I want to acknowledge the staff for their help and effort to make this facility a great environment to work in. I finally had the opportunity to work with the technology transfer office where I would especially thank Alberto and André for their help.

I also want to thank Alessandro who gave me the opportunity to work with his team at the European organization for nuclear research as well as Miranda for her incredible manufacturing skills that really saved me multiple times.

Sport has been a great stress relief and a source of personal development. I would like to thank Sébastien for all our climbing escapades as well as Matthieu for all the torments on the running track. I trusted you on that one. I would also like to thanks Nicolas if it wasn't for his help I might not even have my master degree. I am looking forward to continuing working with him on our startup. I would also like to thank all my friends for their support especially Daniel, Julien, Flavien, Valentin, Mélanie and all the new year's team, always here to hang out and supporting each other. On that note I also want to thank Carmen, Charlotte, Nina, Nicolas, Xavier, Sara and the Vichère team in general for all those precious moment spent together.

My family has been an amazing support throughout my life and of course during this project. I would like to thank my mom, Lucienne, for her support and her appreciation of my work. I would also like to thanks my dad, Florian, for the discussion we have, always finding the good questions that are challenging to answer. I also want to thank my sister Caroline and brother Alexandre. Thank you all for your unconditioned love. Finally I want to express all my love and deepest gratitude for my girlfriend Line who has been in my life for over five year now. She has been the most amazing girlfriend anybody could dream of. Her support, joy of living, positiveness, kindness and beauty have enlighten every day of this thesis and I couldn't be happier than with her. I finally want to thanks her family as well for their support and kindness.

To all, thank you.

*Lausanne, 19 December 2018*

Ludovic Serex

# Contents

Abstract (English/Français/Deutsch)	v
Acknowledgements	xi
List of figures	xvi
List of tables	xviii
Nomenclature	xix
List of symbols	xxi
Introduction	1
<b>1 Introduction</b>	<b>1</b>
1.1 Background . . . . .	1
1.1.1 Additive manufacturing . . . . .	1
1.1.2 Bioprinting . . . . .	2
1.1.3 Biomaterials . . . . .	6
1.1.4 Smart dispensing . . . . .	6
1.1.5 Microfluidics . . . . .	9
1.2 Research strategy . . . . .	9
1.2.1 Problem definition . . . . .	9
1.2.2 Research objective . . . . .	10
1.2.3 Thesis structure . . . . .	10
<b>2 Cryogels</b>	<b>11</b>
2.1 Introduction . . . . .	11
2.2 Probe design and fabrication . . . . .	12
2.2.1 Specifications . . . . .	12
2.2.2 Microfabrication . . . . .	13
2.2.3 Experimental validation . . . . .	15
2.3 Cryogel Synthesis . . . . .	17
2.4 Pore size tuning . . . . .	21
2.4.1 Crystal growth and pores size . . . . .	21
	xiii

## Contents

2.4.2	Cryogel pores size modulation . . . . .	22
2.5	Cryogel 3D printing . . . . .	28
2.6	Collagen coating . . . . .	30
2.7	Cell seeding . . . . .	32
2.8	Conclusion . . . . .	34
2.8.1	Summary . . . . .	34
2.8.2	Discussion and outlook . . . . .	35
<b>3</b>	<b>Cell concentration</b>	<b>37</b>
3.1	Introduction . . . . .	37
3.2	Concentrators design . . . . .	39
3.2.1	Specifications and design choice . . . . .	39
3.2.2	Hydrodynamic focusing . . . . .	41
3.2.3	Crossflow filter . . . . .	48
3.2.4	Probe Final Design and Setup . . . . .	60
3.3	Bioprinting at high cell concentrations . . . . .	62
3.3.1	Materials and methods . . . . .	62
3.3.2	Results . . . . .	63
3.4	Bladder organoid bioprinting . . . . .	65
3.4.1	Motivation . . . . .	65
3.4.2	Protocol . . . . .	66
3.4.3	Results . . . . .	68
3.5	Conclusion . . . . .	75
3.5.1	Summary . . . . .	75
3.5.2	Discussion and outlook . . . . .	76
<b>4</b>	<b>Biomaterials 3D printing</b>	<b>79</b>
4.1	Introduction . . . . .	79
4.2	Improving structural stability . . . . .	80
4.2.1	Bio-ink modification . . . . .	80
4.2.2	Co-extrusion printing . . . . .	82
4.2.3	Liquid printing . . . . .	86
4.3	Conclusion . . . . .	88
4.3.1	Summary . . . . .	88
4.3.2	Discussion and outlook . . . . .	88
<b>5</b>	<b>Conclusion and outlook</b>	<b>91</b>
5.1	Summary of results . . . . .	91
5.2	Conclusion . . . . .	92
5.3	Future applications of the technology . . . . .	93
<b>6</b>	<b>List of publications</b>	<b>95</b>

<b>A</b>	<b>Exploited technologies</b>	<b>97</b>
A.1	Polyimide-SU8 . . . . .	97
A.2	Silicon . . . . .	98
A.3	3D printing . . . . .	99
<b>B</b>	<b>Cryogel synthesis calculus</b>	<b>101</b>
B.1	Introduction and definition of aims . . . . .	101
B.2	Protocol . . . . .	101
<b>C</b>	<b>Collagen coating of cryogels</b>	<b>107</b>
C.1	Introduction and definition of aims . . . . .	107
C.2	Quantification of adsorption of collagen to cryogels . . . . .	108
C.3	Surface versus Volume localization . . . . .	110
C.4	Fibril formation and homogeneity . . . . .	114
C.5	Permanent modification . . . . .	115
C.6	Conclusion . . . . .	119
<b>D</b>	<b>Thermodynamic model</b>	<b>121</b>
<b>E</b>	<b>Conductive cryogels</b>	<b>125</b>
E.1	Introduction . . . . .	125
E.2	Implementation and results . . . . .	125
E.3	Conclusion . . . . .	127
<b>F</b>	<b>Calculation steps for hydrodynamic focusing design</b>	<b>129</b>
<b>G</b>	<b>Organoids culture and protocol</b>	<b>131</b>
G.1	Material . . . . .	131
G.2	Media . . . . .	131
G.3	Organoid fixing and staining . . . . .	132
G.3.1	Protocol . . . . .	132
G.3.2	Material . . . . .	133
<b>H</b>	<b>Multi-material printing</b>	<b>135</b>
H.1	Intoduction . . . . .	135
H.2	Implementation and results . . . . .	135
H.3	Conclusion . . . . .	136
<b>I</b>	<b>Microfluidic for 3D printing</b>	<b>137</b>
I.1	Introduction . . . . .	137
I.2	Probes . . . . .	137
I.2.1	Multi-Material probe . . . . .	137
I.2.2	Mixing probe . . . . .	139
I.2.3	Adjustable resolution probe . . . . .	140

## Contents

I.2.4	Concentration probe . . . . .	142
I.3	Discussion and conclusion . . . . .	142
	<b>Bibliography</b>	<b>166</b>

# List of Figures

1.1	Bioprinted structures . . . . .	3
1.2	Additive manufacturing setups used for 3D bioprinting. . . . .	5
1.3	State of the art bioprinting of various bio-inks . . . . .	7
1.4	Improved dispensing tools. . . . .	8
2.1	Cryo-probe process flow . . . . .	13
2.2	Microfluidic extrusion head for cryogel 3D printing . . . . .	15
2.3	Meander mixer efficiency . . . . .	15
2.4	Hydrophobic coating . . . . .	16
2.5	Temperature sensor characterization . . . . .	17
2.6	Probe dynamic thermal characterization . . . . .	18
2.7	Cryogel synthesis . . . . .	19
2.8	Confocal micrograph of cryogel structures . . . . .	21
2.9	Bulk Cryogel structure . . . . .	22
2.10	Pore size modulation in cryogel . . . . .	23
2.11	Ice crystal growth analysis by DSC . . . . .	26
2.12	Printer setup . . . . .	28
2.13	Printed Cryogel structure . . . . .	29
2.14	pH optimization for collagen coating . . . . .	31
2.15	Confocal micrograph of coated collagen on cryogel . . . . .	32
2.16	SEM micrograph of a NOR-10 cell in a cryogel . . . . .	33
2.17	Confocal micrograph of cryogels seeded with NOR-10 cells . . . . .	34
3.1	From focusing to concentration, working principle . . . . .	40
3.2	Hydrodynamic concentrator working principle . . . . .	42
3.3	Simulation of hydrodynamic focusing . . . . .	44
3.4	Concentration probe process flow . . . . .	45
3.5	Hydrodynamic concentrator . . . . .	46
3.6	Crossflow filter concentrator working principle . . . . .	48
3.7	Fluid behavior at a 90 degree bifurcation . . . . .	49
3.8	Vertical flow optimization . . . . .	51
3.9	Exposition and etching process optimization . . . . .	53
3.10	Crossflow filter implementation . . . . .	54

## List of Figures

3.11	Crossflow filter concentrator performance . . . . .	55
3.12	Microfluidic mixing . . . . .	58
3.13	Herringbone mixer fabrication . . . . .	59
3.14	Printing setup . . . . .	61
3.15	Pure collagen printing . . . . .	64
3.16	Cell isolation and seeding . . . . .	66
3.17	BME dome printing . . . . .	67
3.18	Organoids bright field image . . . . .	69
3.19	Sliced organoids H&E staining . . . . .	70
3.20	Immunostaining of sliced printed organoids . . . . .	72
3.21	Immunostaining of a 4 $\mu$ m thick slice of control organoids . . . . .	73
4.1	Bioprints stability . . . . .	80
4.2	Alginate-collagen printing . . . . .	81
4.3	Alginate collagen printing . . . . .	82
4.4	Pluronic F-127 printing . . . . .	83
4.5	Co-extrusion 3D printed dispensing tool . . . . .	84
4.6	Co-printed support and soft bioinks . . . . .	85
4.7	Liquid printing schematic . . . . .	86
4.8	Collagen printing . . . . .	87
A.1	Polyimide technology . . . . .	98
A.2	Silicon technology . . . . .	99
A.3	Additive manufacturing technology . . . . .	100
C.1	Setup used to quantify collagen coating of cryogels. . . . .	108
C.2	Uptake efficiency of collagen onto cryogels as a function of pH. . . . .	110
C.3	Evaluation of the gel penetration depth and surface layer thickness. . . . .	112
C.4	Surface layer thickness and volume penetration depth. . . . .	113
C.5	Collagen intensity over cryogel pores . . . . .	114
C.6	Loss of collagen during washing and fixing steps. . . . .	116
C.7	Fraction of leachable collagen. . . . .	117
C.8	Morphology of 3T3-J2 cells on collagen coated cryogels . . . . .	118
C.9	Quantification of spreading of 3T3-J2 cells on collagen coated cryogels . . . . .	118
E.1	SEM imaging cryogel seeded with boron doped diamonds . . . . .	126
E.2	Spectral impedance measurement of conductive cryogel . . . . .	127
H.1	Double probe mounting . . . . .	136
I.1	Multi-channel print head . . . . .	138
I.2	Print head based on flow focusing . . . . .	140
I.3	Herrigbone micro-mixer integrated at the tip of the probe. . . . .	141



# Nomenclature

2D	Two dimensions
3D	Three dimensions
AAD	Adipic acid dihydrazide
BME	Basement membrane extract
BSA	Bovine Serum Albumin
CAD	Computer aided design
CK	Cytokeratins
CMC	Sodium carboxymethyl cellulose
dECM	Decellularized extracellular matrix
DEP	Dielectrophoresis
DI	Deionized
DNA	Deoxyribonucleic acid
DRIE	Deep reactive ion etching
ECM	Extracellular matrix
EDC	1-ethyl-3-(3-dimethylaminopropyl)carbodiimide hydrochloride
EFR	Extracellular matrix flow rate

## Chapter 0. Nomenclature

FACS	Fluorecent assisted cell sorting
FDM	Fused deposition modeling
H&E	Hematoxylin and eosin
HEPES	4-(2-hydroxyethyl)-1-piperazineethanesulfonic acid
IPA	Isopropyl alcohol
MES	Morpholino-ethanesulfonic acid
MBM	Mouse bladder medium
PBS	Phosphate buffered saline
PCL	Poly-caprolactone
PFA	Paraformaldehyde
ROI	Region of interest
SFR	Solution flow rate
SL	Stereolithography
UP3	Uroplakin III
UV	Ultra violet
WFR	Waste flow rate

# List of symbols

## Constants

Symbol	Description	Value	Unit
$g$	Gravity on earth	9.807	$[m/s^2]$
$k$	Boltzmann constant	$1.38 \cdot 10^{-23}$	$[m^2 \cdot kg/s^2/K]$
$\rho_{water}$	Water density	997	$[kg/m^3]$
$\pi$	PI	3.1415	$[-]$

## Variables

Symbol	Description	Unit
$a$	Half channel width	$[m]$
$A$	Constant	$[-]$
$\alpha$	Correction constant for syringe pump error	$[-]$
$b$	Half channel height	$[m]$
$C_{out}$	Cell concentration at the output	$[cells/m^3]$
$C_p$	Heat capacity	$[J/m^3/K]$

## Chapter 0. List of symbols

$D_h$	Hydraulic diameter	$[m]$
$G_n$	Total Gibbs free energy	$[J]$
$G_{n^*}$	Maximum total Gibbs free energy	$[J]$
$G_S$	Surface Gibbs free energy	$[J]$
$G_V$	Volume Gibbs free energy	$[J]$
$g_V$	Normalized Gibbs free energy	$[J/m^3]$
$\gamma$	Surface energy	$[J/m^2]$
$h_V$	Enthalpy	$[J]$
$\kappa$	Flow ratio between $Q_w$ and $Q_{in}$	$[-]$
$L_f$	Latent heat	$[J/m^3]$
$l_{sheet}$	Withdrawn sheet flow size	$[m]$
$\mu$	Liquid viscosity	$[N \cdot s/m^2]$
$\mu_c$	Concentrated solution viscosity	$[N \cdot s/m^2]$
$n_0$	Number of molecules in analyzed volume	$[-]$
$n_{cells}$	Number of cells	$[-]$
$n_r$	Number of mixed nuclei	$[-]$
$P$	Pressure	$[Pa]$
$\phi$	Volume fraction of occupied by particles	$[-]$
$\phi_{max}$	Maximum volume fraction of occupied by particles	$[-]$
$Q$	Flow rate	$[m^3/s]$
$Q_e$	Flow rate in extraction channel	$[m^3/s]$
$Q_m$	Flow rate in main channel	$[m^3/s]$
$R$	Fluidic resistance	$[Pa \cdot s/m^3]$

$r$	Spherical nucleus radius	[m]
$r_*$	Critical radius	[m]
$rcf$	Relative centrifugal force	[-]
$R_v$	Volume ratio	[-]
$\rho$	Liquid density	[kg/m <sup>3</sup> ]
$\rho[\nu]$	Phenomenological parameters [Quemada, 1977]	[-]
$s_V$	Entropy	[J/K]
$T$	Temperature	[K]
$T_m$	Transition temperature	[K]
$U_m$	Particle mean velocity	[m/s]
$U_p$	Particle migration velocity	[m/s]
$V_{in}$	Input volume	[m <sup>3</sup> ]
$V_{out}$	Output volume	[m <sup>3</sup> ]
$V_w$	Waste volume	[m <sup>3</sup> ]



# Introduction

Since the year 2000, the increased incidence of vital organ failure combined with rising success of organ transplant outcomes, induced a shortage of donated organs [Abouna, 2008]. Simultaneously, the democratization of additive manufacturing technology occurred as the main patents covering the field became public domain, resulting in the commercialization of a number of low-cost three dimensions (3D) printing machines and design software. Contemporaneously, a key biological discovery was made in 1997, highlighting the advantages of cell culture in a three dimensional matrix [Weaver et al., 1997]. The conjunction of these elements started the 3D bioprinting trend, which implements the simultaneous deposition of cells with a bio-material in which they can grow in a 3D environment, these elements being deposited in a layer by layer, organized fashion. This technology holds promise in numerous fields such as tissue engineering and regenerative medicine to produce cartilage constructs, skin or cardiac valves among others, as well as full organ printing for clinical uses, high throughput assays for drug screening with 3D tissues and cancer research opportunities [Ozbolat et al., 2016]. In 2011 bioprinting was at the beginning of the hype cycle with high hopes and expectations for the technology [Fenn et al., 2011]. The first bioprinting attempts showed promising results. However, after several years of research, most of the promises of bioprinting have yet to come to fruition. Those remain elusive for multiple practical reasons that will be further highlighted and addressed throughout this thesis.

## 1.1 Background

### 1.1.1 Additive manufacturing

3D printing, also commonly referred to as additive manufacturing or rapid prototyping, is a set of techniques that consist in building 3D parts layer by layer. This fabrication principle dates from the early 1980s [Kodama, 1981] and has seen a number of different implementations based on the use of multiple deposition techniques [Kodama, 1981]. Most

## Chapter 1. Introduction

common implementations are extrusion-based systems, material jetting, powder bed fusion processes or sheet lamination processes among many others [Gibson et al., 2015]. While photopolymers and thermoplastic polymers were initially used in 3D printing techniques, the range of materials that can be used has been significantly widened, and includes metals [Todd, 2018, Todd, 2018], ceramics [Eckel et al., 2016] and biomaterials [Hockaday et al., 2012a, Jang et al., 2018, Murphy and Atala, 2014, Kolesky et al., 2016, Pataky et al., 2012]. Current researches in this field include the development of “smart materials” [Sydney Gladman et al., 2016, Khoo et al., 2015, André, 2018] that can evolve with time and bring additional functions to the fabricated objects. If 3D printing was first used for automotive and aerospace applications [Guo and Leu, 2013, Chu et al., 2015], many other application fields currently use these techniques, including medical applications [Rengier et al., 2010, Prasad and Smyth, 2016, Bose et al., 2017, Davia-Aracil et al., 2018], prosthetics [Torabi et al., 2015], tissue engineering [Zhang et al., 2017, Wu et al., 2016, Dvir-Ginzberg et al., 2003, Zadpoor and Malda, 2017, Roth et al., 2004], biosensors [Lind et al., 2017], microfabrication [Vaezi et al., 2013, Au et al., 2016] or even construction [Salet et al., 2017] and the food industry [Kouzani et al., 2017]. With hobbyists now having access to 3D printing, it is likely that its field of applications will expand even more.

### 1.1.2 Bioprinting

Thanks to this recent democratization of 3D printers, the field of bioprinting is evolving at an unprecedented rate. New materials and printing methods are being developed, improving cell viability and structural stability [Kolesky et al., 2014, Pati et al., 2014]. The demonstration of cell-laden decellularized extracellular matrix (dECM) bioprinting further steered the aspiration toward tissue engineering as dECMs are capable of providing an optimized micro-environment conducive to the growth of three-dimensional structured tissues [Pati et al., 2014]. The lack of structural stability of these materials was mitigated by coprinting poly-caprolactone (PCL) framework as support, as illustrated in figure 1.1 A. Similarly to standard fused deposition modeling (FDM), extrusion-based bioprinting can benefit from sacrificial materials in order to produce overhanging structures. This concept was successfully demonstrated by [Skardal et al., 2010], using a combination of two bio-inks, tetra polyethylene glycol solution to culture cells and agarose as support material. The 3D printing of a tubular like structure was achieved as shown in figure 1.1 B and was successfully kept in culture for up to 28 days whilst retaining its original shape and keeping a high cell viability.

Thanks to those remarkable advancements in bioprinting techniques, bioprinting is now used to reproduce cartilage [Markstedt et al., 2015], skin [Lee et al., 2013, Vijayavenkataraman et al., 2017], blood vessels [Billiet et al., 2014, Xu et al., 2018] and more recently, skeletal muscles [Kim et al., 2018a]. Human scale tissue can currently



## 1.1. Background

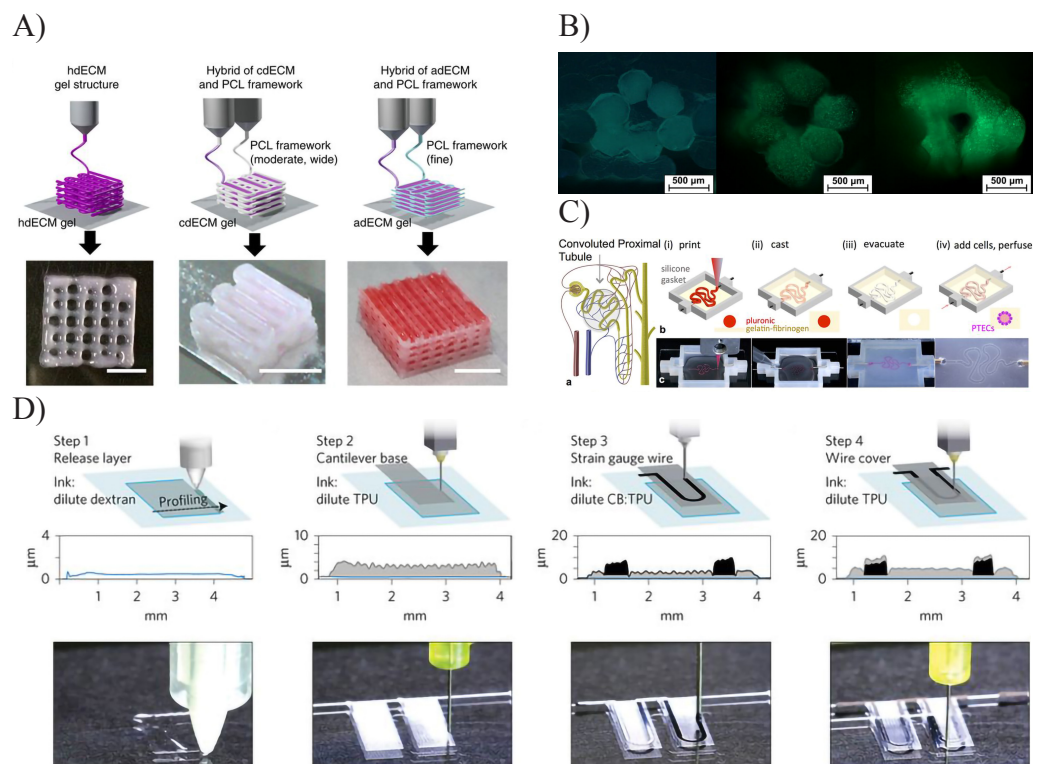


*Figure 1.1 – Bioprinted structures: A) Printed decellularized extracellular matrix with polycaprolactone support material (reproduced with permission from [Pati et al., 2014]). B) Tubular like structure made of TetraPac13-crosslinked hydrogel (reproduced with permission from [Skardal et al., 2010]). C) Bioprinted sacrificial pluronic as mould to produce a perfusable model of a kidney proximal tubule (reproduced with permission from [Homan et al., 2016]). D) Cantilever-based strain gauge for cell beating measurement printed with bio-materials (reproduced with permission from [Lind et al., 2017]).*

be printed, which was impossible a few years ago [Kang et al., 2016]. Additionally to additive manufacturing, bioprinting has also been used for mould creation as demonstrated by [Homan et al., 2016] where the shape of a proximal tubule (in the kidney) was bioprinted with sacrificial pluronic and casted with gelatin fibrinogen. The mould could then be dissolved and cells seeded to produce a perfusable model of a kidney proximal tubule on a chip as shown in figure 1.1 C. This revealed to be promising for the creation of customizable organ on a chip platforms for drug toxicity testing. Lately, the 3D printing of sensors using bio-inks was demonstrated [Lind et al., 2017]. A cantilever-based strain gauge was successfully printed (figure 1.1 D) and its surface properties could be adapted to produce the desired cellular phenotype allowing the culture of cardiac cells and the study of dose-response to drugs that influence contraction strength or beat rate, further widening the field of application of bioprinting

Among all the additive manufacturing implementations, four are frequently used for bioprinting, namely extrusion, inkjet, laser induced forward trans-

## Chapter 1. Introduction

fer (LIFT) and more recently stereolithography (SL) [Derakhshanfar et al., 2018, Vijayavenkataraman et al., 2018, Cui et al., 2017]. The working principle of each printing technology is illustrated in figure 1.2.

**Extrusion:** The working principle of extrusion-based 3D printing is relatively simple. The bio-ink is pushed through a tubing either by means of pressure or by using syringe pumps. The liquid is routed to a moving head and, in most cases, is dispensed on a surface through a simple needle. The moving head can then execute any movement in 3D thus dispensing the liquid in a 3D fashion to create the designed tissue, much like in standard FDM techniques. Because of this resemblance, open source FDM printers can be bought at a low price and transformed to accommodate bio-ink compatible extrusion tool. This method is simple and can be operated with a wide range of printing speeds and bio-ink viscosities. It also allows multi-material printing and is compatible with the handling of cells, which explains its success in 3D bioprinting. Extrusion-based 3D printing is paving the way in bioprinting and most of the works presented earlier were made using extrusion-based 3D bioprinting.

**Inkjet:** This techniques consists of creating a disruption in a micro-channel filled with bio-ink. This disruption, usually created using either a piezoelectric actuator or a micro-heater, will travel along the micro-channel and expel a droplet of liquid at the outlet. This printing head can then be moved around and bio-ink droplets can be dispensed on demand on the surface below. Whilst this technology is very well mastered in the paper printing industry, it remains difficult to use for bioprinting as only a limited range of viscosities can be used thus limiting the choice of bio-inks as well as the maximum printing height as it will be further discussed in chapter 4. However, good precision in positioning the cells on the printing bed can be achieved with this method and successful 3D prints were demonstrated [Pataky et al., 2012]. It was also proven that the disruption created to expel the droplet isn't harmful to cells [Xu et al., 2005]. Despite limited use, this technology remains of interest for printing on reasonably uneven surfaces as the dispensing tool can be kept a few millimeters off the surface.

**Lift:** Laser induced forward transfer is very similar to inkjet as a disruption is created to eject a droplet. Bio-ink is deposited over a donor substrate and laser can be aimed at any part of the plate to produce a droplet. Once the laser hits the donor plate, the energy is absorbed and a disruption is created, expelling a droplet on the printing bed. Moreover, the donor plate can be moved to deposit the droplet at a targeted location. Combined with a microscope, it is possible to aim at single cells with the laser and deposit them at a desired position on a substrate. Different droplet sizes can be produced [Duocastella et al., 2007] and two dimensions (2D) printing was successfully produced proving the feasibility and biocompatibility of the technique [Gruene et al., 2011]. However, being bounded to the same range of viscosity as inkjet, no truly 3D printed structures were successfully achieved. Nevertheless, this technology is of great interest for precise cell placement. Multiple cell types can be brought in close proximity and printed in a 3D environment

## 1.1. Background

allowing the study of co-cultures with defined organization to mimic *in-vivo* tissue environments.

**Stereolithography:** This printer implementation is completely different from the ones presented earlier. A bath of crosslinkable bio-ink is prepared and cured layer by layer using ultraviolet (UV) light. To pattern each layer, either a digital micro-mirror device is used providing relatively fast process with a resolution of about ten micrometers, or a laser scans the surface offering a higher resolution but longer process times. Two photon polymerization has also been tested offering nano-meter scale resolution at the expense of printing volume and speed [Vijayavenkataraman et al., 2018]. The high resolution that can be achieved by SL printing [Gibson et al., 2015] is fueling interest for this technology and starts to be used for bioprinting [Kim et al., 2018b]. However, its reduced biocompatibility resulting from the use of UV light coupled with the often toxic photo-initiators as well as the limitation to one bio-ink at a time in commercial printers and low cell concentration, limit the practical use of SL technology in bioprinting [Vijayavenkataraman et al., 2018]. Those constraints are being tackled and 3D hydrogel structures structure were printed without cells [Arcaute et al., 2006]. Despite having no seeded cell, those structures can find use in cell guidance enabled by the high resolution as highlighted by [Curley et al., 2011]. Moreover, SL bioprinting has been shown to be compatible to a certain extent with cells [Soman et al., 2013] and multi color printing was demonstrated in a research setting highlighting the possibility to change the printed material properties on the fly [Pet, 1996, Powell et al., 2018]. Applications have yet to be found for this method of printing but will certainly play an important role in the future of bioprinting.

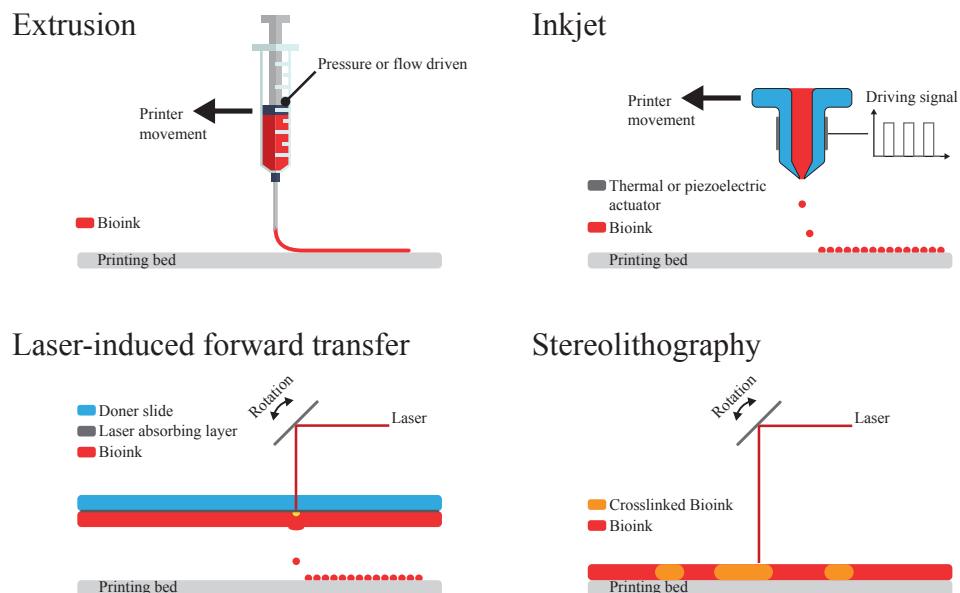


Figure 1.2 – Working principle of most common additive manufacturing techniques used for 3D bioprinting.

## Chapter 1. Introduction

There are several other emerging biofabrication strategies [Pedde et al., 2017]. Those methods could be used to generate specific types of cell-based tissues such as tendons or blood vessels using textile-based bio weaving [Akbari et al., 2016]. However as mentioned earlier, among 3D printing methods, extrusion-based processes are increasingly popular [N. Turner et al., 2014] as they are relatively cheap, easy to use, thus with a wide range of bio-ink viscosities, and with biocompatible materials. They enable relatively fast prints in large printing volumes. However, this printing technique suffers from its limited types of printable materials as only fast crosslinking materials can be used for bioprinting and very little improvements have been made to address this particular issue.

### 1.1.3 Biomaterials

High print quality, such as high resolution, high aspect ratio and complex structures was achieved using standard additive manufacturing techniques. The choice of printed material is often a key parameter to this print quality. However, unlike for standard additive manufacturing, where the inks are chosen and engineered to provide the best mechanical properties such as rigidity, fast crosslinking speed or quick solidification upon deposition in order to achieve the highest print quality, in bioprinting, bio-inks are primarily chosen for their biocompatibility and must be adapted to fit as well as possible printing requirements. Unfortunately better mechanical properties enabling high print quality often translate into poor biocompatibility. Very few biomaterials exist that both integrate seamlessly with bioprinting hardware and are optimally compatible with living cells [Skardal and Atala, 2014]. Figure 1.3 highlights some examples of bioprints. Agarose, alginate or pluronic F-127 produce good results in terms of shape. However these hydrogels are known to present poor biocompatibility in the sense that whilst not dying immediately, cells do not multiply or spread in these materials and ultimately die because of the lack of attachment sites in the hydrogel. In contrast, matrigel, gelatin methacrylate (GelMA) or collagen that are known to allow the growth of stable cell colonies and even promote organogenesis in the case of matrigel, do not produce high quality prints. The ability to print new kinds of biomaterials or the extrusion of multiple materials that fulfill support and cell hosting purposes separately as illustrated in figure 1.1 A is key for further advancement in bioprinting.

### 1.1.4 Smart dispensing

In addition to better bio-inks, the need for a higher printing resolution [Chia and Wu, 2015, Ozbolat and Hospodiuk, 2016, Duan, 2017] as well as a better control over the printed material to answer the need to print complex structures for cells [Liu et al., 2017, Hardin et al., 2015, Nie et al., 2017] are often highlighted to further increase extrusion-based bioprinting capabilities. These enhanced functionalities will

## 1.1. Background

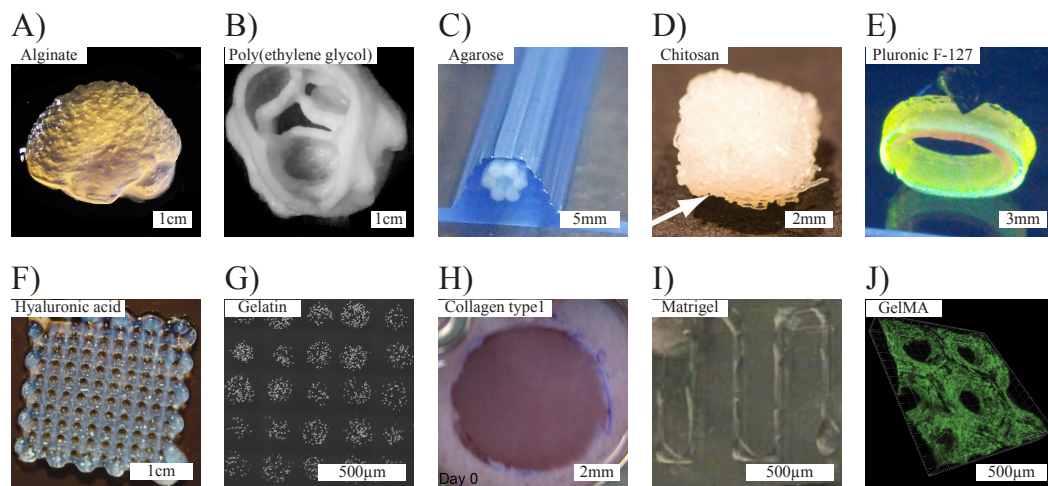


*Figure 1.3 – State of the art bioprinting of various bio-inks: A) 3D printed alginate brain shape with anatomical features (reproduced with permission from [Hinton et al., 2015]) B) aortic valve construct bioprinted from PEG (reproduced with permission from [Hockaday et al., 2012b]) C) bioprinted agarose filaments (reproduced with permission from [Norotte et al., 2009]) D) 3D bioprinted chitosan scaffold (reproduced with permission from [Ye et al., 2014]) E) bioprinted Pluronic F-127 in a fluorescent tube (reproduced with permission from [Müller et al., 2015]) F) hyaluronic acid bioprinted grid (reproduced with permission from [Pescosolido et al., 2011]) G) bioprinted gelatin using laser direct-writing (reproduced with permission from [Raof et al., 2011]) H) collagen type I construct for skin tissue regeneration (reproduced with permission from [Michael et al., 2013]) I) single bioprinted GelMA monolayer (reproduced with permission from [Snyder et al., 2011]) J) 3D bioprinted hepatic carcinoma cell-laden Matrigel graft (reproduced with permission from [Gauvin et al., 2012]). The cleavage between easily printable material (A to E) and poorer printable properties (F to J) can be observed.*

be critical as it is observed that bioprinting increasingly aims toward regenerative medicine [Hospodiuk et al., 2017, Tan et al., 2017, Yu et al., 2016, Duan, 2017] and the development of 3D model systems in cell biology, which have recently emerged as important tools to study cellular behavior. This arises from the finding that cell physiology is quite different in a 2D versus 3D environment [Rhee, 2009] leading to more relevant cell phenotype in a 3D environment [Hakkinen et al., 2011]. Furthermore, the ability to put different cell types in proximity has been shown to enable complex structures formation [Kengla et al., 2015].

To answer these needs, the development of dispensing tools that can be fitted on a 3D extrusion-based bioprinter are being developed to replace simple needles that are often used as printing heads to dispense the bio-inks and cells. In figure 1.4 A, a multi-material dispensing head developed by [Liu et al., 2017] allows for the rapid switching between multiple bio-inks. It was used to print multi-color nanosilicate aqueous suspensions but also multiple cell types in 5% GelMA and 1% alginate allowing a greater control over cell positioning in the printed structure. The use of a temperature control system



## Chapter 1. Introduction

integrated in the printing head (figure 1.4 B) was demonstrated by [Billiet et al., 2014]. By controlling the extrusion temperature, the viscosity of the bio-ink could be varied, enabling higher printing precision of gelatin methacrylamide constructs by avoiding spilling of the bio-ink. To further increase printing resolution, co-extrusion needles were also developed as shown in figure 1.4 C. The printing resolution could then be modulated through flow focusing. Finally, using similar coaxial nozzles (see figure 1.4 D), multiple flow layers were produced by [Jia et al., 2016] allowing the direct printing of perfusable vascular constructs.

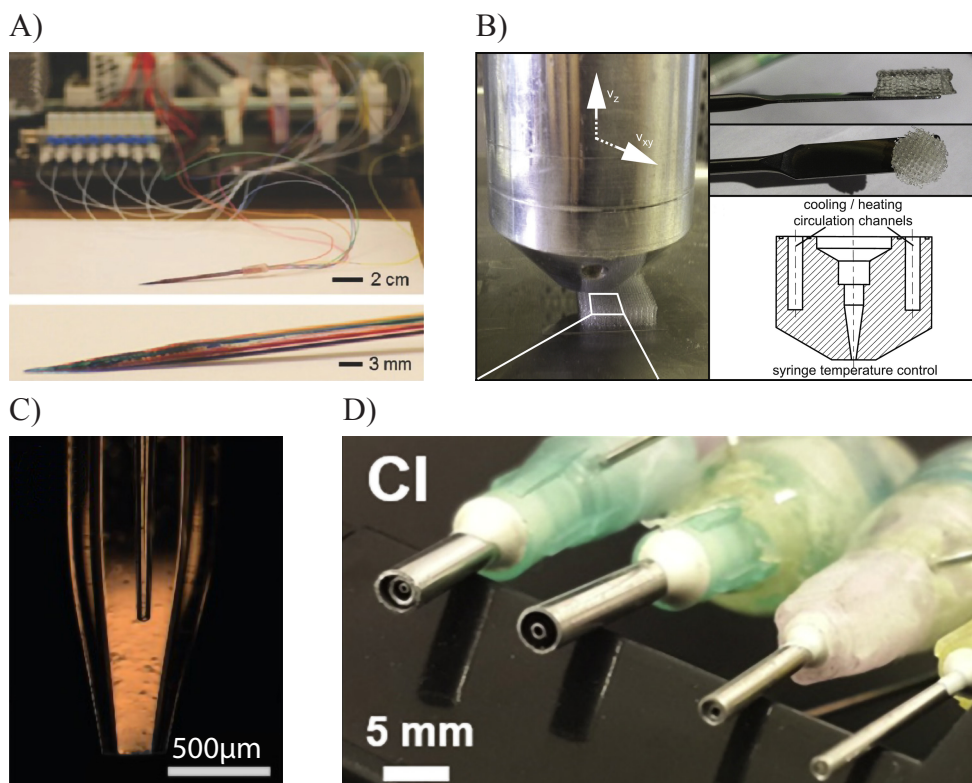


**Figure 1.4** – Improved dispensing tools: A) Concatenate capillaries produced a multi-material dispensing tool (reproduced with permission from [Liu et al., 2017]). B) Temperature controlled extrusion tool to enable the control over printed material viscosity (reproduced with permission from [Billiet et al., 2014]). C) Co-extrusion tool allowing the creation of coaxial flow. By adjusting sheet flow, the printing resolution could be tuned (reproduced with permission from [Nie et al., 2017]). D) Co-extrusion tool allowing the printing of multi-compartment fibers (reproduced with permission from [Jia et al., 2016])

Those printing heads, while bringing new functionalities to the bioprinter, remain limited as they are usually made from off the shelf material such as needles. This approach does not allow for much freedom and do not enable fine control over extra cellular matrix (ECM) dilution, creation of material gradient or control cell concentration for example.

### 1.1.5 Microfluidics

To further overcome these limitations, extrusion-based 3D printing can benefit from complex microfluidic systems, which can carry out a number of fluidic manipulation functions in the micro-scale. Microfluidic has seen major developments in past years, and has contributed to the emergence of the concept of “*Lab on a chip*” by allowing the implementation of many fluidic functions such as micro-mixers, [Stroock et al., 2002, Liu et al., 2004, Lee et al., 2011] switching valve, [Braschler et al., 2007, Liepsch et al., 1982, Devaraju and Unger, 2012] flow focusing, [Knight et al., 1998] particles focusing, [Martel and Toner, 2014, Xuan et al., 2010, Aoki et al., 2009] in-channel particles detection [Gascoyne and Jody Vykoukal, 2002] or particles and cell sorting [Gascoyne and Jody Vykoukal, 2002, Huang et al., 2004, Valero et al., 2010, Yamada and Seki, 2005] in compact, microfabricated devices.

The addition of microfluidic technologies to the bioprinter’s dispensing tool has the potential to enable the bioprinting of new materials, further improve printing resolution, enable easy creation of gradients, or enable manipulation of cells within the extrusion nozzle allowing to print at high cell concentration for example. Multi-material dispensing tools could ease the co-extrusion of multiple materials to fulfill structural support and cell hosting separately purposes. Microfluidic mixers can be implemented in the printing head to allow the printing of multi-component resins without prior mixing, overcoming the problem of aging of biomaterial in the printing cartridge [Malda et al., 2013]. Miniaturized sensors, detecting flow rate [Carsten Haber, Marc Boillat and van der Schoot, 2005], temperature [Lerchner et al., 2008], viscosity [Alveringh et al., 2017] or liquid composition [Rafeie et al., 2017], could also be used to obtain finer feedback control over the printing process.

## 1.2 Research strategy

### 1.2.1 Problem definition

Even though the requirements to produce high quality bioprints are complex, as of today, very limited control is possible on the bio-inks and cells being printed. This is partly due to a lack of functionalities in bioprinters’ extrusion head. These limitations can be addressed in part using microfluidics to produce probes that can be fitted as a printing head on an extrusion-based bioprinter. Those probes can utilize knowledge acquired by “*lab on a chip*” technology over the years and create “*lab on a tip*” where fluidic manipulations such as mixing, concentrating or measurements can be performed on bio-ink and cells thus just before printing. Probes to target specific hurdles in bioprinting can then be engineered.

## Chapter 1. Introduction

### 1.2.2 Research objective

Three main components are required in order to produce high quality bioprints. First, a source of cells that are readily available, easy to expand in culture, nonimmunogenic and that can reproduce all the functions of the tissue or organ system [Murphy and Atala, 2014, Berg et al., 2014] is needed. Second, biomaterials that are suitable for cell culture and allows embedded cells to express their full phenotype are needed. These biomaterials need to be shaped into a 3D construct mimicking the desired tissue. Finally, the complexity of organs must be reproduced. This requires the production of gradients of bio-materials with different properties, to place different type of cells at different places at different concentration in the tissue.

This thesis is an attempt to marry microfluidics with bioprinting to address some of these limitations. The objective here is to leverage the development made in the microfluidic field for "*lab on a chip*" and use these concepts to create smart dispensing tools for bioprinters. The probes will then be used in a biological setting to showcase the possibility of such a technology.

### 1.2.3 Thesis structure

Multiple dispensing probes were developed that address three of the current limitations in 3D bioprinting. In **Chapter 2** a microfluidic probe is developed allowing for the reliable 3D printing of cryogels. Despite being a promising bio-material, it has hardly been used in 3D printing because of the harsh synthesis environment. The development of a dispensing probe enabling the printing of cryogels demonstrates the use of "*lab on a tip*" to widen the range of printable bio-materials. In **Chapter 3** the cell concentration issue is addressed. As conveying high cell density through tubing poses multiple problems, a concentrator allowing the last second cell concentration of the printed solution is presented. The possible applications of the device are also further discussed in this chapter. Finally, in **Chapter 4** the material trade-off exposed above is addressed. In this chapter, the discussion of support material is presented and possible implementations are discussed. Moreover, in **Appendix H**, the assembly of multiple probes is demonstrated to produce a gradient of different material, highly useful in biology for cell proliferation and differentiation by using growth factor for example. Finally, in **Appendix I**, it is also demonstrated that "*lab on a tip*" can have applications beyond bioprinting. Smart printing heads that allow the use of new materials, enhancement of the print resolution, or allow the printing of composite parts and multi-material parts that were only possible using expensive 3D printing techniques are presented.



# Cryogels

## 2.1 Introduction

Cryogels are highly elastic hydrogels synthesized in a frozen state [Plleva et al., 2007, Okay, 2014], and possess a series of advantageous properties. They are mechanically robust [Bencherif et al., 2013], macroporous, [Plleva et al., 2007] and present high pore interconnectivity, [Hwang et al., 2010, Bencherif et al., 2013], shape memory [Newland et al., 2015] and injectability [Bencherif et al., 2014, Newland et al., 2015, Bédurier et al., 2015]. Cryogels are useful in a wide range of applications ranging from cartilage tissue engineering [Hwang et al., 2010] and neural repair [Bencherif et al., 2014, Bédurier et al., 2015] to vaccination [Bencherif et al., 2015] and blood filtration [Derazshamshir et al., 2016].

Yet, cryogels are rarely used as a material of choice for 3D bioprinting because of inherent difficulties in their synthesis. It is indeed not only necessary to freeze these materials on a cold substrate, but appropriate timing of the crosslinking reaction with respect to freezing is needed to guarantee their advanced properties [Bencherif et al., 2013]. Even so 3D printing of cryogels has already been demonstrated, [Pham et al., 2008, Adamkiewicz and Rubinsky, 2015] multiple key elements were not fulfilled to have an easy, repeatable printing. Indeed without last second mixing of the cryogels components, the crosslinking reaction starts in the printer's tank leading to a change in properties of the printed material over time. Those changes can have dramatic effect on the final material properties. Moreover, the lack of heater on the dispensing tool forces the use of high flow rates to avoid freezing of the solution inside the dispensing tool's channels. Because of those restrictions, the printing resolution is compromised leading to chaotic prints not suitable for tissue engineering and to a high variability in the printed material properties.

In this chapter, a microfluidic dispensing probe is presented featuring a microfluidic mixer for on-the-fly mixing of multiple components and allowing printing of cryogels

## Chapter 2. Cryogels

onto a cryogenic stage. The probe also features an integrated heating element that also acts as temperature sensor to control the deposition temperature of the liquid cryogel precursors avoiding these liquids to freeze within the probe. As it will be demonstrated in this chapter, the control of the dispensed solution's temperature allows for on the fly tuning of the pore size of the cryogels.

For bioprinting applications, it is important to control the interaction of cells with the printed gels [Frisch and Francis, 1994]. Cryogel based on carboxymethylcellulose inks do not offer noticeable cell adhesion *per se*, but provide a substrate for the display of specific cell adhesion molecules [Bédier et al., 2015]. Here, the known affinity of collagen type I to carboxymethylcellulose [Cundall et al., 1979] is used to provide the cryogels with an optimized sub-micrometric pore lining consisting of covalently attached collagen molecules. It will be shown that this provides efficient cell adhesion for the fibroblast line NOR-10 allowing cell culture in the printed cryogels. The local pore size modulation enabled by on-the-fly temperature control via dispensing probe will be used to produce preferential cell seeding areas allowing for selective cell seeding.

Finally the effect of pore size tuning on the microscopic structure of the cryogel will be assessed using differential scanning calorimetry coupled with a basic thermodynamic model. This chapter is in part based on the published paper entitled "Pore Size Manipulation in 3D Printed Cryogels Enables Selective Cell Seeding" [Serex et al., 2018b].

## 2.2 Probe design and fabrication

### 2.2.1 Specifications

To manufacture cryogels, monomer and crosslinker solutions must be dispensed at temperature below freezing. Moreover as a two folds decrease in reactivity is usually observed by ten degree in temperature drop, for the crosslinking reaction to occur in a reasonable amount of time at  $-20^{\circ}\text{C}$  a fast reaction is needed. Thus the compounds reacting must be mixed at the last second to avoid the crosslinking to occur before the solution is frozen. Finally, depending on the molecular weight and concentration of monomer, the bio-ink can become extremely viscous.

To answer the complex needs for cryogels 3D printing, two main functionalities will need to be implemented in the dispensing tool. First a micro-mixer will be implemented to mix all the components of the cryogel at the last second. To have a low risk of clogging and a simple fabrication process, a diffusion-based micro-mixer has been chosen. A suitable residence time providing adequate mixing and allowing for the crosslinking reaction to begin was chosen. The second implemented feature is a heater. A platinum track will be deposited on the backside of the dispensing tool. In addition to be a stable element, platinum has a large and linear temperature coefficient of resistance

## 2.2. Probe design and fabrication

[Belser and Hicklin, 1959]. A four-point configuration allows to supply power with a current to the tracks to generate heat and to measure the temperature through the voltage drop across the platinum track simultaneously.

The technology chosen to manufacture the cryogel dispensing tool is based on bonding micro-manufactured silicone wafers to glass. As silicon exhibits a high thermal conductivity of  $84\text{W}\cdot\text{m}^{-1}\cdot\text{C}^{-1}$ , higher than many metals, it allows to establish a homogeneous temperature within the probe even at its very tip, avoiding freezing. It also allows for the use of anodic bonding to close the channels. This bonding being one of the strongest known, it allows for the use of the high driving pressure required as the monomer used for carboxymethylcellulose-based cryogels have viscosity ranging from  $1\text{mPa}\cdot\text{s}^{-1}$  to  $20\text{mPa}\cdot\text{s}^{-1}$  depending on the molecular mass and concentration used.

### 2.2.2 Microfabrication

The micromanufacturing process flow is depicted on Figure 2.1.

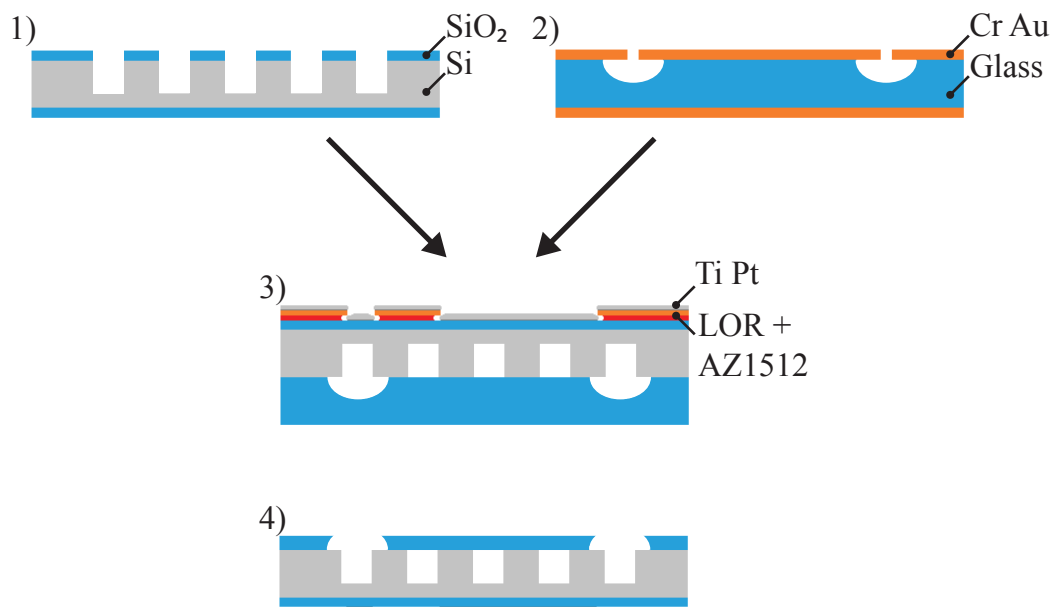


*Figure 2.1 – Cryo-probe process flow. Step 1, a double side polished  $380\mu\text{m}$  thick silicon wafer with  $500\text{nm}$  layer of wet oxide is patterned with the micro-channels layout. Step 2, a Borofloat<sup>®</sup> 33,  $145\mu\text{m}$  thick glass wafer is coated with a chromium and gold mask, is patterned with the inlets layout which are etched in hydrofluoric acid. Step 3, both wafers are aligned and bonded.  $20\text{nm}$  thick Titanium,  $380\text{nm}$  thick platinum tracks are deposited on the silicone wafer and structure via lift-off. Step 4, The glass wafer is ground to reveal the inlets and the probes are diced.*

## Chapter 2. Cryogels

A 500nm layer of wet oxide is first grown on a double-side polished silicon wafer and patterned to create a hard mask. The pattern is then transferred into the silicon through deep reactive ion etching to create 200 $\mu\text{m}$  deep channels (figure 2.1-1). The top layer of oxide is then etched away to expose the silicon for anodic bonding. The backside layer of oxide is kept for later insulation of the conductive tracks. Next, a borofloat<sup>®</sup> 33 glass wafer is structured to provide the future inlets of the probe. For this, four layers (chromium 20nm, gold 500nm, chromium 20nm, gold 500nm) are deposited by sputtering at high temperature to avoid pinholes in the hard mask and patterned using ion beam etching through 5 $\mu\text{m}$  thick patterned AZECI resist. The wafer is then etched in hydrofluoric acid to define the future inlets of the probe. The chromium and gold mask is subsequently removed chemically (figure 2.1-2). The glass and silicon wafers structured as described above are cleaned using a piranha etch and then bonded together by anodic bonding. To do so the wafers are put in contact right after the pirhana cleaning and placed in a furnace. They are heated to 420°C were both of their dilatation match to avoid any remaining constraint once cooled (This is true for borofloat<sup>®</sup> 33 glass wafers and silicon wafers). Finally 800V are applied to the system with the cathode on the silicon and the anode on the glass. The voltage is kept until the current drops below 2mA for a full wafer bonding, which usually takes 10 minutes. The wafers are let to cool down over night. The back side of the silicon wafer is then further processed to define the electric tracks. For this, AZ1512 on LOR resist is deposited and patterned to create a lift-off mask. 20nm of titanium and 380nm of platinum are then sputtered (figure 2.1-3) and the wafer is transferred into a stripping solution with ultrasound agitation to perform the lift-off. It is important to tune the electric track dimension to adjust its resistance to the electric power supply. If the resistance is too high for the electric source, it won't deliver the right amount of power and the probe wont heat properly. The glass wafer is then ground to open the inlets. The assembly is finally diced, allowing to open a lateral outlet (figure 2.1-4).

The dispensing probe produced is shown in Figure 2.2. On the front side two inlet channels are used for conveying the cryogel components toward the micro-mixer and one is designated for purging the probe with water. The micro-mixer is a meander 48cm long and has a 200 $\mu\text{m}$  by 200 $\mu\text{m}$  square section. Its residence time is 10s at flow rates suitable for 3D printing. Two squares empty areas reduce the surface in contact between the borofloat<sup>®</sup> 33 glass and the silicon wafers to enhance bonding quality. The outlet is on the transverse edge of the chip and is opened during the dicing step. This configuration allows the chip to be used vertically and to dispense the liquid on a surface during printing. The backside of the probe consists of the four point platinum track on a SiO<sub>2</sub> layer for insulation.

## 2.2. Probe design and fabrication

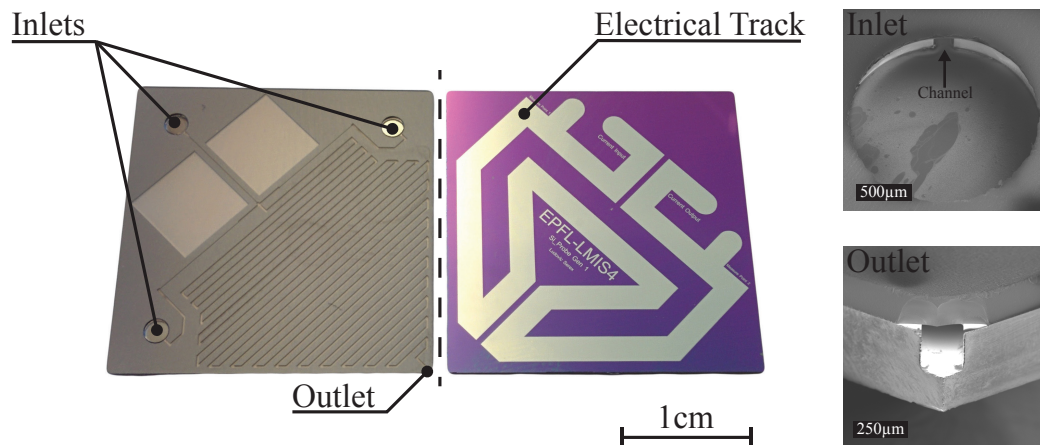


*Figure 2.2 – Microfluidic extrusion head for cryogel 3D printing. On the left image the front side of the device is shown featuring the three inlets as well as the meander used for mixing. In the middle the backside of the device is shown with the platinum track featuring four points for simultaneous heating and temperature measurement. The outlet is at the tip of the probe on its edge. Inlet with the start of one channel and outlet on the edge can be seen on the SEM pictures on the right.*

### 2.2.3 Experimental validation

The dispensing probe has a microfluidic part and an electric part for temperature control. The primary function of the microfluidic circuit is to ensure proper mixing of the liquids fed at the inlets, before they reach the tip of the probe. This was visually verified by injection of two dyed glycerol solution to mimic the cryogel monomer viscosity at the inlets and controlling their homogeneous mixing at the outlet. The results are shown in figure 2.3 where the two colored material can clearly be seen side by side at the beginning of the meander and getting gradually mixed downstream until an homogeneous solution is obtained at the outlet of the probe. This last-second mixing also contributes to the final cryogel pore size and structure.

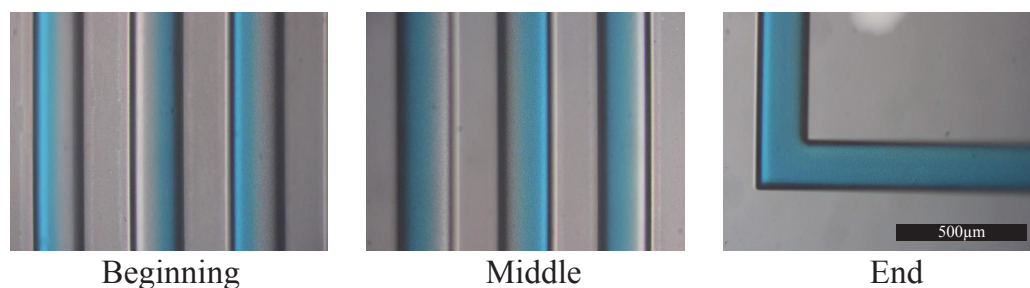


*Figure 2.3 – Optical micrograph of the meander mixer in the probe. White and blue glycerol solutions are injected at the two inlets and the homogeneity of the solution is monitored along the channel from the injection point on the left to the outlet on the right.*

## Chapter 2. Cryogels

One unexpected behavior of the probe was the hydrophilicity of the silicon and glass which attracts the cryogel solution at the tip of the probe as it is mainly water-based (see figure 2.4 A). This prevents proper dispensing of the solution on the printing bed. For practical reasons, a gap is provided between the probe and the bed much like in the case of the deposition of thermoplastic filament in standard fused deposition modeling. Thus, the solution, instead of being deposited on the bed will stick to the probe and form a droplet at its surface. The droplet will fall once it gets too big resulting in large drops deposited on the printing bed instead of a fine printed line. To prevent this behavior, an hydrophobic coating is applied to the tip of the probe. The probe is first cleaned with isopropyl alcohol (IPA) in an ultrasonic bath and rinsed with DI water. A 2 minutes oxygen plasma (5sccm at 100W) is performed to activate its surface. The tip of the probe is then dipped in a 10% 1H,1H,2H,2H-Perfluorooctyltriethoxysilane (667420-5G from Sigma) in Hexadecane (H6703-1L from Sigma) solution for 15 minutes. It is then rinsed using IPA and dried before use. The effect of the hydrophobic coating is shown in figure 2.4 B where water is now dripping out of the probe instead of sticking to it. Thanks to this coating, proper deposition on the printing bed could be achieved.

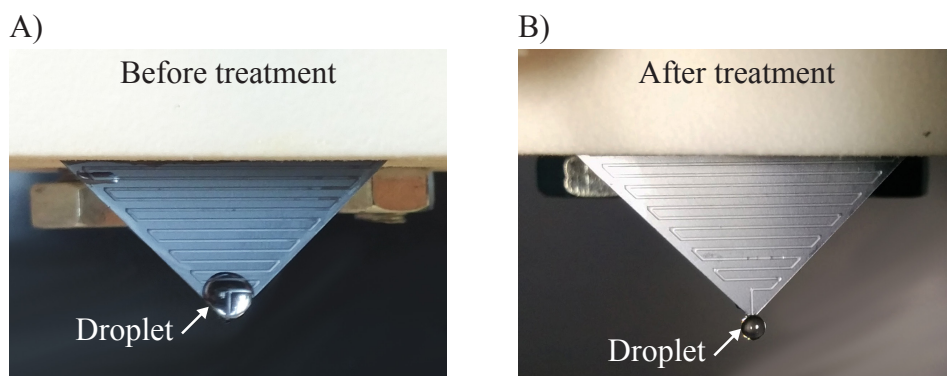


*Figure 2.4 – Hydrophobic coating at the tip of the probe enables proper dispensing of liquid onto printing bed. A) Water is dispensed through a probe without coating. Due to hydrophilicity of the silicon and glass the droplet sticks to the probe preventing proper dispense. B) Droplet of water at the tip of the probe after hydrophobic coating. The droplet hangs from the probe, facilitating its dispense.*

The probe heater can be fully characterized in two experiments. First the probe was tested with steady currents of different intensity and the track's resistance was measured. The probe temperature was calculated using the variation in resistivity of the platinum tracks with temperature. These measurements were confronted to infrared measurements to ensure their accuracy, using a Fluke TiRx thermal imager camera as presented in figure 2.5. Both curves can be fitted using a square model according to Ohm's law of thermal power  $P = R \cdot I^2$  where  $P$  is the dissipated power,  $R$  the platinum track resistance and  $I$  the flowing current. The mismatch between both curves can be explained by the fact that the probe is not a perfect black body thus leading to less infrared radiation at a given temperature.



## 2.3. Cryogel Synthesis

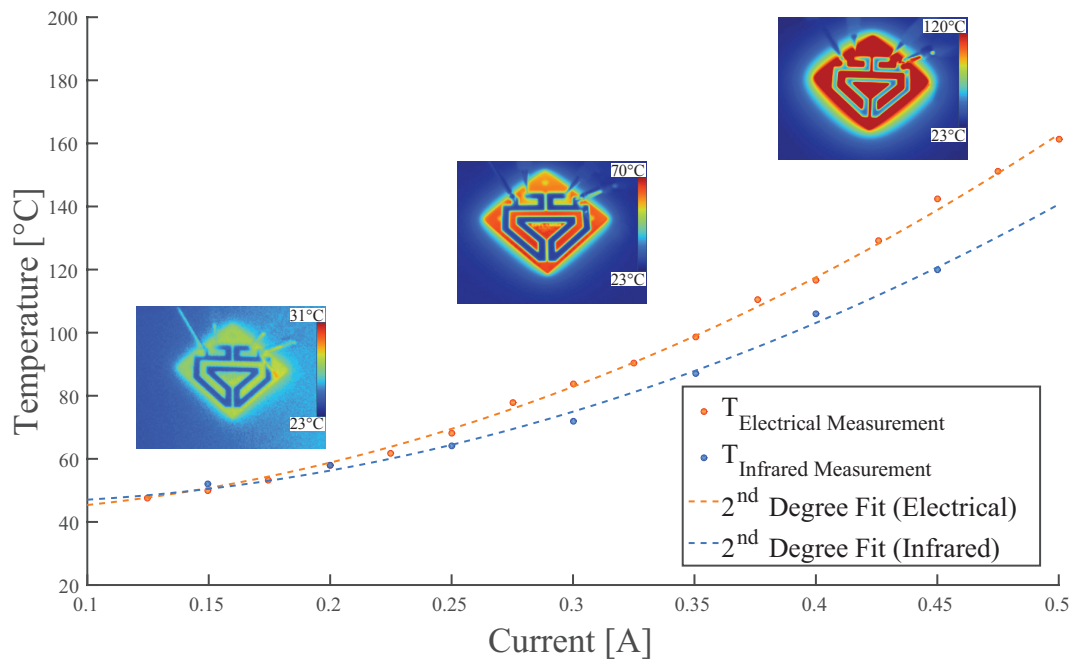


*Figure 2.5 – Temperature sensor characterization. Different constant current are applied on the input pads. The voltage is measured at the measurement pads. Due to the variation in platinum resistivity with temperature, the temperature of the probe can be computed from the input current and measured voltage. The electrical measurements are confronted with infrared measurements. Camera output pictures are displayed along the graphic to illustrate the heating of the probe.*

The transient thermal behavior of the probe was also assessed. Using a NI USB-6008 DAQ a current step was applied to the probe and the temperature increase of the probe using the embedded sensor was measured. Currents ranging from 150 mA to 600mA were applied. The results are shown in figure 2.6. The curves allow the estimation of the rate of temperature rise in the probe. Initially, it is over 15 °C/s at 600mA, with a time constant of  $6.46 \pm 0.08$  seconds. This means that by using a 1A source the probe can be heated up at a rate of 45°C/s. With such a temperature increase rate, and using PID regulation of the temperature, the probe temperature can be easily adjusted during the printing process.

## 2.3 Cryogel Synthesis

The principle behind cryogel synthesis is to crosslink a monomer below the freezing point its solvent. In the present case the solvent is water and the temperature at which the polymerization reaction must occur is below 0°C. Typically the actual operating temperature is -20°C, which induces a drop in reaction speed. Generally there is a two fold decrease in reaction speed by 10°C reduction of the temperature. However the advantage of crosslinking at temperature bellow freezing in water is that ice crystals

## Chapter 2. Cryogels

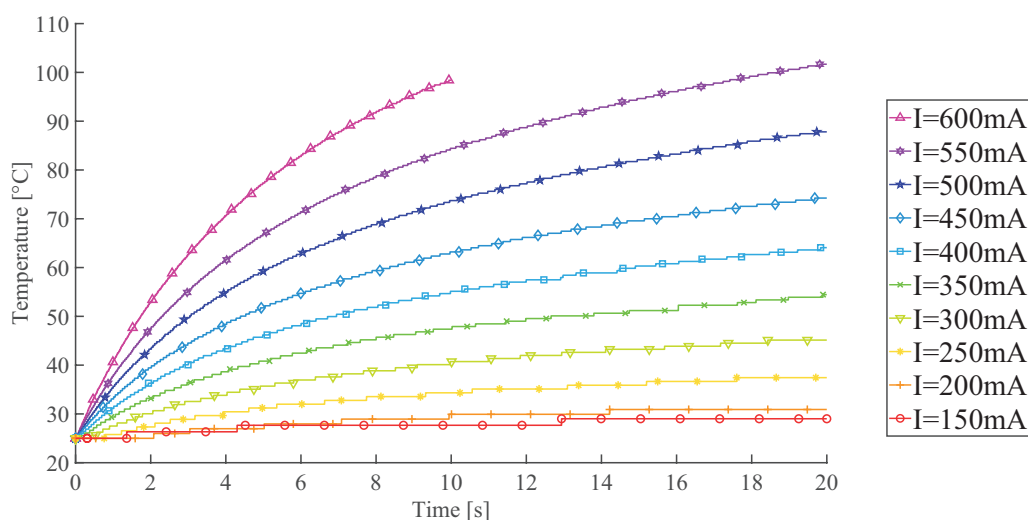


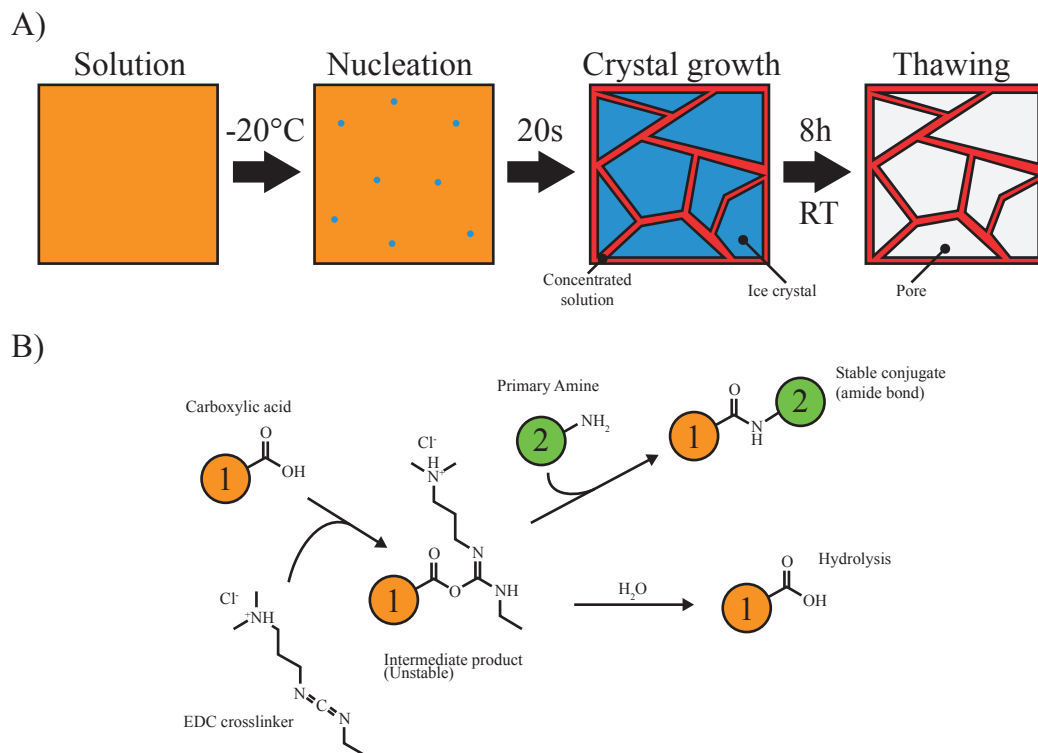
*Figure 2.6 – Probe dynamic thermal characterization. Current steps of different intensities were applied on the probe (from 150mA to 600mA) and the voltage evolution is monitored and converted into temperature measurements. The time response of the probe can then be computed.*

will form. Ice crystals are formed of water only [Halde, 1980] which concentrate all the monomer and crosslinker at the interface between the ice crystals. This phenomenon of cryo-concentration allows to have a high amount of monomer at the ice crystals interfaces thus speeding up the crosslinking reaction and producing dense polymer walls. Moreover once the reaction has occurred, the whole cryogel is thawed leaving a macro porous gel with pores placed where ice crystals were located as shown in figure 2.7 A. Those pores are inter-connected and their size depends on the freezing conditions as well as on the solution properties such as monomer concentration, monomer molecular weight, pre-crosslinking status, etc. [Okay, 2014].

Sodium carboxymethyl cellulose (CMC)  $M_w=250k$ , adipic acid dihydrazide (AAD), N-(3-dimethylaminopropyl)-N'-ethylcarbodiimide chloridate (EDC), 6-aminofluorescein, Morpholino-ethanesulfonic acid (MES), and 4-(2-hydroxyethyl)-1-piperazineethanesulfonic acid (HEPES) buffer were purchased from Sigma-Aldrich. All the following solutions are made in deionized (DI) water. A 2% in weight CMC solution and a 50mg/ml AAD solution were prepared in DI water and a MES buffer solution was prepared with an adjusted pH to 5.5. Upon mixing, the components will react following the reaction depicted in figure 2.7 B. The EDC will combine with carboxyl groups on the CMC to form an intermediary unstable molecule. It will then react with the amine groups on the AAD completing the crosslinking. However for the reaction to occur, the carboxyl group should be protonated and the amine not. The pKa of the carboxyl group is around 7 and the one of a standard amine is around 9. For the carboxyl group to be protonated, the pH must be lower than the pKa of the molecule. Therefore an amine with a low pKa must be used. Two different type of amine exhibit a low pKa.



## 2.3. Cryogel Synthesis



Aromatic amines can be used but they are unstable and toxic or a component from the hydrazine family can be used as their oxygen atom will stabilize the amine, lowering its pKa. Adipic acid dihydrazide typically has a pKa of 5 [Sigma Aldrich, 2019]. Therefore the crosslinking reaction can occur with a pH ranging from 5 to 7. It is important to note that for each crosslink reaction, a  $H^+$  atom is released thus rising the pH of the solution. To avoid a pH shift which would modify the reaction speed or even stop it, a buffer is added to the mixture. The buffer needs to be free from carboxyl which would react with the amine and free from phosphate which would react with EDC. MES (for low pH cryogels) and HEPES (for high pH cryogels) are good candidates for this purpose as they fill those requirements and their pKa (of 6.15 at 20°C for MES and 7.55 at 20°C for HEPES) is in the target range of pH needed for the reaction to occur. The full calculation is presented in appendix B.

The microfluidic probe has the ability to mix at the last second the components of the cryogel. Therefore cryogels at low pH can be used for printing. This is an advantage as at low pH (5.5), many carboxyl groups are protonated leading to faster reaction speeds whereas at higher pH (7) the reaction is slowed down. In adverse conditions, curing reaction can take more than a week at -20°C. Without the use of a micro-mixer, it is necessary to perform the crosslinking reaction at a higher pH as all the components

## Chapter 2. Cryogels

are mixed in the reservoir of the printer and a higher pH limits the occurrence of the reaction in the tank before printing. It is important to bear in mind that chemical reactions typically slow down by a factor of two every 10°C in temperature difference. Therefore at room temperature only a few hours of printing was possible before the components react in the tank and an extensive curing time was needed at -20°C. With a micro-mixer the components are stable in the tank and the curing time can be decrease to a few hours at -20°C.

However four components need to be mixed and some in small amount. The exact calculation for the amount of each components is presented in Appendix B. To simplify, some components are premixed to end up with only two solutions to mix. The separation of the components needs to be carefully through to avoid any unwanted reaction to occur within the syringes. The solution for syringe 1 contains 2mL of CMC solution with 28μL of AAD solution and 200μL of buffer solution and is loaded into a 2.5mL syringe from ILS (Stuetzerbach, Germany). The solution for syringe 2 only contains 10mg of EDC dissolved in 0.5mL of DI water, loaded in a 500μL syringe. Both syringes are placed on a neMESYS® syringe pump system and connected to the probe through standard tubing. To allow for confocal imaging, the cryogels need to be made fluorescent. The addition of 2μL of 1mM 6-aminofluorescein in the solution of syringe 1 produce covalently bonded dyes within the cryogel matrix allowing for its imaging under confocal microscopy. To prepare 6-aminofluorescein in DI water, NaOH at three times the wanted molar concentration of 6-aminofluorescein needs to be added to render it soluble in a polar environment.

One could be tempted to have CMC present in syringe 2 as well, which would allow to have the same volume in both syringes and use the same flow rates, thus without diluting the final CMC concentration in the final mix. However, by doing so EDC will react with the CMC and in absence of AAD, the intermediary molecule will get hydrolyzed thus depleting the EDC in the solution. The printed cryogels will be only partially crosslinked leading to cryogel without pores. Such a structure can be observed in figure 2.8 A whereas a proper cryogel structure with homogeneous pores can be seen in figure 2.8 B.

To print cryogels, the bed of the printer must be cooled down to sub-zero temperatures. An aluminum bed has been manufactured to fit in the printer. Using dry ice, the aluminum bed can be cooled down to -80°C. Then, a wafer with a conductive track similar to the one of the probe described earlier is placed on the surface of the bed, the bed temperature can be electrically adjusted from -80°C to -20°C by balancing joule heating and dry ice cooling while monitoring the temperature.

To obtain a uniform printing thickness it is important to match the injection speed with the printing speed. The used printing speed was 1cm·s<sup>-1</sup>. A flow rate of 110 μL/min for the CMC precursor and 22μL/min for the EDC solution is compatible with the printer

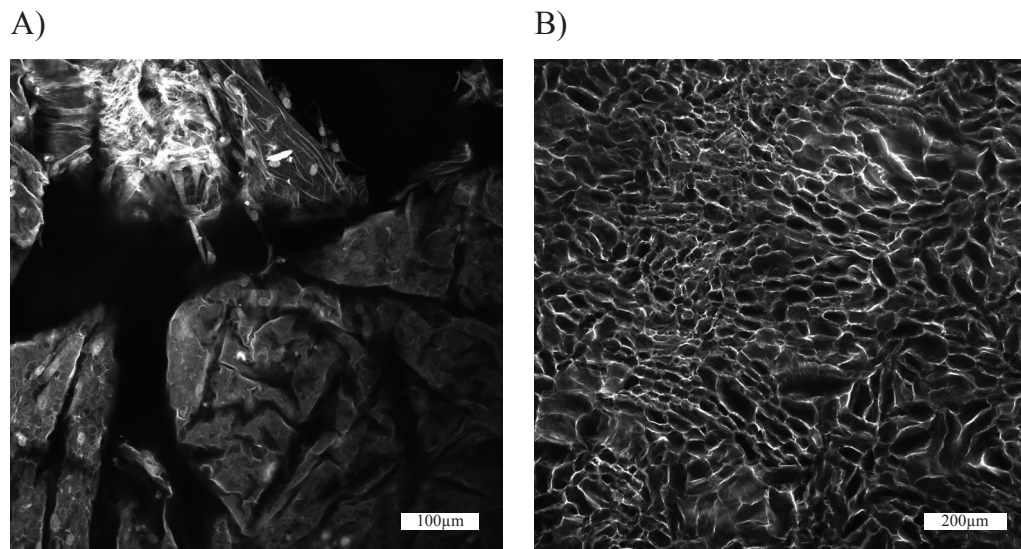


*Figure 2.8 – Confocal micrograph of cryogel structures. A) Unproper allotment of the chemicals in the syringes will lead to partially crosslinked cryogels that do not display coherent pore structure. B) When the chemicals are correctly allocated in the syringe, full reaction can occur under cryoconcentration leading to the highly interconnected structure intended in cryogels.*

settings, allowing to deposit a continuous line of material. The current in the probe is adjusted to tune the probe temperature, similarly, the bed temperature is adjusted by Joule effect and the printing sequence is started. Once the sequence is completed the manufactured gel is easily detached from the surface of the wafer and can be transferred onto a pre-cooled aluminum plate in a freezer. The cryogels are left for curing at  $-20^{\circ}\text{C}$  overnight and then autoclaved in phosphate-buffered saline PBS solution. They are then stored at  $5^{\circ}\text{C}$  in PBS.

## 2.4 Pore size tuning

### 2.4.1 Crystal growth and pores size

Cryogel pore size depends on many parameters, among them monomer properties, monomer concentration, cross-linker concentration and curing temperature [Okay, 2014]. Moreover, the degree of crosslinking of the monomer before freezing will influence the pores size as well. It was therefore hypothesized that a change of the probe temperature could change the pores size of the final structure by influencing the crosslinking speed thus the crosslinking state after the 10 seconds residence time in the probe before printing.

Another advantage of printed cryogels over bulk cryogels is the pore size homogeneity. It is known that in larger cryogels, pore size becomes very heterogeneous due to altered

## Chapter 2. Cryogels

thermal transfer with increasing distance from the cold source [Savina et al., 2016]. This leads to the fusion of the ice crystals far from the cold source. It can be seen on figure 2.9 A, B were a large disc of cryogel was synthesized in bulk. On the edge of the disk near the cold source pores are homogeneous but quickly merge together leading to elongated pores toward the center. This heterogeneity leads to poor strength of the cryogel and makes the control over the pore size impossible. It is possible to decrease these disparities in pore size by pre-cooling the monomer solution as well as by mixing while freezing [Savina et al., 2016]. However, for small structures it is difficult to apply local mixing. When the material is 3D printed, large ice crystals cannot form as the monomer and crosslinker are printed only in small amounts and frozen in a fraction of a second, only allowing the formation of small ice crystals. This results in a very homogeneous pore size distribution with variations of only a few micrometers in size between pores as seen in figure 2.10 C, D. Finally, printed cryogels were freeze dried and their porosity was measured using mercury porosimetry. It revealed a structure with a porosity above 91%, in part with literature, [Okay, 2014] suggesting a highly interconnected structure.

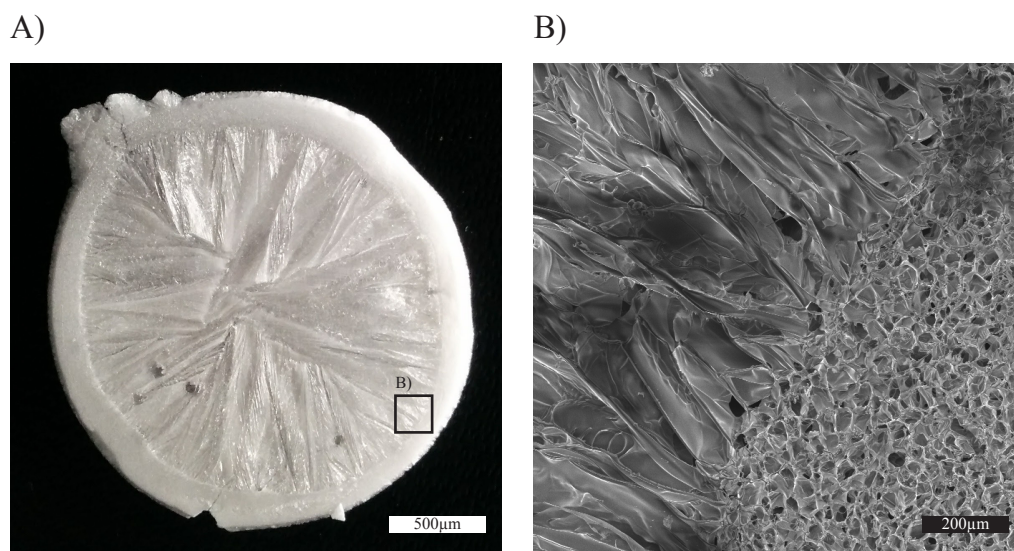


*Figure 2.9 – Bulk cryogel structure A) A 2cm in diameter disc of cryogel was synthesized in bulk in between two glass slides spaced by 500µm. The cryogel structure appears smooth on the edge of the disk but large pores forms and converge towards the center of the disk. B) SEM micrograph at the intersection between the smooth region and the large pores region reveals that small pores are actually merging together leading to the large pores.*

### 2.4.2 Cryogel pores size modulation

Using a confocal microscope coupled with image analysis, the average pore size of the cryogel printed on a  $-80^{\circ}\text{C}$  and  $-20^{\circ}\text{C}$  bed were evaluated. The data are presented in



## 2.4. Pore size tuning

figure 2.10 A, B respectively for three values of the probe temperature 25°C, 50°C and 100°C.

First, a change in the cryogel pore size can be observed for varying bed temperature, in accordance with literature [Okay, 2014]. More interestingly, the temperature at which the solution is printed has a major effect on the pore size as well. Higher probe temperatures are associated with significantly smaller pore size. The possibility to modulate the pore size by simply changing the probe's temperature is of major interest as it allows to rapidly print cryogels with local variations in pore size thanks to the low thermal time constant of the probe. The pore size achieved ranges from over 20 $\mu\text{m}$  (figure 2.10 C) which is suitable for cell culture, to 4 $\mu\text{m}$  (figure 2.10 D) where the cells get blocked by the gel whilst allowing the media and different cytokines to diffuse through it freely.

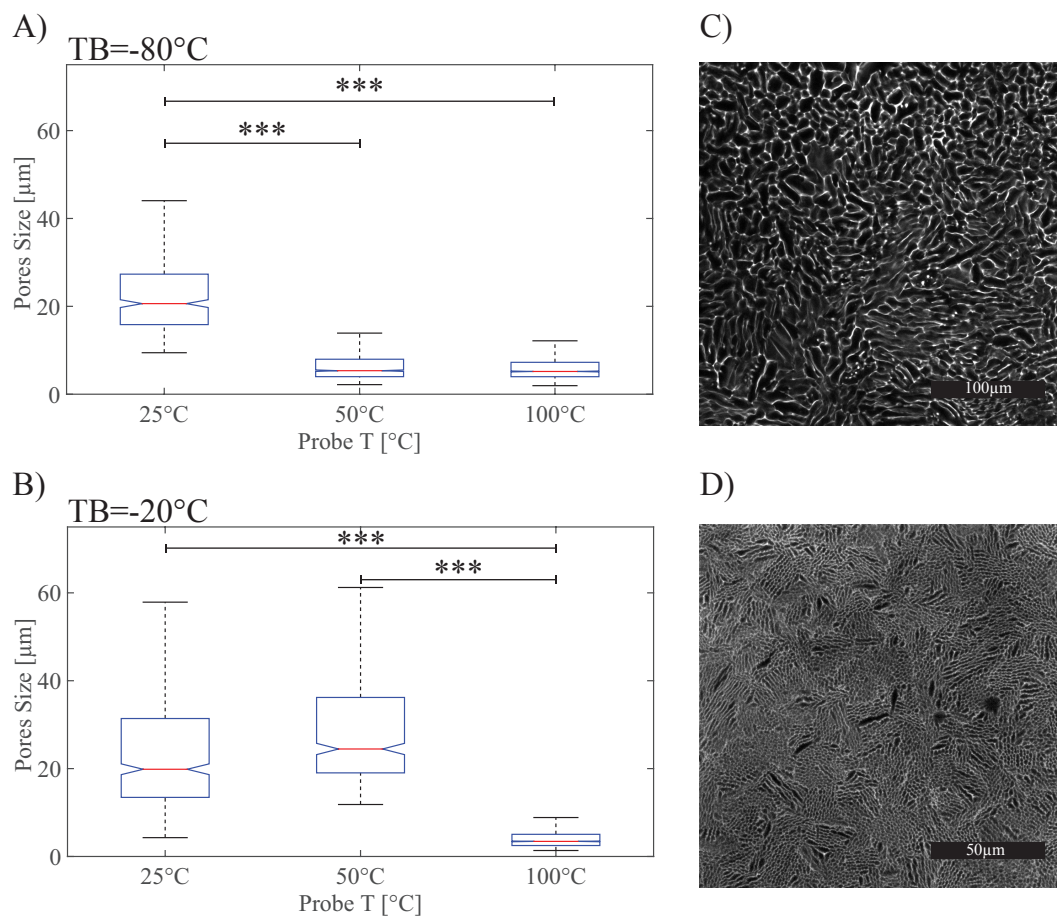


**Figure 2.10 – Pore size modulation in cryogel.** A) Pore size of cryogels printed on -80°C bed with the probe at 25°C, 50°C and 100°C B) Pore size of cryogels printed on -20°C bed with the probe at 25°C, 50°C and 100°C. \*\*\* indicating a p-value lower than 5%. TB=Temperature of the bed C) Confocal micrograph of large pores, D) Confocal micrograph of small pores

Three main phenomena dictate the crystal growth in the cryogel. A mechanical component of the crystal growth in a viscous solution, a thermodynamic and a kinetic

## Chapter 2. Cryogels

component, which dictate the amount of ice forming. The variation in pore size between the cold probe and the heated probe can be explained solely by mechanics. As the ice crystals are growing, water is removed from the premix in the direct vicinity of the ice crystals. The more the ice crystals grow the denser the monomer gets around them, which quickly increases its viscosity thus stopping the ice crystal growth and defining the crystal maximal size and thus the cryogel pore size. When the probe is heated, the premix is already partially crosslinked when deposited on the cold surface hence denser. The viscosity at which the crystal is stopped is therefore reached faster resulting in smaller ice crystal thus in an overall smaller pore size.

To further investigate if the phenomenon driving ice crystal growth is kinetics, thermodynamics or a combination of both, differential scanning calorimetry (DSC) was performed on various samples. DI water provided a base line for these DSC measurements as water has been extensively studied by DSC [Wilson et al., 1999]. A premix of cryogel was then measured. It consists of 3% 250kD CMC, similar to the one used for 3D printing, mixed with AAD and MES. This premix contains all the ingredients of the cryogel except the crosslinker. This sample provides a model of how ice crystal would grow in printed cryogels without the probe heating the premix. Another sample contained the premix with the crosslinker and the sample was left for crosslinking for 2 hours before measurement. This sample provides a model of the printed cryogel with the probe heating the material before printing. Finally, as the concentration of premix is low, a crosslinked scaffold was also measured. To do so 20 $\mu$ L cryogels were synthesized and freeze dried. They were then rehydrated with DI water. By controlling the rehydration, samples with high amount of crosslinked material (30% instead of 3% in crosslinked premix) could be analyzed, increasing the signal. The four samples were measured on a DSC 8000 (Perkin Elmer) with sample size between 20 and 30 mg. The measurements were adjusted for the drift of the machine using isothermal measurements, corrected for the scanning rate and normalized for the weight allowing to extract the heat capacity of the samples. To avoid super cooling problems, the samples were first brought to -60°C and a waiting period of three minutes was observed. The temperature ramps were made as followed: First heating from -60°C to -20°C at 5°C·min<sup>-1</sup>, from -20°C to -10°C at 2°C·min<sup>-1</sup>, from -10°C to -60°C at 1°C·min<sup>-1</sup>, from -6°C to -3°C at 0.5°C·min<sup>-1</sup>, from -3°C to 2°C at 0.2°C·min<sup>-1</sup>, and finally from 2°C to 10°C at 2°C·min<sup>-1</sup>. It is important to increase the temperature quickly at the beginning of each measurement because at low temperatures, small amount of ice is melting and fast temperature sweep requires more energy thus provides a stronger signal. The heating rate is decreased around 0°C as a lot of energy is required to melt the ice. The measurements are presented in figure 2.11 A. As expected, a large amount of energy is needed around 0°C for melting the of ice. The heat capacity of water and ice measured are coherent with values found in literature. By integrating the surface under the curve, the latent heat can be evaluated to 3.345·10<sup>5</sup>J·kg<sup>-1</sup>, which is very close to values found in literature for ice. The small spikes along the curves are artifacts caused by the change of scanning rate. They come for the

## 2.4. Pore size tuning

PID regulation of the machine taking some time to reach the specified temperature ramp. Those artifacts do not influence in a significant way the measured values.

In figure 2.11 A the difference between DI water and premix and more interestingly for this study the difference between uncrosslinked premix and crosslinked premix is clearly visible. Where for water all the volume of the sample is frozen as soon as the temperature drops below 0°C, some water remains unfrozen until -20°C for the premix and until -30°C for the crosslinked premix and in higher quantity. The amount of unfrozen water at incubation temperature of the cryogel indicates a change in the wall thickness and composition as water left unfrozen remains between ice crystals creating thicker and less dense walls around the pores. At a typical incubation temperature of -20°C thicker walls are expected for cryogels printed with heated probe than cryogel printed with a the probe at room temperature.

Because of super cooling, those measurements were done by thawing the samples. In another experiment, the sample were frozen and multiple temperatures cycles between -10°C and -5°C were performed. These heat flow cycles are plotted in figure 2.11 B. This temperature range was chosen based on the previous measurements (figure 2.11 A) as in this range water is already melting. It can be seen that for the DI water the curve is flat indicating that no water is melting and that the ice temperature is changing whereas for the the other sample, water is already melting. Additionally all the curves are symmetric and centered around 0mW. In figure 2.11 C the area under the cooling curve is plotted in blue, whereas the area of the heating curve is plotted in red, demonstrating the similarity of these areas. Multiple cycles were performed and an error below 3% is observed on these measurements. This shows that the freezing process is completely reversible and the formation of ice crystals can be studied by thawing in this context. Furthermore even when analyzing the most concentrated samples (the rehydrated scaffold), no asymmetry can be detected, except for PID limitation of the machine, thus even at high scan rate (figure 2.11 D). Even so phase transitions are not instantaneous and have their own kinetics [Tobergte and Curtis, 2013], these observations indicate that the ice crystal growth is not limited by their kinetics but dominantly by thermodynamic processes. Finally, it is observed in figure 2.11 C that there is a small difference in energy needed to freeze the different samples. It can come from the added EDC in the case of the difference between premix and crosslinked premix or from monomer concentration differences for the case of the scaffold sample. Further DSC measurements can be made to reveal if the crosslinking of the CMC indeed changes its affinity with water and thus has an impact upon the cryogels' wall composition or if the affinity of the monomer remain constant during the whole crosslinking process. This differences being small especially between premix and crosslinked premix, they can be neglected as well and the process approximated to a pure thermodynamic process. From a thermodynamic point of view, ice formation is associated with a change in Gibbs free energy  $\Delta G_n$  from the passage of one molecule from one phase to another ( $\Delta G_V$ ) and the creation of a new interface ( $\Delta G_S$ ) [Tobergte and Curtis, 2013].

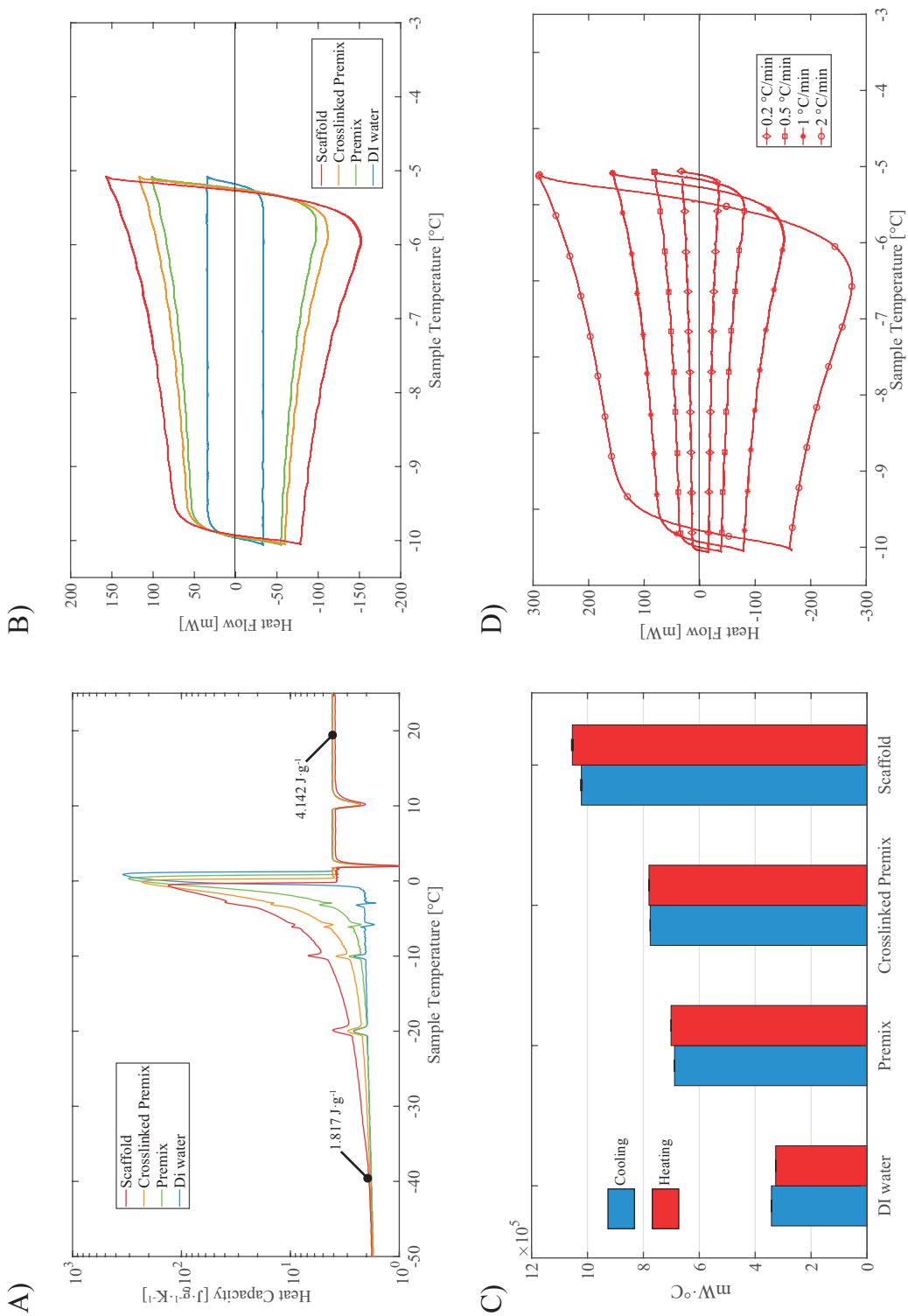


Figure 2.11 – Ice crystal growth analysis by DSC in DI water, cryogely premix containing all chemical but crosslinker, crosslinked premix and hydrated scaffold (60% mass of DI water). A) Heat capacity of the sample vs. temperature. B) Measured heatflow while cycling temperature between  $-10^{\circ}C$  and  $5^{\circ}C$ . C) Absolute value of the area under the curves in B while cooling in blue and heating in red. D) Measured heatflow while increasing scanning speed on the most concentrated sample (hydrated scaffold).



## 2.4. Pore size tuning

Using the Gibbs free energy definition, a simple model can be written assuming constant pressure and temperature.

$$\Delta G = \Delta H - T \cdot \Delta S \quad (2.1)$$

$$\Delta G_{water} = -\Delta G_{ice} \quad \text{at equilibrium} \quad (2.2)$$

With  $G$  the Gibbs free energy,  $H$  the enthalpy and  $S$  the entropy of the system. The second equation simply states that at equilibrium, the free energy of a molecule in the ice is inversely proportional to the free energy of a molecule in the remaining water. The enthalpy of the freezing water is well known for water and can be calculated by integration of the graph in figure 2.11 A over the temperature. A value of  $335 \text{ J} \cdot \text{g}^{-1}$  was found and corresponds to values reported in the literature. The entropy of the system at a given temperature can be retrieved from the same figure. It is therefore possible to calculate the free Gibbs energy for both uncrosslinked premix and crosslinked premix. At the printer's bed temperature of  $-20^\circ\text{C}$  the values are  $\Delta G_{uncrosslinked}=167 \text{ J} \cdot \text{g}^{-1}$  and  $\Delta G_{crosslinked}=215 \text{ J} \cdot \text{g}^{-1}$ . Where  $\Delta G_{uncrosslinked}$  and  $\Delta G_{crosslinked}$  represent the total free energy of the sample for uncrosslinked premix and crosslinked premix respectively. The free energy of the uncrosslinked sample is lower than the free energy of the crosslinked sample, indicating an environment more favorable to crystal growth within the uncrosslinked sample, resulting in thicker wall for cryogels printed with heated probe than cryogel printed with a the probe at room temperature as expected from figure 2.11 A.

This can be verified on the images of the structure of the cryogel obtained by confocal imaging (see figure 2.10 C and D). Using image analysis methods, the wall thickness was found to be 2.2 times smaller in uncrosslinked samples (cold probe) than in crosslinked samples (heated probe). The concordance between both these observations, optical micrograph of the structure as well as DSC measurements coupled with simple thermodynamic equations, further demonstrates that a thermodynamic model is appropriate in this case. It shows that heating the probe not only modifies pore size but also the thickness and density of the pore walls. Those modifications can have an impact on future coating of the cryogels as well as on cell behavior in the cryogel [P.Mecham, 2011]. More complex thermodynamic model would give further insight about the ice crystal formation. A model taking into account nucleation points is described in the appendix D. In figure 2.10 it was shown possible to tune the pore size of the cryogel even at incubation temperature of  $-80^\circ\text{C}$ . At this temperature, from figure 2.11 A, all the water is frozen. It should therefore be possible to tune the pore size of the cryogels without inducing modification in the thickness and density of the pore walls.

## 2.5 Cryogel 3D printing

The use of the probe enables the 3D printing of cryogels. To do so, a custom setup was built as shown in figure 2.12. A computer was used to control the 3D printer as well as a Nemesys syringe pump system to achieve precise flow control. The 3D printer was bought from He3D and customized to use the probe as printing head. A heated printing bed was made using the same technology as the one presented in figure 2.5. Dry ice was disposed on the bed to keep it at  $-80^{\circ}\text{C}$  and the heating bed allowed to precisely tune the bed temperature between  $-80^{\circ}\text{C}$  to above  $0^{\circ}\text{C}$ . Thereafter, the 3D printing of cryogels is similar to the 3D printing process of more conventional materials. The 3D geometry to be fabricated, described by a STL file, is sliced in layers. Each layer is sequentially fabricated by disposing material on top of the previous layer, using adequate manufacturing parameters. The resulting part was kept frozen for curing before thawing to reveal a macro-porous scaffold. Figure 2.13 A depicts the process of fabrication of a two compartments structure with an overhanging lid showcasing the probe capabilities. A major concern in 3D bioprinting is the interconnection between printed layers: when printing multiple layers the first layer needs to be solid before depositing the second one while at the same time providing an interpenetration of the polymer network between layers, required for layer adhesion. In the case of cryogels the layer are frozen but not yet crosslinked. Therefore the layers are hard enough to print on.

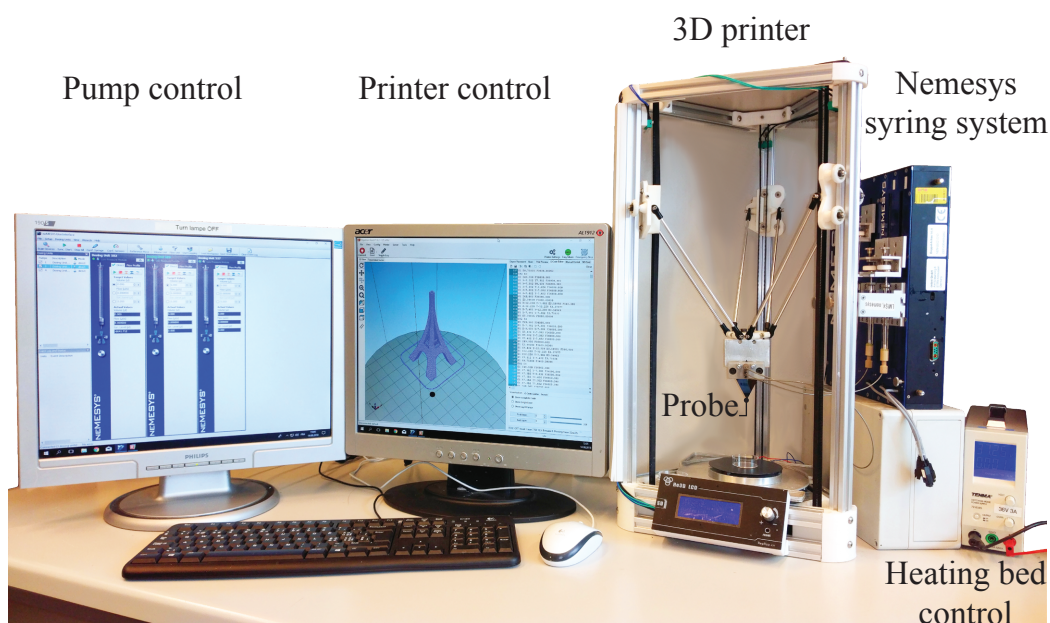


*Figure 2.12 – Printer setup. The computer control of the syringe and printer is on the left, the printer with a mounted probe and a heating bed is in the middle. The syringe pumps are placed vertically on the right of the printer and are located as close as possible from the printing volumes to limit dead volume in the tubing. On the far right there is a current source controlling the bed temperature.*

## 2.5. Cryogel 3D printing

The application of another layer melts the surface of the previous layer, mixing the gel components before refreezing. This results in a uniform block of gel with a continuity of the pores as shown in figure 2.13 B. Thus, once thawed, the printed part inherits very strong mechanical properties and extensive reversible compressibility of cryogels produced in bulk by molding [Bédurier et al., 2015]. These properties are mandatory to carry out the sterilization, washing, coating and seeding sequence described below, which produces high shear force on the cryogels. The micrograph also demonstrates how self organization of the cryogel ink leads to an intricate pore structure with micrometer thin walls even though the intrinsic resolution of the 3D printer is  $300\mu\text{m}$  because of the  $200\mu\text{m}$  nozzle opening and ink spreading.

By modulating the temperature of the probe during printing, areas with different pore

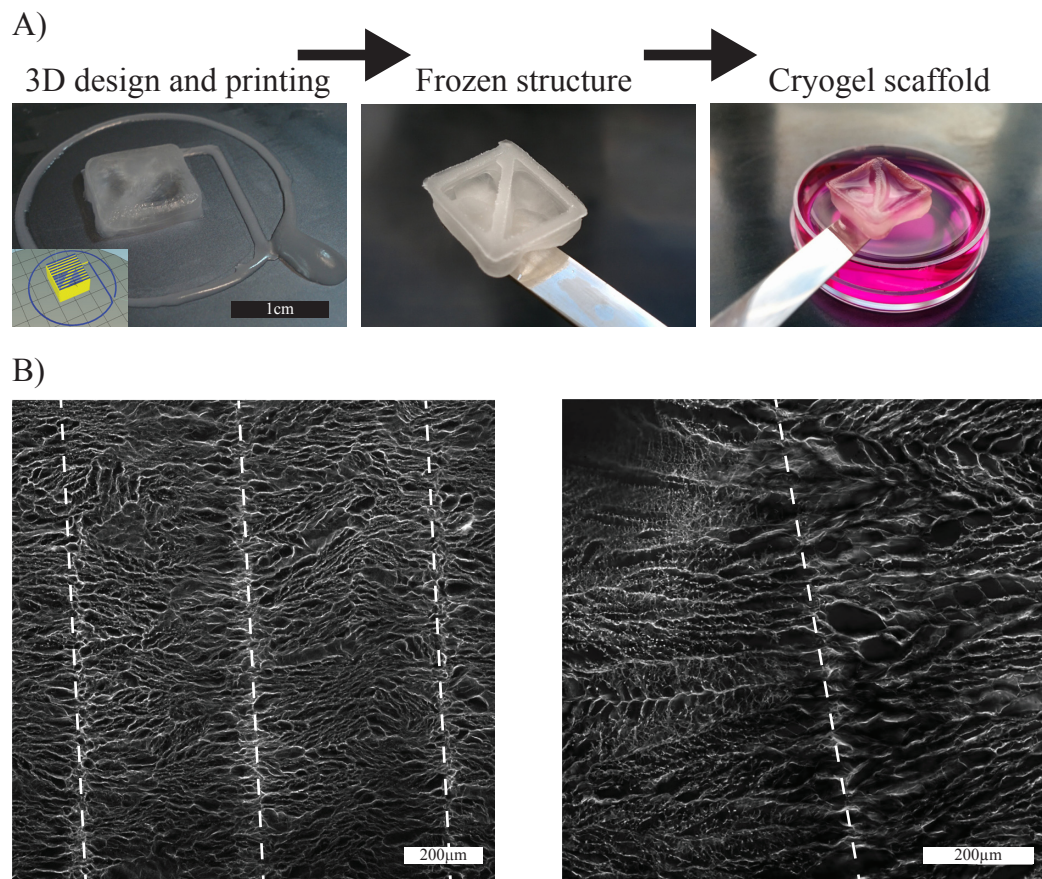


*Figure 2.13 – Example of a printed Cryogel structure. A) Sequence of fabrication of a 3D printed cryogel. A 3D path is created by computer aided design (CAD). Printing yields a frozen structure; after cryoincubation and thawing, the macroporous scaffold is ready for coating and cell culture. B) left, confocal micrograph highlighting the connection between printed layers B) right, a confocal micrograph showing the pore size transition from small pores (left) size to large pores size (right).*

## Chapter 2. Cryogels

sizes can be defined. Such change in pore size is shown on the micrograph presented in figure 2.13 C. The size of the pores changes by a factor ten between two consecutive layers. Furthermore, thanks to the ability to quickly change the temperature of the probe, this transition between small pores and large pores can be achieved at any position during the printing allowing to create pore size small enough to block cells, thus on multiple plans of the printed structure.

### 2.6 Collagen coating

CMC cryogels are not suited for cell culture as is. As their surface do not exhibit any cell adhesion marker, cells will not spread at their surface. To remedy this situation, a collagen coating protocol was developed. Collagen type I is common in the native tissue and provides support for most cells in the body [Alberts et al., 2002]. Therefore, a coating of this type would provide suitable adhesion queues for many types of cells. Full characterization of the coating and protocols can be found in the appendix C. The credit for the development of the coating on bulk cryogel for skin fibroblasts goes to Aleksandra Filippova and its optimization for 3T3 cells to Ariane Rochat. The coating has then been adapted for printed cryogels.

It is known that pH modulates collagen behavior and conformation [Freudenberg et al., 2007, Marelli et al., 2015]. In turn pH will have a major influence on how the collagen coats the surface of the cryogel. To assess the coating quality, fluorescent collagen (appendix C) and cryogel coated at different pH were imaged under confocal microscopy. The coating should be localized at the surface of the cryogel walls so that it is in contact with cells to be seeded later, it has to be homogeneous and the collagen shouldn't leach from the cryogels. The influence of pH over the collagen intake as well as the depth of penetration within the cryogel wall is shown in figure 2.14 A and figure 2.14 B respectively. Even so collagen absorption is high above pH=3 (figure 2.14 A), to obtain a surface coating it is important to coat at a pH close to 4 to avoid the collagen from percolating into the cryogel walls as highlighted by figure 2.14 B.

Figure 2.15 is a confocal image of the resulting coating at different values of the pH. The coating is uniform, with the highest collagen concentration (yellow-white) localized near or at the pore surface. At pH=2.5 (figure 2.15 A) the collagen can be seen on the whole pore wall thickness indicating collagen penetration into the CMC limiting the coating efficiency as all the collagen wont be in contact with cells. Worst, at pH=5 (figure 2.15 C) the formation of collagen fibers is observed, highlighting poor coating uniformity and creating the risk of pore clogging. The localization of the collagen in the vicinity of the pore lining at pH=4 (figure 2.15 B) lies close to the resolution of the confocal microscope used, demonstrating a second level of self organization in addition to the cryogel pore structure. At this value of the pH, the coating maximizes the collagen usage with maximum collagen intake and proper localization near the wall, were cells will adhere.



## 2.6. Collagen coating

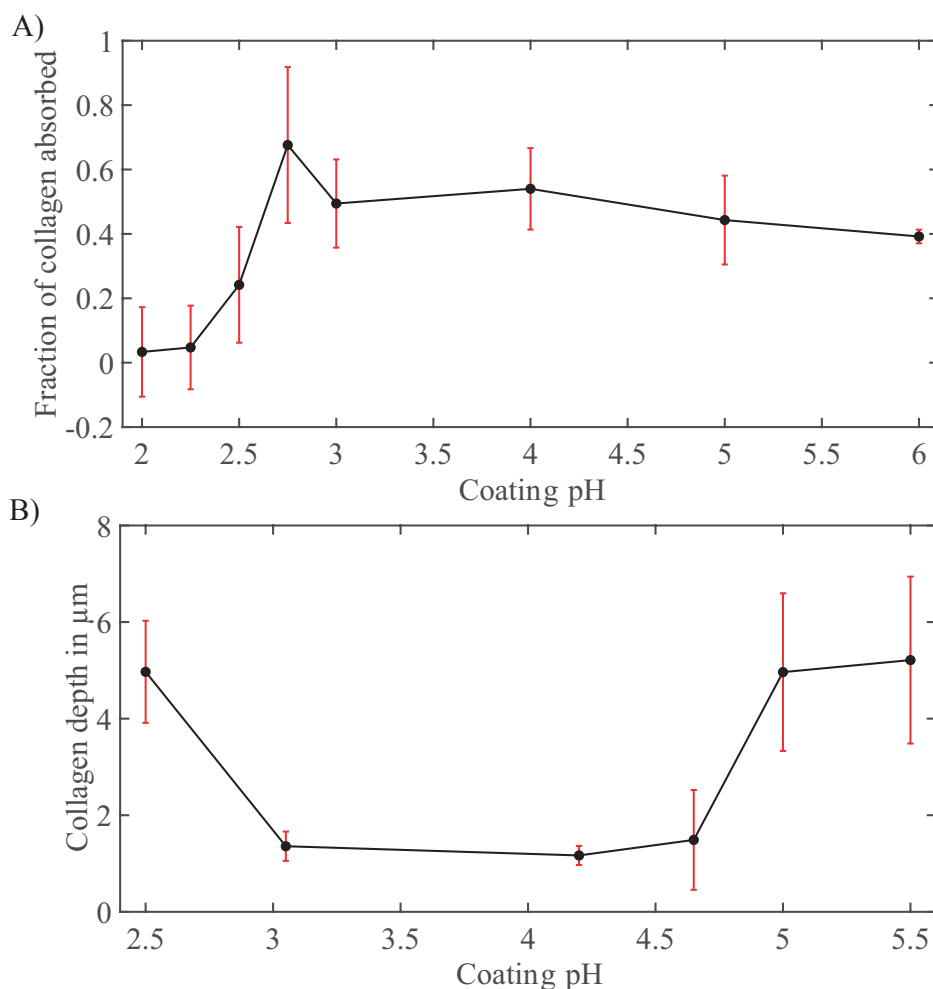


*Figure 2.14 – pH optimization for collagen coating. A) Fraction of collagen absorbed in the cryogel in function of the coating pH B) Collagen penetration depth in the pores wall as a function of the coating pH. Credit: Aleksandra Filippova*

To ensure permanent attachment of the collagen to the cryogels, EDC (1-ethyl-3-(3-dimethylaminopropyl)carbodiimide hydrochloride) is used to form stable amide bonds. The full protocol for collagen coating is presented hereafter. In this section each washing step corresponds to placing the cryogel on the membrane of a vacuum filtration device with a pneumatically applied depression of 1.5 kPa to empty the pores of the cryogel from liquid. Then the cryogel is placed in a chosen solution to fill the pore space. In this way a very uniform coating can be achieved up to the center of the structure. First the cryogels are washed with DI water. A second washing step is performed with 100mM sodium-acetate at pH=4. A solution of 1mL of 3mg/mL collagen in 10mM HCl (C4243 from Sigma-Aldrich) and 4mL 100mM sodium acetate is prepared, resulting in a 0.6mg/mL collagen solution. The cryogels are then placed once again on the vacuum filter at -1.5kPa and soaked in the collagen solution. The excess collagen is removed by two additional washing steps first in 100mM sodium-acetate at pH=4 then with

## Chapter 2. Cryogels

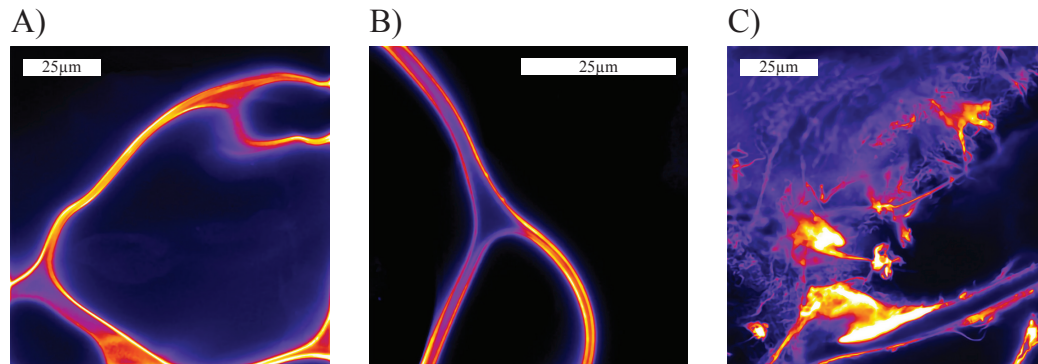


*Figure 2.15 – Fluorescent collagen was coated on cryogel and imaged using confocal microscopy. It allows for the visualization of the coating quality. A) Cryogel coated at pH 2.5 exhibits good collagen intake but the collagen has penetrated deep within the cryogel wall. B) Cryogel coated at pH 4 resulted in the best coating quality with large collagen intake localized at the wall surface. C) Cryogel coated at pH 5.5 creates collagen fibers. Credit: Aleksandra Filippova*

DI water. A solution of EDC 3mg/mL in MES 200mM pH=5.5 is then prepared fresh. The cryogels are placed on the vacuum filter at -1.5kPa and then soaked in the EDC solution to fix the collagen. Multiple washing steps are then performed in the following order. Washing in  $\text{Na}_2\text{CO}_3$  100mM then in a 1% amino ethanol solution followed by DI water, HEPES 0.5M at pH=7.4 and again in DI water. Finally, the cryogels undergo two successive washing steps in PBS. The cryogels can be stored in sterile PBS before cell seeding. The resulting conformation of the coated collagen has not been studied. This didn't pose any problem for cell adhesion with the cell types used in this work. However cell adhesion might depend upon the collagen conformation at the surface. If cell adhesion problems surfaced with the use of this coating in conjunction with other cell types, further investigation of the effect of pH and EDC on the collagen conformation could be made to further optimize the coating to specific cell types.

### 2.7 Cell seeding

Due to the harsh conditions of cryogel synthesis, autoclave sterilization, and coating, cells should not be printed simultaneously with the cryogel. However thanks to a porosity above 90% as well as good mechanical properties, cryogels are known to act similarly to sponges and cells can be seeded to their center [Bédurier et al., 2015]. Post-fabrication seeding of cryogels brings the advantage of not exposing the cells to harmful chemicals or ultraviolet light, which increases cell viability and reduce mutation. NOR-10 cells were passaged twice a week and cultured in DMEM media with 10% fetal bovine serum and 1% Penicillin Streptomycin, further referred to simply as "cell culture medium". The cells were used until passage 10 after purchase. For cryogel seeding, a suspension of 1 million cells per mL in culture media was prepared. The collagen-

## 2.7. Cell seeding

coated cryogels were placed on the vacuum filter and then soaked twice in the cell suspension for homogeneous seeding density. The cryogels were then placed in culture in 6 well plates with 2mL standard media for a week. Finally, cryogels were fixed after culture with 4% PFA, followed by cell membrane permeabilisation with 1% tween 20 (P2287 solution from Sigma-Aldrich) and stained with DAPI (Sigma-Aldrich D1306) and phalloidin green (A12379 from ThermoFisher) according to the manufacturers' protocols. The resulting gels were imaged using scanning electron microscopy (SEM) imaging and a LSM 700 inverted confocal microscope from ZEISS. On figure 2.16 a NOR-10 cell was captured using SEM imaging on a fixed, freeze dried and carbon coated cryogel sample. The cell (artificially colored in blue) adheres and spreads well on a pore surface. It is assumed that freeze drying does not alter the cryogel structure [Okay, 2014].

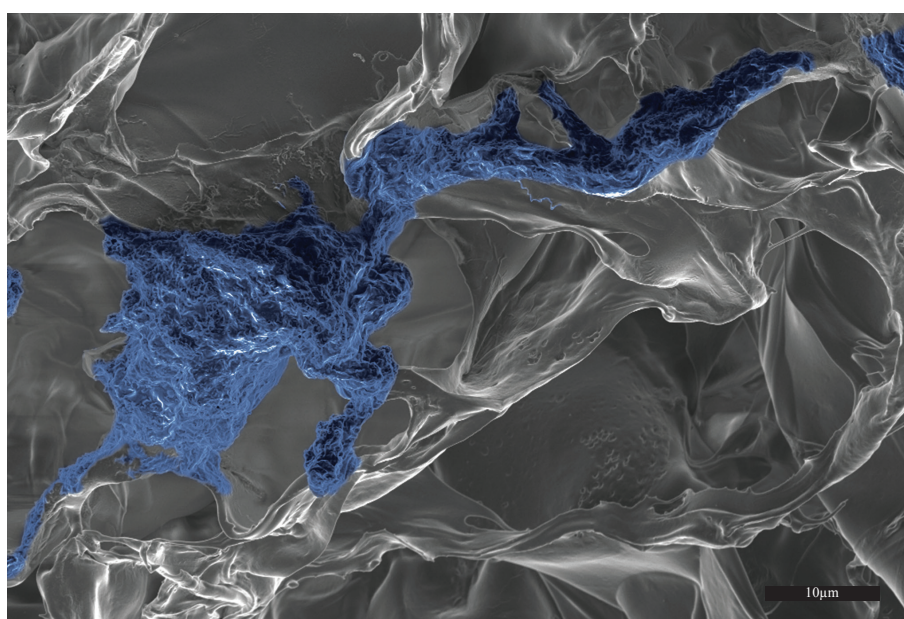


*Figure 2.16 – SEM micrograph of a NOR-10 cell adhering on a cryogel pore's surface*

To have a better view of the seeded cells, confocal microscopy is used as it is possible to image the cells in the bulk of the printed cryogel with a wider field of view than with SEM. Figure 2.17 A shows the cells seeded at the center of a 250 μL cryogel. Thanks to the high porosity of the cryogels as well as the seeding method, cells can be seeded to the center of our cryogel which is several hundred microns thick, with a good uniformity. This result demonstrates that the collagen-coated 3D printed cryogels provide a suitable environment for 3D cell culture. One major limitation when seeding cells in 3D printed cryogels is that the opportunity to place the cells in specific areas of the gel using the printer is lost. However, being able to tune the pore size at will, cells can be guided and seeded in specific places anywhere in the printed structure. As illustrated in figure 2.17 B, cells can only colonize sections of the cryogel with 25 μm pores but are stopped by 5 μm ones. In this way only a specific part of the cryogel can be seeded with cells.

## Chapter 2. Cryogels

Nevertheless the barrier created by the small pores remains permeable to nutrients and cytokines.

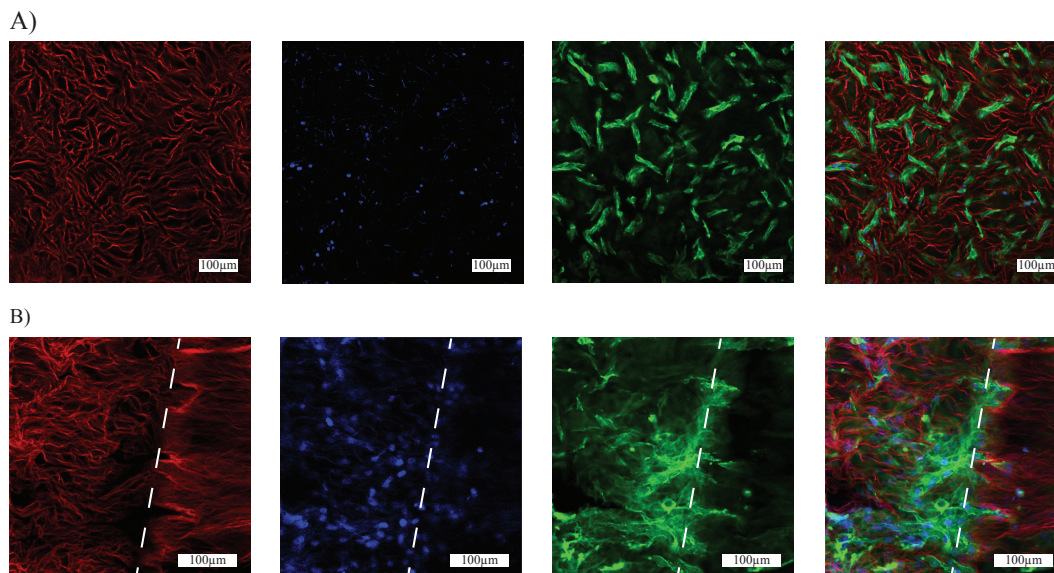


*Figure 2.17 – Confocal micrograph of cryogels seeded with NOR-10 cells. From left to right the staining are: cryogel structure in red (rhodamine), cells nucleus in blue (DAPI), actine in green (phalloidin) and all the channels merged. A) Inside of 25 μm pore cryogel section. Cells are evenly distributed in the cryogel and exhibit nice spreading. B) The transition from 25 μm pores to 5 μm pores forms a barrier for cells. The cells cannot spread further due to the small pore size. This result highlight the possibility to chose specific seeding areas based on the cryogel pores size.*

## 2.8 Conclusion

### 2.8.1 Summary

This first chapter presents the implementation of a printing head containing a micro-mixer for bringing into contact reactants while they are being dispensed, and an integrated heater and temperature sensor. This allowed printing of 3D cryogels with high repeatability. Moreover the electrical control of the probe temperature allowed rapid modulation of the local properties of the printed gels, in this case pore size. Thanks to the fast time response of the microfabricated probe, these changes in pores size could be produced on-the-fly, while printing. The self-organizing pore formation in cryogels [Pileva et al., 2007, Okay, 2014] allowed to generate local pore structures far beyond the resolution of the basic commercial 3D printer used. Such hierarchic organization has been reported for other cryogenic printing processes [Wang et al., 2017b]. Here, the use of temperature control allowed the probe allowed the local control of the pore size. DSC measurements as well as a simple thermodynamic model of the ice crystal formation within the cryogel during synthesis allowed for a deeper understanding of the mecha-



nism behind the pores formation and opened the door to further process optimization, potentially allowing better control over the pores size. In addition, the pore surface coating of collagen I adds another level of spatial organization, with sub-micrometric resolution. Cell culture was demonstrated to be possible in these cryogels using NOR-10 fibroblasts. The high porosity of the material makes it possible to seed cells up to the center of the structure post-printing. This two steps process of printing then seeding allows for the complete sterilization of the cryogel. Moreover the possibility to locally seed the cryogel through pores size tuning was demonstrated.

### 2.8.2 Discussion and outlook

The use of 3D printed cryogels of chosen pore size is of interest in various research domains. This material exhibits good mechanical properties and can be sterilized by autoclave, facilitating potential *in-vivo* uses. Cryogels can be compressed to a great extent [Bédurier et al., 2015, Bencherif et al., 2015], allowing the development of injectable 3D-printed cryogel structures [Bédurier et al., 2018]. The tunability of the pore size could also be used for filtering applications [Chen et al., 2017, Uygun et al., 2015]. The possibility to culture NOR-10 cells in selected regions of the printed gel was also demonstrated. Collagen coating was used to mediate adhesion of this fibroblast cell line, but if necessary, the coating could be adapted to host other cell types. For instance, cryogels can be coated with poly-L-ornithine PLO and laminin to permit culture of neural cells [Bédurier et al., 2015]. Using the methodology presented in this chapter, it may be possible to print multiple compartments where different types of cells can be seeded and cultured separately. Such type of design would allow the study of co-cultures in 3D, with different cells sharing common media and communicating through cytokines but never being in direct contact. This technique could therefore be used to evaluate different modes of cellular communication and their importance.

Finally, the formation of ice currently serves as an internal support during printing; after crosslinking and thawing, only the soft 3D printed cryogel suitable for cell culture remains. The microfabricated printing probe has a third inlet, through which pure water can be injected, transforming into ice in contact with the printer bed, for use as sacrificial layer. This opens the door to the fabrication of better overhanging structures than the ones done using capillary forces allowing the fabrication of perfusion pathways that could help seeding cells in centimeter large cryogels as well as surpassing the diffusion limit of nutrients for cells, making possible the fabrication of large scaffold for 3D cell cultures. Further work on gel mechanical stability is needed in the bio printing field [Hospodiuk et al., 2017] and the possibility to use computer assisted technology to blend in a smart way multiple materials could allow the printing of biomaterials with high cell compatibility and good mechanical properties. [Lee and Yeong, 2016] In this framework, cryogels could provide the structural stability, serve as cell seeding guides for larger structures as well as be an active scaffold (see appendix E) that can be blended

## Chapter 2. Cryogels

with other hydrogels to better mimic the complexity of native tissues.

Printing ice presents advantages as discussed before. However, it poses some challenges. For example, the higher the printed structure the slower it freezes (even in controlled environment as the thermal conductivity of the air is very low) this delay in freezing directly impacts the resolution of the printed structures because of surface tension. It is a major limitation of this technique. It could be improved by printing more viscous solutions in cold environment or in another immiscible cold liquid such as PFA with high thermal coefficient.

# Cell concentration

## 3.1 Introduction

Cryogels allow cells to be cultured in 3D printed structures. Despite being in a 3D culture, it is not clear whether the cells are locally in a 2D environment as they are adhering to the pore's wall surfaces. A popular approach to bioprinting is to print cells directly mixed with bio-ink, thus encapsulating them in ECM and insuring the cells interactions with their environment in all directions. This approach was used in various studies aiming at printing tissue such as blood vessels [Xu et al., 2018], skin [Vijayavenkataraman et al., 2017], liver tissue [Bhise et al., 2016] as well as structures with macro pores to favors nutrient distribution [Zhu et al., 2018]. Moreover, cells cultured in a 3D environment have been shown to better recapitulate cellular interactions seen *in-vivo* [Alhaque et al., 2018].

Usually, in the bioprinting field, to keep cell viability high, the printing cell density is low in order to reduce shear stress in tubing, which is detrimental to cells [Li et al., 2018]. It results in printed tissues with much lower cell density (usually neighboring 1 million cells per milliliter of solution) than typically found in the human body which has been estimated to 120 million cells per milliliter in average, considering a 75 kg average human [Bianconi et al., 2014]. This presents problems as inter-cellular communications heavily relies on inter-cellular distance [Bianconi et al., 2014] and thus on the cell concentration. It plays an important role in cell behavior as it influences proliferation, differentiation, and motion [Edelman, 1988, Lauffenburger and Horwitz, 1996]. Moreover as cells are seeded at low concentration, extremely long time in culture are needed to reach cell confluency in the tissue as the proliferation rate of cells is exponential [Iloki Assanga et al., 2013]. Increasingly, bioprinting is carried out at high cell concentration yielding better results. A high concentration of fibroblasts has been shown to alter the collagen matrix [Shigeto Abr, Beat U. Steinmann, Larry M. Wahl, 1979], microfibers with 10 million pancreatic cells per milliliter were shown to exhibit tissue morphology and functions such as islet formation and insulin secretion [Onoe et al., 2013] and

### Chapter 3. Cell concentration

high cell concentrations enabled the printing of cardiac [Hinton et al., 2015] and muscle tissues [Kim et al., 2018a].

However, working with high concentrations of cells in bioprinting is often inappropriate, as a large quantity of cells is lost in the printer dead volume, and the cells are subjected to large shear forces because of the high viscosity of the printed solutions. Concentrating cells right before printing is therefore of interest in the field of bioprinting.

As cell-cell communication is usually achieved through the secretion of soluble cytokines and chemokines, it is possible to estimate the minimum concentration at which communication is efficient by studying the diffusion of those cytokines and chemokines. Theoretical maximum cell to cell communication distance by diffusion has been calculated to be as high as  $250\mu\text{m}$  for a communication time of 10 to 30 minutes [Alsson, 1997]. However that diffusion coefficient depends on the cytokine molecular weight and the environment in which it is diffusing. This can increase the diffusion coefficient by two order of magnitude. *In-vitro*, shorter communication distances have been reported, in the range of  $40$  to  $60\mu\text{m}$  for endothelial cells [Lee et al., 1994]. Taking into consideration a concentration of 1 million cells per milliliter (which is standard in bioprinting), a distance of  $100\mu\text{m}$  separates each cell if the distribution is homogeneous. This distance is larger than the reported effective communication distance between cells in culture. Applying the same calculation to a concentration of 10 million cells per milliliter (which corresponds to high cell concentration 3D printing reported in literature) leads to a distance between cells of only  $46\mu\text{m}$ . This shorter distance is within effective communication distance for cells and was shown to produce printed components that exhibit tissue like morphology and functions. By concentrating cells at the tip of the printer, to at least ten million cells per milliliter, it would possible to print tissue with biologically relevant cell concentrations, without wasting a large number of cells in dead volumes or subjecting them to high shear stress. Furthermore, as cell have been observed to move away from each other after a division to remain in that communication range of  $40$  to  $60\mu\text{m}$  [Lee et al., 1994], the distance between cells will remain homogeneous and will rapidly decrease in tissue printed at higher cell concentrations, thus reaching confluency.

In this chapter, multiple focusing and concentration devices will be evaluated and a concentrator that can be used as a dispensing tool for an extrusion bioprinter will be designed and characterized. Solutions containing live cells will be concentrated at the tip of the printer allowing for the printing at high cell concentration without the hurdle to work with high cell concentration solutions. As a demonstration, NOR-10 fibroblast cells will be printed in a collagen solution demonstrating the use of such dispensing tools for bioprinting applications. Finally, the probe concentration capabilities will be used to print stem cells at different concentrations in order to produce bladder organoids. The collaboration with Kunal Sharma from the Laboratory of Microbiology and Microtechnology at the Ecole Polytechnique Fédérale de Lausanne on the organoid culture was crucial for the success of this experiment as he provided the cells, cell culture protocols as well as insight on staining protocols as well.

## 3.2 Concentrators design

### 3.2.1 Specifications and design choice

In the literature, microfluidic cell concentration devices are not very common, however there is number of paper presenting devices aimed at focusing particles inside a microfluidic channel. To this end, multiple physical phenomena can be used such as hydrodynamic effects, dielectrophoresis (DEP) or acoustic waves and have been demonstrated in various microfluidic settings [Xuan et al., 2010]. Once particles have been focused it is trivial to make a concentration device by simply removing the excess liquid, as demonstrated in figure 3.1. After focusing, the concentration is locally increased and the excess liquid is withdrawn resulting in an overall increase in concentration and a decrease in flow rate. However, most particle focusing devices have been developed to be used in a static environment, contrary to our case where the concentrator needs to work on a moving printing head. Moreover a minimum flow rate is required to achieve an adequate printing speed. Some concentration techniques do not work at flow rates compatible with printing or can not reach biologically relevant cell concentrations. Finally some concentration implementations can be difficult to use on a printing head depending on their size or complexity. To select and develop a suitable concentrating device, a thorough list of needs for the concentrator must be made and the existing focusing and concentration devices reviewed.

For a cell concentrator to work as a printing head of a 3D bioprinter, the following requirements need to be fulfilled. It should concentrate cells to above 20 million cells per milliliter to reach adequate cell concentrations close to *in-vivo* concentrations [Bianconi et al., 2014]. Because high accelerations can occur on the printing head during printing, the concentrator must be resilient to accelerations. The concentration device needs also to be small as a heavy and large printing head wouldn't be convenient. The concentrator should provide output flow rates close to  $5\mu\text{L}\cdot\text{s}^{-1}$  in order to have an adequate printing speed. Finally as the printing head is moving, easy to operate devices are preferred solutions.

Inertial focusing has first been considered as it occurs naturally in microfluidic channels and has already been exploited to make efficient focusing devices [Di Carlo et al., 2007]. In this phenomenon, particles or cells migrate across streamlines due to inertial forces at low Reynolds numbers. In straight channels this phenomenon is believed to be caused by the balance of lift forces due to the parabolic velocity profile and the interaction between the particle and the channel walls. However this process produces multiple focal points which in turn makes the collection of the particles problematic. Moreover, the process is particle size dependent, which would make the probe sensitive to the type of cells introduced. This is the case for multiple devices based on this concept presented in literature such as spiral channels [El Hasni et al., 2011, Xiang et al., 2018] or a bio-particle concentrator [Martel et al., 2015]. Moreover, inertial focusing is a slow

### Chapter 3. Cell concentration

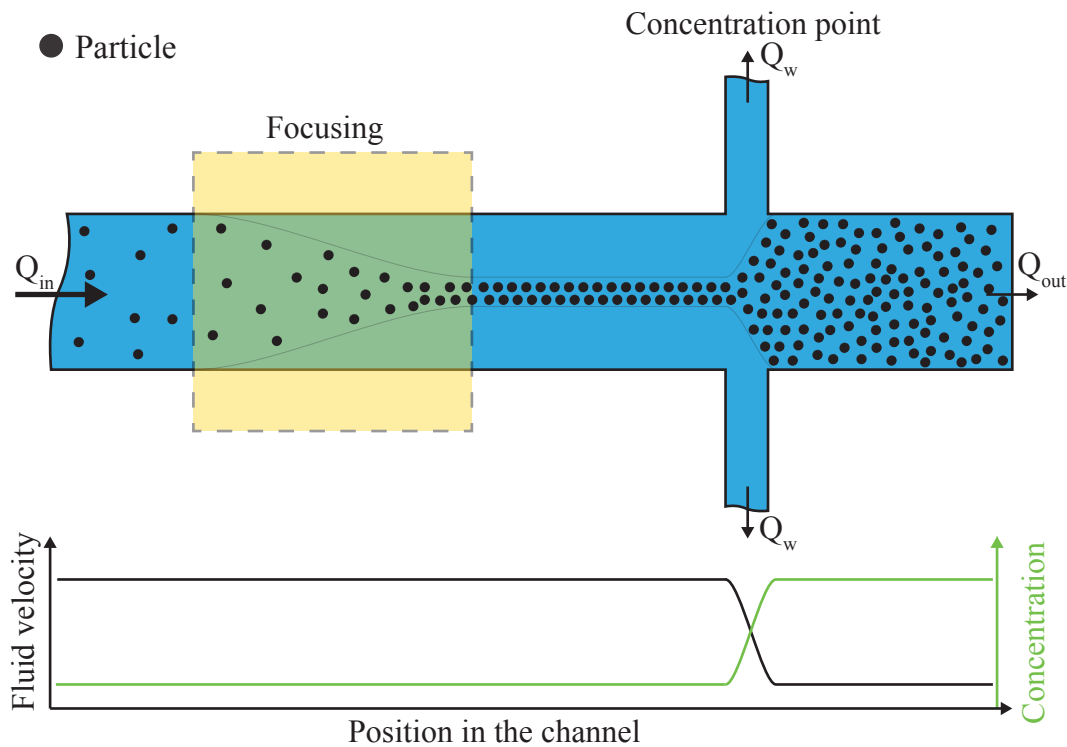


*Figure 3.1 – Working principle of a microfluidic concentrator device based on focusing principle. A flow with particles is injected in the device at a flow rate  $Q_{In}$ . The particles are then focused in the channel using any focusing principle, locally increasing the particle density. At the concentration point, the excess liquid is removed at a speed  $Q_w$ , effectively increasing the concentration in the channel. Finally the concentrated solution exits the device at a flow rate  $Q_{Out} = Q_{In} - 2 \cdot Q_w$ . A graphic of the concentration and fluid velocity along the channel is also provided.*

process. Using design rules from [Di Carlo, 2009] the minimal length for efficient inertial focusing can be estimated to over 37cm, which is not realistic to implement on a printing head. Finally, drop in concentration efficiency above 1 million cells per milliliter were highlight for concentrator based on this phenomenon [Martel et al., 2015].

Controlled incremental filtration, based on pushing particles through streamlines using regularly spaced pillars, can also be used to concentrate particles [Gifford et al., 2014]. However this process requires extremely long channels and any interaction between particles and pillars can impair the cell enrichment effect. Particles denser than its carrying liquid phase would not enter a vortex [Haller et al., 2015]. It is therefore possible to use vortices to guide particles or cells. This principle was used for plasma extraction [Haller et al., 2015] and particle focusing [Choi and Park, 2008] and could be used for cell concentration. However, vortices forms under very specific flow conditions, which could impair concentration reproducibility in printing configuration where flow must be started and stopped frequently. Extraction devices exploiting sedimentation were

## 3.2. Concentrators design

considered as they can achieve exceptionally high concentrations over a short distances thus whilst being easy to use [Forchelet, 2017]. However these devices might reveal to be too sensitive to the acceleration of the printing head. Active focusing devices using dielectrophoresis [Zhu and Xuan, 2009], light [Zhao et al., 2007] or acoustic waves [Shi et al., 2008] are also appealing but remain difficult to implement on a moving head and can be harmful for the cells as well.

Finally a hydrodynamic focusing based device presented by [Yamada and Seki, 2006, Aoki et al., 2009] would allow the concentration of particle very efficiently. Hydrodynamic focusing devices are very compelling and elegant solutions as they can be designed to be clogging proof and do not need any precise flow control. However the functioning mechanism as depicted in figure 3.1 is limited by the efficacy of the focusing. In point of fact, to obtain a factor 10 concentration in a  $200\mu\text{m}$  wide channel, the particles must be focused in a  $20\mu\text{m}$  zone at the center of the channel. The sheet flow, free of particles, can then be withdrawn, resulting in the wanted concentration. If the focusing is not as efficient as predicted or if the focused beam of particles is not perfectly centered in the channel, it could impair the concentration performance of the device. In regards of those difficulties, alongside with an hydrodynamic focusing design, a crossflow filter will be studied. Such a design has the advantage to be robust and have the potential to strongly concentrate particles. However such a device requires precise flow control and is subjected to clogging if not used properly.

### 3.2.2 Hydrodynamic focusing

#### Design, theory and calculation

It is possible focus particles in flow using hydrodynamic phenomena [Aoki et al., 2009]. The working principle of a particle concentrator using this technique is depicted in figure 3.2. The focusing part consists of multiple extraction channels that withdraw part of the liquid from the main channel to reinject it downstream. As both ends of each extraction channel are connected to the main channel, the pressure applied to the extraction channel depends upon the distance between the inlet and outlet of the extraction channel and on the fluidic resistance of all the channels between inlet and outlet. It is thereby possible to precisely control the flow passing through each extraction channel by tuning its fluidic resistance. The main objective of the extraction channels are to remove liquid from the main channel without removing particles. This goal can be reached by one of two means. The extraction channels can be design smaller than the particle diameter but it would render the concentrator vulnerable to clogging. Conversely, it is possible to limit the size of the withdrawn sheet flow to smaller than the particles radius. In that case even with wide extraction channel, no particle should enter the extraction channel [Yamada and Seki, 2006].

### Chapter 3. Cell concentration

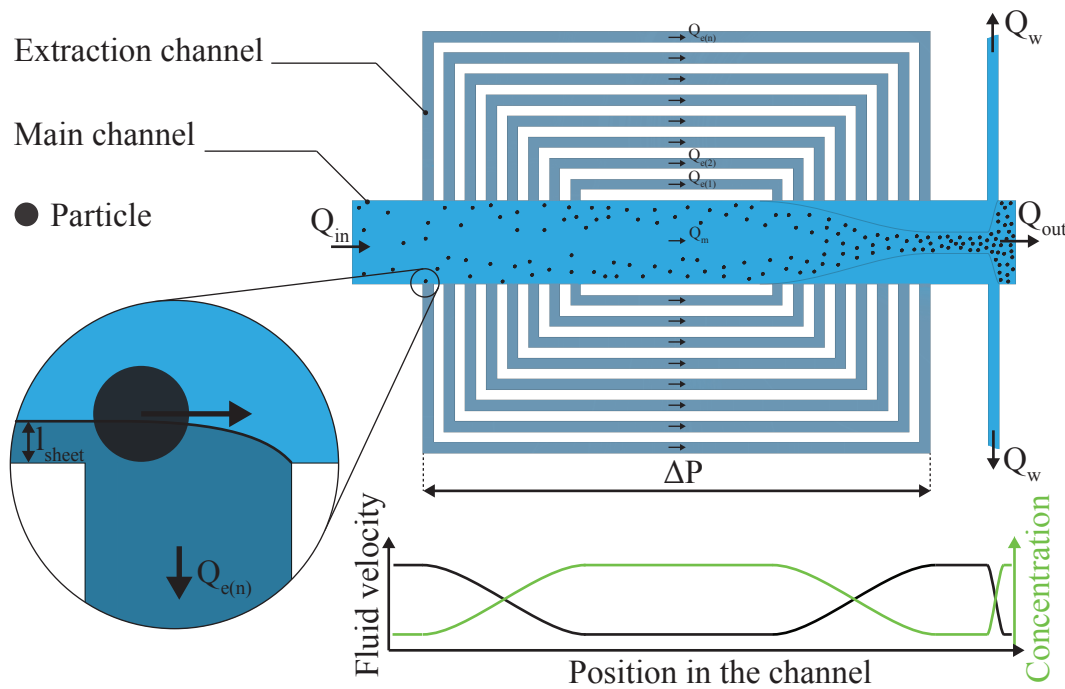


*Figure 3.2 – Working principle of a hydrodynamic concentrator. Flow is segmented by the small side channels and reinjected downstream. The withdrawn flow is small enough so that the extracted sheet flow size is smaller than the radius of the particles preventing them to get dragged into the side channels regardless of the size of the side channels. Upon flow reinjection cells are focused and then concentrated. A graphic of the concentration and fluid velocity along the channel is also provided.*

Using a solution of the Navier-Stokes equations for incompressible Newtonian fluids in no slip conditions at steady state [Constantinescu, 1995], the flow rate in a duct can be linked to its dimensions as shown in equation 3.1, for a duct with a rectangular section. It is also possible to link the flow rate to the fluidic resistance through the pressure (Eq. 3.2), to compute the mean fluidic resistance of multiple parallel channels (Eq. 3.3) and the flow rate to generate a specific sheet flow size (Eq. 3.4). This last expression is valid only if parabolic flow profile is well established [Lee et al., 2006]. If the height of the channel becomes smaller than its width this approximation no longer stand and must be replaced by the integration of the flow velocity profile as defined in the supplementary material of [Kim and Kim, 2014].



### 3.2. Concentrators design

$$Q = -\frac{a^3b}{6\mu} \cdot \frac{dP}{dx} \cdot \left[1 - \frac{192a}{\pi^5b}\right] \cdot \sum_{n=1,3,5}^{\infty} \frac{\tanh(n\pi b/2a)}{n^5} \quad (3.1)$$

$$P = R \cdot Q \quad (3.2)$$

$$R_{//} = \frac{1}{\frac{1}{R_1} + \frac{1}{R_2} + \dots + \frac{1}{R_n}} \quad (3.3)$$

$$Q_e = \frac{l_{sheet}}{2a} \cdot Q_{m(i)} \quad (3.4)$$

Where  $Q$  is defined as the flow rate,  $a$  and  $b$  the half width and half height of the channel respectively,  $\mu$  the viscosity of the fluid,  $P$  the pressure,  $R$  the fluidic resistance and  $l_{sheet}$  withdrawn sheet flow size. It can be seen that the width, depth and length of the channel influence the fluidic resistance.

Using these equations as described in appendix F, it is possible to fully design a focusing device base on a hydrodynamic principle. The focusing devices features extraction channels with a unique length and width tailored to remove a constant sheet flow of  $5\mu\text{m}$ . As each extraction channel is designed to remove  $5\mu\text{m}$  of sheet flow from the  $200\mu\text{m}$  width channel, 18 extraction channels from each side are needed to center the particle in a  $20\mu\text{m}$  beam in the middle of the channel thus allowing a maximum theoretical concentration of ten folds.

Flow simulation can provide a visualization of the flow inside the channels. For this device eight extraction channels were modeled on one side of the device to confirm if the design creates the intended effect. Ansys 16.2 is used with the fluent module to model the device in 2D. Water is used as liquid for the model and is injected at the inlet at a flow rate of  $10\text{mm}\cdot\text{s}^{-1}$  and flows from left to right toward the outlet set as pressure with zero Pascal applied. The boundary conditions are set as no slip for the wall of the device and the initial conditions were set with zero velocity inside the channels. The mesh was a simple tetrahedral mesh with progressive mesh size. Coarser mesh is present in the main channel and is refined toward the small extraction channels in order to have at least ten nodes in the width of each extraction channel. This allows the proper simulation of the parabolic flow profile even in smaller channels. Moreover a finer mesh with a size of  $0.1\mu\text{m}$  was made at one inlet of an extraction channel to closely visualize the flow in that region. The flow velocity through the device is depicted in figure 3.3 A. Part of the liquid passes through the extraction channels inducing a flow speed reduction toward the middle of the chip and gets reinjected downstream. The streamlines are presented in figure 3.3 B and indicates the flow pattern. Particles tend to follow these steam lines. Even though the extraction channels are larger than the

### Chapter 3. Cell concentration

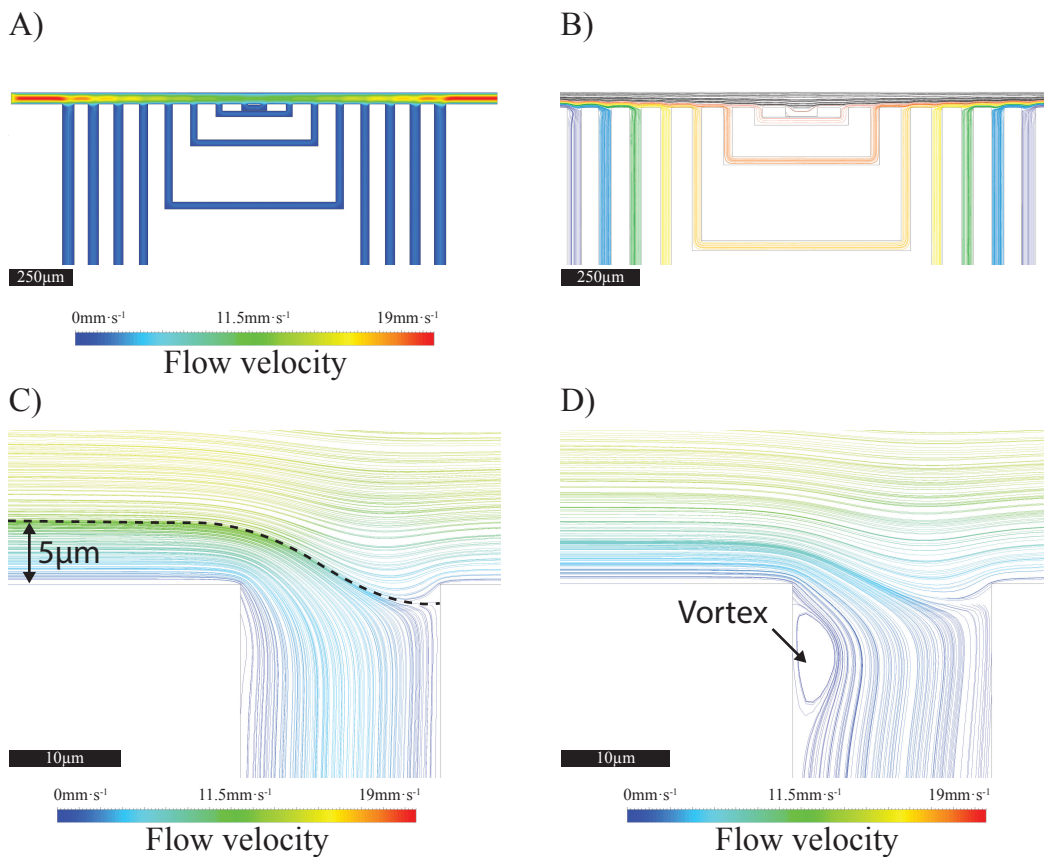


*Figure 3.3 – Simulation of hydrodynamic focusing. A) Flow velocity in a subset of side channels. B) Streamlines in the subset of side channels highlighting the flow pathway. The colors indicates different flow lines. C) Zoom over the streamline at one intersection between the main channel and the side channel highlighting the withdrawn sheet flow. D) Zoom over the streamline at one intersection between the main channel and the side channel showing possible vortices under unfavorable conditions.*

particles, the particles do not enter these channels if the sheet flow extracted from the main channel does not exceed the half diameter of the particle. By plotting the streamlines at the entrance of an extraction channel, this sheet flow thickness can be visualized (figure 3.3 C). As the extracted sheet flow is 5 μm thick no particles larger than 10 μm should be dragged in the extraction channels. Therefore, the particles should follow the streamlines and be led from the the center of the main channel toward the extraction channel on the side, at which point they wont enter them and slide along the edge of the main channel. Upon liquid reinjection, the particles will get pushed toward the center of the channel, thus focusing them in the center of the main channel.

The simulation also revealed a concerning property of the extraction channel. Under certain conditions of flow and channel size, vortices might form at the intersection (figure 3.3 D). As the simulation was made in 2D, it assumes an infinite height thus

promoting this phenomena. Vortices are to be avoided as they reduce the amount of liquid withdrawn from the main channel, reducing its efficiency, and creating a depression zone that might catch particles.

### Probe fabrication and performance

The probe was micromanufactured using a similar manufacturing process as the one described in chapter 2. This process is summarized in figure 3.4. A resist layer was deposited a standard 525 $\mu\text{m}$  thick silicon wafer with 2 $\mu$  of silicon oxide (wafer 1). The resist is structured using direct laser writing (step 1) allowing flexibility in terms of design. The oxide layer is etched forming a hard mask (step 2). The silicon is then etched using a standard Bosch process (step 3). The remaining oxide is etched away to reveal the silicone for anodic bonding (step 4). In the meantime, a Borofloat<sup>®</sup> 33 wafer (wafer 2) is drilled to form the inlets of the probe (step 1'). Both wafers are cleaned in a piranha bath and dried before being stacked and bonded using anodic bonding (step 5). The stack can be diced to release the chips and open the outlets.

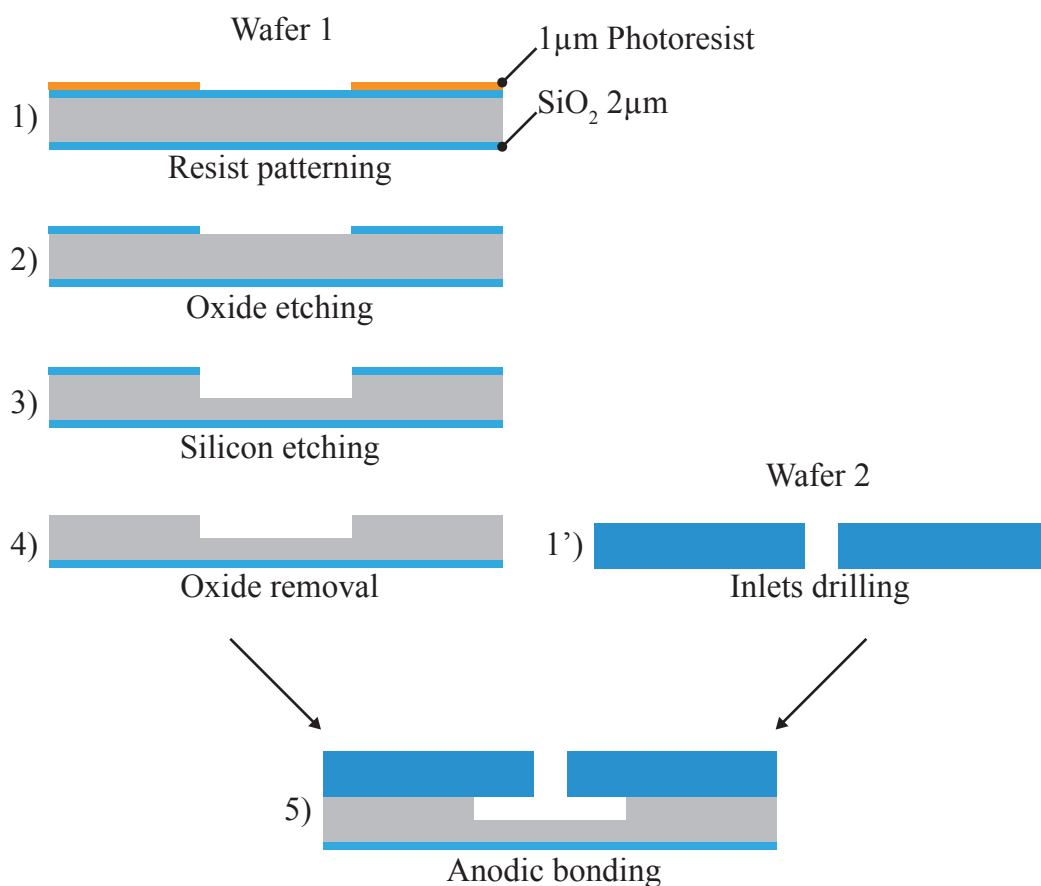
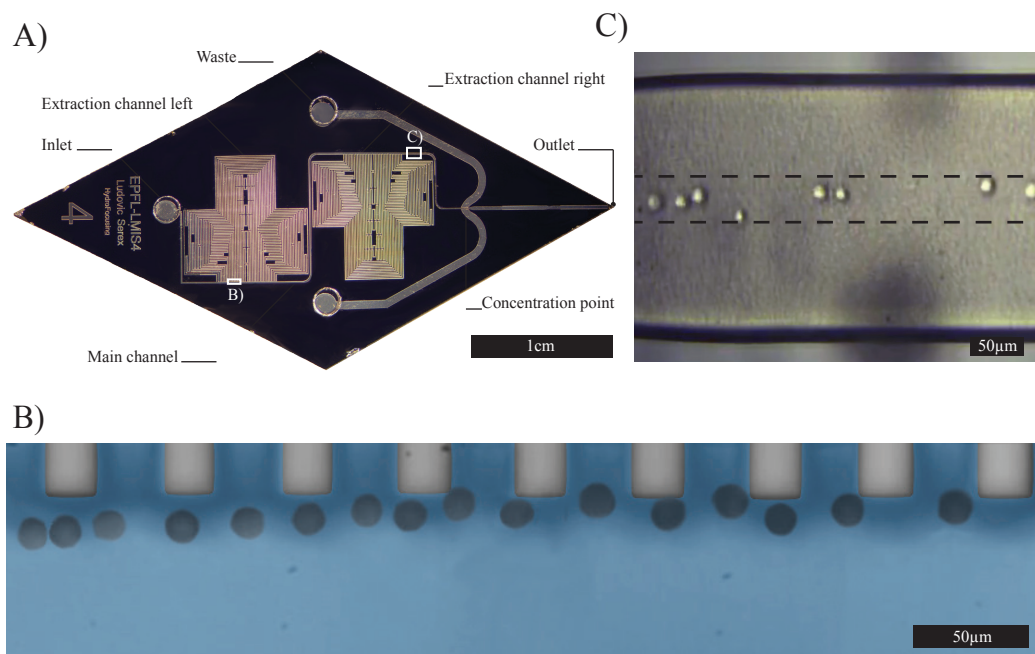


Figure 3.4 – Process flow for silicon glass concentration dispensing probe.

### Chapter 3. Cell concentration

The final probe is depicted in figure 3.5 A. It is composed of one inlet where the low concentration cell solution is injected in the main channel. The extraction channels have been implemented in two steps to better exploit the available space on the printing head. After focusing, the sheet flow is removed thanks to two waste channels and discarded. The concentrated solution exits the probe by the output at the tip. To ensure proper dispensing, the hydrophobic coating presented in chapter 2.2.3 is performed at the tip of the probe as well. In figure 3.5 B, an overlaid image shows the trajectory of a single cell passing near extraction channels. One can see the cell approaching the side of the channel at every channel passed. The cell stops progressing laterally once it arrives at the main channel's side. Even though the extraction channels are larger than the cell dimension, the cell does not enter them. This configuration insures that the probe does not clog, should a cell or a particle inadvertently pass into an extraction channel. After extraction and reinjection, the cells are focused in the center of the main channel as shown in figure 3.5 C thus without need of any complex flow control.



*Figure 3.5 – Results of the hydrodynamic focusing probe. A) Picture of the probe depicting its layout. B) Cell traveling from left to right toward the extraction channels without getting withdrawn by them. C) Focused cells in the middle of the main channel.*

### 3.2. Concentrators design

The removal of the sheet flow for the final concentration step revealed to be problematic. Indeed many cells were withdrawn into the waste channels at this step resulting in poor performance of the chip in terms of concentration. It has been noticed that from the point of focusing to the concentration point, cell focusing was deteriorating. As cells had migrated from the center of the channel, they were caught into the flow  $Q_w$ . In first approximation, particles must follow the streamlines inside a channel thus should remained focused in the main channel "indefinitely", especially as the Reynolds number in this device is rather low (typically in the range of  $10^{-4}$ ). However the lift force [Asmolov, 1999] and wall effect phenomena [Zeng et al., 2005] that were discarded as focusing possibility because of their inherent low focusing speed can move particles through streamlines. As depicted in figure 3.5 A there is a significant distance between the focusing point and the concentration point as the extraction channels take a lot of space on the chip. The lift force and wall effects could have time to move particles out of focus. Those force evolve in a complex fashion within the channel making them hard to compute [Di Carlo et al., 2009]. However using an approximation [Di Carlo et al., 2007] it is possible to estimate the lateral speed of a particle in the main channel (see equation 3.5).

$$U_p = \frac{\rho U_m^2 a^3}{2\pi\mu D_h^2} \cdot f_c(R_c, x_c) \quad (3.5)$$

With  $U_p$  the particle migration velocity,  $U_m$  the particles mean velocity,  $D_h$  the hydraulic diameter and  $f_c(R_c, x_c)$  a lift coefficient function that is dependent on the position of the particle within the cross-section of the channel. Using an approximation of particles in a flow between to parallel plates  $f_c(R_c, x_c)$  can be set to 0.5. By applying equation 3.5 to the concentrator dimension, a lateral displacement speed of the particles can be estimated at  $186\mu\text{m}\cdot\text{s}^{-1}$  considering a flow speed of  $0.1\text{m}\cdot\text{s}^{-1}$  in the channel. It result in a  $9.3\mu\text{m}$  lateral displacement of the particles from the center of the channel. As explained in chapter 3.2.1, a slight change in the focusing can partially compromise the concentration capabilities of the probe and might explain its poor performance.

Moreover steric congestion at the focal point can also impair the concentration similarly as in [Martel et al., 2015] where the concentration yield decreased dramatically above one million cell per milliliter due to this phenomenon. The use of vortices produced by Herrigbone like structure could be used to keep cells from moving from the center point [Choi and Park, 2008] alongside with other design optimizations to reduce the channel length between focusing and concentration point. Hydrofocusing-based concentrators present the advantage to be extremely easy to use. However because of the limited maximum concentration they can provide, they are not suited to serve as a printing head for a bioprinter aiming at printing tissue with 10 million cells per milliliter. They

## Chapter 3. Cell concentration

are however convenient for concentrating solutions from 10 thousand cells per milliliter to 1 million cells per milliliter as presented by [Martel et al., 2015]

### 3.2.3 Crossflow filter

#### Design, theory and calculation

The functioning principle of a crossflow filter is illustrated in figure 3.6. Liquid containing a low concentration of particles is injected in the main channel at a flow rate  $Q_{in}$ . The surrounding liquid is removed at a flow  $Q_w$  and the particles are retained from going to the waste channels by pillars forming a barrier along the main channel. It results in a decrease of the flow rate in the main channel and in an increase of the particle concentration. Similar filters were already implemented for white blood cells and red blood cell separation and have shown to be effective in retaining cells [Chen et al., 2008].

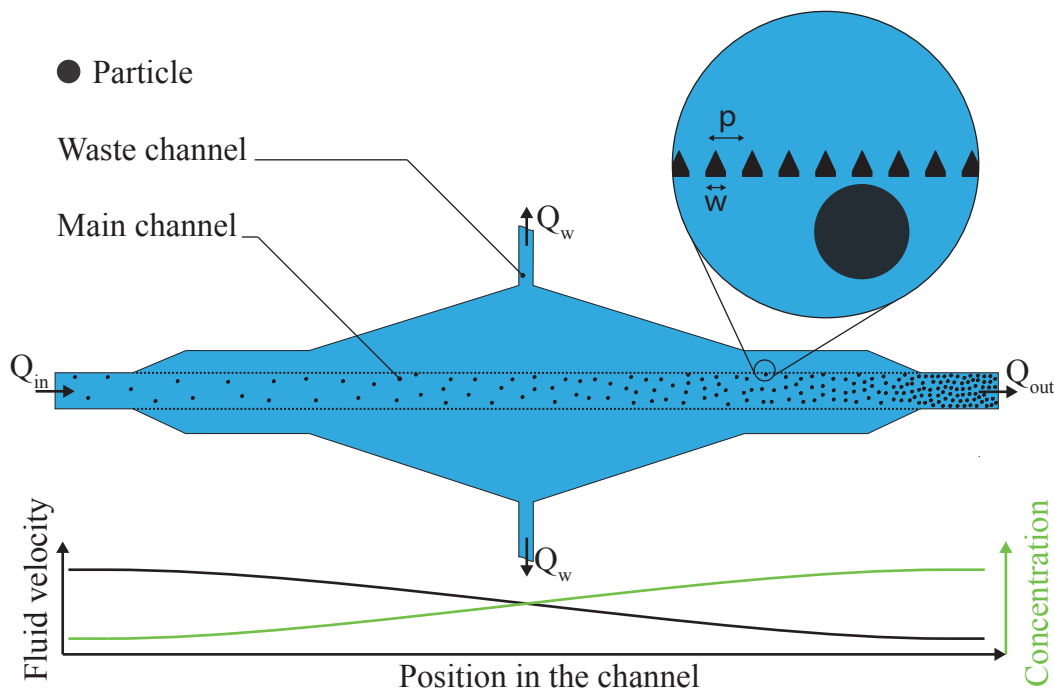


*Figure 3.6 – Working principle of a crossflow filter concentrator. A solution with cells is injected at a low concentration in the main channel. Liquid is withdrawn through the waste channels on the side. The filter prevents the cells from going to the waste channel resulting in a higher concentration at the outlet. A graphic of the concentration and fluid velocity along the channel is also provided.*

These devices are however susceptible to clogging, especially at high concentrations and need precise control over the applied and retrieved flow rates  $Q_{in}$  and  $Q_w$ . A first design was implemented utilizing pillars acting as cross-flow filter. The pillars were designed to have a width ( $w$ ) of  $5\mu\text{m}$  and a pitch ( $p$ ) of  $10\mu\text{m}$ . These sizes were chosen so that the

### 3.2. Concentrators design

gap between the pillars would be smaller than the particles that needed to be filtered, in this case less than  $10\mu\text{m}$  and large enough to be easily manufactured with standard microfabrication processes. This design proved to be efficient to concentrate micro beads but revealed ineffective to concentrate cells. Cells can be observed to slip through the pillar by deformation. One obvious improvement to this probe can be to reduce the space between the pillars. However this is not enough as cells can easily be compressed through channels as small as  $2\mu\text{m}$  in width given enough pressure [Shelby et al., 2003]. Moreover etching  $2\mu\text{m}$  wide slits for a thickness of over  $50\mu\text{m}$  is challenging. A better design and a refined manufacturing process are needed to create a suitable cross-flow filter.

To avoid cells passing through the pillars, pressure perpendicular to the pillars must be minimized. The pressure acting against the pillars depends first on the withdrawing flow  $Q_w$  that is set by  $Q_{out}$  thus by the printing speed and by the targeted concentration factor and can not get optimized. It also depends on the flow resistance of the gap between the pillars. To limit the flow resistance in between the pillars, they were designed with a triangular shape as it allows for large surface against the particles and a reduced fluidic resistance as illustrated in the insert in figure 3.6.

The filter is also made as long as possible to implement on a printing head, as more pillars translate to less flow passing in between each pillars thus ultimately less pressure difference to push a cell through the filter. It is however important to insure that the withdrawing flow is being applied homogeneously along the pillars. The study of the flow profile at a T-junction between two channels provides meaningful insight on the flow behavior. The shape of the flow at such intersection is known since the early 80's [Liepsch et al., 1982]. Using Doppler effect, the velocity profile could be drawn as shown in figure 3.7. One can observe the deformation from the standard parabolic profile once

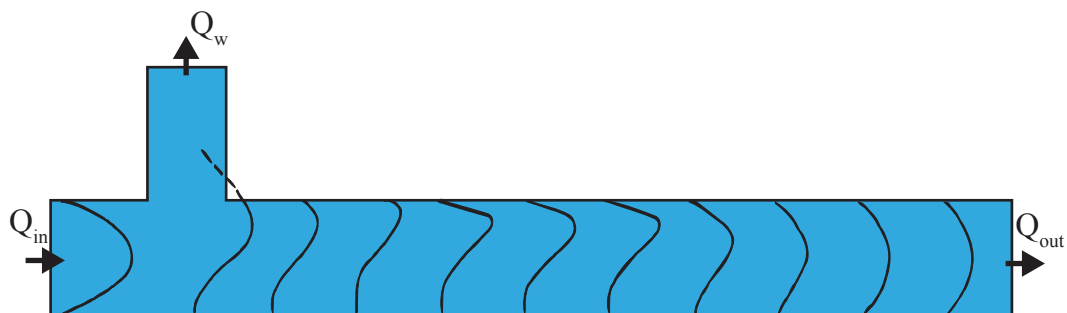


Figure 3.7 – Figure adapted from [Liepsch et al., 1982] showing the velocity contour of the fluid at a 90 degree bifurcation using laser Doppler anemometry measurements.



### Chapter 3. Cell concentration

passing at the junction where the flow profile is pulled upward toward the withdrawing flow. This disruption in the parabolic flow pattern reduces downstream to return to the standard parabolic profile. This results in a lateral flow rate going upward at the intersection then downward during flow stabilization after withdrawing.

The flow at a T-junction was simulated using Ansys 16.2 with the fluent module in 2D with similar meshing and boundary conditions to the previous simulation in chapter 3.2.2. Water was again used as a fluid and flow rates of  $Q_{in}$  of  $10\text{mm}\cdot\text{s}^{-1}$  and  $Q_w$  of  $0.1\text{mm}\cdot\text{s}^{-1}$  were set. The resulting flow lines are plotted in figure 3.8 A. The vertical flow velocity is measured along the black line where the filtration pillars are placed. This vertical flow velocity will be the flow rate going through the pillars directly indicating the pressure experienced by cells along the filter. The vertical flow velocity in the main channel resulting from a single extraction channel is plotted figure 3.8 C in red. One can observe that at the channel intersection, the vertical velocity is high, then drops and a flow in the opposite direction appears. It is due to the restoration of the parabola shape of the flow as described in figure 3.7. If only one channel or a set of largely spaced extraction channels is used to withdraw the liquid from the main channel, only a few pillars will be used to retain the cells thus applying a large strain to the cells. Concentrated rigid micro beads can withstand a large stress without deforming. However in the case of cells this strain will deform the cells and they will pass through the filter and can even lyse through the pillars.

One first possible optimization is to place extraction channels in such fashion that the position of the maximum vertical velocity of one channel is placed at the position of the minimum vertical velocity of the channel preceding it. From the simulation a pitch of  $900\mu\text{m}$  can be used between each withdrawing channel is appropriate. A device with multiple extraction channels was simulated and the vertical velocity in the main channel is plotted in figure 3.8 C in orange. One can observe that the maximum vertical velocity is significantly decreased thus less stress is experienced by the cells. Moreover the vertical velocity is always positive meaning that all the pillars are useful whereas before the pillars placed at the position where the vertical flow rate was negative would have been useless.

The second optimization is to place flow control pillars between the extraction channels and the filter pillars. Those pillars are much larger than the filter pillars and are regularly spaced to provide flow resistance evening out the pressure provided by the extraction channels. This device was also simulated and the streamlines are plotted in figure 3.8 B illustrating how the pillars act to spread the streamline. Moreover, in figure 3.8 C in green the resulting vertical flow velocity is plotted. By adding the pillars, the pressure is further homogenized along the filter pillars making the strain on each cell smaller and more constant.

The homogenization of the pressure using pillars to regulate the flow at the intersection



### 3.2. Concentrators design

can be brought further. By increasing to a maximum the fluidic resistance between each pillars, the pressure could theoretically be totally smoothed out. This can be achieved by placing flow control pillars close from each other and increasing the flow resistance of the channel formed between the pillars. The resulting flow velocity of such a device is plotted in figure 3.8 C in blue. The pressure flow velocity is now constant across the whole filter. In the end the solution of spaced pillars presented in figure 3.8 B is retained as it is much easier to manufacture and and more resilient in term of clogging and provides a pressure along the filter pillars quite constant.

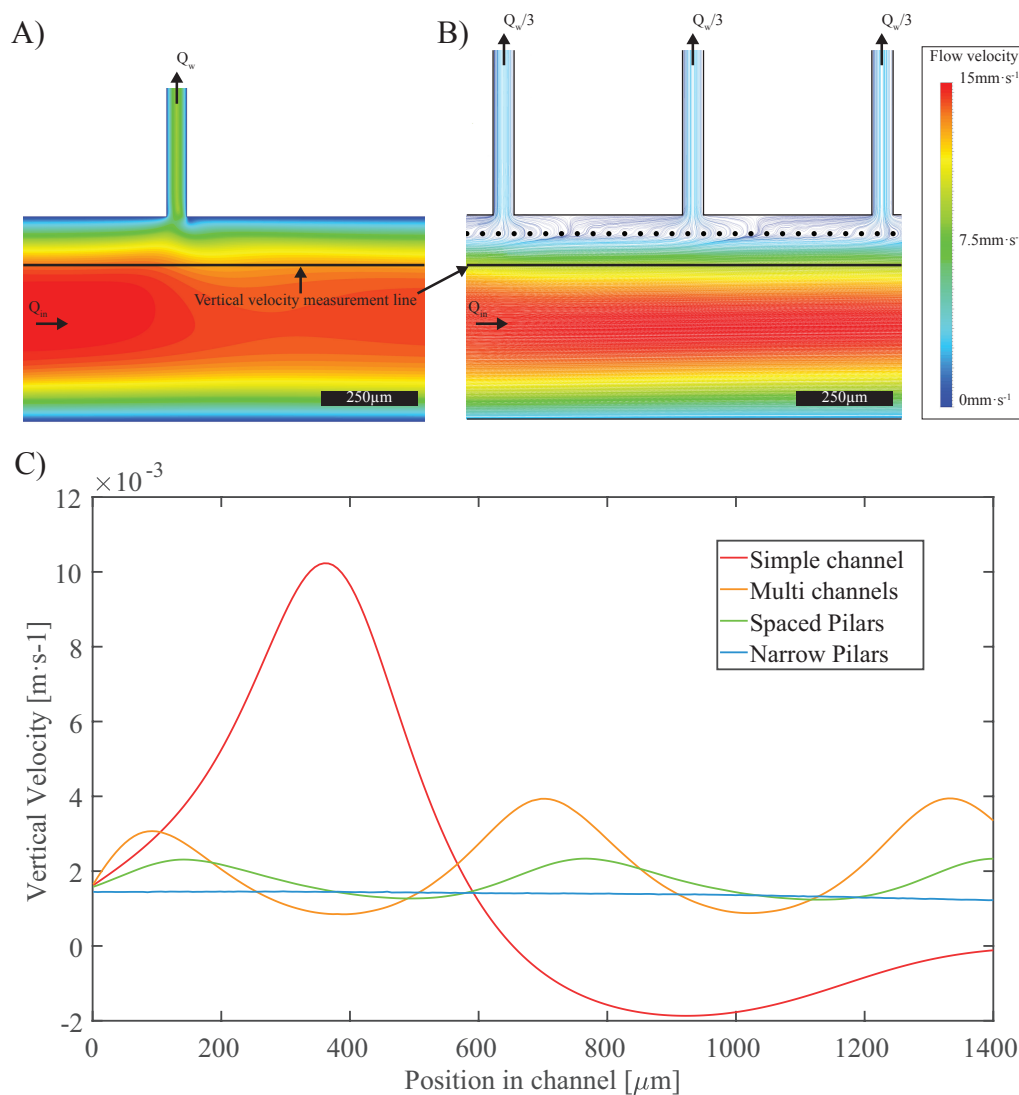


*Figure 3.8 – Optimization of the vertical flow to reduce pressure between pillars and stress on cells. A) Flow lines at a simple T-junction. The black line illustrate where the vertical flow velocity is calculated B) Flow lines at multiple T-junctions with flow regulation pillars. The black line illustrate where the vertical flow velocity is calculated C) Calculated vertical flow velocity along the filtering pillars for single channel, multi channels and multiple channels with flow management pillars implementations.*

## Chapter 3. Cell concentration

### Probe fabrication and performance

The manufacturing of standing pillar only  $2\mu\text{m}$  apart and  $2\mu\text{m}$  wide is challenging. As the pillars are a repetitive structure, exposition through a standard mask available in cleanroom creates interference pattern resulting in undefined structures. To remedy this problem, the exposition was made using direct writing on a Heidelberg VPG200. However the tool is calibrated to expose openings such as the general shape of the channel. The pillars on the other hand are detoured. The laser must expose everywhere around the pillar but not the pillar. This results in an over exposition of the resist around the pillars thus in pillars not well defined, smaller than designed and with a higher pitch than expected (see figure 3.9 A). For such structure detouring one needs to under expose slightly to avoid the small pillars structure to get exposed. To fully develop the resist the development time should be doubled afterward to allow all the resist to be nicely removed in the large openings. The resulting pillars are well defined and with a proper pitch as shown in figure 3.9 B. Moreover, standard etching steps of Bosch process are either designed to etch large exposed surface of silicon by using longer  $\text{SF}_6$  etching steps and shorter  $\text{C}_4\text{F}_8$  passivation steps or to etch narrow regions with shorter  $\text{SF}_6$  steps and longer  $\text{C}_4\text{F}_8$  steps to reduce scalloping. Typically at CMi the standard process for large exposed areas is 8 seconds  $\text{SF}_6$  at 300 sccm and 1800W followed by a 2 seconds  $\text{C}_4\text{F}_8$  step at 150sccm and 1800W allowing fast etching but large under etch. For smaller exposed areas the standard process is 5 seconds  $\text{SF}_6$  at 300 sccm and 1800W followed by a 2 seconds  $\text{C}_4\text{F}_8$  step at 150sccm and 1800W which etch vertically but is slow and because of the long  $\text{C}_4\text{F}_8$  step, micro-masking occurs in large exposed areas. The concentrator is composed of large exposed surfaces to the plasma (in the channels) and very small regions in between the filtering pillars.

The addition of an oxygen plasma step was shown helpful in reducing scalloping and with fine tuning of each plasma step, deep trenches can be etched [Abdolvand and Ayazi, 2008]. The scalloping can be further decreased by shortening each plasma step. Indeed shorter etching step leads to smaller under etch but also a slower etch rate. A 3 seconds  $\text{SF}_6$  at 300 sccm and 1500W followed by a 2 seconds  $\text{C}_4\text{F}_8$  step at 300sccm and 1500W and a 1 second  $\text{O}_2$  step at 300sccm and 1500W recipe was used for the etching. As the plasma step are rapid, the frequency had to be fixed as the AMS200 cannot fine tune the plasma frequency that quickly. The chosen frequency is set at 323kHz as it minimizes the reflected power for the etching step which is the most important one. Using this process the pillars could be etched in a clean manner. However, micro-masking occurs in large exposed areas leading to spikes formation. Those spikes can be numerous and would damage the cells passing in the channel. To resolve this issue, the temperature of the chuck was raised from  $0^\circ\text{C}$  to  $10^\circ\text{C}$  to reduce the passivation layer thickness created during the passivation step. Using those parameters, the etching resulted in nicely defined pillars as well as very smooth surfaces in the channels (figure 3.9 D).

### 3.2. Concentrators design

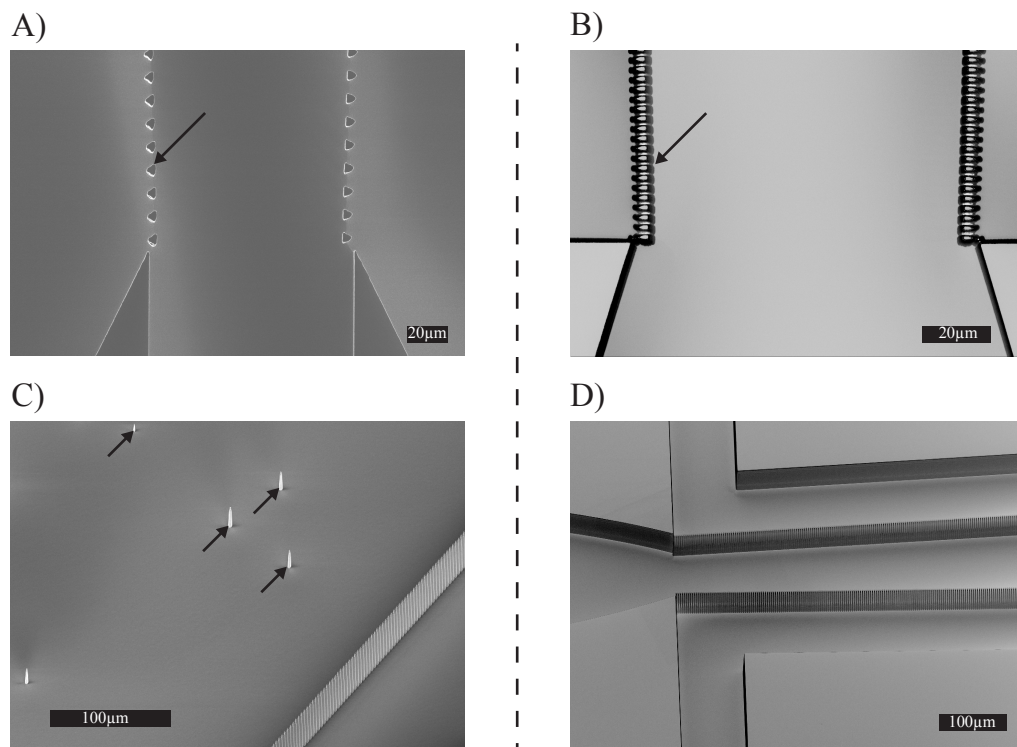


*Figure 3.9 – Optimization of exposition and etching parameters during manufacturing. Effect before optimization on the left and after on the right of the dotted line. A) Overexposed pillars are thin and with large pitch as shown by the arrow. B) After dose adaptation the pillars have the proper pitch and dimensions. C) Micro-masking result in spikes in the main channel (arrows). D) After process optimization a clean etch is achieved for large surface area as well as in between pillars.*

Apart from the exposition and etching optimization, a very similar process flow as presented in figure 3.4 was used. To further narrow the gap between the filtering pillars, a 500nm oxidation step was added after etching (step 4). This oxide layer does not impair the anodic bonding process and provides numerous advantages. It narrows the gap between pillars for a more efficient filter and smoothens the remaining scalloping effect making a very smooth surface. Finally, the whole channels' surface material is glass or silicon oxide, which is adequate for cells.

The concentrator device resulting from optimization is shown in figure 3.10. The low magnification image (figure 3.10 A) shows the main channel without any micro-masking artifact. The filtration pillars (arrow 1) and the flow regulation pillars (arrow 2) are also visible. On the side the last extraction channel can be seen as well as the output of the probe on the top right corner. In figure 3.10 B, a higher magnification of the concentration pillars is shown. Some residual scalloping can be seen on the wall. However, at this scale, the scalloping do not interfere with the flow. Most importantly, the gap between the pillars is open all the way to the bottom assessing the good function

### Chapter 3. Cell concentration

of the optimized deep reactive ion etching (DRIE) process. It can be seen however that the pillars are not perfectly straight (figure 3.10 C). Indeed the gap between each pillar shortens by 678nm from the top to the bottom over the 51.8 $\mu\text{m}$  depth of the device (tilt adjusted). This phenomenon is well known with DRIE processes and could be further optimized. However this is time consuming and would not dramatically improve the device performances. Finally one can observe that the mask shape for the pillar is well preserved.

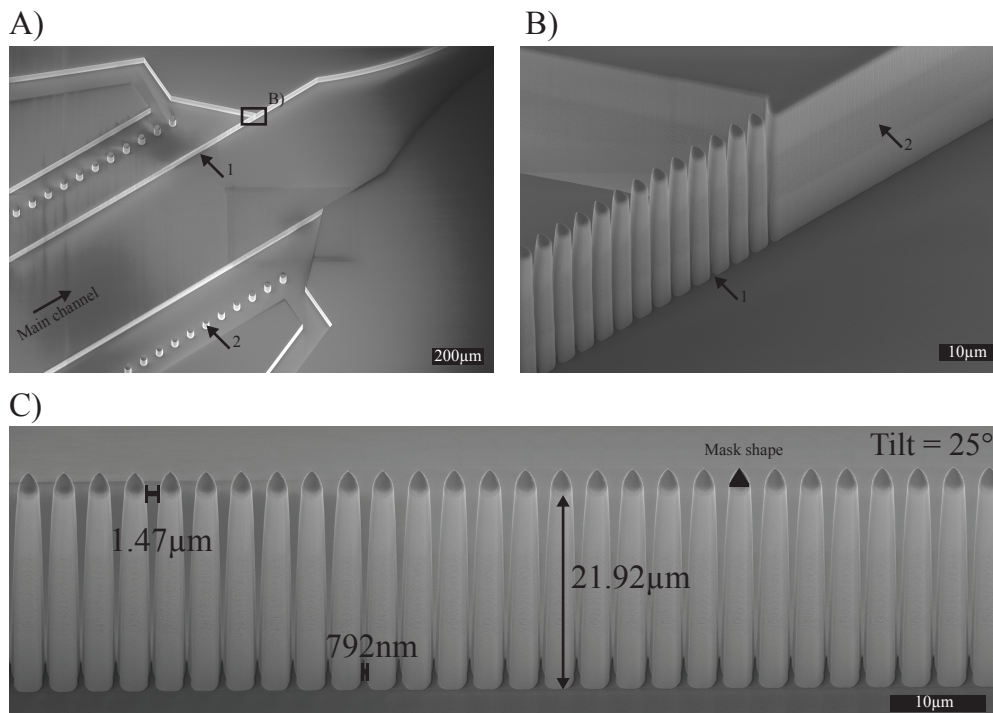


*Figure 3.10 – Implementation of the crossflow filter A) Global view of the device before the outlet (top right of the picture). The crossflow filter is visible (1) as well as the flow regulation pillars (2). On the side the last waste channel is visible as well. B) Close up of the filter pillars revealing that they are etched to the bottom of the main channel (1). Some remaining scalloping can also be observed (2). C) Front view of the pillar allows the measurement of the parameters of the filter.*

The probe concentration capabilities were assessed using living cells. NOR-10 cells were cultured using similar methods describe in chapter 3.3.1. They were placed in suspension at three different starting concentrations of 750 thousands, 2 million and 5 million cells per milliliter. The solutions were perfused in the probe using a syringe pump and the ratio between  $Q_w$  and  $Q_{in}$  was varied. A flow ratio of 0, means that no liquid is withdrawn through the side channels resulting in no concentration, and a flow ratio of 0.9, means 90 percent of the liquid is withdrawn through the side channels resulting in a ten folds concentration.

After concentration by the probe, the samples are collected in a buffer solution composed

### 3.2. Concentrators design

of Hoechst staining, targeting cells nucleus as well as live/dead viability staining assay that dyes living cells in green and dead cells in red. The sample and buffer solutions were steered thoughtfully and dispensed on a hemocytometer with a  $100\mu\text{m}$  tall chamber for counting. The amount of buffer solution was adjusted to sufficiently dilute the sample in order to stay within the hemocytometer specifications and was factored in for the final concentration calculation. For each concentration step, five samples were taken and two pictures were taken on each sample to cover most of the surface of the hemocytometer. Using a fluorescent microscope and thanks to the stainings present in the buffer solution, cells could be easily counted using a FIJI script. Knowing the field of view of the microscope and the hemocytometer dimensions, the concentration factor could be computed. The measured concentrations are presented in figure 3.11 A.

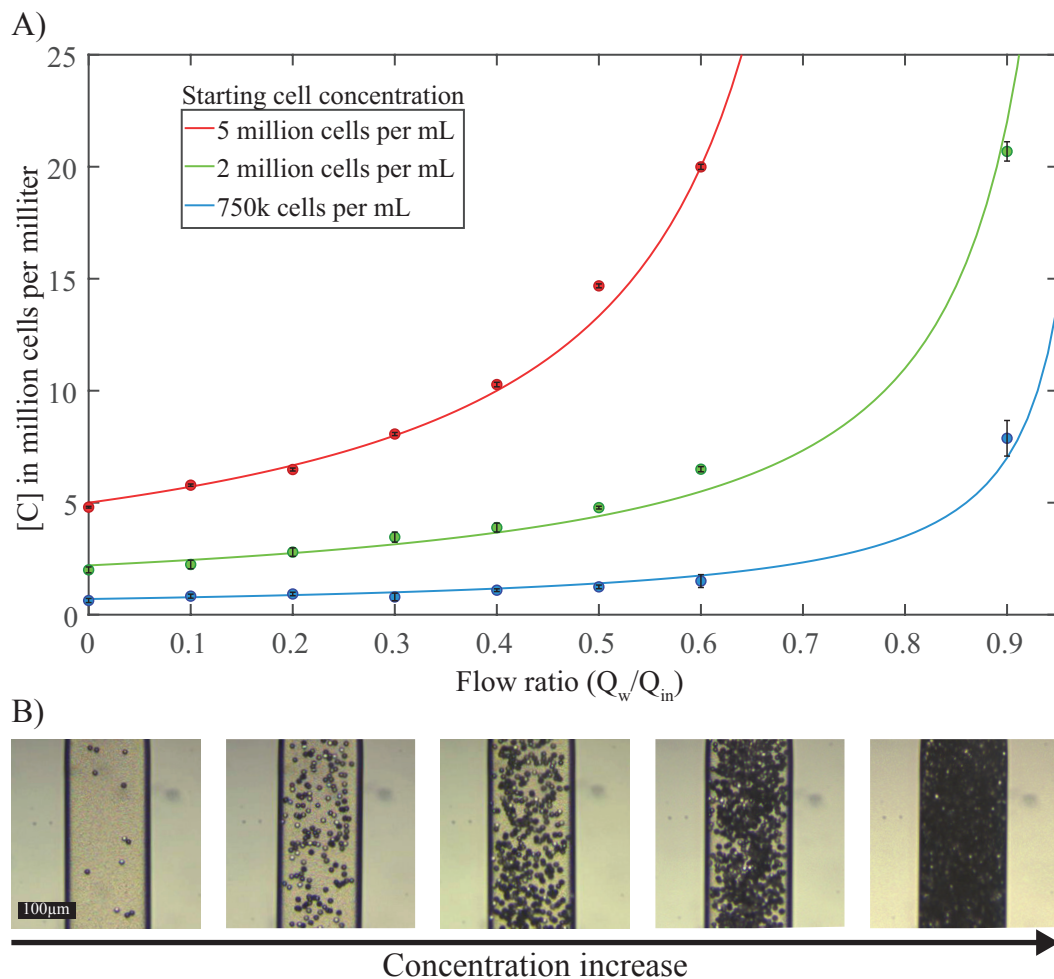


*Figure 3.11 – Crossflow filter concentrator performance. A) Cell concentration at the outlet of the probe for different flow ratios ( $Q_w/Q_{in}$ ). The higher the ratio the more liquid is withdrawn from the waste channels resulting in a higher concentration. Data points and fit with the model described in equation 3.7 (continuous line) are plotted. B) Micrograph of the outlet channel at different concentrations.*



### Chapter 3. Cell concentration

The concentration increase is not linearly dependent of the flow ratio between  $Q_w$  and  $Q_{in}$ . This can easily be modeled using the definition of concentration as described in equation 3.6. With  $C_{out}$  the concentration at the outlet,  $n_{cells}$  the number of cells in the solution,  $V_{out}$  the volume exiting the probe,  $V_{in}$  the volume entering the probe and  $V_w$  the extracted volume of liquid during the concentration phase. Rearranging the terms gives equation 3.7 where  $A$  is a constant,  $\kappa$  is the flow ratio  $Q_w/Q_{in}$  and  $\alpha$  an adjustment factor that take into account any error from the syringe pump. This last factor is typically 1 as Nemesys syringe pump system is very accurate if use with proper syringes.

$$C_{out} = \frac{n_{cells}}{V_{out}} = \frac{n_{cells}}{V_{in} - V_w} = \frac{n_{cells}}{V_{in} \cdot (1 - \frac{V_w}{V_{in}})} \quad \forall V_{in} > 0 \quad (3.6)$$

$$C_{out} = \frac{1}{A} \cdot \frac{n_{cells}}{1 - \alpha\kappa} \quad (3.7)$$

The model fitting the data points is presented in figure 3.11 A in a continuous line. The concordance of the model with the measurements insures that little to no cell pass through the filter. If this was occurring, a decrease in the number of cells at the outlet would cause a substantial mismatch between measurement and model would be observed. The size of the particles is not taken into consideration in this model. It would only produce a plateau of maximum concentration, which would be dependent on the size of the concentrated particles. The concentration of particles through the variation of the flow ratio  $Q_w/Q_{in}$  can be imaged at the output of the probe and is shown in figure 3.11 B.  $8\mu\text{m}$  beads were used for those images for contrast purposes.

The question of viability of the cells passing through the device could be answered as well. It is indeed not obvious if the cells can survive transit through the probe. The stress against the pillars could be enough to kill cells. Therefore, the viability is assessed at the output of the probe. As explained the cells were also dyed with a live and dead viability staining assay. In addition to counting cells, the FIJI script draws a region of interest (ROI) around each cell and evaluates the intensity of live and dead fluorescence in the ROIs. The script can output the number of live cells and dead cells. Controls with living cells and another with cells killed with ethanol were used to define the intensity threshold for living cells and dead cells in FIJI macros. The light intensity of the microscope as well as the gain were kept constant throughout the whole experiment and a cell viability above 97% was obtained for all concentrations.

Those tests have shown that the probe can concentrate particles and cells without efficiency loss thus up to very high concentrations. However at higher flow ratios between  $Q_{in}$  and  $Q_w$  one can observe an instability in the system. The closer this ratio is to 1 the steeper the concentration slope becomes (see figure 3.11). This phenomenon

### 3.2. Concentrators design

poses two problems. First, any error in the flow rates be it  $Q_{in}$  or  $Q_w$  will result in large variations in concentrations. Second, if because of this error the concentration gets too high, the probability of clogging the probe increases. A parry to those problems will be presented in chapter 3.2.4. The probes has shown its capabilities for concentrating cells in culture media. However if one wants to use this probe for 3D printing, cells must be in ECM. Common ECM such as alginate, collagen, fibrinogen, Cultrex, etc. are often available in liquid form. They are however much more viscous than culture media, up to 20 times more viscous for collagen according to the manufacturer data sheet. This viscosity impairs the filtration method as the pressure drop between the pillars becomes large enough to push the cells through the filter. To circumvent this issue cells can be concentrated in media and the concentrated solution mixed with ECM downstream.

Multiple micro-mixers have been devised for microfluidic applications [Nguyen and Wu, 2005]. Static micro-mixers have the advantage of being passive structures that provide efficient mixing in laminar conditions and that can be integrated directly in the print head nozzles used for 3D printing. As presented in chapter 2, the use of a meander-based static micro-mixer for performing the mixing of slow reacting materials used to 3D print carboxymethylcellulose-based cryogels is possible. However because of the space used for cell concentration the mixing must occur faster and the use of a more efficient micro-mixer is needed.

For ease of fabrication planar static micro-mixers where first investigated with obstruction in the channel [Bhagat et al., ] or tesla micro-mixers [Bhagat and Papautsky, 2008] as they can be fabricated without any additional step to the process flow. The mixer were tested and compared to standard diffusion to assess their efficiency. For accuracy with regards to viscosity, glycerol 80% was used to simulate ECM as its viscosity at room temperature approaches the viscosity of collagen, around 30cps ( $0.03 Pa \cdot s$ ) for glycerol [Segur, 1953] and 20cps ( $0.02 Pa \cdot s$ ) for collagen [Advanced BioMatrix, 2018]. Water was used to simulate the media with cells as the cell concentration even at a high concentration of 40 million cells per ml does not increase substantially the viscosity as calculated in equation 3.8 from [Quemada, 1977]. The increased viscosity due to cell concentration was found to be 25% which behaves like normal water.

$$\mu_c = \mu \cdot \left(1 - \frac{\phi}{\phi_{max}}\right)^{-\rho[\nu]} \quad (3.8)$$

With  $\mu_c$  the viscosity of the concentrated solution,  $\mu$  the viscosity of the media,  $\phi$  the volume fraction occupied by the cells (in this case using particles with  $10\mu\text{m}$  in diameter one obtain a 8% fraction volume at 40 million cell per milliliter),  $\phi_{max}$  the maximum volume fraction occupied by the cells, (considering undeformable sphere is 74%) and  $\rho[\nu]$  is a phenomenological parameter which in this case is equal to 2 [Quemada, 1977].

### Chapter 3. Cell concentration

Micro-mixers were built using the same process flow presented in figure 3.4 and are composed of three channels merging into one where the mixer is implemented. In white, undyed water is injected through the main channel and glycerol 80% dyed in blue is injected through both sides of the main channel and into the mixer. On the side of the mixer a scale in *mm* was engraved to visualize the position in the channel. The results are presented in figure 3.12 A. Both obstruction and tesla mixer are meant to enhance mixing by locally increasing the Reynolds number in the channel either with obstacles or by increasing the flow speed in the restriction of the tesla mixer. By plotting the light intensity across the channel (see measurement line in figure 3.12 A), the homogeneity of the solution can be evaluated. For an efficient mixing, the solution, thus the light intensity across the channel, should be homogeneous. In figure 3.12 B, it is observed that both tesla and obstruction mixers do not perform any better than simple diffusion

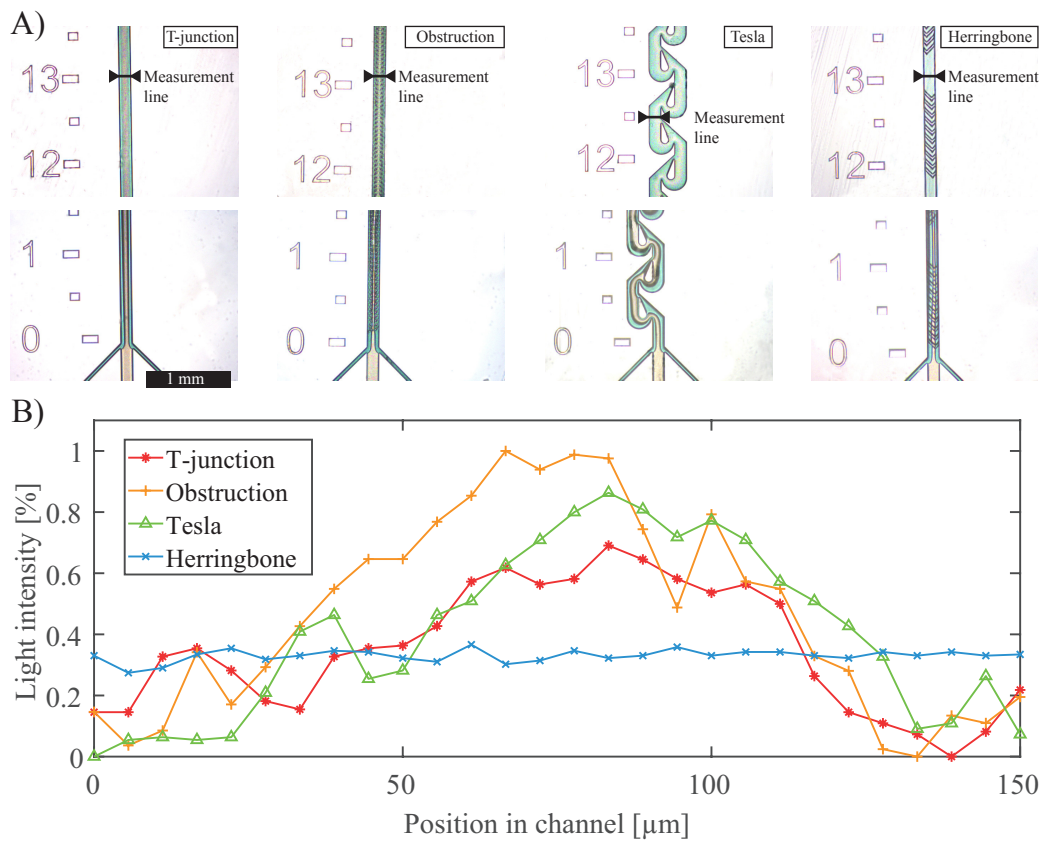


Figure 3.12 – Evaluation of three different mixer in comparison with standard diffusion. A) In blue glycerol 80% simulating ECM and in transparent DI water simulating the media with cells. The mixing can be see at the injection point and at 12 mm from it. The first column is a T-junction mixer showing simple diffusion of the two liquid. The second column shows a channel to which obstructions are added, and the third column a Tesla mixer is presented. Both designs were inspired from [Bhagat and Papautsky, 2008]. The last column a herringbone mixer. The scale bar applies for all pictures. B) Plot of the light intensity across the channel 12 mm downstream of the injection point.



### 3.2. Concentrators design

as the intensity increases in the middle of the channel, indicating undyed water has not yet been mixed. Moreover even so all dimensions are larger than cells, the pillars in the obstruction design and the restriction in the tesla revealed themselves to be very sensitive to clogging and might even damage cells.

Therefore Herringbone mixers [Stroock et al., 2002] were tested as they are considered to this day among the best performing micro-mixers [Lee et al., 2011]. However the manufacturing process is slightly more complex than the other mixers. Indeed it is a two layer process as shown in figure 3.13. One must first open into an oxide the channels layout to create a hard mask (step 2 in figure 3.13 A) and then align the groove of the herringbone to the channel. The silicon can be etch through the resist (step 4). After resist removal, the pattern can be transferred through the hard mask to the bottom of the channel (step 5). The process is then similar than the one presented in figure 3.4 to finish the probe. The groove at the bottom of the channel can be seen in figure 3.13 B.

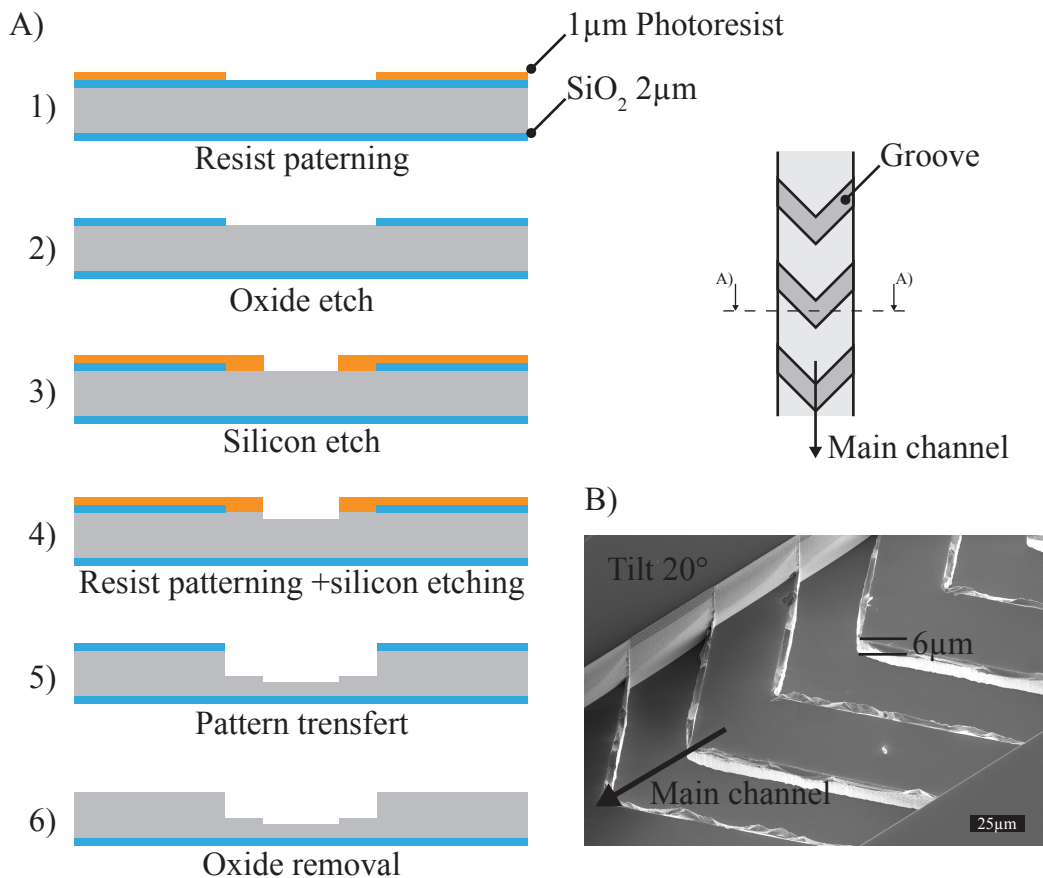


*Figure 3.13 – Fabrication steps for a Herringbone mixer. A) the steps with the top view of the design on the right. B) SEM micrograph of the groove 18 μm deeper than channel's bottom, adjusted for tilt.*

## Chapter 3. Cell concentration

A depth of  $15\mu\text{m}$  was targeted as to respect design rules from [Stroock et al., 2002]. A final depth of  $18\mu\text{m}$  (adjusted for the tilt) was achieved and has proved to be efficient as shown in figure 3.12 A. When passing above the first groove, the liquid starts to swirl thus increasing the surface between the two phases favoring diffusion. After only a few millimeters, the solution is homogeneous as seen in figure 3.12 B where the light intensity across the channel is constant.

Even so the process is more complex, it can be implemented at the tip of the concentration probe. It will insure that even viscous materials will be homogeneously mixed in structures of only a few millimeters in length thus insuring a good dispersion of cells in the ECM before dispensing.

### 3.2.4 Probe Final Design and Setup

In the previous sections, two methods of concentration were evaluated, one based on hydrodynamic focusing (chapter 3.2.2), which is easy to manufacture and operate and present the advantage to be clogging proof and a crossflow filter method (chapter 3.2.3), which despite requiring precise flow control allows for very efficient cell concentration. Although the hydrofocusing method presents many advantages, efficient concentration of particles was never obtained. The crossflow filter method will be used for the following experiments.

The full setup has many similarities with the setup presented in figure 2.12 for cryogel printing. However a few improvements were performed regarding the flow control and probe interfacing. As presented in figure 3.11, the probe presents an instability at high cell concentrations where small variations in flowrate can result in high discrepancies in the concentration. Moreover the output flow is the difference between  $Q_{in}$  and  $Q_w$  thus when both flows are of similar magnitude for high cell concentrations, any variation can stop the flow in the main channel which results in clogging or in back-flows (for  $Q_w > Q_{in}$ ) which would allow air from the output to enter the tip and introduce bubbles in the system. To remedy this issue the system must be as rigid as possible to avoid any tubing dilatation and retraction that can cause flow variations. To do so PEEK tubings were used with an internal diameter of  $350\mu\text{m}$ , allowing cells to pass without lysing, and an outer diameter of  $1/4$  inch. Thanks to their wall thickness and material these tubings are extremely rigid. They were also cut as short as possible to minimize dead volumes thus whilst allowing travel movement of the printer. The tubing was fixed to the probe using the system depicted in figure 3.14 A where the tubing is pinched by a ferrule and pushed against the chip where an O-ring provide additional sealing. This method allows to reversibly connect the tubing with minimum dead volume and good sealing to the probe. Moreover glass syringes with Teflon plungers were used. This syringes are autoclavable which is mandatory to work with cells and have no stick and slip effect, which would induce flow instability as well.

### 3.2. Concentrators design

The final probe is shown in figure 3.14 B. The solution with cells is injected through the inlet and passes through the main channel where the crossflow filter is implemented. The waste channels remove the excess media, which is discarded. The chosen ECM can be injected through the ECM inlet and is injected just before the herringbone mixer, where the solution is homogenized before being dispensed at the outlet preemptively coated with the hydrophobic coating presented in chapter 2.2.3. This way cells can be printed in ECM without waste as it would have been if cells were suspended in ECM from the beginning. By controlling each flow it is possible to choose the desired cell concentration for printing, the only limitation being that at high concentration factors the outlet flow is very low, thus the printing speed can be dramatically reduced. Unfortunately  $Q_{in}$  flow rate cannot be indefinitely increased as it would mean increasing  $Q_w$  as well thus increasing the stress on the cells against the filter. This would make the cells lyse through the filter. Typical inlet flow speed of 1 to 2  $\mu\text{L}\cdot\text{s}^{-1}$  were used.

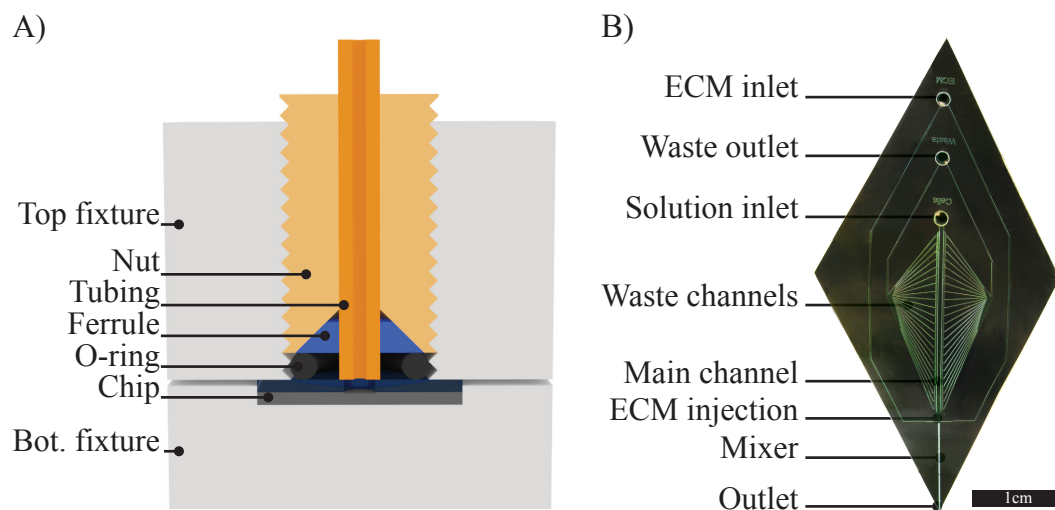


Figure 3.14 – Final printing setup. A) Schematic for the fluidic connection to the probe B) Picture of the probe depicting its layout.

Moreover with this setup it would be possible to concentrate at maximum packing density then dilute to the wanted concentration. As the maximum packing density is constant, it would get rid of the instability of the probe. This technique wasn't use as it presents a high risk of clogging the probe. Finally, it is possible to use multiple probes next to each other, thus allowing multi-material printing as presented in appendix H.

### 3.3 Bioprinting at high cell concentrations

#### 3.3.1 Materials and methods

##### Cell culture

NOR-10 fibroblasts cells were used as a cellular model for the experiments. Those cells are issued from a widely used inbred strain and are commonly used in biology [Koltzschner et al., 2003, Grinnell, 2003, Petrie and Yamada, 2015, Rhee, 2009, Dallon and Ehrlich, 2008]. Fibroblasts are the most abundant cells in connective tissue and are responsible for its organization and maintenance [Grinnell, 2003]. It is therefore important to master the printing of connective tissues before envisioning to print wider structures. NOR-10 fibroblast cells were used for the characterization of the probe as well as for printing. They were passaged twice a week and cultured in DMEM medium with 10% fetal bovine serum and 1% penicillin streptomycin, further referred as standard media. Cells were cultured and used at passage below 10 to avoid excessive mutations in their genome. To assess cell spreading in the gel, the nucleus as well as the cytoskeleton of the cells were stained using 4',6-Diamidino-2-Phenylindole, Dihydrochloride (D1306 from thermofisher) and Alexa Fluor™488 Phalloidin (A12379 from thermofisher) by following the manufacturer protocol. This protocol will be further mentioned as DAPI actine staining.

##### ECMs

Pure collagen (C2124-50mL) was purchased from Sigma-Aldrich. A solution of half stock collagen and half standard media was prepared and the pH corrected to pH=7 using a 0.1 molar NaOH filtered solution (for 2mL of collagen and 2mL of DMEM media 180 $\mu$ L of NaOH 0.1M was found to bring the pH back to 7). All solutions were prepared on ice to avoid for the collagen to crosslink. The prepared solutions can then be loaded in a sterilized syringe for printing. The syringe was also kept at 0°C.

##### Printing

The probe, tubing and connection were autoclaved before use. The probe was mounted on the printer as explained in chapter 3.2.4 and the bed heated to 37°C. The syringes with all the solutions were placed on the syringe pump in vertical position. It is important to place them vertically as cell sediment at about 10 $\mu$ m·s<sup>-1</sup> in the syringe. If placed horizontally, cell will sediment to the side of the syringe in a few minutes and won't be dispensed, whereas if placed vertically, cells will sediment toward to syringe outlet. The concentration at the outlet of the syringe was measured over time to assess that sedimentation in the syringe does not impact the final concentration. This is true as long as the used flow rates make the piston of the syringe move faster than the cell sediment

### 3.3. Bioprinting at high cell concentrations

and that the syringe pump are not stopped for an extended period of time. A sterile Petri dish is then placed on the heating bed and the printing program is started.

#### 3.3.2 Results

##### NOR-10 bioprinting

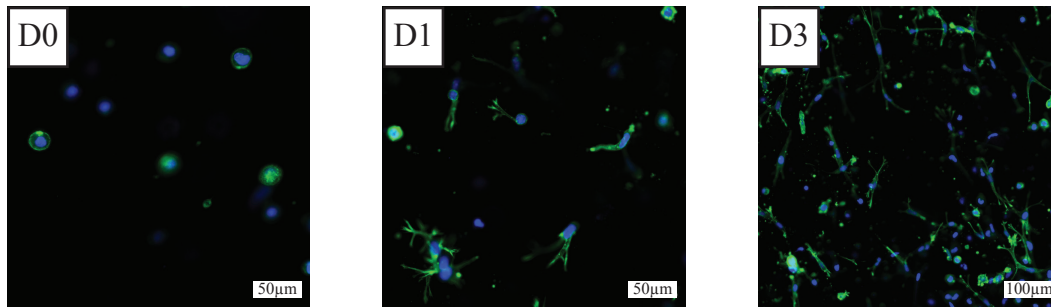
A pure collagen solution was used as it is the principal ECM present in connective tissues [Grinnell, 2003], which is the native tissue of fibroblasts [Novotny and Gnoth, 1991]. A cell solution of 2 million cell per milliliter in standard media was loaded at the probe solution inlet and as well as pure collagen at the ECM inlet (see figure 3.14). Low concentration was set to be 1 million cell per milliliter (concentration often used in literature) and high cell concentration to be 10 million cells per milliliter. To do so the cell solution flow rate (SFR) was set to  $1\mu\text{L}\cdot\text{s}^{-1}$ , the waste flow rate (WFR) to  $0\mu\text{L}\cdot\text{s}^{-1}$  and the ECM flow rate (EFR) to  $1\mu\text{L}\cdot\text{s}^{-1}$ . The resulting solution is then 1 million cells per milliliter mixed in collagen. For the concentrated solution the flow rate were set as follow. SFR was set to  $1\mu\text{L}\cdot\text{s}^{-1}$ , WFR to  $0.9\mu\text{L}\cdot\text{s}^{-1}$  and EFR to  $0.1\mu\text{L}\cdot\text{s}^{-1}$ , resulting in a cell concentration of 10 million cells per milliliter mixed in collagen. It is important to note that by changing the output concentration, the output flow rate changes as well. Therefore the printing speed should be adjusted accordingly to keep the same amount of dispensed liquid per printed distance. The resulting prints were incubated for 10 minutes at  $37^{\circ}\text{C}$  to crosslink the collagen then media was added to the Petri dish. The printed tissues were then kept in culture for three days without changing media to avoid cytokines dissolution. Samples were fixed using 4% paraformaldehyde (PFA) and stained with DAPI actine staining at day 0 (just after seeding), 1 and 3. The cells were then images using a Zeiss LSM700 confocal microscope. The results are shown in figure 3.15.

Just after seeding all the cells are round as one could expect from a cell suspension as they didn't have time to spread yet. Because the pictures are taken using a confocal microscope, all the cells visible on the pictures are from the same plan in the tissue and not from the whole volume of the gel. This allows to have cells in focus and also to better appreciate the cell concentration. Because of the increased concentration it is observed that cells are effectively much closer from each other at higher concentration than at standard seeding concentration of 1 million cell per milliliter.

After a day of culture, cells have already spread, showing the good biocompatibility of the collagen with the cells. Indeed right after polymerization of the collagen matrix, cell start to remodel it [Link, 1994]. There are however notable differences in the spreading of cells at high density versus the spreading at low density. More actin filaments are present at high density and cells resemble more to the ones of *in-vivo* tissue [Novotny and Gnoth, 1991]. The morphology at low concentration in the present study

### Chapter 3. Cell concentration

#### Low Concentration



#### High concentration

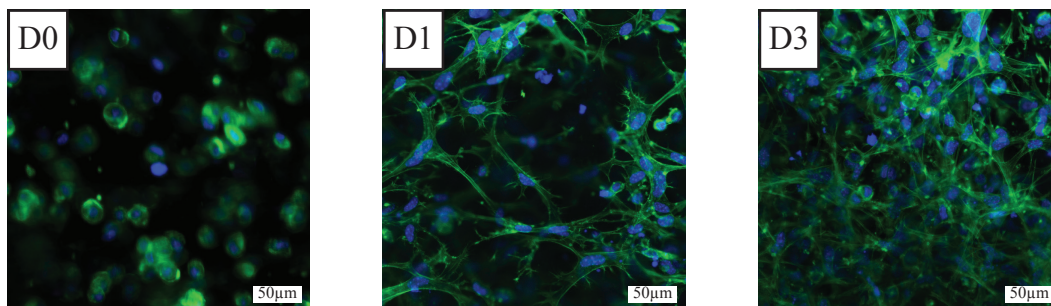


*Figure 3.15 – Printed NOR-10 cells in pure collagen matrix at 1 million cells per milliliter (top) and at 10 million cells per milliliter (bottom) concentration. The culture was imaged a day 0, 1 and 3 using confocal microscopy. Cells were stained for nucleus (blue DAPI) and actine (green Phalloidin).*

is closely resembling the morphology of a previous study done at low concentration as well ( $10^5$  cells per milliliter) [Koltzsch et al., 2003]. Cells seeded at higher density on the other hand spreads over larger distances. They resemble cell culture done at 1 million cell per milliliter, observe in previous research [Kol, 2003], where the addition of platelet-derived growth factor was needed to achieve this result. This indicates that higher seeding concentrations might result in more growth factor secreted by cells within the culture, thus favoring the cell colonization of the matrix.

After only three days of culture, one can observe the confluence of the cells in the tissue seeded at high density, which is not the case for the tissues seeded at low density. This is important as cells will provide tissue stability faster thus facilitating maintenance operations such as media change, staining or other manipulation of the tissue. Moreover, as cells arrive to confluence faster, less cell divisions are needed thus less mutations will occur [Boesen et al., 1994]. This aspect will become increasingly important in tissue engineering as printed tissue will be implanted *in-vivo* and high cell mutations can lead to cancer [Lengauer et al., 1998]. Moreover no additional growth factor was needed thus further reducing the risk of tissue inflammation after implantation [Vajanto et al., 2002, Lykissas and Gkiatas, 2017].



## 3.4 Bladder organoid bioprinting

### 3.4.1 Motivation

Organoids are *in-vitro* methods that allow recapitulation of organ like physiological features. These miniaturized versions of organs have applications in the domain of tissue repair and drug toxicity testing and have been produced for several key organs [Kretzschmar and Clevers, 2016]. Organoids are usually cultured in a 3D environment, usually in a dome of matrigel or basement membrane extract (BME), bathed in a liquid media supplemented with specific growth factors. Organoids can be started from the two main types of stem cells either using pluripotent embryonic stem cells and their synthetic induced pluripotent stem cell counterparts or organ restricted adult stem cells. Both approaches depend upon the expansion potential of normal stem cells in culture.

Even though organoids were used in 3D printing [Schneeberger et al., 2017], the printing of organoids has not yet been achieved. In this section, the bioprinting aspect is limited to high cell content droplets and their deposition but this is still useful to produce organoids with high throughput, as organoids are emerging to be a valuable platform to develop *in-vitro* models for studying pathophysiological and organogenesis related issues [Peng et al., 2018]. Using the microfluidic tools developed here, improvements to organoid production and repeatability are targeted. Bladder organoid yield high clinical potential as bladder cancer as well as bladder infections have a high incidence. Those organoids could be used as *in-vitro* models to test medications and understand how diseases spread. However bladder models were only recently developed, primarily for cancer study [Wang et al., 2017a, Lee et al., 2018b]. It is also of interest to reproduce healthy bladder organoids as they can be used to model infections. Those organoids can then be injected with bacteria as it was demonstrated for intestinal organoids [Williamson et al., 2018]. A normal urinary bladder consists of muscles, connective tissues and on the inner layer, urothelium. The urothelium usually is 3 to 6 cell layer thick and is composed of a basal cell layer followed by an intermediate cell layer and finally umbrella cells that are the most inner layer of the bladder [Jost et al., 1989]. Thus to model bladder reaction to infection only the urothelium needs to be replicated.

Generally making any fully differentiated organoid involves different methods such as the isolation of epithelial cells after mechanical chopping and collagenase digestion as described in Figure 3.16 A. In the specific case of mouse urinary bladder organoids, scraping uroepithelial cells or mechanical chopping and collagenase digestions did not result in a full differentiated organoids. Only the basal and intermediate cells could be observed in those organoids, which were confirmed by presence of CK5, CK7 and absence of CK20, UPIIIa staining. However, it was observed that selective isolation and enrichment for umbrella cell populations from a mouse urinary bladder resulted in a fully differentiated mouse bladder organoid.



### Chapter 3. Cell concentration

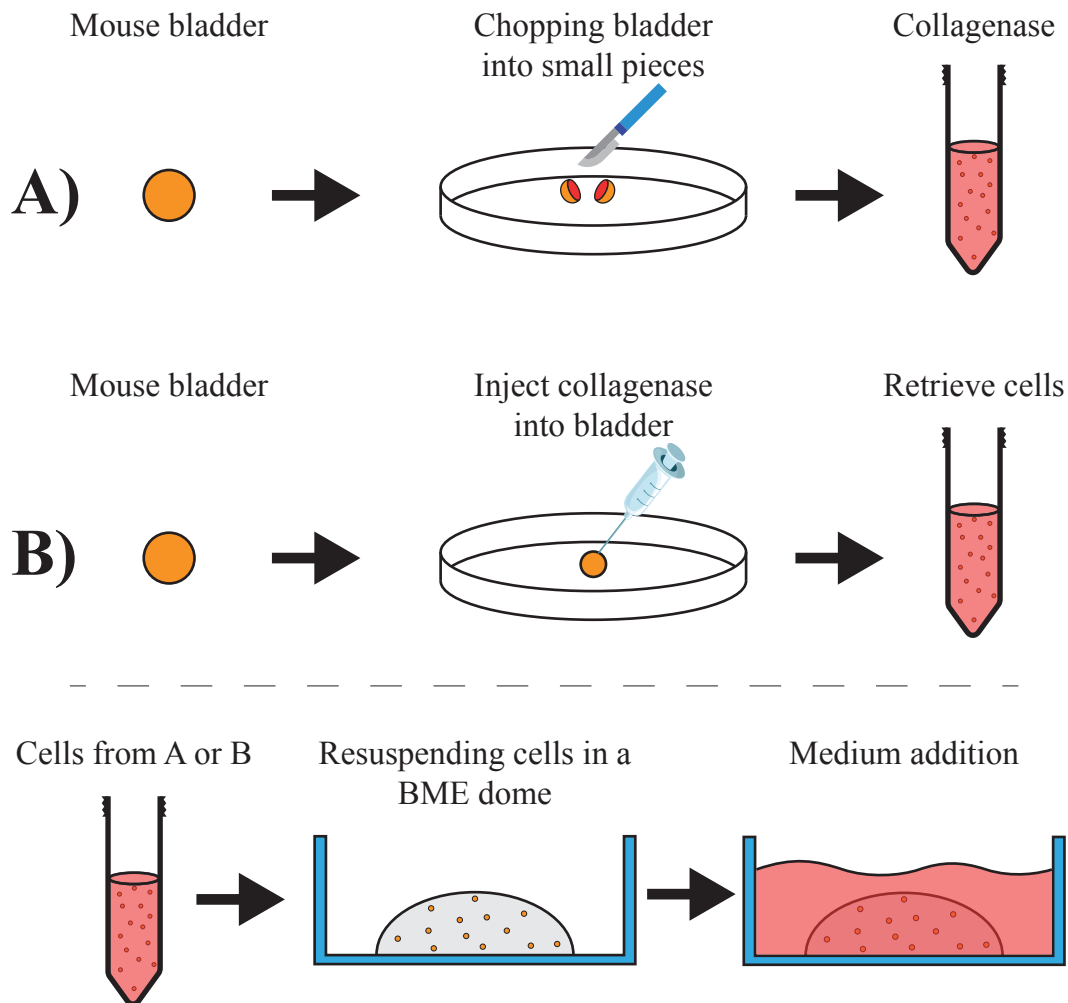


*Figure 3.16 – Cell isolation and seeding. Two cell isolation methods are possible. Either by tissue chopping and collagenase treatment (A), or through collagenase micro-injection(B). Isolated cells are then seeded in a BME dome and cultured in MBM.*

#### 3.4.2 Protocol

In order to prepare mouse bladder organoids, 4 months C57Bl/6 mice were sacrificed to isolate uroepithelial cells. In order to isolate 103-104 uroepithelial cells, 500  $\mu$ L TryPLE was injected into the lumen of a clamped mouse urinary bladder with a micro-syringe. Following micro-injection, the clamped mouse urinary bladder was placed inside a 50ml Falcon tube surrounded by 20ml DMEM medium. The Falcon tube containing mouse urinary bladder is incubated for 1 hour inside a cell culture incubator at 37 °C and 5% CO<sub>2</sub>. The mouse urinary bladder is then washed with DMEM containing 20% FBS as described in Figure 3.16 B.

To create the organoids, the isolated cells must be placed in BME domes. In this case the dome was made using RGF BME, type2, 17.45mg/ml (from Cultrex, catalog #:

### 3.4. Bladder organoid bioprinting

3533-005-02, lot #: 40763K17). First, using an eppendorf 5702 centrifuge with a 8x15mL swing-bucket rotor (A-8-17) of radius 12.8 cm, the cell suspension is centrifuged at 1300rpm (relative centrifugal force (rcf)=242·g, g being the gravity on earth) for 5 minutes. For accurate reproduction of the experiment with a different centrifuge, the relative centrifugal force must be used instead of rpm. It is then resuspended at the wanted concentration in a custom mouse bladder medium (MBM) developed for the culture of those organoids (see appendix G.2). From that point on, all pipette tips, falcon tubes and other material must be coated with 1% Bovine Serum Albumin (BSA). The solution is then used to coat surfaces and no washing step is required.

An inherent property of the concentration probe we developed is that media in which the cells are suspended will be mixed with the ECM in contrast with pipetting where cells are centrifuged, all the media removed and the pellet mixed in ECM. In most cases, the dilution of the ECM will weaken the structural stability of the ECM. In the case of Cultrex, a solution composed of 75% Cultrex diluted with 25% of media containing cells, was found to have enough mechanical stability to form acceptable domes.

To produce the BME domes, the solutions are loaded in syringes and once the flow rates are stable, the probe is positioned over a preheated incubate plate (fluorodish FD35-100 from thermofisher) and the dome starts to form. The setup to produce the dome is illustrated in figure 3.17 A. As the plate is placed over a hotplate at 37°, the base of the dome quickly solidifies and the tip of the probe is pulling the dome up during dispensing by capillary forces. This results in high and well defined domes (see figure 3.17 B). The plates are stored for 10 minutes upside down in the incubator for the cultrex to crosslink

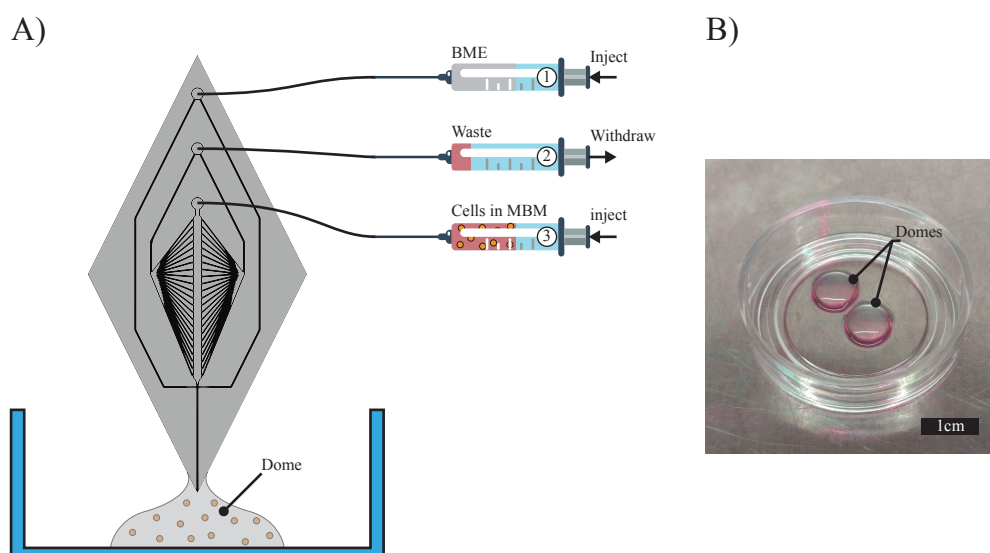


*Figure 3.17 – BME dome printing. A) Schematic of the setup for BME dome printing. B) Printed domes.*

### Chapter 3. Cell concentration

and MBM is added to the dish. To assess the effect of cellular concentration over the formation of organoids, uroepithelial cells were seeded in basement membrane extract (BME) domes at 125 thousand, 500 thousand and 2 million cells per milliliter in 75% cultrex 25% media and incubated for two weeks to let the organoids form.

The targeted cellular concentrations for organoid formation were based on previous work on organoid culture by Kunal Sharma. They are not at the maximum concentration of the probe and could also be achieved by standard pipetting. In fact, as a control, organoids were also produced by pipetting. After thorough mixing BME and cells were dispensed in a preheated incubate plate, on a hotplate at 37°C. The plates are stored for 10 minutes upside down in the incubator for the cultrex to crosslink and MBM is added to the dish. However the use of the probe provides several advantages compared to the pipetting method. First, the solution homogeneity is much better using the probe in term of cell concentrations and constant volumes can reliably be dispensed. Indeed the viscosity of the Cultrex makes the pipetting difficult, producing domes of different volumes. Moreover the mixing is rather difficult, which results in unhomogeneous concentrations. It also introduces bubbles in the mixture resulting in material loss or badly shaped domes. All those hurdles are alleviated with the use of the probe and the production of homogeneous domes is easier. Finally using the probe, the concentration within the dome can easily be adapted just by changing the flow ratio instead of having to redo the whole process.

During incubation, the organoids have the tendency to migrate toward the bottom of the dome. Should they touch the culture plate, they would flatten and transform into a 2D culture. To avoid this, after a week of incubation, the organoids are subcultured. To do so, first the MBM is removed from the well to be passed and replaced with 500  $\mu$ L of ice cold MBM. The BME dome is mechanically scraped and suspended in the cold MBM. The medium is then collected and put in a pre-coated 15ml Falcon tube with 1% BSA and centrifuged at 800 rpm ( $rcf=92\cdot g$ ) for 5 minutes. The supernatant is withdrawn and the organoids are then resuspended in cultrex and new domes are formed. MBM is poured on top and the organoids incubated for one more week.

#### 3.4.3 Results

To assess the morphology of the organoids and see if they developed properly, the organoids are imaged in their dome using bright field imaging after 14 days of incubation. In figure 3.18 A, Cultrex printed at 125 thousand cells per milliliter reveals no organoid formation, only single cells can be observed. A similar observation is made for domes seeded at 2 million cells per milliliter where the cells degraded the Cultrex domes and migrated toward the culture plate resulting in a 2D culture. This highlights the need for a high enough cell concentration in order to get organoid formation. However the solution does not lie in printing at extremely high concentrations. The ideal concentration thus

### 3.4. Bladder organoid bioprinting

resides in a bracket where organoids can form. This further incentivize the use of the probe as it can easily tune the cell concentration within the dome in a precise way in contrast with standard pipetting. In figure 3.18 B, the printed cell at 500 thousand cells per milliliter, resulted in organoids (arrow). The variation of contrast within the cellular construct indicates the formation of a lumen. The control using standard pipetting at 500 thousand cells per milliliter also yielded organoids as seen in figure 3.18 C. The presented organoids are spherical as it can be expected for such cell culture [Lee et al., 2018b]. However, some organoids were presenting different morphology in both printed and control cultures (see figure 3.18 D). It is supposed that it is the result of passaging organoids after the first week of culture. This action might have damaged forming organoids leading to more random shapes. This phenomenon implicated only on portion of the organoids and should not impact their behavior.

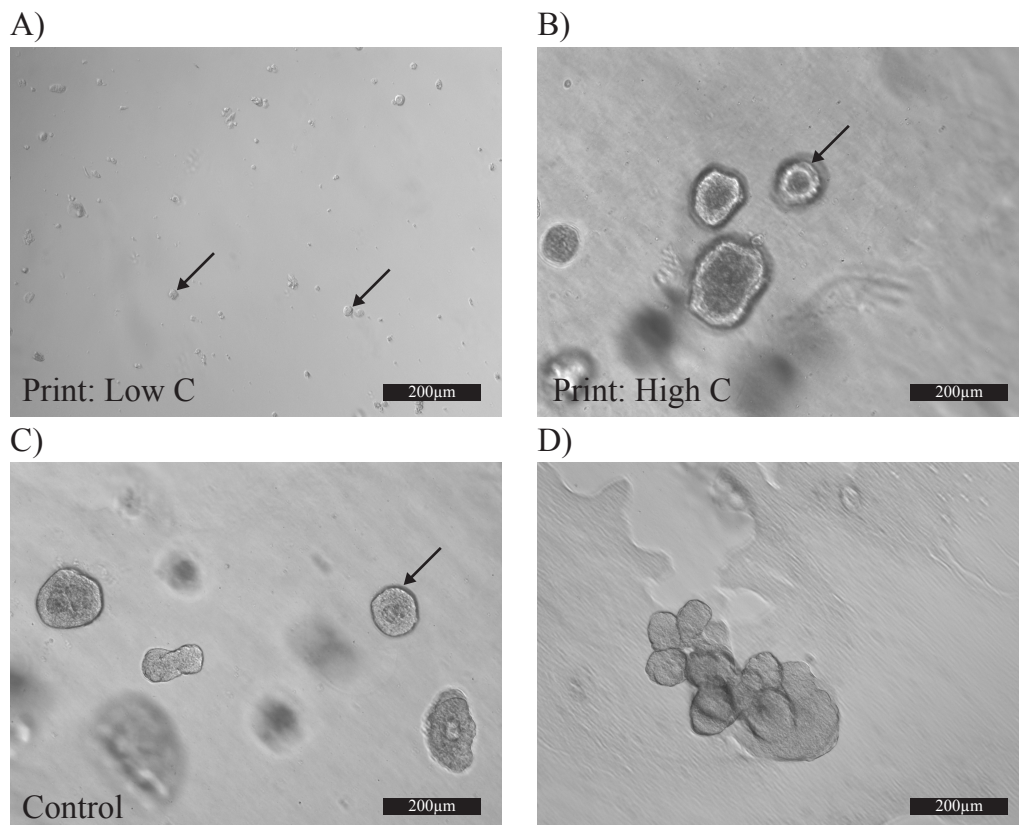


*Figure 3.18 – Organoids bright field imaging after two weeks in culture. A) Micrograph in the dome at low concentration shows the lack of organoid formed as only single cells are present (arrows). B) Micrograph in the dome at high concentration. In this case, organoids were formed (arrow). C) Micrograph in the control dome made by pipetting. In this case as well, organoids were formed (arrow). D) Deformed morphology probably resulting from organoid passaging.*

As organoids measure several tenth of micrometers in diameter, staining can get complicated as the dye must diffuse through the full tissue. This is of importance for

### Chapter 3. Cell concentration

immunostaining as a decrease of the signal toward the center of the organoids could either be attributed to diminution of the targeted epitope or a depletion of the staining solution toward the center. Moreover having to image 3D tissue will produce background noise even with the use of a confocal microscope.

To remedy to this issue, the organoids were cut in  $4\mu\text{m}$  thick slices thus eliminating the diffusion problem and background noise. For obvious reasons, the samples that didn't yield in any organoids were not processed further. To perform the slicing, the fully differentiated organoids are fixed with 4% PFA for 6 hours with occasional mechanical dissociation with a pipette tip. The incubation time for fixation depends upon the method used for staining fixed samples for immunofluorescence. Generally paraffin embedded samples require longer time of incubation in PFA to properly crosslink the sample. The BME is also degraded by PFA fixation during this incubation. The fixed organoids are then washed with PBS and then centrifuged at 800 rpm ( $\text{rcf}=92\cdot\text{g}$ ) for 5 minutes in a 1% BSA pre-coated 15ml falcon tube. The organoids are washed twice with PBS to remove any remaining residues of PFA. The organoids are then resuspended in  $50\ \mu\text{L}$  of prewarmed Histogel at  $50\ ^\circ\text{C}$  and pipetted out as a small hemispherical dome inside a 1cm Tissue-Tek Cryomold. The cryomold is placed on a cold ice plate for solidification. Subsequently to solidification, the hemispherical Histogel is processed for paraffin embedding. The embedded samples were then cut into  $4\mu\text{m}$  slices.

Hematoxylin and eosin (H&E) staining is a standard staining method to evaluate tissues morphology. Eosin is a pink acidic dye that binds to most proteins present in the cytoplasm as well as in intracellular membranes and extracellular fibers. Hematoxylin on the other hand is used to stain acidic structures in purple. Deoxyribonucleic acid (DNA) is especially targeted resulting in purple nuclei. For primary morphology assessment, the organoid slices were stained using H&E staining.

A lumen is clearly visible for the printed organoids (figure 3.19 A), for the control by pipetting (figure 3.19 B) as well as for the organoids presenting an odd morphology (figure 3.19 C). The organoids are three to four layer thick as previously reported by [Horsley et al., 2018] and reflect the native urothelial architecture.

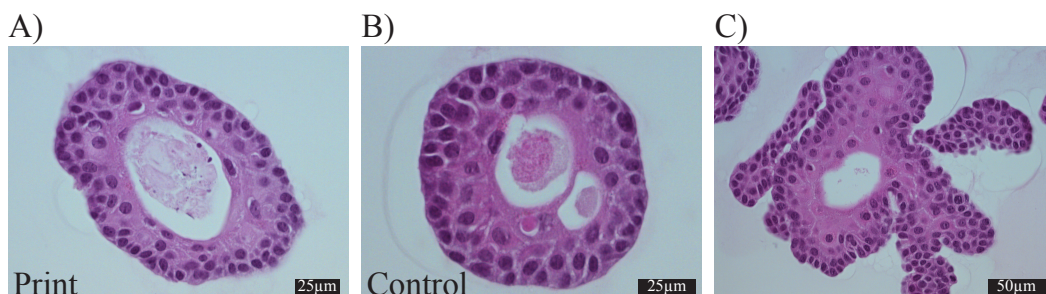


*Figure 3.19 – Sliced organoids H&E staining for the high concentration print (A), the pipette control(B) as well as the deformed morphology organoid(C).*

### 3.4. Bladder organoid bioprinting

To further assess tissue morphology and structure, immunostaining was performed on the organoid slices. Multiple proteins were targeted (see table in appendix G) in order to reveal inherent cell organization within the organoids structure. The most important staining that were used are summarized in figure 3.20 for printed organoids and in figure 3.21 for control organoids produced by pipetting. The immunohistochemical stains used were CD44, cytokeratins (CK)5, CK8, CK13 and uroplakin III (UP3) which should all be present in differentiated urothelial tissues [Riedel et al., 2001]. Those target proteins are chosen as they are expressed differently in a basal, intermediate or umbrella cell. Based on the spacial location of the staining, it is possible to assess what type of cells are present in the organoids and if they form a structure similar to *in-vivo* bladder structures. As in terms of organoid development, shape and composition, both printed and control organoids are extremely similar. Therefore the following remarks on the immunostaining results can be applied to both organoid cultures.

**CD44** is a common cell-surface glycoprotein associated with cell-cell interactions, cell adhesion and migration [Ponta et al., 2003]. This marker should be present throughout the whole organoids and is used to provide information on the cohesion between cells within the organoid. The lack of this protein would indicate the presence of a mere cell aggregate and not a coherent cell arrangement. Figure 3.20 A and 3.21 A show the presence of CD44 at the edge of each cell, indicating a connection between the cells in the organoids. This confirms cells interactions.

**CK13** is a characteristic staining for urothelium [Riedel et al., 2001] and should be present in most of the organoid, especially in the basal and in the intermediate cell region. In figure 3.20 B and 3.21 B CK13, seems to be more abundant in the intermediate layer only. A faint fluorescence is still observed in the basal region. This might indicate that the basal layer is not fully developed in the organoids

**CK5** is present in normal keratinizing epidermis and squamous mucosal epithelium, as well as in basal cells or myoepithelial cells of the breast, salivary glands, and prostate [Edgecombe et al., 2012]. As it can be observed in figure 3.20 C and 3.21 C, CK5 is present mostly on the outer edge of the organoids indicating that the basal layer is indeed present in the organoids.



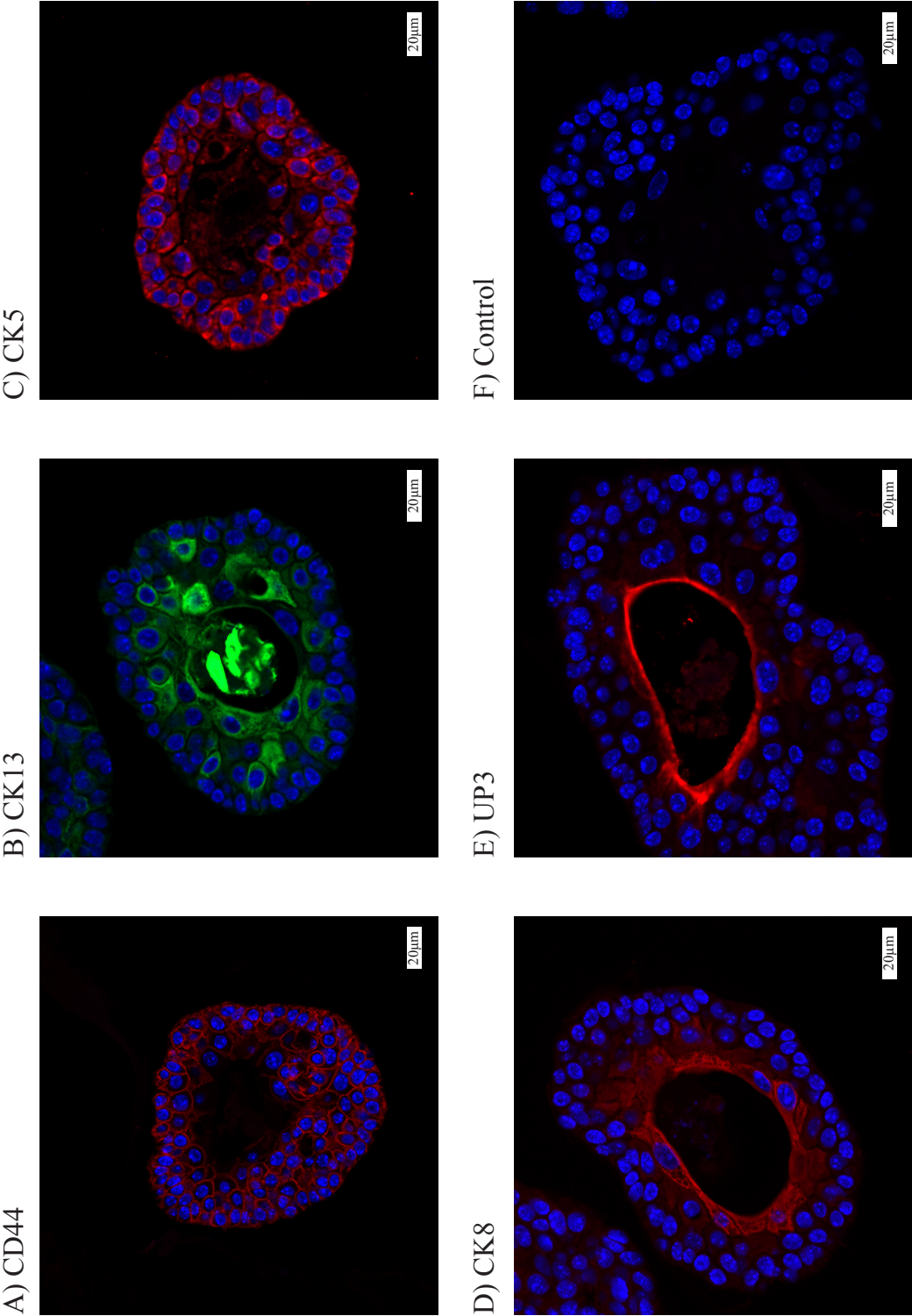


Figure 3.20 – Immunostaining of a 4µm thick slice of printed organoids: A) Organoid slice where cells are stained for nucleus in blue with DAPI and CD44 in red B) Organoid slice where cells are stained for nucleus in blue with DAPI and CK13 in green C) CK5 D) Organoid slice where cells are stained for nucleus in blue with DAPI and CK8 in red E) Organoid slice where cells are stained for nucleus in blue with DAPI and UP3 in red and F) are the control where no primary antibody where added on the sample and only the secondary antibody to set the gain threshold.



### 3.4. Bladder organoid bioprinting

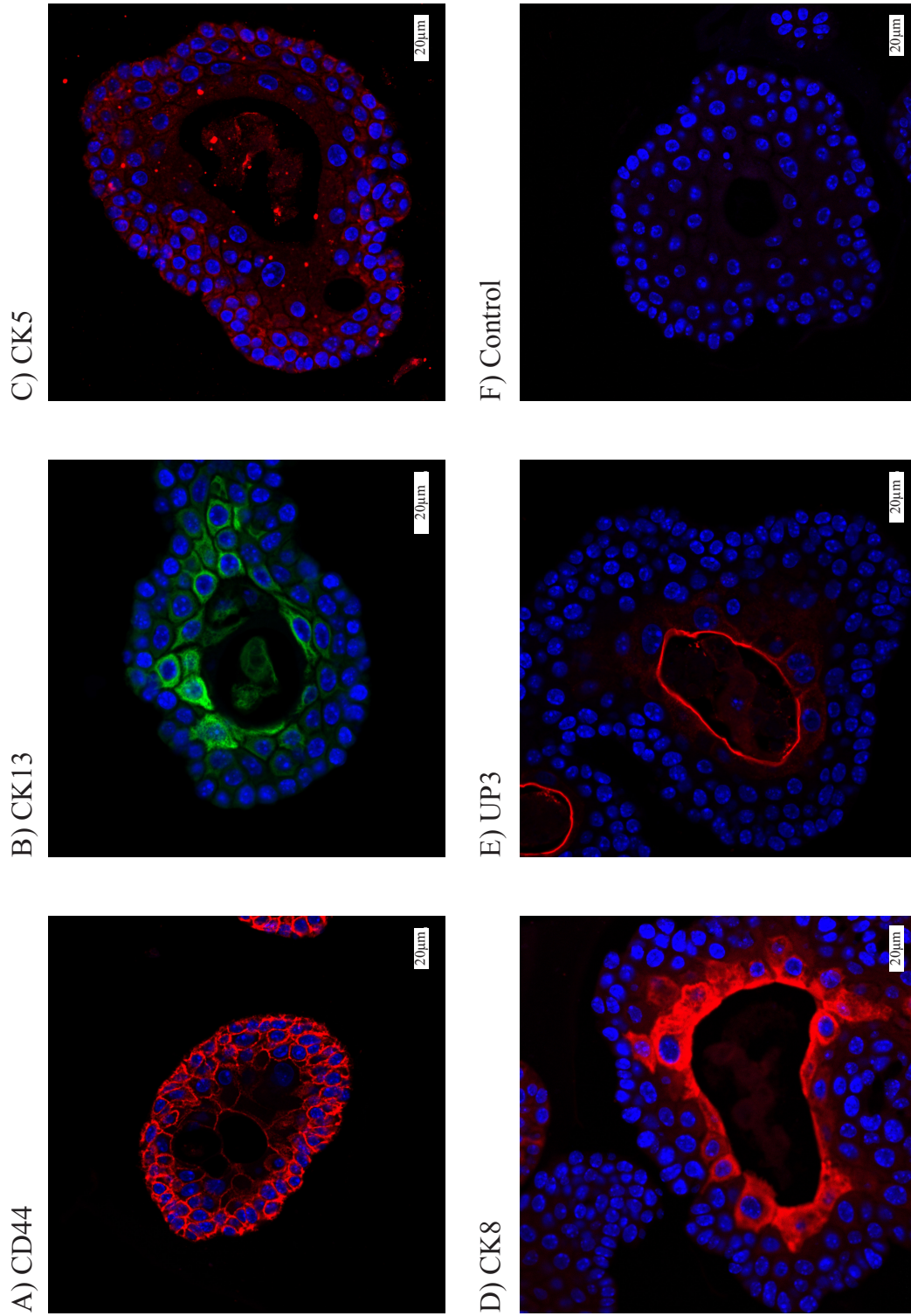


Figure 3.21 – Immunostaining of sliced control organoids: A) Organoid slice where cells are stained for nucleus in blue with DAPI and CD44 in red B) Organoid slice where cells are stained for nucleus in blue with DAPI and CK13 in green C) CK5 D) Organoid slice where cells are stained for nucleus in blue with DAPI and CK8 in red E) Organoid slice where cells are stained for nucleus in blue with DAPI and UP3 in red F) are the control where no primary antibody where added on the sample and only the secondary antibody to set the gain threshold.

### Chapter 3. Cell concentration

**CK8** is predominantly found in the umbrella region and a in smaller amount in the intermediate cell layer as well. It was reported from [Horsley et al., 2018] that CK8 was found throughout the full organoid however the organoids presented in their research were three to four layers thick compared to the four to six layer in our case. Moreover their imaging method consists in confocal stack to see in depth which bare some limitations such as noise from surrounding layers as well as limited working distance. These limitations could have contributed in the interpretation of having CK8 throughout the organoids. Indeed, in the case of sliced organoids as presented here, the full depth of the organoid layer can be observed in details. It reveals that CK8 is predominately present near the umbrella cells (see figure 3.20 D and 3.21 D).

**UP3** is the specific urothelial differentiation marker [Riedel et al., 2001] and is found on the apical cells [Horsley et al., 2018] located in the inner organoid. This specific marker shows a unique membrane specialization present in mammalian urothelium [Sun et al., 1996]. As it can be seen in figure 3.20 E and 3.21 E, this marker is present and precisely define the lumen's perimeter. It indicates a full differentiation of the umbrella cells in the organoids.

**Control** samples where no primary antibody but only secondary antibody was added to the sample were imaged and used to set the maximum gain the microscope. Figure 3.20 F and 3.21 F, shows the control where only the DAPI can be seen in blue and no other fluorescence, setting the highest gain usable for imaging to avoid any false positive. These controls were made for mouse and rabbit secondary antibodies. However the signal between each staining whilst above negative control, are not made at the same gain thus they cannot be compared in term of expression level by comparison of intensity but only in terms of localization, which is on interest for us.

These stainings demonstrate that cells undergone differentiation as the cells in the inner region of the organoid do not present the same phenotype as the cells in the outer region. Organoids exhibiting all the layers present in urothelium with basal cells and the outer edge, an intermadiate layer and a fully differentiated umbrella cell layer could be reliably produced using the probe. Moreover, this cellular architecture is similar to what is found in native bladder from C57Bl/6 mice when similar staing are applied [Kunal and Serex, 2018]. At the time of writing, such organoids were only produced by Michael M. Shen laboratory as well as John McKinney laboratory where the protocol originate and has yet to be publish.

## 3.5 Conclusion

### 3.5.1 Summary

From a biological point of view, printing at high concentration is of major importance as it brings the cells closer to their neighbors allowing for a better cell to cell communication [Lee et al., 1994]. Additionally, because of the higher seeding density, less cell divisions are needed to obtain cell confluency in the tissue thus limiting the risk of mutations. A reasonable increase in concentration yielded in major improvements to the 3D cell culture due to the exponential nature of cell proliferation [Iloki Assanga et al., 2013] and quadratic nature in cytokine diffusion over distance [Alsson, 1997].

To ease working at high cell concentrations in bioprinting, a concentrator that could work at the tip of a moving printing head was developed. The principle of converting focusing devices to concentrator has been explained and a concentrator based on a hydro-focusing principle was developed. Even though the focusing worked, a noticeable decrease in concentration efficiency was noticed. This was in part due do to lift force and wall effects that would reduce the focusing efficiency before the concentration point. Hydrodynamic concentrators often are limited in yield as demonstrated in [Martel et al., 2015]. Therefore, this solution was discarded in favor of a more direct approach. A crossflow filter was developed that allowed a significant cell concentration increase with high viability. Because of the low Young's modulus of the cells, many design tweaks and process optimizations were needed to achieve an adequate concentration of cells over shorter distances than in previously presented works [Chen et al., 2008] allowing the integration of concentrators on a tip of a 3D printer's head.

Printing collagen in combination with NOR-10 cells was successfully used as a model to demonstrate the capabilities of the probe in a bioprinting setting. The cells that were printed at high concentration showed better phenotype than the ones printed at low concentration. Moreover, starting from a high concentration, cells reached confluency in only three days of culture in collagen, which was not achieved when starting from a low concentration. Organogenesis is heavily reliant on cell to cell communication and thus upon concentration. Organoid printing was shown possible with this probe and a window of cell concentration yielded to actual organogenesis. At too low concentration no organoids were formed and at too high cell concentration, cells would degrade the matrix and sediment at the bottom of the Petridish converting the 3D culture in a 2D culture and incapacitating the organoid formation. At the right concentration, fully differentiated healthy bladder organoids formed.

### 3.5.2 Discussion and outlook

In theory it would be possible to reach any final cell concentration from any starting dilution. Yet the higher the concentration factor the lower the output flow rate for a given inlet flow. For extreme concentration factors, the output flow rate becomes too slow for printing at a reasonable speed. Increasing the inlet flow rate allows to increase the overall printing speed to a certain extent but does lead to increased sheer forces over the cells within the crossflow filter to the point where they will lyse. It is however possible to further enhance the cell dispensing system we developed in different ways. The crossflow filter could be elongated to further distribute withdrawal of the liquid, or multiple probes could be placed next to each other multiplying the concentration at a given speed and inversely. Bringing two probes together also allows the use of multiple materials thus the easy creation of material gradients and co-cultures of different types of cells as demonstrated in appendix H. The system presented in this chapter made the manipulation of the viscous ECM much easier as all the mixing steps are happening on chip instead of being performed using pipettes that introduce bubbles and generate waste. It can be easily adapted to other printers to bring more freedom of design to biologist, including cell concentration, multi-material and ECM concentration control and gradient formation.

The printing of organoids has also been achieved not only proving the fact that cells are handled gently by the probe, not damaging cells as sensitive as primary cells, which are much more sensitive than immortalized cell lines such as NOR-10 but also further demonstrating the importance of cell concentration in a culture. Withal, organoids needed to be passaged after a week of culture as they finally migrated toward the bottom of the BME dome. A solution against that could be to culture the dome upside down every two days to minimize the effect of gravity. It was also shown that if cells are at a too high concentration, this sedimentation effect occurs faster. One idea could be to print a ring at very high cell concentration and a dome a lower concentration in the middle. The cells in the ring would provide the cytokines and the cells in the dome could proliferate in the proper environment.

Using microfabricated probes performing cell concentration immediately before they are dispensed can be further developed and impact many applications. In the bioprinting area, for which the probe presented in the present chapter was developed, it allows to print at high cell concentrations. The system we presented can be easily adapted to other printers to bring more freedom of design to biologist, including cell concentration, multi-material and ECM concentration control and gradient formation. Organoid printing was shown possible with this probe and a small window of cell concentration yielded to actual organogenesis. It is reasonable to assume that this window will change with the cell type and BME used. The use of this probe could allow the procedural testing of all concentration of BME and cells automating the process, easily finding the best material and concentration to produce a given organoid. Additionally, this printing

### 3.5. Conclusion

method can be combined with other organoid fabrication methods [Peng et al., 2018] that could help mass produce organoid with repeatable size and shape. Combined with organoid micro-injection [Williamson et al., 2018] as well as new imaging methods [Peng et al., 2018] organoids could become part of high throughput screening for drug testing, providing accurate cellular models thus bringing down the research cost for new drugs. Finally in a completely different setting, the crossflow filter can be used to filter debris smaller than cells in solution. Compared to standard filtering that would stop the cells and let the debris pass through, this technique does the opposite. Used prior to fluorescent assisted cell sorting (FACS) this probe would allow the reduction of noise coming from debris or red blood cells present in samples coming from biopsies. These samples are increasingly used in clinic as using FACS on biopsies allows the identification of cancers



# Biomaterials 3D printing

## 4.1 Introduction

Often, the materials used for bioprinting are selected either because of their compatibility with cell growth and function or because of their crosslinking or extrusion characteristics [Murphy and Atala, 2014]. This is because material properties allowing the printing of high quality structures, such as rigidity or quick solidification, often translate to poor biocompatibility. Therefore, in literature, for cells embedded in the bio-ink, the focus of a studies are either targeted toward material biocompatibility [McBeth et al., 2017, Gao et al., 2015a, Stratesteffen et al., 2017] with extended work on cell behavior but very limited information over material printability or, inversely, the focus is aimed at material printability [Bertassoni et al., 2014, Forget et al., 2017, Armstrong et al., 2016, Shang et al., 2017, Fan et al., 2016, Liu et al., 2017], with limited analysis over cell behavior. Only recently studies have started to focus on both aspects [Lee et al., 2017, Yang et al., 2018, Liu et al., 2018]. However, because of cell sensitivity to environmental cues such as mechanical [Rhee, 2009], chemical [P.Mecham, 2011] or even electrical [Min Zhao, Huai Bai, Entong Wang, John V. Forrester, 2004], no perfect material has been found yet to fulfill both mechanical stability and biocompatibility inducing the adequate behavior in cells.

Moreover, as cells are directly embedded into the hydrogel during printing, only limited options are available to tailor the hydrogel properties to better suit additive manufacturing needs. UV crosslinking at the tip of the printer showed to improve the printing resolution [Ouyang et al., 2017] but photoinitiator as well as UV light can be toxic to cells. Thermosetting materials such as agarose, best mimic the process of standard FDM 3D printing and can produce nice prints [Norotte et al., 2009]. They are however often too stiff and lack adhesion sites for cells to allow for cell culture within the hydrogel. Ionic crosslinking used for alginate for example also produces good printing [Hinton et al., 2015] but faces stiffness and adhesion issues as well.



## Chapter 4. Biomaterials 3D printing

Three main biomaterial were used in this thesis, CMC based cryogels, collagen and cultrex. Because cryogels are printed on a cold bed, the printed material instantly freezes, allowing it to support its own weight. It is therefore possible to print multiple layers (see figure 4.1 A) and using capillary forces, overhanging structures could be printed as well. The conditions of cryogel synthesis are however not suitable for coextrusion with living cells. Concerning the printing of biomaterial exhibiting good biocompatibility such as collagen or cultrex, well defined 3D prints could not be achieved as, these materials are in the liquid form and can take up to 30 minutes to fully crosslink. Once dispensed on a surface, capillary forces will deform the printed layer. Moreover until the first layer is crosslinked, it is impossible to print a second one, rendering 3D printing impossible in a reasonable time scale. To analyze cell behavior in a 3D environment, dome shapes were printed as shown in figure 4.1 B. These domes need to be printed directly in sterile Petri dishes as these hydrogels (with Young's modulus in the range of kPa for collagen [Holder et al., 2018]) are too weak to be transferred from a printing bed to a culture plate.

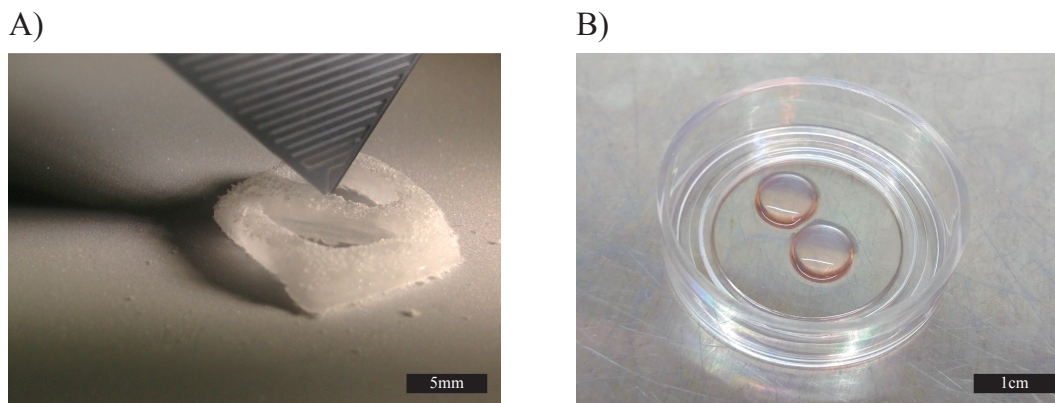


*Figure 4.1 – Bioprints stability A) Printed cryogels can withstand their own weight thanks to freezing allowing 3D structures to be printed. B) Printed Cultrex does not polymerize rapidly prohibiting the structuring of this gel.*

These domes are enough to produce organoids as they provide suitable 3D environment for small cell structures to form. However for tissue engineering, these biocompatible materials need to be reliably 3D printed. In this chapter three methods allowing the printing of soft bio-inks are described.

## 4.2 Improving structural stability

### 4.2.1 Bio-ink modification

The use of composite materials can improve bioinks mechanical stability. In the case of collagen, the addition of alginate was considered. The alginate-collagen mixture can

## 4.2. Improving structural stability

then be printed on an agarose gel bed containing  $\text{CaCl}_2$ .  $\text{Ca}^{2+}$  ions that will diffuse from the bed to the alginate, which will rapidly crosslink [Lee and Mooney, 2012] thus providing structural stability. However alginate is not easily mixed to collagen as the alginate molecules react with cations to form a gel [Lee and Mooney, 2012] and, at  $\text{pH}=2$  (collagen stock solution), the collagen is positively charged. By mixing both alginate and collagen as is, a pellet of collagen and alginate will form. To remedy this issue, the collagen surface charge can be reverted by changing the  $\text{pH}$  of the stock solution [Freudenberg et al., 2007] thus allowing the mixing of alginate and collagen. It is achieved by rapid mixing of  $11 \mu\text{L}$  of  $\text{Na}_2\text{CO}_3$  1M to 1ml of collagen (C4243 from Sigma-Aldrich) on ice to reverse the collagen surface charge followed by the addition of 1ml of alginate 4% in DMEM media.

Because of the fast crosslinking speed provided by the alginate, multiple layers could be printed. A printed structure of alginate-collagen mixture on an agarose bed is shown in figure 4.2 A. The printed tissue is incubated at  $37^\circ\text{C}$  to allow collagen crosslinking. Media is added to a Petri dish and the gel transferred in it for incubation (figure 4.2 B).

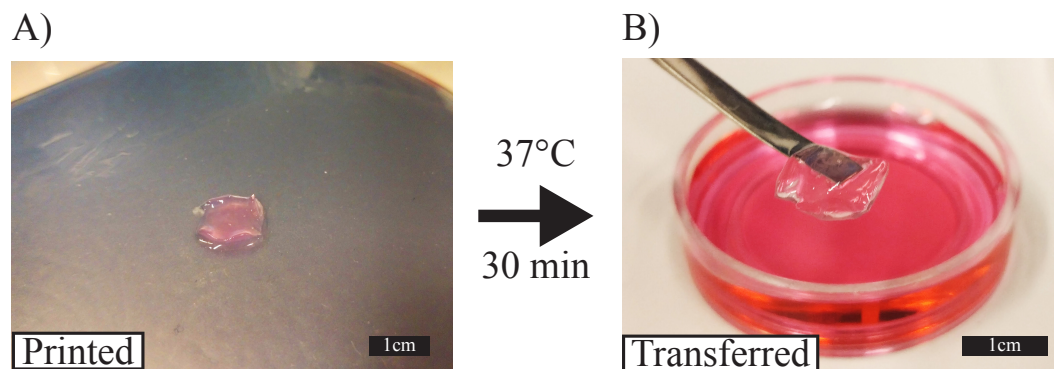


*Figure 4.2 – Printing process with collagen-alginate bio-ink A) Printed structure on agarose bed loaded with  $\text{CaCl}_2$  to rapidly crosslink the alginate B) The structure can be easily transferred into an incubator for collagen crosslinking and then into cell culture media.*

Using NOR-10 cells and the concentration probe presented previously, tissues with a concentration of 10 million cells per milliliter in alginate-collagen mixture could be printed. After 7 days of culture, samples were fixed using 4% paraformaldehyde (PFA) and stained following the protocol from chapter 3.3.1 at day 0 (just after seeding), 1, 3 and 7 and imaged on a confocal microscope. The results are presented in figure 4.3. At day 0 cells are spherical and a homogeneous cell distribution can be observed. After a day of culture, a few cells start sprouting and the number of cell spreading increases until day 7. Cells exhibit a morphology similar to cells cultured at low concentration in collagen but with the addition of lysophosphatidic acid (LPA) [Koltzsch et al., 2003] which has been shown to promote actin stress fibers and focal adhesions [Nobes and Hall, 1995]. Moreover, even after seven days of culture, cells didn't reach confluency contrarily as when cultured in collagen.

## Chapter 4. Biomaterials 3D printing

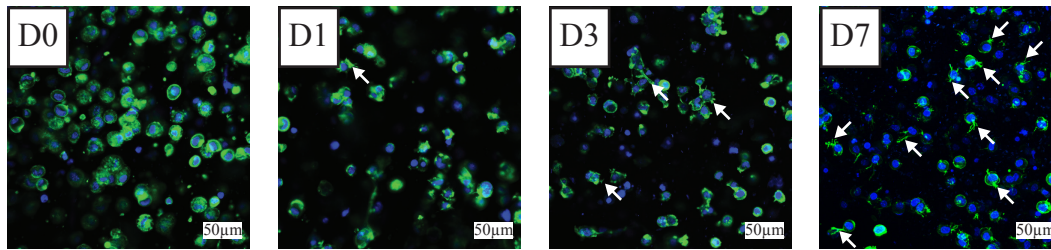


*Figure 4.3 – Printed NOR-10 cells in alginate-collagen matrix at 10 million cells per milliliter. The culture was imaged a day 0,1,3 and 7 using confocal microscopy. Cells were stained for nucleus (blue DAPI) and actine (green Phalloidin). Arrows point at cell sprouting.*

As fibroblasts are sensitive to biomechanical and biochemical cues [Rhee, 2009], the addition of alginate, whilst improving the mechanical stability of the bioink, degraded the bioink biocompatibility. To solve this issue, the selective dissolution of alginate after printing and crosslinking of collagen was attempted. The goal is to remove the alginate once the printed tissue is transferred into media. Citrate is known to degrade alginate matrices [Grünhagen and Lieshout, 2002]. A special media for the dissolution of the alginate was prepared as follows: 100µL of citrate solution in DI 0.5M was added to 10ml of standard media. The pH was then corrected using 90µL HCl 0.5M in DI. The printed gels were cultured for 24 hours in this media after printing in order to dissolve the alginate. Unfortunately, the extended exposition of cells to the media heavily impacted their viability. To reduce the exposition time of the cells to the citrate, the alginate concentration was reduced in order to accelerate its dissolution. However this reduced the mechanical stability of the gel. A suitable equilibrium, where the gel is mechanically stable enough for printing and dissolves quickly was not found. Nevertheless, the addition of alginate in the structure drastically improved the mechanical stability of the printed tissue enabling its transfer and manipulation, but decreased the hydrogel biocompatibility. The approach of composite bioinks is of interest as it can provide bioinks more suited for printing whilst providing cues for cell growth.

### 4.2.2 Co-extrusion printing

By printing a rigid support material alongside with a more biocompatible, cell-laden hydrogel the function of the support and of biocompatibility can be decoupled. The support material is printed layer by layer leaving gaps to be filled later on with softer biomaterial. This approach has already been implemented and proven very effective [Pati et al., 2014, Kang et al., 2016]. The support material must be non toxic to cells and provide adequate support to the printed structure. PCL has been used as a material of choice for this purposes as it is bio-degradable and has a low melting point of around 60°C [Serrano et al., 2004]. It is however hard to remove it from the printed structure once printed and 60°C is too high for direct co-extrusion with cells. Pluronic F-127 is another non toxic material that gels rapidly when a temperature threshold is reached.

## 4.2. Improving structural stability

This threshold varies upon the pluronic concentration [Gioffredi et al., 2016]. This gel has been used as a temporary scaffold [Kang et al., 2016] as it can be easily removed by cooling the printed structure, liquefying the pluronic.

20% w/w pluronic F-127 (P2443-250G from Sigma-Aldrich) was diluted in DI water. This ink is liquid at room temperature and solidifies rapidly when dispensed on a heated bed at 37°C. It is therefore ideal for co-extrusion alongside with other bioinks and cells. As highlighted in [Ouyang et al., 2017] the crosslinking of the material just before printing improves the resolution of the prints by diminishing the ink spreading on the bed upon dispense. In this case, by heating the dispensing tool, a better resolution could be achieved. To assess the bioink properties, two test structures were printed. A 3cm high (150 layers) Eiffel tower (figure 4.4 A). It showcases the ability of the bioink to be printed in multiple layers with overhanging structures. To achieve such height, the hotplate was not enough to keep the top of the structure, hence a climatic chamber where air at 40°C, saturated in water was injected. A second structure was printed with two compartments. Those compartments were filled with blue and red dyed water (see figure 4.4 B). This shows the ability of the bioink to contain liquid materials in a designated place. Most ECM appropriate for cell culture are liquid and take time to solidify. Pluronic can be used to print complex structures that will support cell containing soft bioinks during their curing process. The pluronic can then be removed simply by cooling the printed structure.

Having multiple extrusion heads for each extruded material increases the printing time as for each material switching, the extrusion head must be swapped. A joined output for multiple channels allows the printing of different materials just by switching the flow

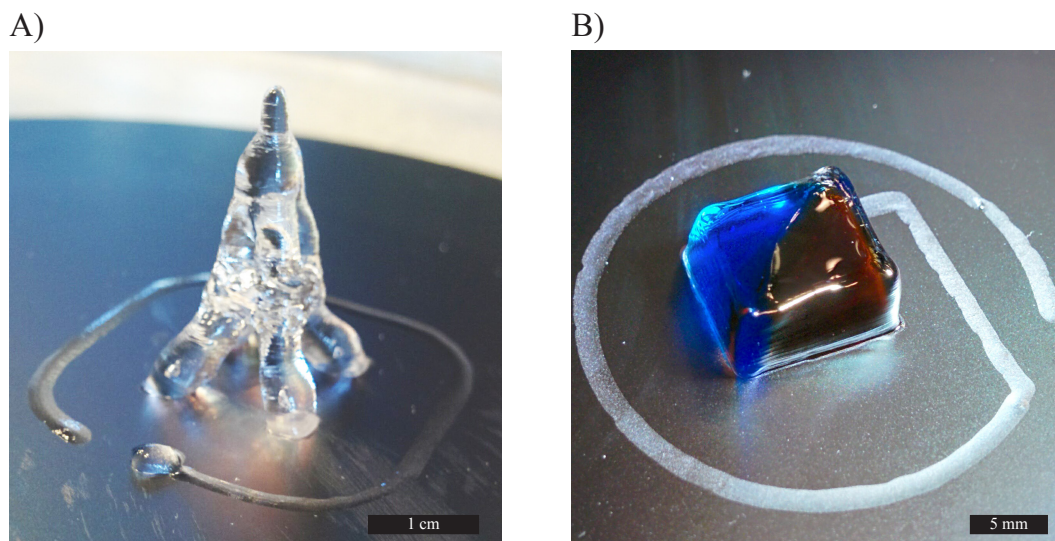


*Figure 4.4 – Pluronic F-127 printing. A) 3cm high (150 layers) Eiffel tower printed in pluronic F-127 B) A two compartments structure filled with blue and red dyed water.*



## Chapter 4. Biomaterials 3D printing

rates of the printed materials without the need of changing the printing head. Such probe is demonstrated in appendix H and was fabricated using micromanufacturing methods. In the case of support material, it is however interesting to create a coaxial output flow in order to either encapsulate the bioink of interest as presented in [Onoe et al., 2013], or to create a support structure with the cell-laden bioink coated around thus support filament. Standard micro-fabrication techniques based on photolithography do not allow the creation of coaxial devices. Stereolithography (SL) on the other hand allows for a complete freedom of design and coaxial channels can easily be printed. Moreover, with the increase of resolution of commercial SL 3D printers, it is becoming an interesting tool for microfluidic chips fabrication.

Using CAD, a dispensing tool for two materials with coaxial output channels was designed (figure 4.5 A) and printed (Perfactory<sup>®</sup> 4 Mini XL from Envisiontec). Despite a claimed pixel size of  $22\mu\text{m}$ , the  $150\mu\text{m}$  gap between the two channels could not be resolved by the machine (see arrow in figure 4.5 B). Designing larger channels would significantly reduce the resolution of the printing head which is no desirable. To obtain a high resolution, the probe was printed in two parts (figure 4.5 C). A capillary was glued on the inner part of the probe to serve as a center channel. The center channel's diameter is  $165\mu\text{m}$  and the outer channel's diameter is  $500\mu\text{m}$ . Both channels can be addressed independently as shown in figure 4.5 E and F. Furthermore, the use of a capillary for the

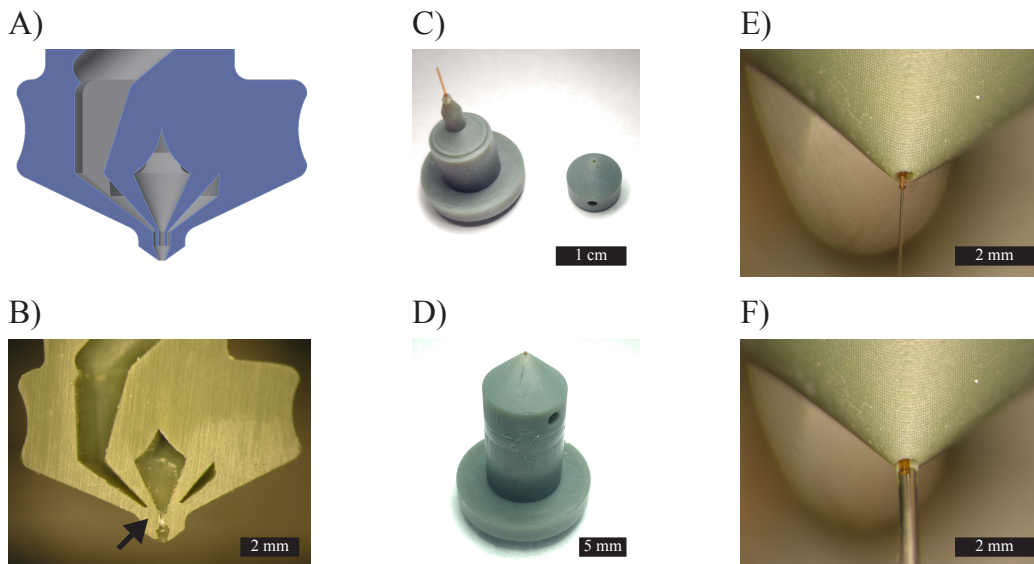


*Figure 4.5 – Co-extrusion 3D printed dispensing tool. A) CAD of the probe manufactured by SL showing the co-extrusion channels. B) Half cut of the co-extrusion probe showing the two channels could not be directly defined. C) A two-part probe design allowing the smallest channels to be made using a capillary. D) Manufactured co-extrusion probe with an inner channel diameter of  $165\mu\text{m}$  and an outer channel diameter of  $500\mu\text{m}$ . E) Probe's tip with water flowing through the inner channel. F) Probe's tip with water flowing through the outer channel.*

## 4.2. Improving structural stability

inner channel allowed for the implementation of the inner channel protruding further than the outer channel. This will have an impact upon the printing later on. Finally despite being 3D printed and made of plastic, this printed probe can still be heated up to 140°C which is enough for most bioprinting applications. Heating can be achieved by coiling a wire around the probe and inputting a current. This heating method is not as efficient nor as precise as the one presented in chapter 2 but it provides satisfactory results when an approximate temperature has to be reached.

Because no functioning vascular systems are in place in printed structures, the nutrient intake for the seeded cells relies on diffusion. The diffusion speed of nutrients in the printed tissues dictates the maximum size that can be printed as for large structures, cells at the center will not be supplied with nutrient and will die. This maximum viable printing size is around a few hundreds of micrometers. To work around this limitation and print larger structures, macroporous structures are often printed. The holes in such structures provide ways for cell-culture media to flow freely and bring nutrients deeper in the printed tissue. Grids are often printed to provide macro pores as they are easy to produce and are regular structures.

As in previous experiments, glycerol 80% was used to simulate soft ECM. In figure 4.6 A, using the coaxial probe, with pluronic F-127 as outer flow and blue dyed glycerol as the inner flow, a grid structure could be printed with glycerol trapped within a pluronic layer. The blue glycerol has been shaped over multiple layers whereas if only the glycerol is printed the printing results in a shapeless puddle. Printing with the structural ink in the outer flow makes sense only if one want to keep the supporting material in the final tissue as demonstrated in [Gao et al., 2015b] where the supporting material acts as the wall of a tube. If on the other hand, one wants to remove the structural gel after printing, using it in the inner flow allows to shape the negative of the chosen design. As

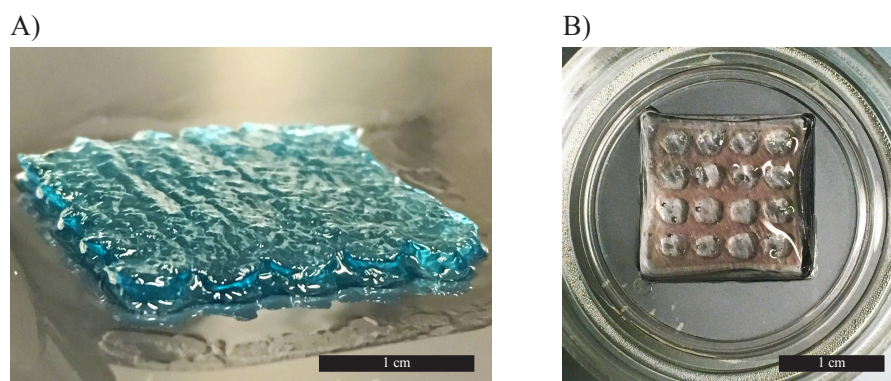


*Figure 4.6 – Co-printed support and soft bioinks. A) Printed grid structure with blue glycerol in the probe's inner flow and pluronic F-127 in the outer flow. B) Printed grid structure with pluronic F-127 in the probe's inner flow and collagen in the outer flow. The pink grid is made of collagen 3mg/mL.*

## Chapter 4. Biomaterials 3D printing

an example, to create a grid, a square boundary is printed with pillars evenly spaced within this boundary. The pluronic will form the pillars and the ECM will coat the surroundings. Such a structure was printed using collagen 3mg/mL as outer flow and pluronic F-127 as the inner flow and is shown in figure 4.6 B. The grid in pink is formed of collagen 3mg/mL. It can be incubated at 37°C for 30 minutes to crosslink the collagen and the pillars can be dissolved in cold media leaving only the grid. However this can only be achieved if the inner capillary protrudes out of the probe as it is the case in figure 4.5 E and F as it allows the fusion of the support material layers. This is achieved by printing with a layer height slightly lower than the deposited height, forcing the capillary to enter in contact with the previously deposited support layer. It allows to push aside any material that could remain between the support layers thus insuring a proper fusion between them.

Using this co-extrusion approach, it is possible to split the needs of structural stability and biocompatibility of the hydrogel. The support material and the cell-laden bioink can be printed next to each other using a single extrusion head. Because pluronic was used as support material, it can easily be washed away by washing the printed structure in media cooled down below 10°C. Even though the remaining structure is mechanically weak, it is submerged in media that supports its weight during the incubation phase.

### 4.2.3 Liquid printing

Another approach to shape bioinks is to print them directly into a supporting material. A container filled with a gel is placed under the printer in place of a standard printing bed. The bioink is then dispensed directly into the gel, the latter serving as a support for the printed material as shown in figure 4.7. This technique has the advantage to allow

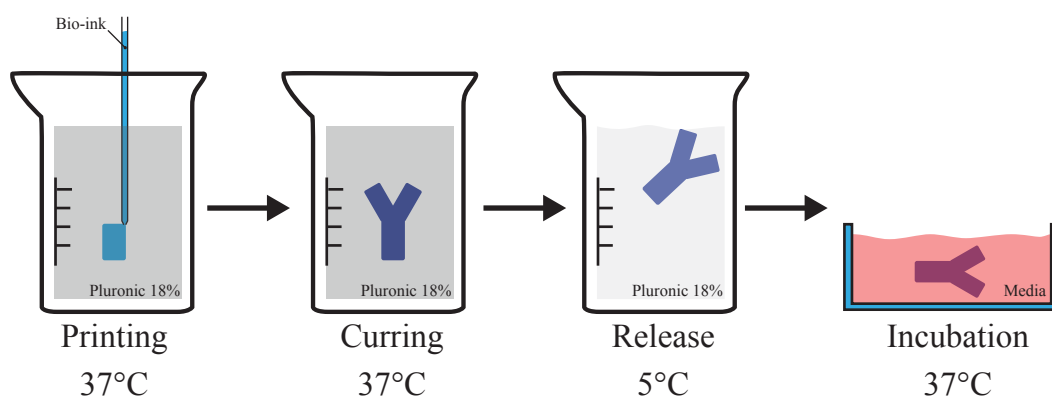


*Figure 4.7 – Liquid printing schematic: Bioink is printed into a pluronic gel which provides support to the liquid bioink. After printing, the bioink is incubated for curing. Then the pluronic is liquefied at 5°C, freeing the printed structure which is then transferred in cell culture media for incubation.*



## 4.2. Improving structural stability

the printing of high aspect ratio and overhanging structures without the need to print support material. This printing methods has been demonstrated by [Hinton et al., 2015] and more recently in [Rocca et al., 2018] to print alginate structures. Thanks to the supporting material, this methods has the potential to enable the rapid printing of large scale structures [Hajash et al., 2017]. It is therefore interesting to investigate whether this method of printing can be adapted to print materials that support cell growth and differentiation such as collagen.

A beaker filled with pluronic F-127 18% w/w and heated at 37°C was prepared and placed on the heating bed of the printer to maintain its temperature. For this experiment, no special printing head was used. A simple needle is the best dispensing tool in this case as a small cross section is preferable in order to displace a minimum the supporting gel. A solution of collagen 3mg/mL with 1 million NOR-10 cell per milliliter was prepared similarly as in chapter 3.3.1 and kept on ice throughout the whole experiment to avoid premature collagen crosslinking. The printer was set to a speed of  $1\text{cm}\cdot\text{s}^{-1}$  and the collagen was extruded at  $5\mu\text{L}\cdot\text{s}^{-1}$  inside the pluronic-filled beaker. Using those parameters, a 5mm in diameter, 1 cm high (21 layers) tube was printed and can be seen in figure 4.8. After printing, the collagen is held in place by the pluronic gel. The beaker is covered with parafilm and placed in an incubator at 37°C for 30 minutes to let the collagen set. The beaker is then transferred into a fridge to cool and liquefy the pluronic, freeing the collagen structure. Using a spatula the structure can be scooped out of the beaker. Pluronic gel is still covering the collagen tube and provides support during transfer. The tube is plunged into cold media were the remaining pluronic dissolves, totally freeing the structure. The media can be changed and the tube incubated. The

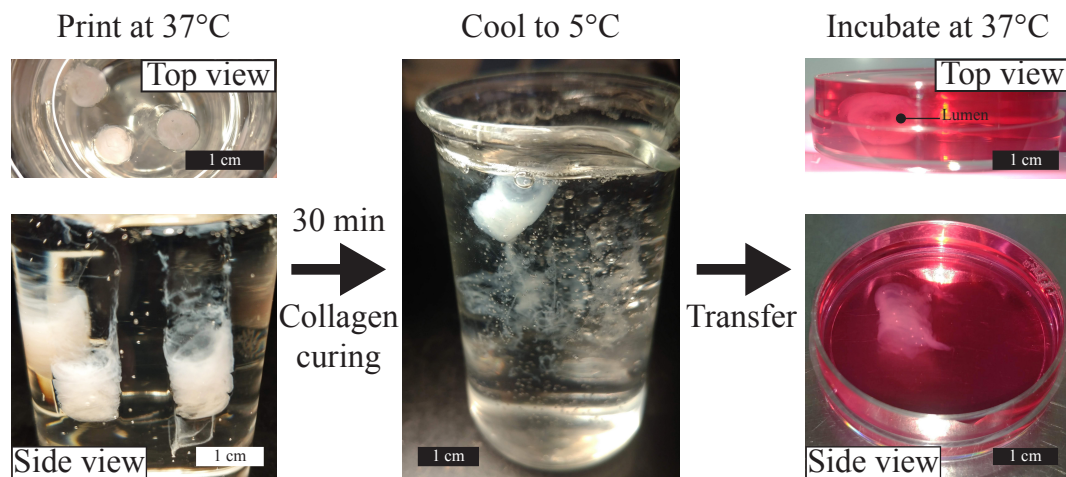


*Figure 4.8 – Collagen printing. Three tubes of pure collagen were printed directly into a beaker filled with pluronic F-127 18% w/w at 37°C. After 30 minutes in the incubator to let the collagen set, the beaker was cooled to 5°C, liquefying the pluronic, freeing the collagen structures. The collagen tubes were then collected and placed in culture media. The lumen can be seen on the top view of the tube.*

## Chapter 4. Biomaterials 3D printing

whole process is illustrated in figure 4.8 where the printed tube with its lumen can be seen in media in the top view of the structure.

The use of supporting gel allowed to print a tube made of collagen loaded with cells, with a large aspect ratio in a simple manner. This printing technique has been shown to function for alginate in previous work and is now usable with softer, slow crosslinking bioinks as well.

### 4.3 Conclusion

#### 4.3.1 Summary

In this chapter three methods to enhance the 3D printing of soft biomaterials were presented. The modification of a collagen based bioink was made by the addition of alginate to create a composite bioink that presents adhesion cues for cells as well as enhanced rigidity and fast crosslinking to enable multilayer printing of the bioink. This new bioink could be printed over several layers and seeded cells were observed to spread in it. However cell spreading and multiplication was less important than for bioinks made purely of collagen indicating that a global Young's modulus change and dilution of cell adhesion sites following the addition of alginate significantly reduce the biocompatibility of the bioink.

To cope with the reduced biocompatibility of the collagen following its mixing with a structurally strong gel, the cell-laden gel was co-printed with a gel dedicated for the support. To ease the printing process, a dispensing tool with coaxial extrusion channels was manufactured. Thanks to its inner channel protruding out of the probe, it allowed the simultaneous multi-layer dispensing of both the structural gel and the cell-laden. Finally the collagen was printed directly into pluronic used as support. With this method, collagen could be laid in 3D with ease, cured and transferred into an incubator for cell culture, opening the door to the manufacturing of large prints made entirely with soft bioinks.

#### 4.3.2 Discussion and outlook

The mixing of two bioinks allows to adjust the properties of the resulting mixture. Unfortunately, for the present case, it deteriorated the ink biocompatibility. Other types of bioinks are being developed that combine nano particles to improve the mechanical stability of hydrogel through ionic bonding [Lee et al., 2018a] or that are engineered from the bottom up by making them sensitive to some enzymes secreted by the cells [Chandrawati, 2016, Xing et al., 2011]. Such developments are out of the scope of this thesis but may bring innovative solutions to improve the quality of bioprints. The possibility to decouple the stiff gel used to build the structure of the printed tis-

### 4.3. Conclusion

sue and the gel that interacts with the cells was demonstrated by encapsulating the cells in the soft gel and embed these cell containing droplets into the structural gel [Kamperman et al., 2017].

The use of 3D printing to create dispensing tools for bioprinting alleviates the need of complex engineering skills and heavy infrastructures such as cleanrooms and could spread the use of more complex dispensing tools for bioprinters. The advances in standard 3D printing enable microfluidic functionalities such as valves and multiplexer [Gong et al., 2016], micro-mixer [Rafeie et al., 2017] or multi-jet [Gong et al., 2016] to be implemented in 3D printed extrusion heads. This could in turn benefit bioprinters by providing new a layer of control over the dispensed biomaterials. Moreover using tools such as the nanoscribe, extremely fine 3D printed output channels could be added at the tip of silicon based probes such as the concentrator, combining the advantages of both technologies.

The printing of liquid bioinks within a supporting gel is promising as high aspect ratio structures can be easily printed and then transferred into culture. For this demonstration, no special printing head was used in this case. To enable the printing of more complex tissues, multiple needles could be placed next to each other allowing the deposition of multiple cell types in close proximity. By rotating the printing head for it to always face the printing direction, similarly to a cutter plotter, the printed layers would remain parallel. In the case of the printed tube, multiple cell layers could be printed in close proximity in a single pass. Blood vessels with vascular smooth muscle cells, endothelial cells, and fibroblasts layer [Nicolas Heureux et al., 1993] could be printed with ease. To enable the printing at an angle, a degree of freedom can be added to the printer by allowing the beaker containing the structural gel to be tilted in the same fashion as computer numerical controlled milling machines. The resolution of the printer can also be optimized through the optimization of the needle's shape in order to reduce the displacement of the supporting gel during printing [Hajash et al., 2017].



# Conclusion and outlook

## 5.1 Summary of results

New opportunities often arise when merging different technologies together. By applying concepts developed over the years for *lab on chip* applications to bioprinting, this work attempted to provide enhanced dispensing tools bringing new functionalities to bioprinters. This approach enabled the following advancements:

- A first dispensing tool was developed featuring a micro-mixer as well as temperature control system. This enabled the reliable printing of cryogels. This material, while exhibiting exceptional properties, was rarely used in bioprinting because of its synthesis complexity. These difficulties are now addressed by the dispensing head we created, allowing the use of this material for bioprinting, showcasing how microfluidics can enable the use of new types of materials for bioprinting applications.
- The successful 3D printing of cryogels was performed and the modulation of the pore size through the modulation of the dispensing tool's temperature was demonstrated. The effect of pore size modulation over the cryogel properties was further investigated using DSC and modeled through thermodynamics.
- A collagen coating was developed and implemented on the printed cryogel, enabling the seeding and culture of NOR-10 cells within the printed scaffold. The modulation of the pore size during printing allowed for the selective seeding of the cells within the printed structure. This task was previously challenging for matrices that require post-printing cell seeding could be performed seamlessly.
- The development of a cell concentrator adapted to be fitted as a printing head was performed. It encompasses a micro-mixer allowing the probe to be used with most of the available bio-inks. Using it, NOR-10 cells could be printed in a collagen matrix and control over the cellular concentration in the tissue was possible. The

## Chapter 5. Conclusion and outlook

printed tissues were cultured and the benefit of using high cell concentrations could be assessed.

- Bladder organoids were produced using the concentration probe. The use of the probe simplified the process of synthesis of the organoids by granting an efficient mixing of the BME and cells, even for small amounts of liquid. The deposition of the droplet containing cells was also facilitated. The amount of seeded cells was found to have an impact over the culture outcome.
- Because many available bio-inks have long crosslinking times, multi-layer deposition of these bio-inks is challenging. Multiple printing techniques were explored to enable the structuring of such bio-inks. A coaxial extrusion probe was developed, allowing the simultaneous deposition of a structural ink and a cell-laden liquid bio-ink. The concept of liquid printing was also tested for bioprinting applications.
- The proof of concept of an extrusion head fabricated through additive manufacturing was made. It widens the possible range of applications of the technologies presented in this thesis by making the design and fabrication of such a device available to other researching groups without access to advance microfabrication methods.

### 5.2 Conclusion

Until now, extrusion-based bioprinting methods have often been limited to dispensing cell-laden bio-inks that can be rapidly solidified by photopolymerization or physical cross-linking. Adding microfluidic functionality to the printing head of the bioprinter allows the development of 3D printing beyond simple dispensing. This development is essential as an additional level of complexity is involved, when making biological constructs out of different types of cells and multiple scaffold materials, compared to more conventional 3D printing, that is usually done using a single material at a time. Additionally, the use of cells in bioprinting applications requires more care than the typical materials used in conventional additive manufacturing techniques. Bioprinting is often described as the key development that is essential for the development of artificial organs and engineered biological tissues, but to obtain the level of complexity needed to form such intricate cell constructs, major improvements in 3D printing techniques are still to be reached. This research has demonstrated that the integration of microfluidic functions into print heads could be key to achieving an important goal in the development of bioprinting.

The approach taken in this thesis was strongly oriented toward engineering thinking. Multiple existing solutions were evaluated and modified to fit defined technical specifications. However, the developed tools allowed the discovery and exploitation of new properties. As an example, the pores size modulation in cryogels was not expected to be

### 5.3. Future applications of the technology

achievable through the modulation of the tool's temperature. It was leveraged to change the pore size faster than by modulating the whole printing bed temperature, enabling the pores size modification during printing and thus the creation of sites propitious for cell seeding and sites unfavorable to cell seeding enabling the selective post-printing cell seeding of the scaffold. The use of the concentration probe enabled to easily change the cell seeding concentration without having to prepare multiple solutions as it needs to be done by standard pipetting. This study highlighted that organoids form only in a window of cellular concentration

It is often highlighted that more reproducible bioprints are needed to further advance in the bioprinting field [Kesti et al., 2016, Ouyang et al., 2017, Zhu et al., 2018]. The concepts developed in this thesis could enhance printing reproducibility by providing tools enabling the standardization of bioprinting parameters. The new layer of control allows not only to optimize printing speed and material deposition rate, but also material concentration, cell concentration, material gradient as well as support material position to create high quality prints.

### 5.3 Future applications of the technology

The technology developed in the research presented in this thesis is at an early stage and possible future improvements to it were discussed at the end of each chapter. Nevertheless, at the current stage, its application in conjunction with new materials that are being developed could already improve the quality of the printed structures.

For example, the study of the effect of cell concentration on organogenesis could be combined with the use of basement membrane extract tailored for the organoid [Broguiere et al., 2018] to remove variation arising from the use of animal-derived hydrogels. Microgel-based hydrogels grant more modularity in the hydrogel by decoupling the gel in contact with the cells and the structural gel [Kamperman et al., 2017]. This is done through encapsulation of cells in hydrogel beads optimized for their culture. Those beads are in turn encapsulated in a hydrogel, which provides adequate support for 3D printing applications. It would be possible to encapsulate the cells in soft hydrogels, concentrate the hydrogels micro beads and mix them in a mechanically strong hydrogel, all of which could be performed using the printing head we developed and presented in the present thesis. Moreover, as a mixer is available on the printing head as well, nano-particles could be added and mixed, providing better structural stability [Lee et al., 2018a] or environmental cues from within the hydrogel [Trampe et al., 2018]. DNA hydrogels are increasingly popular because of their versatility [Jiang et al., 2016]. By changing the number of DNA strands used for polymerization, their mechanical properties can be modulated. The use of a printing head with multiple inlets and a micro-mixer could provide a platform allowing the printing of hydrogels with multiple Young's moduli. Similarly, different cell binding sites could be added to fit the seeded cells



## Chapter 5. Conclusion and outlook

[Hof and Bastings, 2017]. It would therefore be possible to print tissues with changing characteristics perfectly fitting the locally seeded cells. Finally, 4D printing could add yet another layer of control to the biomaterial printing. Simple 2D printing of shape shifting materials could fold into complex 3D shapes [Sydney Gladman et al., 2016, Ionov, 2018] or could enable movement [Guo et al., 2018].

Combined with dedicated slicers for bioprinting that automatically determine the support material location and sets pumps actuation to create adequate material gradient and matrix composition for each cell type seeded at a targeted concentration within the printed tissue, the novel dispensing methods presented herein have the potential to revolutionize the bioprinting field.

# List of publications

## Related to the thesis

- Serex, L., Braschler, T., Filippova, A., Rochat, A., Béduer, A., Bertsch, A. and Renaud, P. "Pore Size Manipulation in 3D Printed Cryogels Enables Selective Cell Seeding." *Advanced Materials Technologies*, 1700340 (3), 1-8, 2018.
- Serex, L., Bertsch, A. and Renaud, P. "Microfluidics : A New Layer of Control for Extrusion- Based 3D Printing." *Micromachines*, 9(2), 1-11, 2018.
- Béduer, A., Piacentini, N., Aeberli, L., Da Silva, A., Verheyen, C.A., Bonini, F., Rochat, A., Filippova, A., Serex, L., Renaud, P. and Braschler, T. "Additive manufacturing of hierarchical injectable scaffolds for tissue engineering." *Acta Biomaterialia* 76, 71-79, 2018.
- Serex, L. (2017) "Micro-fluidic particle concentrator and filtering device", Patent No. EP17184837.7. CH, European Patent Office.
- † Serex, L., Sharma K., Rizov V., Bertsch A., McKinney J., and Renaud P. "Microfluidic bioprinting head for controlled high cell concentration tissue printing." *Lab on a chip*, 2019

## Other

- Tamayol, A., Akbari, M., Zilberman, Y., Comotto, M., Lesha, E., Serex, L., Bagherifard, S., Chen, Y., Fu, G., Ameri, S.K., Ruan, W., Miller, E., Dokmeci, M., Sonkusale, S., Khademhosseini, A. "Flexible pH-Sensing Hydrogel Fibers for Epidermal Applications." *Advanced Healthcare Materials*, 5, 711–719, 2016.
- Akbari, M., Tamayol, A., Bagherifard, S., Serex, L., Mostafalu, P., Faramarzi, N., Mohammadi, M.H., Khademhosseini, A. "Textile Technologies and Tissue Engineering A Path Toward Organ Weaving." *Advanced Healthcare Materials*, 7, 751–766, 2016.

## Chapter 6. List of publications

- † Fallahi, A.\*, Yazdi, I.\*, Serex, L.\*,1, Lesha, E., Faramarzi, N., Tarlan F., Avci, H., Costa-Almeida, R., Sharifi F., Rinoldi, C., Gomes, M., Shin, S.R., Khademhosseini, A., Akbari, M, Tamayol, A. "Multi-compartment fibers for independent tailoring cell- and tissue-level physical properties" *Biomaterials*, 2019.
- † Berdnikova, A.\*, Müller, L.\*, Boyer, F., Bronuzzi, J., Degrange, J., Haguenaue, M., Leterrier, Y., Mapelli, A., Perez G.F., Ponomarenko, D., Renaud, P., Ricca, R., Serex, L., Veneziano, S., Zhukov, K. "Photopolymer-based Microfluidic Scintillation Detectors" *Journal of Nuclear Materials*, 2019.

† Under redaction process or submitted papers.

# Exploited technologies

The EPFL campus provides multiple services that can be accessed by PhD students allowing the fabrication of custom devices. In the case of this thesis, cleanrooms at CMI as well as the additive manufacturing workshop (AFA) were leveraged to manufacture custom made dispensing devices. Three main technologies were used, each providing advantages and disadvantages.

## A.1 Polyimide-SU8

Polyimide technology was originally developed at EPFL-LMIS4 and has been extensively described by Stefan Metz [Metz, 2003]. This technology was then used in combination with SU-8 to produce high aspect ratio channels [Petitpierre, 2017]. It presents the following features, interesting for the fabrication of dispensing tools. First the shape of the body of the probe is defined by photolithography thus granting a complete design freedom. It allows for easy dispense of water based solutions by making a pointy end to the probe (see figure A.1 A) thus without the need of any hydrophobic coating as presented in chapter 2.2.3. More complex shapes can be imagined to reach specific or narrow spaces and its flexibility can be leveraged to accommodate for topography changes and print on uneven surfaces. Moreover, active elements can be embedded in the polyimide layer easily. This allows to place sensors within the microfluidic channel as shown in figure A.1 B where two squared electrodes can be used for electro-spectroscopy as well as two platinum coils are placed that can be used as flow sensors or heaters.

Despite those advantages, this technology was only used as proof of concept in the present thesis research, because of one major limitation of this technology, which is the maximum operating pressure of the probe. Indeed the bonding between the SU-8 layer and the polyimide is weak thus limiting the pressure that can be used before delamination occurs. As most bio-inks are viscous and high fluid velocity are needed to reach a suitable printing time, high pressures are needed to drive the probe. This technology is however very interesting for other applications of "*lab on a tip*" such as cell manipulation before dispense when in standard cell culture media which could automatize operations or add new functionalities in cell culture such as the dispense of

## Appendix A. Exploited technologies

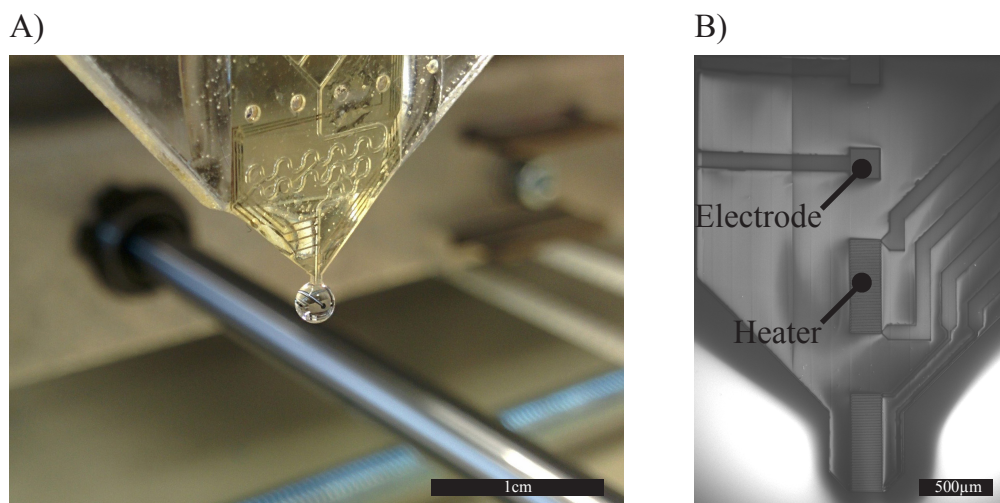


*Figure A.1 – Polyimide technology: A) polyimide probe with three addressable channels, in channel heaters and impedance sensor, mounted on a 3D printer B) scanning electron microscope (SEM) view of the heater and electrodes for impedance measurements on the polyimide that will later be embedded in a SU-8 channel.*

only living cells using dielectrophoresis or the dispense at different cell concentrations in different culture well of a wellplate by counting the number of dispensed cells.

### A.2 Silicon

Silicon-based technology was mainly used throughout this thesis. Using standard micromanufacturing processes it is possible to create very complex microfluidic devices at the wafer scale. The structures' resolution can be higher than using polyimide-SU8, with for example pillars having a  $2\mu\text{m}^2$  base and a  $50\mu\text{m}$  height as shown in figure A.2 A. Moreover, silicon channels can be closed with a glass cover using anodic bonding, which is one of the most efficient bonding allowing the chip to be used with very high driving pressures. Moreover the silicon is a good thermal conductor which can be useful for applications where heating or cooling is involved. Finally, silicon oxide can be grown on the surface of the chip making it extremely resistant to chemicals.

This technology suffers from other limitations such as the hydrophilicity that impairs dispensing as presented in chapter 2.2.3. The shape of the chip is also limited as it must be diced thus only permitting straight lines. One good design has been the diamond shape (figure A.2 B) as it allows the probe to be used vertically as a dispensing tool, with an outlet on the probe's edge. Finally making inlets is not an easy task as it involves etching through the whole thickness of either the silicon wafer, which involves long etching time and backside protection to avoid leaks in the etching machine once the hole is opened,

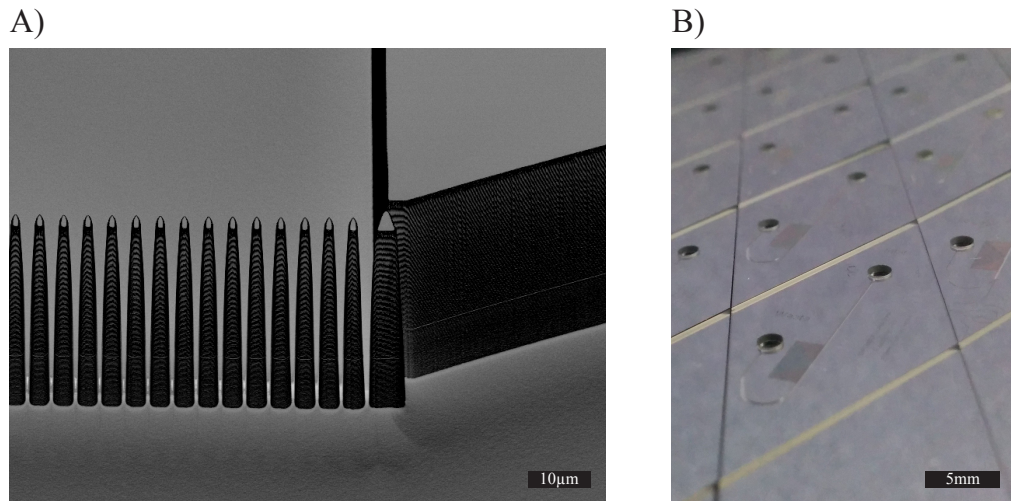


*Figure A.2 – Silicon technology: A) 2 by 2µm in width and 50µm height pillars (adjusted for a 30° tilt) are made showcasing the high aspect ration and high resolution this technology offers. B) Collection of probes on a wafer illustrating the possibility to produce probes at a wafer scale. Those probes dispose of a particle concentrator addressed by to inlet in the glass top and an outlet on the side of the probe. The dicing in diamond shape allows the fabrication of probe with good dispensing profile.*

or the glass wafer, which involves either long wet etching steps or other methods such as sand blasting or drilling. In this case the inlets were done in the glass wafer by drilling at the European organization for nuclear research (CERN) facility. To do so the wafers were fixed on wax and drilled using a 800µm diameter, water cooled diamond drill before bonding.

### A.3 3D printing

Cleanroom processes can be extremely time consuming and money intensive. They are also limited to 2D layer by layer construction limiting the possible designs. In the recent years, standard 3D printing especially using stereolithography (SL) has gained in resolution [Gibson et al., 2015] allowing the 3D printing of microfluidic devices. Using 3D printing allows for an almost complete freedom of design and head as shown in figure A.3 A can be printed using HTM140 resin on a Perfactory®4 Mini XL with ERM from envisiontec. This extrusion head features a heater and can withstand temperatures up to 140°C. It also has a double concentric extrusion channels as shown in figure A.3 B. This kind of coaxial channels are complex if not impossible to built using standard cleanroom processes and was easily made by 3D printing. Much more complex designs can be imagined such as 3D mixers, gradient generators, multiple material extruders and much more.

## Appendix A. Exploited technologies

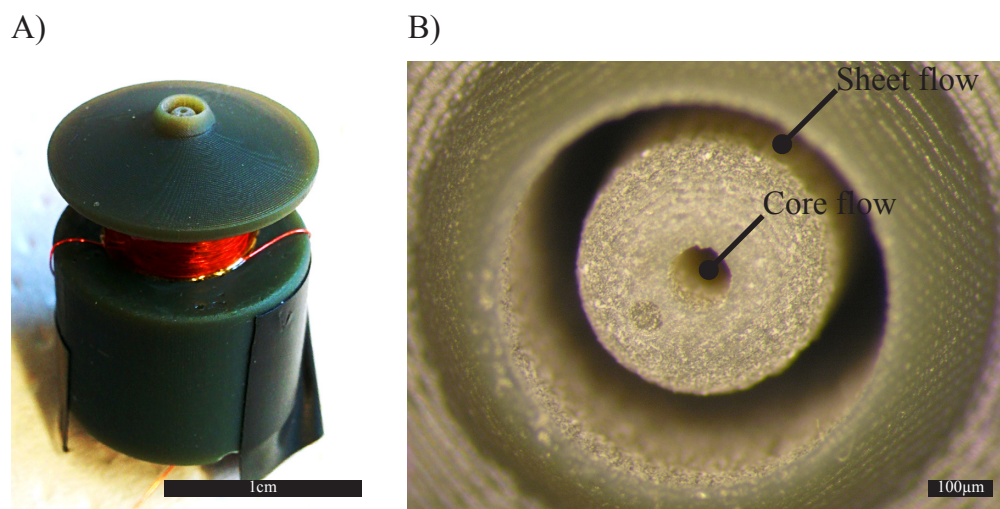


*Figure A.3 – Additive manufacturing technology: A) A fully 3D printed dispensing nozzle in shown. It feature a coaxial extrusion flow which is extremely difficult to obtain by standard photolithography. The probe also feature a heater that can be heated up to 100°C. B) Close view of the coaxial extrusion outlet*

Nonetheless, this technology presents limitations as well. It is impaired by a lower resolution than micromanufacturing processes as this machine can produce parts with a 200µm resolution. Some 3D printers such as the nanoscribe can have much better resolution but with a maximum printing volume of a few millimeters, it is difficult to produce suitable printing heads. One could imagine fabrication the main part of the extrusion head using conventional SL and where high resolution are needed 3D printed structure using the nanoscribe could be preformed. Finally, the limited heat and chemical resistance of the material used in SL can be problematic for certain type of experiments.

Only these three technologies were used in this work as they allow for specific tailoring of each probe for the targeted applications. However, many other manufacturing methods can be used to produce dispensing probes such as polydimethylsiloxane (PDMS) based probe, Poly(methyl methacrylate) (PMMA) casting, standard machining, etc. further widening the horizon for "lab on a tip".



# Cryogel synthesis calculus

## B.1 Introduction and definition of aims

In the chapter 2.3, the basic reasoning behind cryogel synthesis was explained. In this appendix the full calculations for the synthesise of cryogel is developed for any molecule containing carboxyl group. An example is also provided using alginate which is a polysaccharide of 1000 units (unit=residue+carboxyl group) and can be easily derived for CMC cryogels. The chemicals used are listed at the end of the following table.

## B.2 Protocol

Calculus	Example
<p>The polysaccharide can be diluted at any different concentration. <math>L_2</math>[mL] of gel at x% from a solution <math>C_1</math>[g/L] is wanted.</p> <p>Needed concentration:</p> $C_2 = x \cdot 100 \left[ \frac{g}{L} \right]$ <p>Liter of bought solution to use:</p> $\frac{C_1}{L_1} = \frac{C_2}{L_2} \rightarrow L_1 = \frac{C_2}{C_1} \cdot L_2$	<p>In this example alginate was in powder form. For numerical application purposes, 15ml of solution is prepared. A concentration of 2% weight powder in DI water is chose as it results in suitable structural stability of the cryogel.</p>

## Appendix B. Cryogel synthesis calculus

<p>The alginate presents many carboxyl groups that will react during crosslinking. Its concentration can be calculated as folowwed</p> <p>Carboxyl group concentration:</p> $C_{carboxyl} = \frac{C_{gel}}{M_{gel/residue}}$ <p>Through experiment, a good percentage of crosslinked carboxyl group is 10% Therefore, the concentration of crosslinker must be:</p> $C_{crosslinker} = \frac{10}{100} \cdot C_{carboxyl}$	<p>Alginate molar mass:</p> $M_{alginate} = 180 \left[ \frac{g}{mol} \right]$ <p>Protonated alginate molar mass:</p> $M_{alginate \text{ protonated}} = 180 \left[ \frac{g}{mol} \right]$ <p>Gel concentration:</p> $C_{gel} = 20 \left[ \frac{g}{L} \right]$ <p>Carboxyl concentration:</p> $C_{carboxyl} = \frac{C_{gel}}{M_{alginate}} = \frac{20}{200} = 0.1 \left[ \frac{mol}{L} \right]$ <p>Crosslinker concentration:</p> $C_{crosslinker} = \frac{10}{100} \cdot 0.1 = 0.01 \left[ \frac{mol}{L} \right]$
<p>To crosslink the monomer, an amine needs to react with the carboxyl group. A minimum a two amines on a molecule is need to create chains. As we want a constant amount of crosslinked carboxyl group, the concentration of molecule to be added depends on the number of amine in the molecule. The crosslinker concentration becomes:</p> $C_{crosslinker \text{ real}} = \frac{C_{crosslinker}}{\# \text{ of amine}}$	<p>In this example a diamine is used the real concentration becomes:</p> $C_{crosslinker \text{ real}} = \frac{0.01}{2} = 0.005 \left[ \frac{mol}{L} \right]$
<p>From this needed concentration, the mass of compound can be computed.</p> $m = C \cdot M \left[ \frac{g}{L} \right]$ $m_{sol} = m \cdot \text{number of litter} [g]$	<p>Knowing that the molar mass of the used diamine is <math>M_{diamine} = 174 \frac{g}{mol}</math> The mass to add to the solution is:</p> $m = 0.005 \cdot 174 = 0.87 \left[ \frac{g}{L} \right]$ $m_{sol} = 0.87 \cdot 0.015 = 0.01306 [g]$
<p>If the diamine is bought in solution, the amount of solution to add depends on he concentration as followed:</p> $\text{Sol to add} = \frac{m_{sol}}{C_{stock \text{ sol}}}$	<p>In this example the diamine is in a solution at <math>50 \left[ \frac{g}{L} \right]</math>. The amount of solution to add to the mix is:</p> $L = \frac{0.01306}{50} = 0.261 [mL]$

## B.2. Protocol

As shown in figure 2.7, EDC is needed to initiate the reaction. One molecule of EDC is needed per carboxyl group. However as this molecule hydrolyze quickly, a significant safety margin needs to be added. Usually the calculated amount is quintupled.

$$n_{EDC} = 2 \cdot n_{carboxyl}$$
$$m_{EDC} = n_{EDC} \cdot M_{EDC}$$

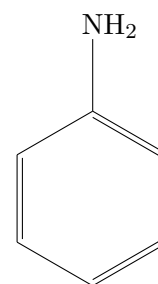
From the previous calculation,  $10 \frac{mmol}{L}$  of carboxyl group needs to be crosslinked.

Therefore for this reaction,  $50 \frac{mmol}{L}$  is needed.

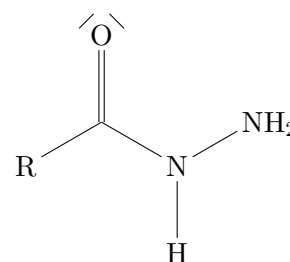
$$n_{EDC} = 0.05 \cdot 0.015 = 0.75 [mmol]$$
$$m_{EDC} = 0.75 \cdot 10^{-3} \cdot 191 = 0.143 [g]$$

For the reaction to occur, the carboxyl group needs to be protonated and the amine group should not. This  $H^+$  will then react with the amine group to form a bond. The pka of a standard carboxyl group is usually in the neighborhood of 6 and the pka of a standard amine around 9. By definition, to be protonated, the pH must be lower than the pka of a molecule. Therefore, in order to meet the conditions for a reaction, one need to find a molecule with an amine group at lower pka. Aromatic amine usually present low pka but are unstable and often toxic. Hydrazide group also offers amine group that have pka as low as 5 [Sigma Aldrich, 2019]. By using those, it is possible to have carboxyl groups protonated and the amine groups un-protonated so the crosslinking reaction may occur.

Aromatic amine:



Hidrazide amine:



## Appendix B. Cryogel synthesis calculus

Moreover at each amin-carboxyl group cross-linking reaction, one  $H^+$  is released thus increasing the pH of the solution. As the reaction is possible only in a short range of pH, a buffer is needed to stabilize the pH. The buffer needs to be carefully chosen as it should not react with EDC (thus free form carboxyl group and from phosphate) and its pka should be close to the target pH to have an efficient buffer.

Buffer equation:

$$pH = pka + \log_{10} \frac{C_{unprotonated}}{C_{protonated}}$$

$$pH = pka + \log_{10} \frac{C_{reactingcarboxyl}}{X - C_{reactingcarboxyl}}$$

X being the needed concentration of buffer. Here again a safety margin of 2 can be added.

In this example MES buffer is used with a pka=6.15.

$$pH = 6 = 6.15 + \log_{10} \frac{0.01}{X - 0.01}$$

$$X = \frac{10}{10^{-0.15}} + 10 = 24.12 \left[ \frac{mmol}{L} \right]$$

Finally the concentration can be converted into mass

$$n = C_{needed} \cdot V_{solution}$$

$$m = n \cdot M$$

MES molecular weight is  $195.2 \left[ \frac{g}{mol} \right]$ .  $50 \left[ \frac{mmol}{mL} \right]$  is needed and the solution volume is 15ml.

$$n = 0.05 \cdot 0.015 = 0.75 mmol$$

$$m = 0.75 \cdot 10^{-3} \cdot 195.2 = 0.1464g$$

Or converted into liter of stock solution with same calculus than prior

Liter of stock solution to put in:

$$\frac{C_1}{L_1} = \frac{C_2}{L_2} \rightarrow L_1 = \frac{C_2}{C_1} \cdot L_2$$

L1 mL of MOS solution at 0.5 Molar is needed and the final concentration has to be  $C_2 = 50 \frac{mmol}{L}$  for 15mL of final solution.

$$L_1 = \frac{0.05}{0.5} \cdot 15 = 0.15 mL$$

On can notice that all the parameters are linearly dependent from each other. Thus all the quantities of solution can be easily scaled up to produce the wanted quantity of gel. Following are the recipe for 1mL of alginate and CMC cryogels.

Alginate	CMC
1ml Alginate 3% w/w in DI water	1ml CMC 1% w/w in DI water
26 $\mu$ L AAD (50mg/mL)	7 $\mu$ L AAD (50mg/mL)
0.1mL MES (pH 5.5, 0.5molar)	0.1mL MES (pH 5.5, 0.5molar)
12mg EDC in 10 $\mu$ L DI	4mg EDC in 10 $\mu$ L DI

## B.2. Protocol

One can produce stock solution with the first three compounds in the list premixed and store it at 4° C. The cryogel will start reacting only when EDC is added. The speed of reaction depends on first the pH of the solution, the lower the more carboxyl groups are protonated thus the more likely the reaction is to occur and second on the temperature, the lower the temperature the slower the reaction roughly the reaction speed drops by factor 2 every 10° C in temperature decrease. Finally it is possible to covalently bind aminofluorescein to the cryogel scaffold to make it fluorescent. To do so, aminofluorescein can be dissolved in water and added to the premix. A very small amount is enough to render the cryogel fluorescent (1mM). To dissolve aminofluorescein in DI water, three times the molarity of aminofluorescein must be added in NaOH (to do a 1 molar aminofluorescein solution, add 3 molar of NaOH to dissolve it). Below is a list of all the compounds used to synthesize cryogels.

Molecule name	Supplier	Reference	Comment
Sodium carboxymethyl cellulose (CMC)	Sigma-Aldrich	419273	Mostly used in this thesis
Alginate	Sigma-Aldrich	A0682	
Adipic acid dihydrazide (AAD)	Sigma-Aldrich	A0638	Crosslinker
Acide 2-morpholinoethanesulfonic hydrate (MES)	Sigma-Aldrich	M2933	pka=6.15. Used for low pH (5-6.8) gel that crosslink quickly
4-(2-Hydroxyethyl) piperazine-1-ethanesulfonic acid, N-(2-Hydroxyethyl) piperazine-N'-(2-ethanesulfonic acid) (HEPES)	Sigma-Aldrich	H3375	pka=7.55. Used for high pH (6.8-8.2) gel that crosslink quickly
N-(3-Dimethylaminopropyl)-N'-ethylcarbodiimide hydrochloride (EDC)	Sigma-Aldrich	E7750	Initiator
6-Aminofluorescein	Sigma-Aldrich	201634	To make scaffold fluorescent



# Collagen coating of cryogels

## C.1 Introduction and definition of aims

This appendix is extracted from the supplementary material of the publication entitled "Pore Size Manipulation in 3D Printed Cryogels Enables Selective Cell Seeding" [Serex et al., 2018b]. The credit for the development of the coating on bulk cryogel for skin fibroblasts goes to Aleksandra Filippova and its optimization for 3T3 cells to Ariane Rochat.

We use collagen coating of cryogels to enable cell adhesion. Collagen I coating is indeed a common technique to increase cell adhesion on various surfaces [Alberts et al., 2002, Sverzut et al., 2012], including epoxide-modified cryogels [Dainiak et al., 2008]. The goal here is to adapt the technique to enable efficient coating of carboxymethyl-cellulose based cryogels [Bédurier et al., 2015].

Carboxymethylcellulose (CMC) is known to have an affinity for collagen, due to polyelectrolyte complex formation [Cundall et al., 1979]. The interaction is known to be optimal at acidic pH, since under these conditions, CMC and collagen carry opposite charges [Cundall et al., 1979]. In coating CMC cryogels with collagen, we pursue four distinct goals:

1. the adsorption of collagen to the cryogels should be maximized
2. at the scale of single cryogel walls (micrometers), the collagen should be preferentially localized to the surface, rather than the bulk, to increase availability for the cells
3. collagen fiber formation [Helseth and Veis, 1981] should be avoided to ensure homogeneity and also to avoid clogging of cryogel pores by large aggregates
4. modification should be permanent, no collagen should leach from the cryogels

Given the pH dependency of the interaction of collagen with CMC, the primary variable to control in collagen coating is the pH. To ensure permanent attachment of the



## Appendix C. Collagen coating of cryogels

collagen to the cryogels, we use EDC (1-ethyl-3-(3-dimethylaminopropyl)carbodiimide hydrochloride) to form stable amide bonds.

### C.2 Quantification of adsorption of collagen to cryogels

To quantify the total adsorption of collagen to CMC cryogels, we expose cryogels of known volume and CMC content to coating solutions, and then measure the amount of collagen remaining in the coating solution by means of the BCA test (Thermo Scientific, Pierce, product #23225).

In detail, we produced 50 microliter cryogels by molding 1mm high sheets of cryogel at  $-20^{\circ}\text{C}$  and stamping 8mm disks, with a concentration of 1% CMC as described in [Cundall et al., 1979]. In order to be able to wash and coat these cryogels while collecting the pore fluid for analysis, we fabricated custom centrifugation devices by hotwelding 40 micron cell strainer mesh to cut 1mL syringes (figure C.1). This device fits into 15mL Falcon tubes, as shown in figure C.1. By centrifugation (1500rpm, 2 minutes, Eppendorf 5810R centrifuge), the gels can be rapidly dehydrated, and the pore liquid recovered in the Falcon tube. By addition of new liquid, the gels can be washed, and the coating steps applied, whereas the pore liquid can be collected in fresh 15mL Falcon tubes for collagen measurement.

In detail, the following protocol was applied for quantification of the adsorbed collagen (with centrifugation between each step, and controls for loss of collagen in the absence of cryogels for each pH):

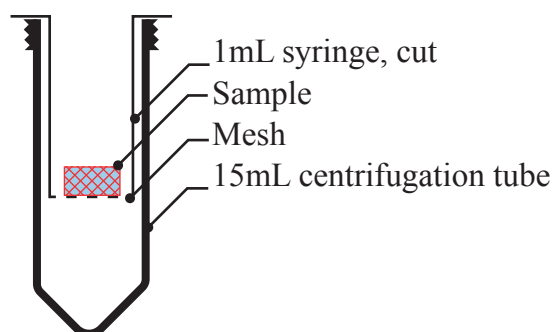


*Figure C.1 – Setup used to quantify collagen coating of cryogels. Upon centrifugation, the cryogel samples are compressed, and pore fluid recovered in the 15mL centrifugation tube. The cryogel is maintained in place by the 40 micron cell strainer mesh hotwelded below the cut 1mL syringe.*

## C.2. Quantification of adsorption of collagen to cryogels

1. 2 times washing with buffer at desired pH (H<sub>3</sub>PO<sub>4</sub>/H<sub>2</sub>PO<sub>4</sub> up to pH 3, Acetic acid/sodium acetate from pH 4 to pH 5, and morpholinoethanesulfonic acid/morpholinoethanesulfonic acid sodium salt for pH 6, 100mM total strength each).
2. Coating: addition of collagen in buffer solution to achieve a theoretical mass ratio of 0.1 compared to the CMC: For this, a mix of 17 microliters of collagen stock solution (3mg/mL in 10mM HCl), 8 microliters of DI, 25 microliters of buffer solution at the desired pH at 200mM is prepared, mixed, and added to dehydrated cryogel on coating device, followed by an incubation for 10 minutes. Prior to centrifugation, the centrifugation device is transferred to a new Falcon 15mL for collection of the pore fluid
3. After centrifugation, 20 microliters of the pore fluid that was collected in the Falcon tube is transferred to a 96 well plate.

Once all the samples collected, the collagen content was determined in the 96 well plate by using the Pierce BCA assay, by addition to of 100 microliters BCA reaction mix (prepared as indicated by the manufacturer, but with addition of small amounts of sodium hydroxide calculated such as to theoretically neutralize the buffers used above to pH 11) to each of the wells, and also to collagen standards in the range of 0.01 to 1mg/mL. The collagen content in each assay well was determined after incubation and spectrophotometric analysis according to the instructions of the manufacturer of the BCA assay (readout at 562nm).

The amount of collagen adsorbed to the cryogels was then determined by the difference between the collagen concentration in the associated control (same buffer, but no cryogel placed in the centrifugation tube), and the amount of collagen remaining the coating solution after having interacted with the cryogel. The uptake efficiency is then calculated from the ratio of collagen adsorbed to the cryogel and the available concentration measured in the associated control without cryogel.

The uptake efficiency as a function of coating pH is shown in figure C.2. Based on the criterion of uptake efficiency alone, one can state that the coating pH should be 2.5 or larger; other than that, the criterion of total collagen adsorption is relatively uninformative.

## Appendix C. Collagen coating of cryogels

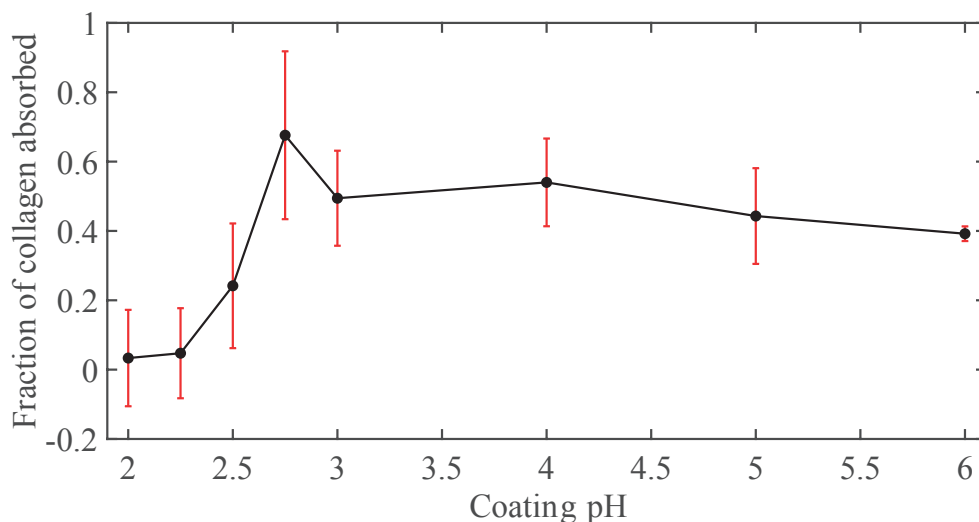


*Figure C.2 – Uptake efficiency of collagen onto cryogels as a function of pH. The collagen uptake efficiency is measured indirectly by the decrease of concentration in the coating solution, as described in the text. Credit: Aleksandra Filippova*

### C.3 Surface versus Volume localization

Our next question relates to the biological availability of collagen. Indeed, we expect cells to be sensible only to collagen coated within nanometers of the surface of the cryogel fibers (which have diameters on the order of micrometers). In order to probe the spatial localization of the collagen coating, we prepared red-fluorescent collagen, by standard methods of protein labeling.

Briefly, collagen (type I, from bovine skin, Sigma C4243) was rhodamine-labelled by standard isothiocyanate chemistry. 1mL of collagen solution (3mg/mL, type I, from bovine skin, Sigma C4243) was made alkaline by addition of 300 microliters of 100mM sodium carbonate. Then, 0.6mg rhodamine isothiocyanate dissolved in 1mL of isopropanol was added, followed by 1mL of deionized water, and vigorous mixing. After incubation of 1h at room temperature, the labeled collagen was precipitated by an excess of isopropanol, centrifuged, and washed three times more with isopropanol, before air drying. To dissolve the labelled collagen, 1mL of deionized water was added, followed by 30 microliters of 1M HCl to achieve a homogeneous, aggregate-free solution.

To understand the localization of the collagen after coating experiments, we generally coated with a solution containing 1/20 of the volume of the solution of labeled collagen prepared above, 1/20 of the volume unlabeled collagen (Sigma C4243), the remainder being a suitable pH buffer (as before).

For ease of imaging and quantification, we prepared classical CMC hydrogels in disk

### C.3. Surface versus Volume localization

shape. For this, we prepared a premix consisting of

- 1mL CMC 3%
- 0.3mL MES pH 5.5, 0.5M
- 21 microliters Adipic dihydrazide, 50mg/mL in water
- 12mg EDC

We mold classical (nanoporous) hydrogels at room temperature between glass slides, with 1mm spacers. After at least 2h of curing in a humidified chamber at room temperature, this gives rise to a transparent sheet of CMC-AAD hydrogel. We punch 8mm disks from these sheets.

We wash these gels extensively with NaOH 100mM, then EDTA 10mM, then PBS, before storing them in PBS. Each solution was incubated with the gels for at least 1h at room temperature. In practice, for each step, we place the disk gels in an excess of the desired liquid in a 50mL Falcon tube. The liquid can be exchanged by letting the gels sediment, followed by removal of the supernatant and addition of the next liquid.

For coating, we remove the PBS and equilibrate the gels for at least 2h with the desired pH buffers, at 100mM total buffer strength each, with occasional gentle agitation. Then, the pre-equilibration buffer is removed, and excess coating solution added (typically, 1mL for 5 disk gels). Coating is let to proceed under continuous manual agitation for 15 minutes. After this, the disks are washed 2 times with deionized water and observed under the confocal microscopy the same day.

We use an approach based on confocal imaging to obtain an estimate of how deeply the collagen molecules penetrate the CMC hydrogel, as shown in figure C.3. First, we obtain a high precision estimate of the fluorescence intensity profile as a function of distance from the gel surface. For this we acquire z-stacks of confocal images of the coated samples (Zeiss, LSM700, 63x oil immersion objective with NA=1.4, figure C.3 A), followed by averaging within each image plane (or reduced regions in case of noticeable slanting of the sample). From the averaging, we obtain a fluorescence intensity profile along the z-axis, as shown in Fig.C.3 B. For deconvolution, we measure the z-axial point spread function using a coverslip coated with a molecular layer of labeled collagen instead of a gel sample, followed by in-plane averaging as before (the point spread function is also shown in figure C.3 B). Given the very good signal to noise ratio of the fluorescence intensity profiles, we directly use Wiener filtering for deconvolution [Qiang Wu, Fatima Merchant, 2008]. With the deconvolved fluorescence intensity profile, we can estimate the mean gel penetration depth of the collagen molecules as well as obtain an indication of whether or not molecules of collagen are present above the

## Appendix C. Collagen coating of cryogels

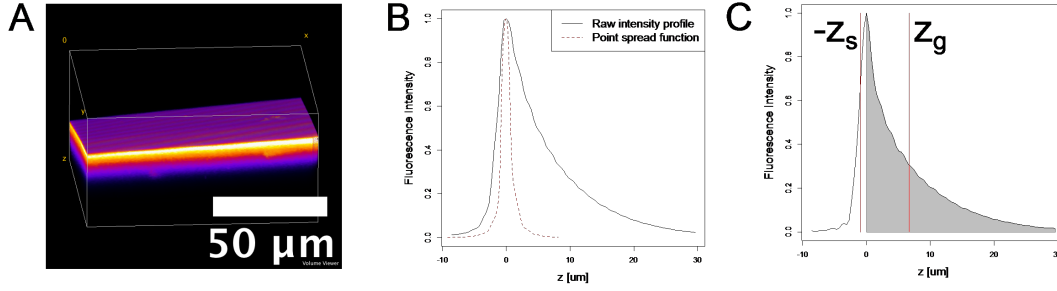


**Figure C.3** – Evaluation of the gel penetration depth and surface layer thickness. Figure C.3 A shows a confocal stack of images acquired near the flat surface of a cylindrical CMC gel that was coated with rhodamine-labeled collagen (in the example, at pH 2.5, according to the method outlined in the text). A heat map was used to illustrate the local fluorescence intensity, yellow-white being the highest, purple-black being the lowest intensity. figure C.3 B shows the extracted intensity profile, along with the z-axis point spread function as measured by acquiring a z-stack of a flat layer of collagen on a glass slide (method described in the text). figure C.3 C shows the deconvolved fluorescence intensity profile, which is slightly narrower than its raw counterpart in figure C.3 B. It also shows the evaluation of the surface layer thickness ( $z_s$ ) and the gel penetration depth ( $z_g$ ).  $z_s$  is evaluated from the negative part of the fluorescence intensity distribution function (with, eq.C.2), whereas  $z_g$  is evaluated from the positive part (grey, eq.C.1). Credit: Aleksandra Filippova

surface of the CMC gel (fibrils or dissolved collagen). As shown in figure C.3 C, we evaluate the gel penetration depth  $z_g$  as the mean depth at which collagen molecules are found, by using the deconvolved fluorescence intensity profile  $I(z)$ :

$$z_g = \frac{\int_0^{\infty} z \cdot I_{(z)} dz}{\int_0^{\infty} I_{(z)} dz} \quad (\text{C.1})$$

where  $z=0$  is defined by the maximum fluorescence intensity, and the positive direction of  $z$  being chosen inward; in practice, the integration bounds are limited to the available slices. The integration domains and  $z_g$  are shown graphically in figure C.3 C.

Likewise, we can define a surface height  $z_s$  by:

$$z_s = \frac{\int_{-\infty}^0 (-z) \cdot I_{(z)} dz}{\int_{-\infty}^0 I_{(z)} dz} \quad (\text{C.2})$$

where again  $z=0$  is defined by the maximum fluorescence, and the sign has been chosen to obtain a positive value. We evaluated  $z_s$  and  $z_g$  for a set of CMC hydrogel disks

### C.3. Surface versus Volume localization

coated at different pH values. Figure C.4 shows the results.

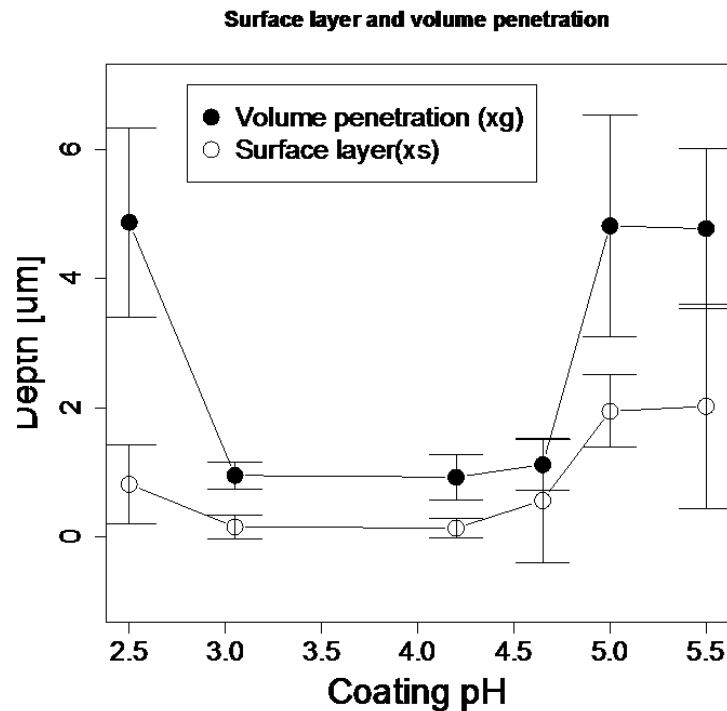


*Figure C.4 – Surface layer thickness and volume penetration depth. Both volume penetration depth  $z_g$  and surface layer thickness  $z_s$  are calculated from fluorescence intensity profiles as outlined in figure C.3, and the text (eq.C.1, eq.C.2). The pH values are measured values. Credit: Aleksandra Filippova*

Figure C.4 indicates the the lowest volume penetration depths are in the range of pH 3.0 to pH 4.2. This implies minimal loss into the bulk volume and suggests this range for coating applications where no distinct free collagen at the surface is required. For some cell types, collagen truly located at the surface of the gels might be required. For such a requirement, the coating conditions at pH 4.65 might be of interest, since volume penetration at this pH is still minimal, whereas some fibrillar material can be found at the surface. At pH 2.5, the affinity of the collagen for the CMC decreases, as apparently the gels slowly loose collagen, which instead coats the glass slides used for observation. At pH 5 and greater, a distinct meshwork of collagen fibers forms at the surface of the disks.

In the main text, we also report the total collagen layer thickness figure 2.14 B. We define

## Appendix C. Collagen coating of cryogels

this with the formalism of a standard deviation:

$$z_t = \sqrt{\frac{\int_{-\infty}^{\infty} (z - \bar{z})^2 \cdot I(z) dz}{\int_{-\infty}^{\infty} I(z) dz}} \quad \text{with} \quad \bar{z} = \sqrt{\frac{\int_{-\infty}^{\infty} z \cdot I(z) dz}{\int_{-\infty}^{\infty} I(z) dz}} \quad (\text{C.3})$$

For reasons of ease of quantification, we used homogeneous disk CMC gels rather than the cryogels to establish figure C.4. The question is therefore whether the results can be transferred to cryogels. We address this question qualitatively in figure C.5 by comparing confocal images from cryogels coated at different pH, using the same procedure as the 2D gels. For the examples given, qualitative agreement between the 2D data and the behavior of the cryogels can be seen.

As shown in figure C.5, at pH 2.5, there is substantial volume penetration in addition to surface coating, recapitulating the data obtained with classical CMC hydrogels in figure C.4. At pH 4, most of the collagen is concentrated within a surface layer of about 500nm, at the limit of resolution of the confocal microscopy without deconvolution. At pH 5.5, massive formation of fibrillar collagen occurs, clogging the pores of the cryogel.

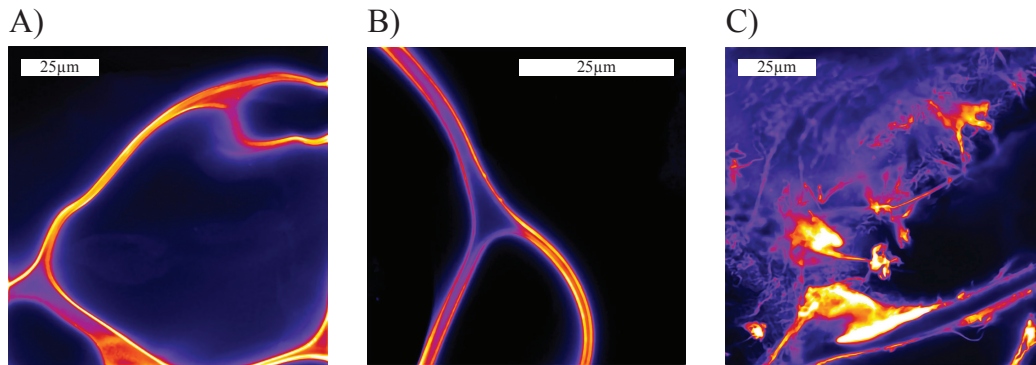


*Figure C.5 – The intensities are relative, as the gains were adjusted to approximately have the brightest pixel at full intensity in each case. Credit: Aleksandra Filippova*

### C.4 Fibril formation and homogeneity

From figure C.5, it is clear that massive fibril formation is clearly not desirable for cryogel coating, as this leads to pore clogging and massive inhomogeneity of the coating.

This implies that figure C.5 can also be used to assess the criterion of fibril formation and homogeneity. From this criterion, the pH needs to be below 5. At pH=4.65, we obtain minor inhomogeneity due to limited deposition of fibrillar material at the surface, whereas at pH 4.2 and below, we obtain fully homogenous coating without detectable



## C.5. Permanent modification

fibril formation. The NOR-10 cells used here adhere and spread on collagen coated at pH 4 (see main text), so given the optimal homogeneity at this pH, we would not recommend to rise the pH more than that. It is however conceivable that other cell types require fibrillar collagen for adhesion, in that case, a pH on the order of 4.65 appears optimal, at least for the batch of collagen used in these experiments.

From figure C.4, there is little change in the collagen coating characteristics between pH 3 and 4. However, in practice, we find that the cryogels re-swell less easily when approaching pH 3, most likely due to protonation of the carboxyl groups. This defines a pH near 4 to be the optimum for coating for adhesion of NOR-10 cells.

## C.5 Permanent modification

Our final question is how to permanently fix the collagen to the cryogels after coating. For this, we use EDC, since EDC is known to efficiently crosslink collagen with carboxylate based polymers [Park et al., 2003], including CMC [Liu et al., 2013]. We crosslink at a pH 5.5 since we know from both homogeneous CMC hydrogel formation (above) and cryogel formation (main text) that this provides a convenient reaction time on the order of about a minute at room temperature for activation of the carboxyl groups.

Two distinct questions arise in the procedure: Firstly, since we change the pH, we need to validate that we do not lose collagen during the procedure; second, we should assert that indeed the collagen has been fixed and cannot be leached from the gels.

To address the question of loss of collagen during the fixing procedure, we proceed as for the measurement of the collagen adsorption efficiency (section 2 of this appendix), but determine the amount of collagen lost not only in the coating solution after equilibration with the gel, but also in the subsequent washing solutions (DI, MES pH 5.5 with and without 10mg/mL EDC, DI). From this, we can monitor the concentration of collagen still present in the cryogel, and thus estimate the losses associated with the washing and fixing steps.

Figure C.6 shows the results. During the washing and fixing step, regardless of whether EDC was present or not, about 25% of the initial collagen content is lost, which represents a fully acceptable fraction.

Next, we addressed the question of collagen leaching by challenging the coated cryogels used to establish figure C.6 with NaHCO<sub>3</sub>, 100mM. As before, we measured the collagen concentration in the pore fluid by centrifugation and BCA quantification. We then calculated the fraction of collagen leached from the gels based on the lost amount as compared to the known amount prior to exposure to the NaHCO<sub>3</sub> solution. Figure C.7 shows the results. Virtually no collagen could be leached from the cryogels fixed with EDC, whereas about 45% of the collagen still present was leached when the cryogels had

## Appendix C. Collagen coating of cryogels

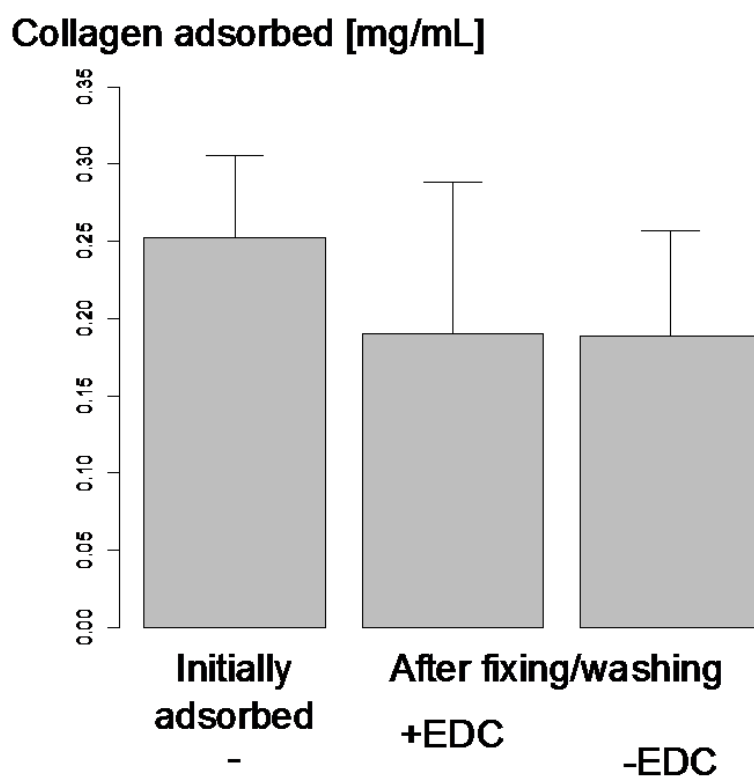


*Figure C.6 – Loss of collagen during washing and fixing steps. After initial coating, we quantified the total loss of collagen during a DI wash, a fixing step at pH 5.5 with or without 10mg/mL EDC, and a second washing step in DI, and estimated the remaining collagen content.*

not been exposed to EDC. This shows the efficiency of fixing the collagen permanently by using EDC; hence, unless it would be found that some cell type is sensitive to chemical modification of the collagen by EDC, we recommend fixation of the collagen as this allows to ensure the presence of a known amount of collagen with minimal leaching over time.

Finally, given that a substantial fraction of non-covalently bound collagen remains associated with the cryogels even under the relatively harsh leaching conditions used for figure C.7, we investigated to which extent the EDC fixing step has an influence on cell adhesion. To do so, we used the disk shaped homogenous CMC/AAD hydrogel model describe earlier in this appendix (section 3), as this allows for direct observation and accurate quantification of the cell population on a flat surface. Further, we restricted ourselves to the fixing step itself and provided collagen directly in a MES buffer solution, pH 5.5, 200mM, 0.2mg/mL collagen, with our without 10mg/mL EDC. Applying this solution will lead to the formation of some collagen fibrils, but this is not of major concern in the homogeneous disk model system as the fibers can be washed away easily afterwards. After coating (15 min incubation), possible remaining EDC was inactivated by washing first 2x in DI water, then in 1% acetic acid for 10 minutes, followed by

## C.5. Permanent modification

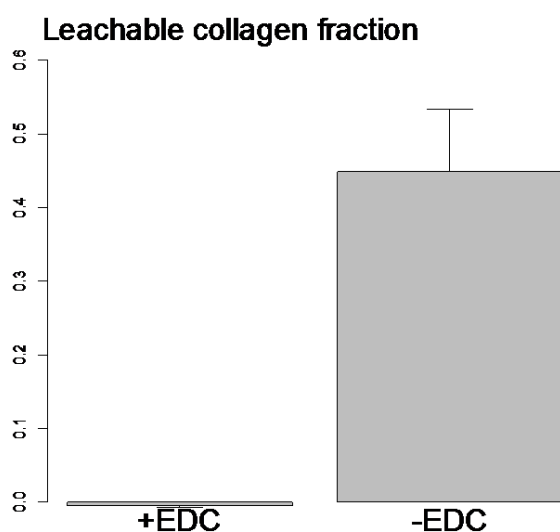


*Figure C.7 – Fraction of leachable collagen. Extraction was by using 100mM NaHCO<sub>3</sub>, and the relative loss of collagen was calculated by comparing the amount of collagen found in the pore fluid after centrifugation (BCA test) to the amount known to be present on the gels (figure C.6).*

Na<sub>2</sub>CO<sub>3</sub> 100mM, and 1% ethanolamine for 10 minutes, another wash with DI, and neutralization in PBS (2x, with 5 minutes equilibration time, and then a third time overnight), followed by storage in PBS. Prior to coating, the gels were autoclaved in PBS, and all solutions were used sterile filtered. The slightly longer EDC inactivation as compared to the main text was motivated by the difficulty of efficiently washing classical hydrogels, which cannot be dehydrated and rehydrated like the cryogels. We also prepared gels without EDC fixation, for which after coating in MES pH 5.5 200mM, we only performed one wash in DI followed by 2x neutralization with PBS.

We placed the disk-shaped hydrogels in wells of 12well plates, and seeded them with gamma-irradiated 3T3 (Swiss 3T3-J2) [Liu et al., 2013], 300'000 cells/cm<sup>2</sup>, 1mL medium in each well (10% bovine serum in DMEM with 1% penicillin-streptomycin). As these cells are irradiated, they do not proliferate, facilitating cell counts over time.

Figure C.8 shows micrographs of the adhesion state of the 3T3 cell population for covalently (+EDC) and non-covalently (-EDC) coated CMC hydrogels at 90 minutes and 24h. Despite the much less extensive washing for the non-covalently coated gels, cell adhesion is noticeable less for the non-covalently coated gels at both 90 minutes and 24h.

We finally investigated in more detail the adhesion of 3T3 cells, by adding non-coated CMC-AAD hydrogels and also control wells to the study underpinning figure C.8. We also extended the time of observation by including time points at 4 days and 1 month. At each time point, and for each coating condition, we quantified the number of spread cells

## Appendix C. Collagen coating of cryogels

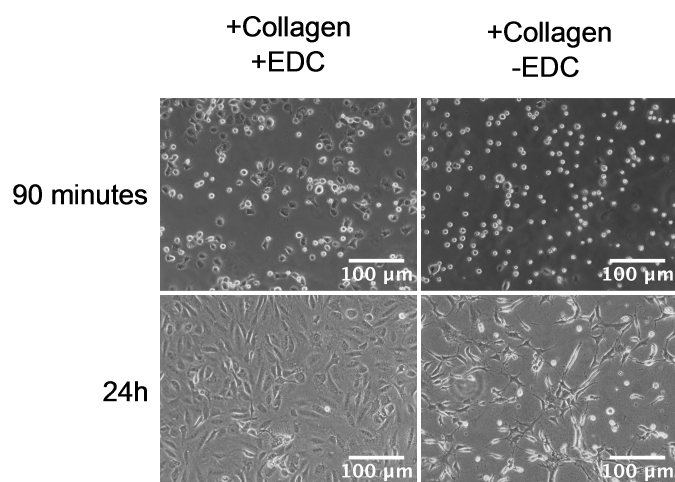


*Figure C.8 – Morphology of 3T3-J2 cells on collagen coated nonporous CMC-AAD hydrogels. Seeding density originally 300'000 cells/cm<sup>2</sup>. Credit: Ariane Rochat*

by analyzing images such as the ones shown in figure C.8. We identified spread cells as cells where at least a part of the cell appeared dark (as opposed to the bright spheres counted as non-spread), and reported their density to the area of observation. The results are shown in figure C.9. They indicate that the 3T3-J2 cells spread approximately similarly on the covalently coated gels as they do on tissue culture plastic, but that spreading was weaker in non-covalently coated gels, and essentially absent in non-coated gels. Statistical testing was performed at each time-point by the number of

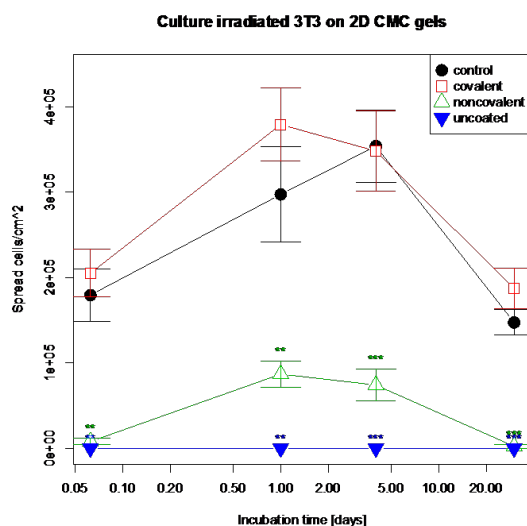


*Figure C.9 – Quantification of spreading of 3T3-J2 cells on collagen coated nonporous CMC-AAD hydrogels as well as uncoated CMC-AAD hydrogels, and positive control (tissue culture plastic). The initial seeding density was 300'000 cells/cm<sup>2</sup>. Credit: Ariane Rochat*

spread cells counted against the control (tissue culture plastic), using unpaired t-tests, without correction for multiple testing. As the cells were irradiated, they slowly die after a maximum of spreading; this occurs with kinetics that is similar on the covalently coated gels as compared to the control conditions (tissue culture plastic).

## C.6 Conclusion

Taken together, the results presented throughout this appendix suggest that optimal coating collagen coating of the the CMC-based cryogels should be performed in the vicinity of pH 4. When lowering the pH further, first different obstacles to successful coating are encountered: first, at about pH 3.0, the cryogels start to become noticeable softer, making the dehydration/rehydration procedure less efficient; next, at about pH 2.5, the collagen starts penetrating deeper into the walls of the cryogels, which we expect to make it less accessible for cells, and finally, at pH 2.25 or lower, nearly no collagen will adsorb to the cryogels anymore. At pH values higher than 4, collagen fibril formation starts to become possible; the extent of fibril formation is noticeable, but still quite acceptable at pH 4.65, but starts to become unacceptable at pH 5 and higher, clogging the pores of the cryogels. These considerations have led to the definition of the collagen coating protocol at pH 4.0 given succinctly in the main text. It allows adherence and spreading of the NOR-10 cells used in this work. ; extension to other cell types might necessitate further testing.



# Thermodynamic model

This appendix is an attempt to create a more complete thermodynamic model about the ice crystal formation in cryogel premix. Such a model could bring more insight on the ice crystal formation and cues for tuning the cryogel structure. From [Tobergte and Curtis, 2013] and by assuming spherical nucleation point, the following equations can be written.

$$\Delta G_n = \Delta G_V + \Delta G_S \quad (\text{D.1})$$

$$\Delta G_V = \frac{4\pi}{3} r^3 \Delta g_V \quad (\text{D.2})$$

$$\Delta G_S = 4\pi r^2 \gamma \quad (\text{D.3})$$

$$\Delta G_n = \frac{4\pi}{3} r^3 \Delta g_V + 4\pi r^2 \gamma \quad (\text{D.4})$$

In this set of equations  $r$  is the radius of the spherical nucleus and  $\gamma$  the surface tension between the solid and liquid phase.  $\Delta G_n$  the total Gibbs free energy of ice formation,  $\Delta G_V$  the Gibbs free energy needed to increase the ice crystal volume,  $\Delta g_V$  its normalization over the volume and  $\Delta G_S$  the Gibbs free energy needed to increase the ice crystal surface. It is interesting to note that  $\Delta g_V$  is positive when  $T > T_0$ , where  $T_0$  is the transition temperature. As  $\gamma$  is always positive, it results in a Gibbs free energy positive thus the new phase is not stable. In the present case it simply means that above transition temperature  $T_0$ , no ice crystal will form whereas when  $T < T_0$ ,  $\Delta g_V$  is negative meaning that there are values of  $r$  where  $\Delta G_n$  is negative resulting in the formation of a new that phase reduces the total Gibbs free energy of the system leading to a stable new phase. Furthermore, by definition,  $\Delta g_V$  can be expressed by change of enthalpy and entropy as in equation D.5. At the solidification temperature  $T_m$  it can be postulated that the change of enthalpy and entropy can be expressed as a function of the latent heat  $L_f$  [Tobergte and Curtis, 2013] leading to the following equation for  $\Delta g_V$  (equation D.8).



## Appendix D. Thermodynamic model

$$\Delta g_V = \Delta h_V - T \Delta s_V \quad (\text{D.5})$$

$$\Delta h_V = -L_f - \int_T^{T_m} \Delta C_p dT' \quad (\text{D.6})$$

$$\Delta s_V = \frac{-L_f}{T_m} - \int_T^{T_m} \frac{\Delta C_p}{T'} dT' \quad (\text{D.7})$$

$$\Delta g_V = -\frac{L_f \Delta T}{T_m} - \int_T^{T_m} \Delta C_p dT' + T \int_T^{T_m} \frac{\Delta C_p}{T'} dT' \quad (\text{D.8})$$

Where  $\Delta C_p$  is the difference of specific heat between the liquid and solid phase and  $\Delta T = T_m - T$ . When integrating  $\Delta g_V$  in  $\Delta G_n$  we get the following formula to calculate the Gibbs free energy of the ice crystal formation:

$$\Delta G_n = -\frac{4\pi}{3} r^3 \left( \frac{L_f \Delta T}{T_m} - \int_T^{T_m} \Delta C_p dT' + T \int_T^{T_m} \frac{\Delta C_p}{T'} dT' \right) + 4\pi r^2 \gamma \quad (\text{D.9})$$

As mentioned earlier there is a nucleus radius  $r_*$  at which the Gibbs free energy will start to drop and even become negative leading to spontaneous ice crystal growth in the premix. This tipping point can be easily calculated by zeroing the derivative of the Gibbs free energy function (equation D.10 and D.11). This radius can then be injected in the Gibbs free energy equation to find the maximum Gibbs free energy point of the system (equation D.13).

$$\Delta G'_n = 0 = -4\pi r_*^2 \left( \frac{L_f \Delta T}{T_m} - \int_T^{T_m} \Delta C_p dT' + T \int_T^{T_m} \frac{\Delta C_p}{T'} dT' \right) + 8\pi r_* \gamma \quad (\text{D.10})$$

$$r_* = \frac{2\gamma}{\frac{L_f \Delta T}{T_m} - \int_T^{T_m} \Delta C_p dT' + T \int_T^{T_m} \frac{\Delta C_p}{T'} dT'} \quad (\text{D.11})$$

$$\Delta G_{n^*} = -\frac{4\pi}{3} \left( \frac{2\gamma}{\frac{L_f \Delta T}{T_m} + C} \right)^3 \left( \frac{L_f \Delta T}{T_m} + C \right) + 4\pi \left( \frac{2\gamma}{\frac{L_f \Delta T}{T_m} + C} \right)^2 \gamma \quad (\text{D.12})$$

$$\Delta G_{n^*} = \frac{4\pi\gamma}{3} \left( \frac{2\gamma}{\frac{L_f \Delta T}{T_m} - \int_T^{T_m} \Delta C_p dT' + T \int_T^{T_m} \frac{\Delta C_p}{T'} dT'} \right)^2 \quad (\text{D.13})$$

With  $C = -\int_T^{T_m} \Delta C_p dT' + T \int_T^{T_m} \frac{\Delta C_p}{T'} dT'$  being used for formula simplification. Using this maximum Gibbs free energy of the system represent the barrier energy needed to start the ice crystal growth. Moreover, except for the surface tension at the interface between water and ice crystal, the formula contains only values that can be deduced from the DSC measurements. Finally using the free Gibbs energy of the system, it is possible to compute the number of nucleation point in a given volume (see equation D.14).

$$n_r = n_0 \cdot e \left( -\frac{\Delta G_n}{kT} \right) \quad (\text{D.14})$$

With  $n_0$  the number of atoms in the analyzed volume,  $n_r$  the number of nucleation site and  $k$  the Boltzmann constant. It is assumed that with less than one nucleation site per  $\text{cm}^3$  no spontaneous nucleation is possible and would require larger super cooling or impurities in the system to serve as nucleation points.

However these equations are extremely sensitive to noise and did not yield solutions approaching expected values. This might also come from the fact that they were developed to describe nucleation in the nm scale in pure materials which might not be the appropriate model for crystals of the size found in cryogels. They could be used to find out pore size and volume fraction within the wall of the cryogels if nucleation ever occurred there. However this small size nucleation happens only at a supercooling much higher than for larger pores. Therefore all water would probably be already frozen in large pores before any in-wall nucleation could occur. Mathematical models that estimate the size and behavior of large crystal size in complex environments such as described in chapter 2 could not be found. Most of the time studies on large ice crystals relies upon empirical analysis [Flores and Goff, 1999]. As the evidence for pure thermodynamic phenomenon driving the crystal growth in CMC cryogels was found, it can

## Appendix D. Thermodynamic model

be of interest to further investigate and develop a complete model as it would grant a deeper comprehension behind the formation of ice crystal during cryogel synthesis and possibly allowing pore size manipulation to a greater extent than presented in chapter 2 which could be of interest in various fields such as cell culture as discussed here but also filtration or plastic surgery. The development of such thermodynamic models are however not in the scope of this thesis.

# Conductive cryogels

## E.1 Introduction

As mentioned in chapter 2.3, because ice crystals grow and remain pure ice, a phenomenon of cryoconcentration occurs, concentrating the monomer and crosslinker molecules to the interface between ice crystals to form a cryogel. In this appendix, conductive particles were added to the premix before cryogel synthesis. In principle, the particles should be subjected to this concentration phenomenon thus reaching the percolation threshold much faster than if particles were simply dispersed in a hydrogel solution. Depending on the properties of the particles, different behavior of the cryogel can be achieved thus allowing the creation of active scaffolds.

## E.2 Implementation and results

For this proof of concept, conductive particles were used in order to increase the cryogel conductivity. Platinum, gold and boron doped diamond microparticles were used with a particle diameter of  $4\mu\text{m}$  in average. Diamond was observed to give the best dispersion in term of homogeneity and stability. However using an ultrasonic horn dispersion of all material of interest were achieved in the premix. One cryogel containing 4% of diamonds was first synthesized and coated with 10nm of carbon and fixed with conductive glue on a SEM mount for better imaging. The picture can be seen in figure E.1. The convoluted structure is clearly visible and diamond particles can be seen trapped in the pores walls. The particles are homogeneously distributed in the material and appear to be in contact indicating that the percolation threshold has been reached.

Platinum gels were giving better results in term of conductivity and are therefore used for characterization. Cryogels were synthesized in bulk, using different particles concentration from 0% to 4% in weight, in between 1.5mm height spacer. After curing, they were punched to produce discs 7mm in diameter. They were then washed in NaOH solution 100mM followed by a wash in 10mM NaOH and then 1nM NaOH. Two rinses were then performed in 5mM NaCl solution and were stored in a 5mM NaCl solution. Those wash were performed to ensure that the conductivity difference measured are coming from the conductive particles trapped in the cryogel scaffold an not from the

## Appendix E. Conductive cryogels

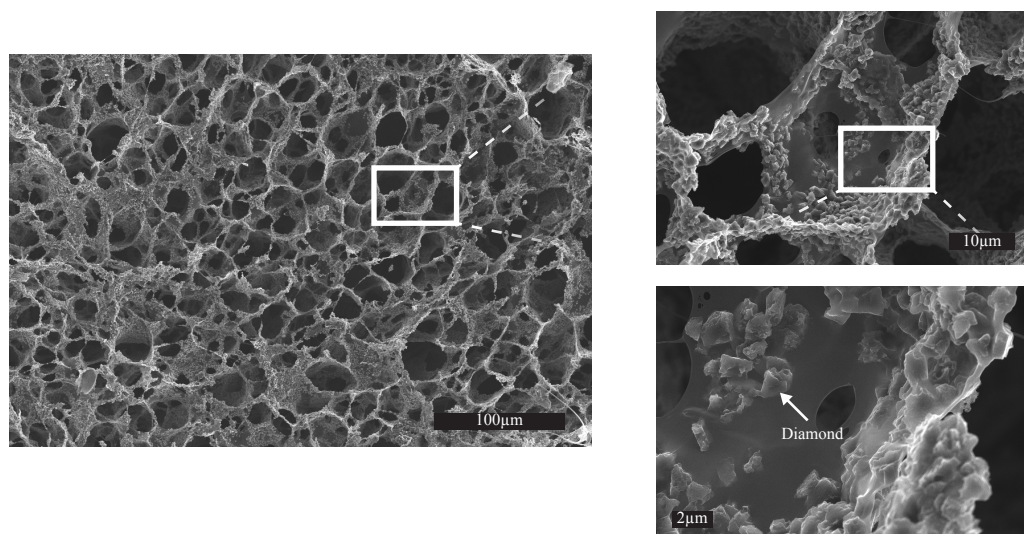


*Figure E.1 – SEM imaging of cryogel seeded with boron doped diamonds*

residual ions from the reaction. The 5 mM NaCl solution was used instead of DI water as it provide a small conductivity to the solution in the pores which is higher than diluted ions that can occur randomly in DI water. The conductivity of the NaCl solution can then be subtracted afterwards. This results in less noise over the measured conductivity.

To perform the measurements, copper tape was first plated with silver using a plating solution from metalor at 1.5V and 20mA for 2 minutes (anode on the copper and cathode on silver wire). Then the silver plated band was dipped in HCl 0.1M (with anode on platinum wire and cathode on the silver band). A current of 20mA was also applied for half the plating time (1 minute) creating Ag-AgCl electrodes well suited for high charge injection. Those bands were taped on a laser cut plastic support with a 1 mm spacer. The cryogel was squeezed between the two electrodes as shown in figure E.2 A. Using an electrospectrometer the module and phase of the cryogel were measured and are plotted in figure E.2 B, C respectively. The Nyquist plot is also shown in figure E.2 D.

One can observe that the resistance of the cryogels remain high and diminish slightly as the particle concentration increase. At 4% the resistance drops dramatically indicating that the percolation threshold has been reached. Usually, to obtain percolation, assuming homogeneously distributed spherical particles, the maximum packing density of 74% volume [N.J.A. Sloane, 1984] must be occupied by particles. If random placement of the particle is taken into account, percolation can occur much faster [Stauffer, 1979]. Usually around 20% of the volume must be occupied by particles. The fact that the percolation threshold is reached at only 4% in concentration in premix is due to the cryococentration effect which will further concentrate the particle in the walls of the cryogel. The phase of the percolated cryogel is zero at low frequencies and inductive at higher frequencies due to setup wire inductance.

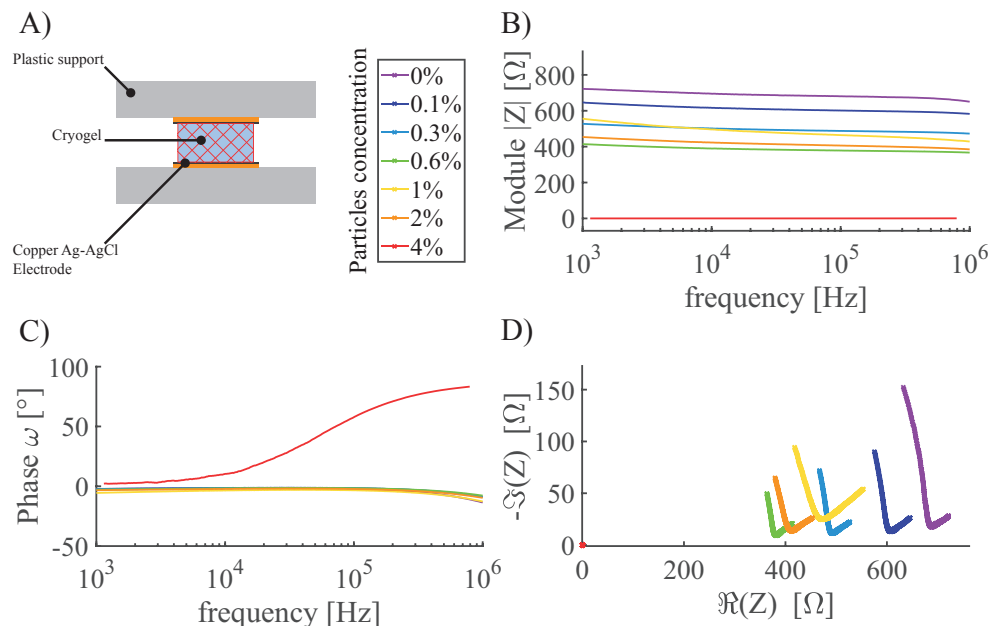


Figure E.2 – Spectral impedance measurement of conductive cryogel. A) Setup to interface the cryogel with the impedance spectrometer. B) Measured modulus of cryogels at different platinum micro-particles concentration. C) Measured phase of cryogels at different platinum micro-particles concentration. D) Nyquist plot of cryogels at different platinum micro-particles concentration.

### E.3 Conclusion

Thanks to cryoconcentration effect, percolation threshold can be obtained at low particle concentration in cryogels. It is however not obvious whether particles would serve as nucleation initiator therefore and be released upon thawing or if they would be trapped within the polymer matrix. In [Tobergte and Curtis, 2013] it is shown that both scenarios could happen depending over the surface energy of the particle/premix interface. Therefore this technique might not work for all types of particle. In this example different conductive particles were used and all were concentrated in the matrix phase. With only 4% in weight of conductive particles, the cryogel could turned conductive. Many application could be derived from conductive cryogels, such as active scaffold for cells, porous bandages with conductive tracks for wound monitoring or high charge injection soft electrodes for electro-stimulation of tissue thanks to the large surface area of the cryogel. Many different particles with different properties can be added to the scaffold to tailor its properties. Many different inks could then be developed and printed using the 3D printer presented in chapter 2.





# Calculation steps for hydrodynamic focusing design

To design the concentrator the calculations have to be made in succession starting from the shortest extraction channel, at the center of the chip, to the longer ones. Most parameters can be fixed leaving only the length and width of each extraction channel to be computed. Assuming a mean cell diameter of  $10\mu\text{m}$ , the extraction channel width must be larger than  $20\mu\text{m}$  to avoid clogging, should one cell pass through it, and have a withdrawing sheet flow size of  $l_{sheet}=5\mu\text{m}$ . Moreover, the probe will be manufactured using standard cleanroom processes thus the depth of all channel will be equal and set to  $200\mu\text{m}$  to diminish shear stress on cells. The width of the main channel will also be set to  $200\mu\text{m}$  for similar reasons. The flow rates are set to be relevant for a bioprinting application, in this case  $Q_{out}$  is set to  $0.5\mu\text{L}$  per minute thus for a ten fold concentration  $Q_{in}$  to  $5\mu\text{L}$  per minute. Finally, the length of the first extraction channel can be set arbitrarily. It is however necessary to choose a length sufficiently high to provide enough flow resistance with the channel's length in order to keep the extraction channel wider than  $20\mu\text{m}$ . The calculation can then be made in the following order.

1. Compute the pressure drop at the boundaries of the extraction channel.
2. Compute the needed flow rate in the extraction channel to achieved the desired sheet flow size.
3. Compute extraction channel width and length.
4. Compute extraction channel flow resistance.
5. Compute the flow resistance of main channel and all parallel extraction channels.
6. Compute the new flow rate in the main channel.
7. Repeat from step one for as many extraction channel as needed.



# Organoids culture and protocol

## G.1 Material

In order to proceed with organoid culture, following material is needed:

- 24 cell culture well plate
- Splitting medium (on ice)
- Complete medium (37 °C)
- BME, on ice (*RGF BME, type2, 17.45mg/ml from Cultrex, catalog #: 3533-005-02, lot #: 40763K17*)
- Fire polished and tapered glass pipette
- 1% Bovine Serum Albumin (BSA)

## G.2 Media

Media preparation for cell and organoid culture: This medium was developed and optimized by Dr. Jasper Mullenders (former Post-Doc, Hans Clevers Laboratory, Hubrecht Institute, Utrecht)

Compounds	Supplier: catalog #	Volume
DMEM/ F12 / HEPES / Glutamax	ThermoFischer: 10565018	200mL
B27	ThermoFischer: 17504044	4mL
FGF7 (100ng/ml) in DMEM/F12	Peptidech: 100-19	40 $\mu$ L
FGF10 (100 ng/ml) in DMEM/F12	Peptidech: 100-26	200 $\mu$ L
A8301 (5 mM)	Tocris Bioscience: 2939	20 $\mu$ L
RhoK inh (10 mM)	Abmole Bioscience: M1817	200 $\mu$ L
Primocin (50 $\mu$ g/ml)	Invivogen	200 $\mu$ L

## Appendix G. Organoids culture and protocol

### G.3 Organoid fixing and staining

#### G.3.1 Protocol

Here is the two day protocol used to perform immunostaining on organoid slices.

Step #	Process	Incubation time	Treatment
DAY 1			
1	Dewax and rehydrate	90 min	Xylo1,100% to70% ETOH, H2O
2	Hydrate	1 x quickly + 2 x 5min	PBS 1x
3	Equilibrate	5 min	Antigen retrieval buffer
4	Heat induced epitope retrieval (HIER)	20min at 95°C	Retriever with 10mM Tri-Na pH6
5	Wash	1 x quickly + 2 x 5min	PBS 1x
6	Permeabilization	15 min	0.2% Triton in PBS 1X
7	Incubation with primary antibody	Overnight at 4 °C under gentle agitation	1% BSA in PBS 1x with primary antibody
DAY 2			
8	Wash	1 x quickly + 2 x 5min	PBS 1x
9	Centrifugation secondary antibody	10 min at 13000 rpm for 5 min	Dilution 1:500 in 1% BSA (PBS 1X)
10	Wash	1 x quickly + 2 x 5min	PBS 1x
11	Incubation with secondary antibody	1.5 hrs at RT	1Y% BSA (PBS 1X)
12	Wash	1 x quickly + 2 x 5min	PBS 1x
13	Nuclear staining (DAPI)	15 min at RT	Dilution (1:1000) in PBS 1X
14	Wash	1 x quickly + 4 x 5min	PBS 1x
15	Mounting	overnight	Fluoromount G

### G.3. Organoid fixing and staining

#### G.3.2 Material

List of anti-bodies used for organoid immunostaining.

Item #	Anti-body name	Supplier: catalog #	Target	Reactivity	Host
1	Anti-CK20 (EPR1622Y)	Abcam: ab76126	CK20	Rat, Humans	Rabbit
2	Na-K ATPase	Abcam: ab198367	Na-K ATPase Pump	Mouse, Humans	Rabbit
3	Anti-RCK103	Thermofischer: RCK103-MA1-06312	CK1,CK5	Humans	Mouse
4	Anti-CK7	Abcam: ab209599	CK7	Mouse, Humans	Rabbit
5	Anti-UPIIIa	Abcam: ab78196	UPIII	Mouse, Humans	Mouse
6	Anti-CD44	Abcam: ab189524	CD44	Mouse, Humans	Rabbit
7	Anti-CK8	Abcam: ab192468	CK8	Mouse, Humans	Rabbit
8	Anti-CK13	Abcam: ab198584	CK13	Mouse, Humans	Rabbit
9	Anti-p63A4	Abcam: ab735	p63	Mouse, Humans	Mouse
10	Anti-Ki67	Spring Bioscience: M3062	Ki-67	Mouse, Humans	Rabbit



# Multi-material printing

## H.1 Introduction

As presented in the chapter 1.1, multiple printing methods exist and can be adapted for 3D bioprinting. However extrusion based 3D printing presents great advantages compared to other methods such as bio-compatibility, compatibility with large number of bio-inks, possibility to implement new functions as it will be presented in appendix I and the ability to print multiple different materials. Apart from dedicated multi-material probe (appendix I.2.1 and chapter 4) most of the presented probe can only dispense one type of material. It is possible to design the probe with multiple concentrator and actuate them separately to create a multi-material concentrating head. However this would result in a rather large design, inconvenient to work with. Although possible, another method is presented here to enable multi-material printing with the previously presented probes.

## H.2 Implementation and results

One solution to print multiple material is to stack two probes back to back. However this way only two probes could be put together to keep access to the inlets of the probes and the dispensing outlet would be separated by the thickness of the wafer. Another solution is to bring them side by side as shown in figure H.1 A with one concentrator probe on the left and one on the right. Both of their tip are put into contact merging together their outlets as shown in figure H.1 B. Both probe can now be used independently and dispense the material at the same point. Using this configuration the need to switch between extruders is circumvented, leading to faster printing, fast material switching and better layer to layer adhesion. A micrograph of a test print is shown in figure H.1 C where yellow and blue alginate were deposited on an agarose bed containing  $\text{CaCl}_2$ . Yellow alginate containing a high beads concentration was deposited using the concentrator 1 and then blue alginate is printed alongside containing a lower concentration of beads.



## Appendix H. Multi-material printing

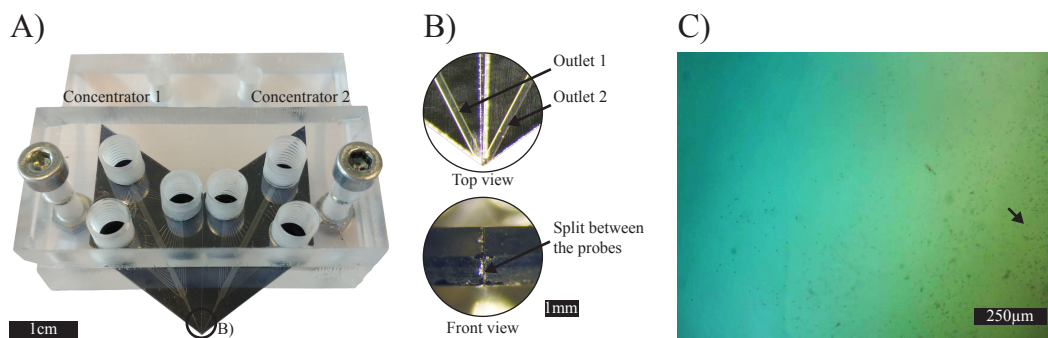


*Figure H.1 – Double probe mounting enabling multi-material printing: A) the mount with two probes side by side with all inlets addressable independently. B) Close view of the outlets of each probe merging into one. C) Blue and yellow alginate printed using both probe allowed the creation of sharp gradients. The arrow point at a particle present in the yellow alginate highlighting the possibility to add particles within the material and using the probe creat particle gradient as well.*

### H.3 Conclusion

This test shows the ability to use multiple probes at once and control them independently. It is then possible to print multiple different materials and, in this case, control the particle concentration independently as well. This opens the door to printing many different ECM with multiple type of cell as well thus without having to switch between printing heads which in turn keeps the printing speed high. On could also imagine to combine probes with different functions such as concentrating probe (presented in chapter 3) for cell printing along side with a multi-material probe (presented in chapter I.2.1) to print different support material or bring growth factor at specific point in the structure allowing the creation of gradient which are crucial to properly drive cell growth.

# Microfluidic for 3D printing

## I.1 Introduction

As it has been demonstrated throughout this thesis, microfluidic technology brings new functionalities to extrusion based 3D printing that can benefit in great extent to 3D bioprinting. This appendix widens the discussion to extrusion based 3D printing in general as many of the technologies developed in the "lab on a tip" framework can be used to print new material using extrusion based 3D printing, thus with refined control over the printed material, thanks to dispensing tools tailored to the application. This appendix is inspired from the published paper entitled "Microfluidics: A New Layer of Control for Extrusion-Based 3D Printing". [Serex et al., 2018a]

## I.2 Probes

Four different printing heads tailored for a specific function are presented here. They are either concepts initially developed in the frame of the thesis and adapted for a different purpose or development that were not advanced enough to have a place in the core of the thesis. Each of the probe either add a new functionality to the printer or allows for the printing of material that were impossible before.

### I.2.1 Multi-Material probe

One limitation of extrusion-based 3D printers is that each print head can only print a single material. Printing an object made of multiple materials is usually achieved by using a 3D printing machine with multiple extrusion heads placed next to each other. By switching between print heads, different materials can then be printed. [Colosi et al., 2017] In addition to requiring specific equipment, printing multi-material components with extrusion-based 3D printers is generally a very slow process, and a smooth transition between printed materials is not always guaranteed. A number of microfluidic systems allowing switching between different liquids have already been presented in the literature, including some that could be implemented in 3D printers. [Devaraju and Unger, 2012]

## Appendix I. Microfluidic for 3D printing

Here, we will show a very simple system that is easy to implement and allows a fast switching between materials.

The print head we designed is composed of three micro-channels merging into one right before the ejection point, as presented in figure I.1 A. Each of these three channels can be connected to a syringe containing a different material and actuated by a syringe pump. By choosing the sequence of actuation of the syringe pumps and synchronizing it with the geometry of the part being built, a seamless transition between multiple materials can be achieved during the object manufacturing process. Furthermore, as microfluidic benefits from very small dead volumes, it is possible to rapidly switch between materials. In our case, a complete transition between two materials can be performed in 500 ms, as presented in figure I.1 B, where the transition between different colored liquids was recorded using a camera connected to a microscope focused at the tip of the print head we used.

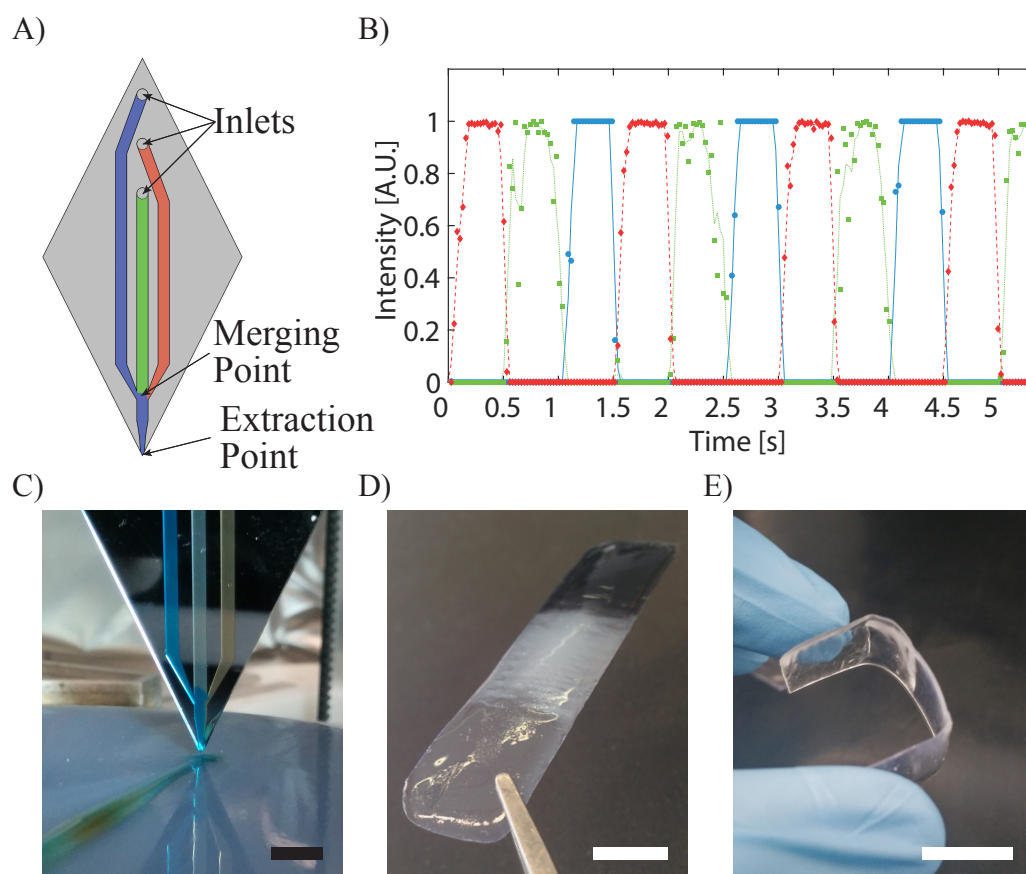


**Figure I.1** – Multi-channel print head. A) Schematic of the microfluidic channel design. B,C) Switching of three colored liquids as recorded at the tip of the print head. D) Clear, white and black part. E) Two-hinge parts printed with two different inks (one rigid and one flexible). All scale bars correspond to 1 cm.

The print head was then mounted on a 3D printer, and colored alginate solutions were printed on an agarose 4% and CaCl<sub>2</sub> 1% bed, inducing the alginate gelation by diffusion of the calcium ions into the alginate deposit. Figure I.1 C shows the smooth transition between colors obtained as the printing process goes.

It is possible to combine extrusion 3D printing with UV light irradiation of the printed layers to print photosensitive inks using the same print head based on merging microchannels. Thus, multimaterial components can be made by the extrusion method by selecting photosensitive resins having the desired properties, chosen from the large catalogue of materials developed for the stereolithography process. By switching between different resins developed by Formlabs<sup>®</sup>, it is possible to print multicolor parts, as shown in figure I.1 D where a clear white and black resins are being seamlessly switched producing multi-color parts. Formlabs<sup>®</sup> also developed flexible resin allowing the printing of rigid and flexible areas. This allows the creation of parts with different Young's moduli. Thus foldable part can be printed as shown in figure I.1 E. this kind of printing was only possible using very expansive multi-jet printers.

### I.2.2 Mixing probe

The micromixer presented in chapter 3.2.3 can be adapted to print to print resins from Formlabs<sup>®</sup> as well. However in contrast to the switching probe presented above, as the different materials can be efficiently mixed, gradients can be created by varying their ratio. As an example, black and white Formlabs<sup>®</sup> resins were printed going from fully black to fully white in a smooth gradient (figure I.2 A). Therefore by adding the 3 primary colors to the mix, any color can be printed in a very simple manner.

Moreover, as efficient mixing is performed, fast-reacting material can be brought in contact, just before they are deposited by 3D printing. As a demonstration, the mixing of two resins based on polyethylene glycol 400 diacrylate, one component containing 3% N,N,N',N' Tetramethyl-ethylenediamine, the other containing 3% benzoyl peroxide. The benzoyl peroxide/amine system is known as an initiator for free-radical polymerization of acrylates [Sideridou et al., 2006] and the reaction is fast when all materials are brought in contact. By adequately choosing the amine component, the crosslinking speed can be adapted. Figure I.2 B shows a 3D printed filament made by mixing these components at the last second.

This allows materials that are not usually used in 3D printing to be printed, such as polymer systems initiated by peroxides, as well as biomaterials such as hydrogels or cryogels. Additionally, more conventional materials can be mixed with a chosen ratio between them, allowing blends of materials to be created. This is of interest in the production of materials with gradients of properties in an object. It can simply be a gradient of colors if two resins of different color are used, but gradients of mechanical

## Appendix I. Microfluidic for 3D printing

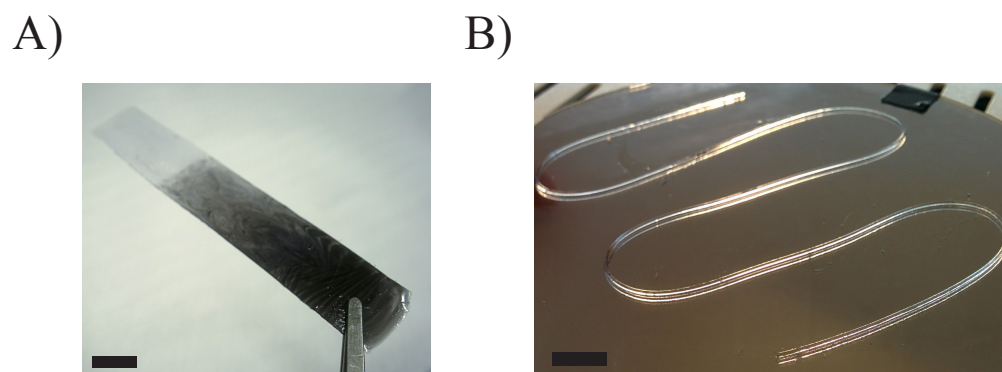


*Figure I.2 – Print head based on flow focusing. A) Principle of hydrodynamic flow focusing with the core flow in blue and the sheath flow in white. B) Flow focusing at different sheath flow/core flow ratios. C) Printed fiber diameter as a function of the flow ratio. D) Printed filament going from small filament (1) to large filament (2) whilst the ratio  $R$  is changed. E) First layer of a printed part with fine edge (1) and coarse filling (2). Scale bars = 5 mm.*

properties can also be fabricated, for example by mixing resins resulting in flexible and hard polymers or by mixing composite resins, charged with a filler material.

### I.2.3 Adjustable resolution probe

Microfluidic flows present a laminar behavior. [Knight et al., 1998] This property can be exploited to change the resolution of the printed material by focusing it while it is dispensed using sheath flows. [Lind et al., 2017] Hydrodynamic focusing only requires a very rudimentary microfluidic setup, the most common configuration being a 3-channel device, where the center flow stream is pinched between two side flow streams, resulting in a shrinking of the width of the center flow. Implementing hydrodynamic focusing in the print head of an extrusion-based 3D printer, its resolution can be not only be significantly increased, but it can be adjusted while printing by simply varying the ratio between the core and lateral flows. Figure I.3 A demonstrates the principle of sheath flow. Alginate filaments (in blue) are focused using de-ionized (DI) water with 4%  $\text{CaCl}_2$ . Depending on the ratio of the alginate core flow to the  $\text{CaCl}_2$  solution sheath flow (figure I.3 B), the obtained filaments can vary in diameter from  $800\mu\text{m}$  to below  $200\mu\text{m}$ , providing a fivefold resolution increase. Figure I.3 C shows the evolution of the size of the deposited filaments as a function of the ratio between sheath and core flows.

One issue of the use of sheath flows for increasing the printing resolution is the fact that the liquid used in the sheath flow for focusing is also “printed” alongside the actual material of interest. In our example, using a water-based solution, large quantities of water are ejected from the probe and may disrupt the printing. In figure I.3 D, a printed filament with changing diameter is presented. The first section of the filament is small

and soaked in the sheath flow that will ultimately dry. The filament then widens and the surplus of liquid produced by the sheath flow becomes almost nonexistent as it is reduced to a minimum. To solve the problem of residual fluid, Perfluoro(methyldecalin) (PFD) was used as sheath flow. Given that it is a highly volatile material, it will quickly evaporate, leaving only the desired focused filament. One limitation of this technique is that when the sheath flow becomes much larger than the core flow, flow instabilities occur, limiting the use of hydrodynamic focusing for enhancing the resolution of the dispensed material. In this case, there is always the possibility of reducing the dimensions of the microfabricated channels provided on the print head for improving the resolution. However, this implies the use of larger values of pressure to drive the various liquids in the microchannels. Furthermore, it is important to note that as liquids are being printed, the tuning of the printed filament through flux control of the core flow only without flow focusing can be achieved. With a constant printing speed, an increase of the flux will result in a larger printed filament (figure I.3 E). This presents the advantage of not having residual liquid from the sheath flow, but the crosslinking must be performed from the probe either by UV light or, in this case, by printing alginate on a  $\text{CaCl}_2$  bed, which is not suitable for high structures.

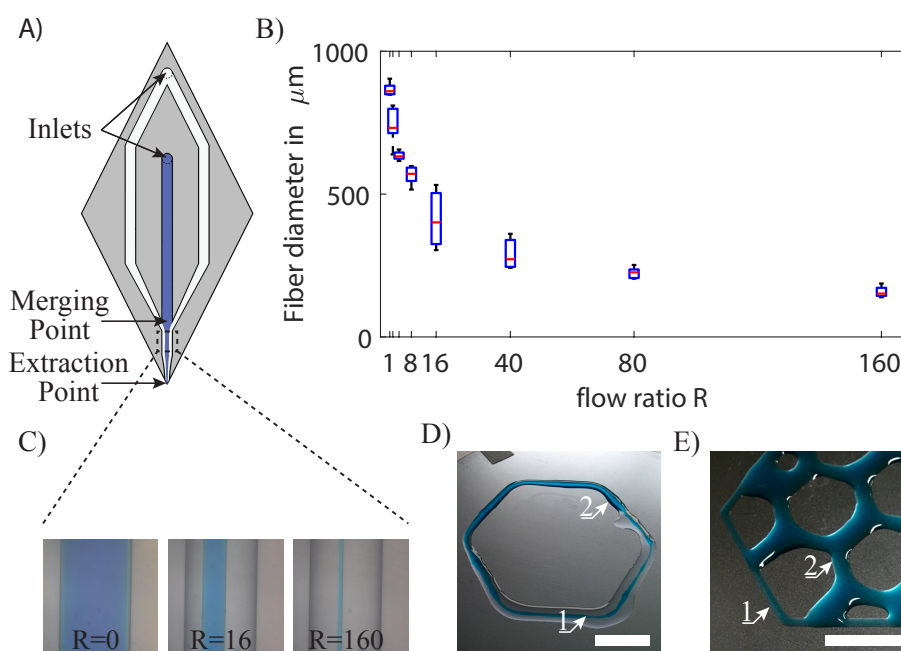


**Figure I.3** – Herringbone micro-mixer integrated at the tip of the probe. A) Colored glycerol streams pushed through a simple T-junction and through a herringbone micro-mixer at 0 mm, 2 mm and 4 mm after the merging point. The mixer allows rapid and efficient mixing of viscous materials. Scale bar =  $300\ \mu\text{m}$ . B) Mixing of white and black Formlabs resins at different ratios results in smooth gradients from one material to the other. Scale bar = 1 cm. C) Printed acrylate filament made using a two-component material. Scale bar = 1 cm.



## Appendix I. Microfluidic for 3D printing

Adjusting the printer resolution on the fly opens new ways of controlling the printed part. It would thus be possible to choose the resolution depending on the importance of the part being printed while printing. This method allows the printing of coarse filament for the filling of the printed part, while at the same time, for the wall, the filament can be refined to obtain fast and precise printing.

### I.2.4 Concentration probe

In this section, the possibility of the probe presented in chapter 3 to concentrate particles is highlighted. Indeed, concentrating particles in solution before their being dispensed by 3D printing can find applications in various fields. It is known that the concentration of particles in composite materials is a major factor in their physical properties. [Alsson, 1997] With the device we presented, the physical properties of the printed composites could be changed during printing. This is of particular interest when high concentrations of filler material need to be present in the printed material, making it very viscous. Concentrating the particles in a composite material at the last second when printing makes it possible to work with diluted (thus of low viscosity) solutions for the whole process and still produce composites of the desired composition, removing the excess liquid just before dispensation.

## I.3 Discussion and conclusion

Extrusion-based techniques are easy to use and are cost effective, but have seen almost no improvement in terms of process development since their creation. On the contrary, microfluidic techniques have seen major developments in terms of device design and fabrication, and these developments can now be applied to significantly improve the print heads of extrusion-based 3D printers.

In this appendix, the integration and adaptation of four microfluidic systems at the tip of the print head of extrusion-based 3D printers to create smart dispensing tools that can perform different functions right before printing has been explored. As demonstrated here, even so the integration of additional functions to print heads is of particular importance for bioprinting applications, it can also benefit extrusion based 3D printing as a whole. We demonstrated fast switching between two or more materials to create multimaterial parts thus without switching printing heads which is time consuming and do not provide seamless transition between materials. On demand resolution enhancing has also been demonstrated. Even so it requires fine tuning and the use of new materials for now expensive such as PFA, it holds the potential to bring finer resolution than actual extrusion based 3D printers. Micro-mixers can be used to prepare hydrogels or cryogels from their components, to insert cells into the printing medium or to create gradients of composition or of cell types while printing. Finally, not only the concentration probe



### I.3. Discussion and conclusion

makes it possible to reach cell concentrations close to native tissue without adverse effects during their manipulation but also enables the concentration of any type of particles that could help building conductive tracks through percolation of conductive particles for electronic printing. Fire retardant, magnetic, piezoelectric and many more type of particles could be added to the solution and concentrated to a meaningful point could allow for truly functional material 3D printing.

Thanks to microfabrication, more complex functions can also be integrated in the print heads, taking advantage of all the knowledge available in the field of Lab on Chip devices, but such developments would probably have precise needs in terms of specific applications. For example, combining fluidic functions with in-channel spectroscopy could provide continuous feedback on the printed material quality, implementing dielectrophoresis electrodes could be used for filtering particles and cells and could make it possible to print only the viable cells, and detecting the passage of cells of interest while they flow through the microchannels and filtering out the excess of liquid medium could make it possible to print each cell at a precisely chosen location. Many other microfluidic functions can be integrated, such as fast switching valves, digital microfluidic, microfluidic gradient generators, cell concentrator or micro-heaters, each bringing the potential of using new materials and developing new applications for extrusion-based 3D printing. The integration of customized microfluidic functions into the print heads of 3D printers has the potential to be a game changer in all fields where additive manufacturing is used and not only in bioprinting.



# Bibliography

- [Pet, 1996] (1996). Color stereophotolithography: A method of 3-d color imaging. *Journal of Imaging Science and Technology*, 40(1).
- [Kol, 2003] (2003). Ca<sup>2+</sup>-dependent Binding and Activation of Dormant Ezrin by Dimeric S100P. *Molecular Biology of the Cell*, 14(February):2372–2384.
- [Abdolvand and Ayazi, 2008] Abdolvand, R. and Ayazi, F. (2008). An advanced reactive ion etching process for very high aspect-ratio sub-micron wide trenches in silicon. *Sensors and Actuators, A: Physical*, 144(1):109–116.
- [Abouna, 2008] Abouna, G. M. (2008). Organ Shortage Crisis: Problems and Possible Solutions. *Transplantation Proceedings*, 40(1):34–38.
- [Adamkiewicz and Rubinsky, 2015] Adamkiewicz, M. and Rubinsky, B. (2015). Cryogenic 3D printing for tissue engineering. *Cryobiology*, 71(3):518–521.
- [Advanced BioMatrix, 2018] Advanced BioMatrix (2018). Viscosity of VitroCol Collagen.
- [Akbari et al., 2016] Akbari, M., Tamayol, A., Bagherifard, S., Serex, L., Mostafalu, P., Faramarzi, N., Mohammadi, M. H., and Khademhosseini, A. (2016). Textile Technologies and Tissue Engineering: A Path Toward Organ Weaving. *Advanced Healthcare Materials*, 5(7):751–766.
- [Alberts et al., 2002] Alberts, B., Bray, D., Lewis, J., Raff, M., Roberts, K., Watson, J. D., Robertson, M., Adams, R., Cobert, S. M., and Goertzen, D. (2002). *Cell Junctions, Cell Adhesion, and the Extracellular Matrix*, volume 4. Garland Science, New York.
- [Alhaque et al., 2018] Alhaque, S., Themis, M., and Rashidi, H. (2018). Three-dimensional cell culture: from evolution to revolution. *Philosophical transactions of the Royal Society of London. Series B, Biological sciences*, 373(1750):20170216.

## Bibliography

- [Alsson, 1997] Alsson, B. E. O. P. (1997). Effective intercellular communication distances are determined by the relative time constants for cyto/chemokine secretion and diffusion. *Engineering*, 94(November):12258–12262.
- [Alveringh et al., 2017] Alveringh, D., Schut, T. V., Wiegerink, R. J., Sparreboom, W., and Lotters, J. C. (2017). Resistive pressure sensors integrated with a coriolis mass flow sensor. *TRANSDUCERS 2017 - 19th International Conference on Solid-State Sensors, Actuators and Microsystems*, (October):1167–1170.
- [André, 2018] André, J.-C. (2018). *From Additive Manufacturing to 3D / 4D Printing 3*. ISTE, London, wiley edition.
- [Aoki et al., 2009] Aoki, R., Yamada, M., Yasuda, M., and Seki, M. (2009). In-channel focusing of flowing microparticles utilizing hydrodynamic filtration. *Microfluidics and Nanofluidics*, 6:571–576.
- [Arcaute et al., 2006] Arcaute, K., Mann, B. K., and Wicker, R. B. (2006). Stereolithography of three-dimensional bioactive poly(ethylene glycol) constructs with encapsulated cells. *Annals of Biomedical Engineering*, 34(9):1429–1441.
- [Armstrong et al., 2016] Armstrong, J. P., Burke, M., Carter, B. M., Davis, S. A., and Perriman, A. W. (2016). 3D Bioprinting Using a Templated Porous Bioink. *Advanced Healthcare Materials*, 5(14):1724–1730.
- [Asmolov, 1999] Asmolov, E. S. (1999). The inertial lift on a spherical particle in plane Poiseuille flow at large Reynolds number. *Journal of Fluid Mechanics*, 381(1999):63–87.
- [Au et al., 2016] Au, A. K., Huynh, W., Horowitz, L. F., and Folch, A. (2016). 3D-Printed Microfluidics. *Angewandte Chemie - International Edition*, 55(12):3862–3881.
- [Bédurier et al., 2015] Bédurier, A., Braschler, T., Peric, O., Fantner, G. E., Mosser, S., Fraering, P. C., Benchérif, S., Mooney, D. J., and Renaud, P. (2015). A Compressible Scaffold for Minimally Invasive Delivery of Large Intact Neuronal Networks. *Advanced Healthcare Materials*, 4(2):301–312.
- [Bédurier et al., 2018] Bédurier, A., Piacentini, N., Aeberli, L., Da Silva, A., Verheyen, C. A., Bonini, F., Rochat, A., Filippova, A., Serex, L., Renaud, P., and Braschler, T. (2018). Additive manufacturing of hierarchical injectable scaffolds for tissue engineering. *Acta Biomaterialia*, 76:71–79.
- [Belser and Hicklin, 1959] Belser, R. B. and Hicklin, W. H. (1959). Temperature Coefficients of Resistance of Metallic Films in the Temperature Range 25° to 600°C. *Journal of Applied Physics*, 30(3):313–322.
- [Bencherif et al., 2014] Bencherif, S., Mooney, D. J., and Renaud, P. (2014). Injectable Cryogels for Neural Tissue Engineering Applications. pages 1134–1136.

- [Bencherif et al., 2013] Bencherif, S. a., Braschler, T. M., and Renaud, P. (2013). Advances in the design of macroporous polymer scaffolds for potential applications in dentistry. *Journal of Periodontal and Implant Science*, 43(6):251–261.
- [Bencherif et al., 2015] Bencherif, S. a., Warren Sands, R., Ali, O. a., Li, W. a., Lewin, S. a., Braschler, T. M., Shih, T.-Y., Verbeke, C. S., Bhatta, D., Dranoff, G., and Mooney, D. J. (2015). Injectable cryogel-based whole-cell cancer vaccines. *Nature communications*, 6(AUGUST):7556.
- [Berg et al., 2014] Berg, E. L., Hsu, Y. C., and Lee, J. a. (2014). Consideration of the cellular microenvironment: Physiologically relevant co-culture systems in drug discovery. *Advanced Drug Delivery Reviews*, 69-70:190–204.
- [Bertassoni et al., 2014] Bertassoni, L. E., Cecconi, M., Manoharan, V., Nikkhah, M., Hjortnaes, J., Cristino, A. L., Barabaschi, G., Demarchi, D., Dokmeci, M. R., Yang, Y., and Khademhosseini, A. (2014). Hydrogel bioprinted microchannel networks for vascularization of tissue engineering constructs. *Lab on a Chip*, 14(13):2202–2211.
- [Bhagat and Papautsky, 2008] Bhagat, A. A. S. and Papautsky, I. (2008). Enhancing particle dispersion in a passive planar micromixer using rectangular obstacles. 085005.
- [Bhagat et al., ] Bhagat, A. A. S., Peterson, E. T. K., and Papautsky, I. A passive planar micromixer with obstructions for mixing at low Reynolds numbers. 1017.
- [Bhise et al., 2016] Bhise, N. S., Manoharan, V., Massa, S., Tamayol, A., Ghaderi, M., and Miscuglio, M. (2016). A liver- on-a-chip platform with bioprinted hepatic spheroids. *Biofabrication*.
- [Bianconi et al., 2014] Bianconi, E., Piovesan, A., Facchin, F., Beraudi, A., Casadei, R., Frabetti, F., Vitale, L., Pelleri, M. C., Tassani, S., Piva, F., Perez-Amodio, S., Strippoli, P., and Canaider, S. (2014). An estimation of the number of cells in the human body. *Annals of human biology*, 40(6):463–71.
- [Billiet et al., 2014] Billiet, T., Gevaert, E., De Schryver, T., Cornelissen, M., and Dubruel, P. (2014). The 3D printing of gelatin methacrylamide cell-laden tissue-engineered constructs with high cell viability. *Biomaterials*, 35:49–62.
- [Boesen et al., 1994] Boesen, J., Niericker, M., Dieteren, N., and Simons, J. (1994). How variable is an spontaneous mutation rate in cultured mammalian cells? *Mutation Research/Fundamental and Molecular Mechanisms of Mutagenesis*, 307(1):121–129.
- [Bose et al., 2017] Bose, S., Ke, D., Sahasrabudhe, H., and Bandyopadhyay, A. (2017). Additive Manufacturing of Biomaterials. *Progress in Materials Science*, 93:45–111.

## Bibliography

- [Braschler et al., 2007] Braschler, T., Theytaz, J., Zvitov-Marabi, R., van Lintel, H., Loche, G., Kunze, A., Demierre, N., Tornay, R., Schlund, M., and Renaud, P. (2007). A virtual valve for smooth contamination-free flow switching. *Lab on a chip*, 7:1111–1113.
- [Broguiere et al., 2018] Broguiere, N., Isenmann, L., Hirt, C., Ringel, T., Placzek, S., Cavalli, E., Ringnalda, F., Villiger, L., Züllig, R., Lehmann, R., Rogler, G., Heim, M. H., Schüler, J., Zenobi-Wong, M., and Schwank, G. (2018). Growth of Epithelial Organoids in a Defined Hydrogel. *Advanced Materials*, 1801621.
- [Carsten Haber, Marc Boillat and van der Schoot, 2005] Carsten Haber, Marc Boillat and van der Schoot, B. (2005). Precise Nanoliter Fluid Handling System with Integrated High-Speed Flow Sensor. *ASSAY and Drug Development Technologies*, 3(2):203–212.
- [Chandrawati, 2016] Chandrawati, R. (2016). Enzyme-responsive polymer hydrogels for therapeutic delivery. *Experimental Biology and Medicine*, 241(9):972–979.
- [Chen et al., 2008] Chen, X., Cui, D. F., Liu, C. C., and Li, H. (2008). Microfluidic chip for blood cell separation and collection based on crossflow filtration. *Sensors and Actuators, B: Chemical*, 130(1):216–221.
- [Chen et al., 2017] Chen, Y., Liu, H., Geng, B., Ru, J., Cheng, C., Zhao, Y., and Wang, L. (2017). A reusable surface-quaternized nanocellulose-based hybrid cryogel loaded with N-doped TiO<sub>2</sub> for self-integrated adsorption/photo-degradation of methyl orange dye. *RSC Adv.*, 7(28):17279–17288.
- [Chia and Wu, 2015] Chia, H. N. and Wu, B. M. (2015). Recent advances in 3D printing of biomaterials. *Journal of Biological Engineering*, 9:4.
- [Choi and Park, 2008] Choi, S. and Park, J. K. (2008). Sheathless hydrophoretic particle focusing in a microchannel with exponentially increasing obstacle arrays. *Analytical Chemistry*, 80(8):3035–3039.
- [Chu et al., 2015] Chu, M. Q., Wang, L., Ding, H. Y., and Sun, Z. G. (2015). Additive Manufacturing for Aerospace Application. *Applied Mechanics and Materials*, 798:457–461.
- [Colosi et al., 2017] Colosi, C., Costantini, M., Barbetta, A., and Dentini, M. (2017). Microfluidic bioprinting of heterogeneous 3d tissue constructs. *Methods in Molecular Biology*, 1612:369–380.
- [Constantinescu, 1995] Constantinescu, V. (1995). *Laminar Viscous Flow*. Springer-Verlag New York, New York, 1 edition.
- [Cui et al., 2017] Cui, H., Nowicki, M., Fisher, J. P., and Zhang, L. G. (2017). 3D Bioprinting for Organ Regeneration. *Advanced Healthcare Materials*, 6(1).

- [Cundall et al., 1979] Cundall, R., Lawton, J., Murray, D., and Phillips, G. (1979). Polyelectrolyte complexes. 2. Interaction between collagen and polyanions. *International Journal of Biological Macromolecules*, 1(5):215–222.
- [Curley et al., 2011] Curley, J. L., Jennings, S. R., and Moore, M. J. (2011). Fabrication of Micropatterned Hydrogels for Neural Culture Systems using Dynamic Mask Projection Photolithography. *Journal of Visualized Experiments*, (48):3–9.
- [Dainiak et al., 2008] Dainiak, M. B., Savina, I. N., Musolino, I., Kumar, A., Mattiasson, B., and Galaev, I. Y. (2008). Biomimetic Macroporous Hydrogel Scaffolds in a High Throughput Screening Format for Cell-Based Assays. *Wiley InterScience*, (24):1373–1383.
- [Dallon and Ehrlich, 2008] Dallon, J. C. and Ehrlich, H. P. (2008). A review of fibroblast-populated collagen lattices. *Wound Repair and Regeneration*, 16(4):472–479.
- [Davia-Aracil et al., 2018] Davia-Aracil, M., Hinojo-Pérez, J. J., Jimeno-Morenilla, A., and Mora-Mora, H. (2018). 3D printing of functional anatomical insoles. *Computers in Industry*, 95:38–53.
- [Derakhshanfar et al., 2018] Derakhshanfar, S., Mbeleck, R., Xu, K., Zhang, X., Zhong, W., and Xing, M. (2018). 3D bioprinting for biomedical devices and tissue engineering: A review of recent trends and advances. *Bioactive Materials*, 3(2):144–156.
- [Derazshamshir et al., 2016] Derazshamshir, A., Baydemir, G., Yilmaz, F., Bereli, N., and Denizli, A. (2016). Preparation of cryogel columns for depletion of hemoglobin from human blood. *Artificial Cells, Nanomedicine, and Biotechnology*, 1401(February):1–8.
- [Devaraju and Unger, 2012] Devaraju, N. S. G. K. and Unger, M. A. (2012). Pressure driven digital logic in PDMS based microfluidic devices fabricated by multilayer soft lithography. *Lab on a Chip*, 12(22):4809.
- [Di Carlo, 2009] Di Carlo, D. (2009). Inertial microfluidics. *Lab on a chip*, 9(21):3038–3046.
- [Di Carlo et al., 2009] Di Carlo, D., Edd, J. F., Humphry, K. J., Stone, H. A., and Toner, M. (2009). Particle segregation and dynamics in confined flows. *Physical Review Letters*, 102(9):1–4.
- [Di Carlo et al., 2007] Di Carlo, D., Irimia, D., Tompkins, R. G., and Toner, M. (2007). Continuous inertial focusing, ordering, and separation of particles in microchannels. *Proceedings of the National Academy of Sciences*, 104(48):18892–18897.
- [Duan, 2017] Duan, B. (2017). State-of-the-Art Review of 3D Bioprinting for Cardiovascular Tissue Engineering. *Annals of Biomedical Engineering*, 45(1):195–209.



## Bibliography

- [Duocastella et al., 2007] Duocastella, M., Colina, M., Fernández-Pradas, J. M., Serra, P., and Morenza, J. L. (2007). Study of the laser-induced forward transfer of liquids for laser bioprinting. *Applied Surface Science*, 253(19):7855–7859.
- [Dvir-Ginzberg et al., 2003] Dvir-Ginzberg, M., Gamlieli-Bonshtein, I., Agbaria, R., and Cohen, S. (2003). Liver tissue engineering within alginate scaffolds: effects of cell-seeding density on hepatocyte viability, morphology, and function. *Tissue engineering*, 9(4):757–766.
- [Eckel et al., 2016] Eckel, Z. C., Zhou, C., Martin, J. H., Jacobsen, A. J., Carter, W. B., and Schaedler, T. A. (2016). Additive manufacturing of polymer-derived ceramics. *Science*, 351(6268):58–62.
- [Edelman, 1988] Edelman, G. M. (1988). *Topobiology : an introduction to molecular embryology*. Basic Books, New York.
- [Edgecombe et al., 2012] Edgecombe, A., Nguyen, B. N., Djordjevic, B., Belanger, E. C., and Mai, K. T. (2012). Utility of cytokeratin 5/6, cytokeratin 20, and p16 in the diagnosis of reactive urothelial atypia and noninvasive component of urothelial neoplasia. *Applied Immunohistochemistry and Molecular Morphology*, 20(3):264–271.
- [El Hasni et al., 2011] El Hasni, A., Göbbels, K., Thiebes, A. L., Bräunig, P., Mokwa, W., and Schnakenberg, U. (2011). Focusing and sorting of particles in spiral microfluidic channels. *Procedia Engineering*, 25:1197–1200.
- [Fan et al., 2016] Fan, R., Piou, M., Darling, E., Cormier, D., Sun, J., Wan, J., and Technologies, P. (2016). Bio-printing cell- laden matrigel-agarose constructs. *J Biomater Appl.*, 31(5):684–692.
- [Fenn et al., 2011] Fenn, J., Lehong, H., and Tv, I. (2011). Hype Cycle for Emerging Technologies , 2011. *Gartner*, 1(July):9.
- [Flores and Goff, 1999] Flores, A. and Goff, H. (1999). Ice Crystal Size Distributions in Dynamically Frozen Model Solutions and Ice Cream as Affected by Stabilizers. *Journal of Dairy Science*, 82(7):1399–1407.
- [Forchelet, 2017] Forchelet, D. (2017). Microdevice for sedimentation-based separation of blood microsamples at the point of collection. page 141.
- [Forget et al., 2017] Forget, A., Blaeser, A., Miessmer, F., Köpf, M., Campos, D. F., Voelcker, N. H., Blencowe, A., Fischer, H., and Shastri, V. P. (2017). Mechanically Tunable Bioink for 3D Bioprinting of Human Cells. *Advanced Healthcare Materials*, 6(20):1–7.
- [Freudenberg et al., 2007] Freudenberg, U., Behrens, S. H., Welzel, P. B., Müller, M., Grimmer, M., Salchert, K., Taeger, T., Schmidt, K., Pompe, W., and Werner, C. (2007).

- Electrostatic interactions modulate the conformation of collagen I. *Biophysical Journal*, 92(6):2108–2119.
- [Frisch and Francis, 1994] Frisch, S. M. and Francis, H. (1994). Disruption of epithelial cell-matrix interaction induces apoptosis. *J. Cell. Biol.*, 124(4):619–626.
- [Gao et al., 2015a] Gao, G., Schilling, A. F., Hubbell, K., Yonezawa, T., Truong, D., Hong, Y., Dai, G., and Cui, X. (2015a). Improved properties of bone and cartilage tissue from 3D inkjet-bioprinted human mesenchymal stem cells by simultaneous deposition and photocrosslinking in PEG-GelMA. *Biotechnology Letters*, 37(11):2349–2355.
- [Gao et al., 2015b] Gao, Q., He, Y., zhong Fu, J., Liu, A., and Ma, L. (2015b). Coaxial nozzle-assisted 3D bioprinting with built-in microchannels for nutrients delivery. *Biomaterials*, 61:203–215.
- [Gascoyne and Jody Vykoukal, 2002] Gascoyne, P. R. C. and Jody Vykoukal (2002). Review Particle separation by dielectrophoresis. *Electrophoresis*, 23:1973–1983.
- [Gauvin et al., 2012] Gauvin, R., Chen, Y. C., Lee, J. W., Soman, P., Zorlutuna, P., Nichol, J. W., Bae, H., Chen, S., and Khademhosseini, A. (2012). Microfabrication of complex porous tissue engineering scaffolds using 3D projection stereolithography. *Biomaterials*, 33(15):3824–3834.
- [Gibson et al., 2015] Gibson, I., Rosen, D., and Stucker, B. (2015). *Additive Manufacturing Technologies*.
- [Gifford et al., 2014] Gifford, S. C., Spillane, A. M., Vignes, S. M., and Shevkoplyas, S. S. (2014). Controlled incremental filtration: a simplified approach to design and fabrication of high-throughput microfluidic devices for selective enrichment of particles. *Lab on a chip*, 14(23):4496–505.
- [Gioffredi et al., 2016] Gioffredi, E., Boffito, M., Calzone, S., Giannitelli, S. M., Rainer, A., Trombetta, M., Mozetic, P., and Chiono, V. (2016). Pluronic F127 Hydrogel Characterization and Biofabrication in Cellularized Constructs for Tissue Engineering Applications. *Procedia CIRP*, 49(iii):125–132.
- [Gong et al., 2016] Gong, H., Woolley, A. T., and Nordin, G. P. (2016). High density 3D printed microfluidic valves, pumps, and multiplexers. *Lab on a Chip*, 16(13):2450–2458.
- [Grinnell, 2003] Grinnell, F. (2003). Fibroblast biology in three-dimensional collagen matrices. *Trends in Cell Biology*, 13(5):264–269.
- [Gruene et al., 2011] Gruene, M., Deiwick, A., Koch, L., Schlie, S., Unger, C., Hofmann, N., Bernemann, I., Glasmacher, B., and Chichkov, B. (2011). Laser Printing of Stem Cells for Biofabrication of Scaffold-Free Autologous Grafts. *Tissue Engineering Part C: Methods*, 17(1):79–87.

## Bibliography

- [Grünhagen and Lieshout, 2002] Grünhagen, T. and Lieshout, D. M. I. V. (2002). Characterisation of the degrading properties of alginate under influence of citrate Supervised by .: *Biomedical Engineering*, (July).
- [Guo et al., 2018] Guo, J., Zhang, R., Zhang, L., and Cao, X. (2018). 4D printing of robust hydrogels consisted of agarose nanofibers and polyacrylamide. *ACS Macro Letters*, 7(4):442–446.
- [Guo and Leu, 2013] Guo, N. and Leu, M. C. (2013). Additive manufacturing: Technology, applications and research needs. *Frontiers of Mechanical Engineering*, 8(3):215–243.
- [Hajash et al., 2017] Hajash, K., Sparrman, B., Guberan, C., Laucks, J., and Tibbits, S. (2017). Large-Scale Rapid Liquid Printing. *3D Printing and Additive Manufacturing*, 4(3):123–131.
- [Hakkinen et al., 2011] Hakkinen, K. M., Harunaga, J. S., Doyle, A. D., and Yamada, K. M. (2011). Direct Comparisons of the Morphology, Migration, Cell Adhesions, and Actin Cytoskeleton of Fibroblasts in Four Different Three-Dimensional Extracellular Matrices. *Tissue Engineering Part A*, 17(5-6):713–724.
- [Halde, 1980] Halde, R. (1980). Concentration of impurities by progressive freezing. *Water Research*, 14(6):575–580.
- [Haller et al., 2015] Haller, A., Spittler, A., Brandhoff, L., Zirath, H., Puchberger-Enengl, D., Keplinger, F., and Vellekoop, M. J. (2015). Microfluidic vortex enhancement for on-chip sample preparation. *Micromachines*, 6(2):239–251.
- [Hardin et al., 2015] Hardin, J. O., Ober, T. J., Valentine, A. D., and Lewis, J. A. (2015). Microfluidic printheads for multimaterial 3D printing of viscoelastic inks. *Advanced Materials*, 27(21):3279–3284.
- [Helseth and Veis, 1981] Helseth, D. L. and Veis, A. (1981). Collagen self-assembly in vitro. Differentiating specific telopeptide-dependent interactions using selective enzyme modification and the addition of free amino telopeptide. *Journal of Biological Chemistry*, 256(14):7118–7128.
- [Hinton et al., 2015] Hinton, T. J., Jallerat, Q., Palchesko, R. N., Park, J. H., Grodzicki, M. S., Shue, H.-J., Ramadan, M. H., Hudson, A. R., and Feinberg, A. W. (2015). Three-dimensional printing of complex biological structures by freeform reversible embedding of suspended hydrogels. *Science Advances*, 1(9):e1500758—e1500758.
- [Hockaday et al., 2012a] Hockaday, L. A., Kang, K. H., Colangelo, N. W., Cheung, P. Y. C., Duan, B., Malone, E., Wu, J., Girardi, L. N., Bonassar, L. J., Lipson, H., Chu, C. C., and Butcher, J. T. (2012a). Rapid 3D printing of anatomically accurate and mechanically heterogeneous aortic valve hydrogel scaffolds. *Biofabrication*, 4(3).

- [Hockaday et al., 2012b] Hockaday, L. A., Kang, K. H., Colangelo, N. W., Cheung, P. Y. C., Duan, B., Malone, E., Wu, J., Girardi, L. N., Bonassar, L. J., Lipson, H., Chu, C. C., and Butcher, J. T. (2012b). Rapid 3D printing of anatomically accurate and mechanically heterogeneous aortic valve hydrogel scaffolds. *Biofabrication*, 4(3).
- [Hof and Bastings, 2017] Hof, K. and Bastings, M. C. (2017). Programmable Control in Extracellular Matrix-mimicking Polymer Hydrogels. *CHIMIA International Journal for Chemistry*, 71(6):342–348.
- [Holder et al., 2018] Holder, A. J., Badiei, N., Hawkins, K., Wright, C., Williams, P. R., and Curtis, D. J. (2018). Control of collagen gel mechanical properties through manipulation of gelation conditions near the sol-gel transition. *Soft Matter*, 14(4):574–580.
- [Homan et al., 2016] Homan, K. A., Kolesky, D. B., Skylar-Scott, M. A., Herrmann, J., Obuobi, H., Moisan, A., and Lewis, J. A. (2016). Bioprinting of 3D Convulated Renal Proximal Tubules on Perfusable Chips. *Scientific Reports*, 6(1):34845.
- [Horsley et al., 2018] Horsley, H., Dharmasena, D., Malone-Lee, J., and Rohn, J. L. (2018). A urine-dependent human urothelial organoid offers a potential alternative to rodent models of infection. *Scientific Reports*, 8(1):1–14.
- [Hospodiuk et al., 2017] Hospodiuk, M., Dey, M., Sosnoski, D., and Ozbolat, I. T. (2017). The bioink: A comprehensive review on bioprintable materials. *Biotechnology Advances*, 35(2):217–239.
- [Huang et al., 2004] Huang, L. R., Cox, E. C., Austin, R. H., and Sturm, J. C. (2004). Lateral Displacement. 304(December 2003):987–991.
- [Hwang et al., 2010] Hwang, Y., Sangaj, N., and Varghese, S. (2010). Interconnected Macroporous Poly(Ethylene Glycol) Cryogels as a Cell Scaffold for Cartilage Tissue Engineering. *Tissue Engineering Part A*, 16(10):3033–3041.
- [Iloki Assanga et al., 2013] Iloki Assanga, S. B., Gil-Salido, A. A., Lewis Lujan, L. M., Rosas-Durazo, A., Acosta-silva, A. L., Rivera-castaneda, E. G., and Rubio-Pino, J. L. (2013). Cell growth curves for different cell lines and their relationship with biological activities. *International Journal of Biotechnology and Molecular Biology Research*, 4(4):60–70.
- [Ionov, 2018] Ionov, L. (2018). 4D Biofabrication: Materials, Methods, and Applications. *Advanced Healthcare Materials*, 1800412:1–14.
- [Jang et al., 2018] Jang, J., Park, J. Y., Gao, G., and Cho, D. W. (2018). Biomaterials-based 3D cell printing for next-generation therapeutics and diagnostics. *Biomaterials*, 156:88–106.

## Bibliography

- [Jia et al., 2016] Jia, W., Gungor-Ozkerim, P. S., Zhang, Y. S., Yue, K., Zhu, K., Liu, W., Pi, Q., Byambaa, B., Dokmeci, M. R., Shin, S. R., and Khademhosseini, A. (2016). Direct 3D bioprinting of perfusable vascular constructs using a blend bioink. *Biomaterials*, 106:58–68.
- [Jiang et al., 2016] Jiang, H., Pan, V., Vivek, S., Weeks, E. R., and Ke, Y. (2016). Programmable DNA Hydrogels Assembled from Multidomain DNA Strands. *ChemBioChem*, pages 1156–1162.
- [Jost et al., 1989] Jost, S. P., Gosling, J. a., and Dixon, J. S. (1989). The morphology of normal human bladder urothelium. *Journal of anatomy*, 167:103–115.
- [Kamperman et al., 2017] Kamperman, T., Henke, S., van den Berg, A., Shin, S. R., Tamayol, A., Khademhosseini, A., Karperien, M., and Leijten, J. (2017). Single Cell Microgel Based Modular Bioinks for Uncoupled Cellular Micro- and Macroenvironments. *Advanced Healthcare Materials*, 6(3).
- [Kang et al., 2016] Kang, H.-W., Lee, S. J., Ko, I. K., Kengla, C., Yoo, J. J., and Atala, A. (2016). A 3D bioprinting system to produce human-scale tissue constructs with structural integrity. *Nature Biotechnology*, 34(3):312–319.
- [Kengla et al., 2015] Kengla, C., Atala, A., and Lee, S. J. (2015). *Bioprinting of organoids*. Elsevier Inc.
- [Kesti et al., 2016] Kesti, M., Fisch, P., Pensalfini, M., Mazza, E., and Zenobi-Wong, M. (2016). Guidelines for standardization of bioprinting: A systematic study of process parameters and their effect on bioprinted structures. *BioNanoMaterials*, 17(3-4):193–204.
- [Khoo et al., 2015] Khoo, Z. X., Teoh, J. E. M., Liu, Y., Chua, C. K., Yang, S., An, J., Leong, K. F., and Yeong, W. Y. (2015). 3D printing of smart materials: A review on recent progresses in 4D printing. *Virtual and Physical Prototyping*, 10(3):103–122.
- [Kim and Kim, 2014] Kim, H. and Kim, J. (2014). A microfluidic-based dynamic microarray system with single-layer pneumatic valves for immobilization and selective retrieval of single microbeads. *Microfluidics and Nanofluidics*, 16(4):623–633.
- [Kim et al., 2018a] Kim, J. H., Seol, Y. J., Ko, I. K., Kang, H. W., Lee, Y. K., Yoo, J. J., Atala, A., and Lee, S. J. (2018a). 3D Bioprinted Human Skeletal Muscle Constructs for Muscle Function Restoration. *Scientific Reports*, 8(1):1–15.
- [Kim et al., 2018b] Kim, S. H., Yeon, Y. K., Lee, J. M., Chao, J. R., Lee, Y. J., Seo, Y. B., Sultan, M. T., Lee, O. J., Lee, J. S., Yoon, S. I., Hong, I. S., Khang, G., Lee, S. J., Yoo, J. J., and Park, C. H. (2018b). Precisely printable and biocompatible silk fibroin bioink for digital light processing 3D printing. *Nature Communications*, 9(1):1–14.

- [Knight et al., 1998] Knight, J. B., Vishwanath, A., Brody, J. P., and Austin, R. H. (1998). Hydrodynamic focusing on a silicon chip: Mixing nanoliters in microseconds. *Physical Review Letters*, 80(17):3863–3866.
- [Kodama, 1981] Kodama, H. (1981). Automatic method for fabricating a three-dimensional plastic model with photo hardening polymer. *Review of Scientific Instruments*, 52(11):1770–1773.
- [Kolesky et al., 2016] Kolesky, D. B., Homan, K. A., Skylar-Scott, M. A., and Lewis, J. A. (2016). Three-dimensional bioprinting of thick vascularized tissues. *Proceedings of the National Academy of Sciences of the United States of America*, 113(12).
- [Kolesky et al., 2014] Kolesky, D. B., Truby, R. L., Gladman, a. S., Busbee, T. a., Homan, K. a., and Lewis, J. a. (2014). 3D bioprinting of vascularized, heterogeneous cell-laden tissue constructs. *Advanced Materials*, 26(19):3124–3130.
- [Koltzschcher et al., 2003] Koltzschcher, M., Neumann, C., Kö, S., and Gerke, V. (2003). Dendritic Fibroblasts in Three-dimensional Collagen Matrices. *Molecular Biology of the Cell*, 14(February):2372–2384.
- [Kouzani et al., 2017] Kouzani, A. Z., Adams, S., Oliver, R., Nguwi, Y. Y., Hemsley, B., and Balandin, S. (2017). 3D printing of a pavlova. *IEEE Region 10 Annual International Conference, Proceedings/TENCON*, (i):2281–2285.
- [Kretzschmar and Clevers, 2016] Kretzschmar, K. and Clevers, H. (2016). Organoids: Modeling Development and the Stem Cell Niche in a Dish. *Developmental Cell*, 38(6):590–600.
- [Kunal and Serex, 2018] Kunal, S. and Serex, L. (2018). Discussion between Ludovic Serex and Kunal Sharma.
- [Lauffenburger and Horwitz, 1996] Lauffenburger, D. A. and Horwitz, A. F. (1996). Cell migration: A physically integrated molecular process. *Cell*, 84(3):359–369.
- [Lee et al., 2011] Lee, C. Y., Chang, C. L., Wang, Y. N., and Fu, L. M. (2011). Microfluidic Mixing: A Review. *International Journal of Molecular Sciences*, 12:3263–3287.
- [Lee et al., 2006] Lee, G.-B., Chang, C.-C., Huang, S.-B., and Yang, R.-J. (2006). The hydrodynamic focusing effect inside rectangular microchannels. *Journal of Micromechanics and Microengineering*, 16(5):1024–1032.
- [Lee et al., 2017] Lee, H., Yang, G. H., Kim, M., Lee, J. Y., Huh, J. T., and Kim, G. H. (2017). Fabrication of micro/nanoporous collagen/dECM/silk-fibroin biocomposite scaffolds using a low temperature 3D printing process for bone tissue regeneration. *Materials Science and Engineering C*, 84(November 2017):140–147.



## Bibliography

- [Lee and Yeong, 2016] Lee, J. M. and Yeong, W. Y. (2016). Design and Printing Strategies in 3D Bioprinting of Cell-Hydrogels: A Review. *Advanced Healthcare Materials*, 5(22):2856–2865.
- [Lee and Mooney, 2012] Lee, K. Y. and Mooney, D. J. (2012). Alginate: Properties and biomedical applications. *Progress in Polymer Science (Oxford)*, 37(1):106–126.
- [Lee et al., 2018a] Lee, M., Bae, K., Guillon, P., Chang, J., Arlov, Ø., and Zenobi-Wong, M. (2018a). Exploitation of Cationic Silica Nanoparticles for Bioprinting of Large-Scale Constructs with High Printing Fidelity. *ACS Applied Materials & Interfaces*, 10:acsami.8b13166.
- [Lee et al., 2018b] Lee, S. H., Hu, W., Matulay, J. T., Silva, M. V., Owczarek, T. B., Kim, K., Chua, C. W., Barlow, L. M. J., Kandoth, C., Williams, A. B., Bergren, S. K., Pietzak, E. J., Anderson, C. B., Benson, M. C., Coleman, J. A., Taylor, B. S., Abate-Shen, C., McKiernan, J. M., Al-Ahmadie, H., Solit, D. B., and Shen, M. M. (2018b). Tumor Evolution and Drug Response in Patient-Derived Organoid Models of Bladder Cancer. *Cell*, 173(2):515–528.e17.
- [Lee et al., 2013] Lee, V. K., Singh, G., Trasatti, J. P., Bjornsson, C., Tran, T. N., Xu, G., Yoo, S.-S., Dai, G., and Karande, P. (2013). Design and Fabrication of Human Skin by 3D Bioprinting. *Tissue engineering. Part C, Methods*, 20(6):1–44.
- [Lee et al., 1994] Lee, Y., McIntire, L. V., and Zygorakis, K. (1994). Analysis of endothelial cell locomotion: Differential effects of motility and contact inhibition. *Biotechnology and Bioengineering*, 43(7):622–634.
- [Lengauer et al., 1998] Lengauer, C., Kinzler, K. W., and Vogelstein, B. (1998). Genetic instabilities in human cancers. *Nature*, 396(6712):643–649.
- [Lerchner et al., 2008] Lerchner, J., Maskow, T., and Wolf, G. (2008). Chip calorimetry and its use for biochemical and cell biological investigations. *Chemical Engineering and Processing: Process Intensification*, 47(6):991–999.
- [Li et al., 2018] Li, H., Tan, C., and Li, L. (2018). Review of 3D printable hydrogels and constructs. *Materials & Design*, 159:20–38.
- [Liesch et al., 1982] Liesch, D., Versorgungstechnik, F., Germany, W., Karlsruhe, U., and Vlachos, N. S. (1982). MEASUREMENT AND CALCULATIONS OF LAMINAR IN A NINETY DEGREE BIFURCATION. I(7):473–485.
- [Lind et al., 2017] Lind, J. U., Busbee, T. A., Valentine, A. D., Pasqualini, F. S., Yuan, H., Yadid, M., Park, S. J., Kotikian, A., Nesmith, A. P., Campbell, P. H., Vlassak, J. J., Lewis, J. A., and Parker, K. K. (2017). Instrumented cardiac microphysiological devices via multimaterial three-dimensional printing. *Nature Materials*, 16(3):303–308.



- [Link, 1994] Link, A. C. (1994). Mini-Review on the Cellular Mechanisms of Disease. 126(1):1–4.
- [Liu et al., 2013] Liu, B., Ma, X., Zhu, C., Mi, Y., Fan, D., Li, X., and Chen, L. (2013). Study of a novel injectable hydrogel of human-like collagen and carboxymethylcellulose for soft tissue augmentation. *e-Polymers*, 13(1):1–11.
- [Liu et al., 2017] Liu, W., Zhang, Y. S., Heinrich, M. A., De Ferrari, F., Jang, H. L., Bakht, S. M., Alvarez, M. M., Yang, J., Li, Y. C., Trujillo-de Santiago, G., Miri, A. K., Zhu, K., Khoshakhlagh, P., Prakash, G., Cheng, H., Guan, X., Zhong, Z., Ju, J., Zhu, G. H., Jin, X., Shin, S. R., Dokmeci, M. R., and Khademhosseini, A. (2017). Rapid Continuous Multimaterial Extrusion Bioprinting. *Advanced Materials*, 29(3):1–8.
- [Liu et al., 2018] Liu, W., Zhong, Z., Hu, N., Zhou, Y., Maggio, L., Miri, A. K., Fraggasso, A., Jin, X., Khademhosseini, A., and Zhang, Y. S. (2018). Coaxial extrusion bioprinting of 3D microfibrinous constructs with cell-favorable gelatin methacryloyl microenvironments. *Biofabrication*, 10(2).
- [Liu et al., 2004] Liu, Y. Z., Kim, B. J., and Sung, H. J. (2004). Two-fluid mixing in a microchannel. *International Journal of Heat and Fluid Flow*, 25:986–995.
- [Lykissas and Gkiatas, 2017] Lykissas, M. and Gkiatas, I. (2017). Use of recombinant human bone morphogenetic protein-2 in spine surgery. *World journal of orthopedics*, 8(7):531–535.
- [Malda et al., 2013] Malda, J., Visser, J., Melchels, F. P., Jüngst, T., Hennink, W. E., Dhert, W. J. a., Groll, J., and Hutmacher, D. W. (2013). 25th anniversary article: Engineering hydrogels for biofabrication. *Advanced Materials*, 25(36):5011–5028.
- [Marelli et al., 2015] Marelli, B., Ghezzi, C. E., Zhang, Y. L., Rouiller, I., Barralet, J. E., and Nazhat, S. N. (2015). Fibril formation pH controls intrafibrillar collagen biomineralization invitro and invivo. *Biomaterials*, 37:252–259.
- [Markstedt et al., 2015] Markstedt, K., Mantas, A., Tournier, I., Martínez Ávila, H., Hägg, D., and Gatenholm, P. (2015). 3D bioprinting human chondrocytes with nanocellulose-alginate bioink for cartilage tissue engineering applications. *Biomacromolecules*, 16(5):1489–1496.
- [Martel et al., 2015] Martel, J. M., Smith, K. C., Dlamini, M., Pletcher, K., Yang, J., Karabacak, M., Haber, D. A., Kapur, R., and Toner, M. (2015). Continuous Flow Microfluidic Bioparticle Concentrator. *Scientific Reports*, 5(1):11300.
- [Martel and Toner, 2014] Martel, J. M. and Toner, M. (2014). Inertial focusing in microfluidics. *Annual review of biomedical engineering*, 16:371–96.

## Bibliography

- [McBeth et al., 2017] McBeth, C., Lauer, J., Ottersbach, M., Campbell, J., Sharon, A., and Sauer-Budge, A. F. (2017). 3D bioprinting of GelMA scaffolds triggers mineral deposition by primary human osteoblasts. *Biofabrication*, 9(1).
- [Metz, 2003] Metz, S. (2003). Polyimide-based microfabrication technologies for micro-electrodes and microfluidic devices in biomedical engineering. page 194.
- [Michael et al., 2013] Michael, S., Sorg, H., Peck, C. T., Koch, L., Deiwick, A., Chichkov, B., Vogt, P. M., and Reimers, K. (2013). Tissue Engineered Skin Substitutes Created by Laser-Assisted Bioprinting Form Skin-Like Structures in the Dorsal Skin Fold Chamber in Mice. *PLoS ONE*, 8(3).
- [Min Zhao, Huai Bai, Entong Wang, John V. Forrester, 2004] Min Zhao, Huai Bai, Entong Wang, John V. Forrester, C. D. M. (2004). Electrical stimulation directly induces pre-angiogenic responses in vascular endothelial cells by signaling through VEGF receptors. *Journal of Cell Science*, 117(Pt 3):397–405.
- [Müller et al., 2015] Müller, M., Becher, J., Schnabelrauch, M., and Zenobi-Wong, M. (2015). Nanostructured Pluronic hydrogels as bioinks for 3D bioprinting. *Biofabrication*, 7(3).
- [Murphy and Atala, 2014] Murphy, S. V. and Atala, A. (2014). 3D bioprinting of tissues and organs. *Nature biotechnology*, 32(8):773–785.
- [N. Turner et al., 2014] N. Turner, B., Strong, R., and A. Gold, S. (2014). A review of melt extrusion additive manufacturing processes: I. Process design and modeling. *Rapid Prototyping Journal*, 20(3):192–204.
- [Newland et al., 2015] Newland, B., Welzel, P. B., Newland, H., Renneberg, C., Kolar, P., Tsurkan, M., Rosser, A., Freudenberg, U., and Werner, C. (2015). Tackling Cell Transplantation Anoikis: An Injectable, Shape Memory Cryogel Microcarrier Platform Material for Stem Cell and Neuronal Cell Growth. *Small*, 11(38):5047–5053.
- [Nguyen and Wu, 2005] Nguyen, N. T. and Wu, Z. (2005). Micromixers - A review. *Journal of Micromechanics and Microengineering*, 15(2).
- [Nicolas Heureux et al., 1993] Nicolas Heureux, Germain Lucie, Labbe Raymond, and Auger Francois (1993). In vitro construction of a human blood vessel from cultured vascular cells: A morphologic study. *Journal of Vascular Surgery*, 17(3):499–509.
- [Nie et al., 2017] Nie, M., Mistry, P., Yang, J., and Takeuchi, S. (2017). Microfluidic enabled rapid bioprinting of hydrogel  $\mu$ fiber based porous constructs. *Proceedings of the IEEE International Conference on Micro Electro Mechanical Systems (MEMS)*, (c):589–591.

- [N.J.A. Sloane, 1984] N.J.A. Sloane (1984). The Packing of Spheres. *Scientific American*, 250(1):116–125.
- [Nobes and Hall, 1995] Nobes, C. D. and Hall, A. (1995). Rho, Rac, and Cdc42 GTPases regulate the assembly of multimolecular focal complexes associated with actin stress fibers, lamellipodia, and filopodia. *Cell*, 81(1):53–62.
- [Norotte et al., 2009] Norotte, C., Marga, F. S., Niklason, L. E., and Forgacs, G. (2009). Scaffold-free vascular tissue engineering using bioprinting. *Biomaterials*, 30(30):5910–5917.
- [Novotny and Gnoth, 1991] Novotny, G. E. and Gnoth, C. (1991). Variability of fibroblast morphology in vivo: a silver impregnation study on human digital dermis and subcutis. *Journal of anatomy*, 177:195–207.
- [Okay, 2014] Okay, O. (2014). *Polymeric Cryogels*. Springer edition.
- [Onoe et al., 2013] Onoe, H., Okitsu, T., Itou, A., Kato-Negishi, M., Gojo, R., Kiriya, D., Sato, K., Miura, S., Iwanaga, S., Kuribayashi-Shigetomi, K., Matsunaga, Y. T., Shimoyama, Y., and Takeuchi, S. (2013). Metre-long cell-laden microfibres exhibit tissue morphologies and functions. *Nature materials*, 12(6):584–90.
- [Ouyang et al., 2017] Ouyang, L., Highley, C. B., Sun, W., and Burdick, J. A. (2017). A Generalizable Strategy for the 3D Bioprinting of Hydrogels from Nonviscous Photocrosslinkable Inks. *Advanced Materials*, 29(8).
- [Ozbolat and Hospodiuk, 2016] Ozbolat, I. T. and Hospodiuk, M. (2016). Current advances and future perspectives in extrusion-based bioprinting. *Biomaterials*, 76:321–343.
- [Ozbolat et al., 2016] Ozbolat, I. T., Peng, W., and Ozbolat, V. (2016). Application areas of 3D bioprinting. *Drug Discovery Today*, 21(8):1257–1271.
- [Park et al., 2003] Park, S. N., Lee, H. J., Lee, K. H., and Suh, H. (2003). Biological characterization of EDC-crosslinked collagen-hyaluronic acid matrix in dermal tissue restoration. *Biomaterials*, 24(9):1631–1641.
- [Pataky et al., 2012] Pataky, K., Braschler, T., Negro, A., Renaud, P., Lutolf, M. P., and Brugger, J. (2012). Microdrop Printing of Hydrogel Bioinks into 3D Tissue-Like Geometries. *Advanced Materials*, 24(3):391–396.
- [Pati et al., 2014] Pati, F., Jang, J., Ha, D.-H., Won Kim, S., Rhie, J.-W., Shim, J.-H., Kim, D.-H., and Cho, D.-W. (2014). Printing three-dimensional tissue analogues with decellularized extracellular matrix bioink. *Nature communications*, 5:3935.

## Bibliography

- [Pedde et al., 2017] Pedde, R. D., Mirani, B., Navaei, A., Styan, T., Wong, S., Mehrali, M., Thakur, A., Mohtaram, N. K., Bayati, A., Dolatshahi-Pirouz, A., Nikkhah, M., Willerth, S. M., and Akbari, M. (2017). Emerging Biofabrication Strategies for Engineering Complex Tissue Constructs. *Advanced Materials*, 29(19):1–27.
- [Peng et al., 2018] Peng, W., Datta, P., Wu, Y., Dey, M., Ayan, B., Dababneh, A., and Ozbolat, I. T. (2018). Challenges in Bio-fabrication of Organoid Cultures. *Adv Exp Med Biol – Cell Biology and Translational Medic*, 5(9):1025–1039.
- [Pescosolido et al., 2011] Pescosolido, L., Schuurman, W., Malda, J., Matricardi, P., Al-haique, F., Coviello, T., Van Weeren, P. R., Dhert, W. J., Hennink, W. E., and Vermonden, T. (2011). Hyaluronic acid and dextran-based semi-IPN hydrogels as biomaterials for bioprinting. *Biomacromolecules*, 12(5):1831–1838.
- [Petitpierre, 2017] Petitpierre, G. C. Y. (2017). A microfluidic brain interface for in vivo recording of neurochemical activity. page 170.
- [Petrie and Yamada, 2015] Petrie, R. J. and Yamada, K. M. (2015). Fibroblasts Lead the Way: A Unified View of 3D Cell Motility. *Trends in Cell Biology*, 25(11):666–674.
- [Pham et al., 2008] Pham, C. B., Leong, K. F., Lim, T. C., and Chian, K. S. (2008). Rapid freeze prototyping technique in bio-plotters for tissue scaffold fabrication. *Rapid Prototyping Journal*, 14(4):246–253.
- [Plleva et al., 2007] Plleva, F. M., Galaev, I. Y., and Mattiasson, B. (2007). Macroporous gels prepared at subzero temperatures as novel materials for chromatography of particulate-containing fluids and cell culture applications. *Journal of Separation Science*, 30(11):1657–1671.
- [P.Mecham, 2011] P.Mecham, R. (2011). *The Extracellular Matrix: an Overview*. Springer Berlin Heidelberg, Washington University School of Medicine, USA, 1st edition.
- [Ponta et al., 2003] Ponta, H., Sherman, L., and Herrlich, P. A. (2003). CD44: From adhesion molecules to signalling regulators. *Nature Reviews Molecular Cell Biology*, 4(1):33–45.
- [Powell et al., 2018] Powell, A., Stavrinadis, A., De Miguel, I., Konstantatos, G., and Quidant, R. (2018). White and brightly coloured 3D printing based on resonant photothermal sensitizers. *Nano Letters*.
- [Prasad and Smyth, 2016] Prasad, L. K. and Smyth, H. (2016). 3D Printing technologies for drug delivery: a review. *Drug Development and Industrial Pharmacy*, 42(7):1019–1031.
- [Qiang Wu, Fatima Merchant, 2008] Qiang Wu, Fatima Merchant, K. C. (2008). *Microscope Image Processing*. Elsevier/Academic Press.

- [Quemada, 1977] Quemada, D. (1977). Rheology of concentrated disperse systems and minimum energy dissipation principle - I. Viscosity-concentration relationship. *Rheologica Acta*, 16(1):82–94.
- [Rafeie et al., 2017] Rafeie, M., Welleweerd, M., Hassanzadeh-Barforoushi, A., Asadnia, M., Olthuis, W., and Warkiani, M. E. (2017). An easily fabricated three-dimensional threaded lemniscate-shaped micromixer for a wide range of flow rates. *Biomicrofluidics*, 11(1):1–15.
- [Raof et al., 2011] Raof, N. A., Schiele, N. R., Xie, Y., Chrisey, D. B., and Corr, D. T. (2011). The maintenance of pluripotency following laser direct-write of mouse embryonic stem cells. *Biomaterials*, 32(7):1802–1808.
- [Rengier et al., 2010] Rengier, F., Mehndiratta, A., Von Tengg-Kobligk, H., Zechmann, C. M., Unterhinninghofen, R., Kauczor, H. U., and Giesel, F. L. (2010). 3D printing based on imaging data: Review of medical applications. *International Journal of Computer Assisted Radiology and Surgery*, 5(4):335–341.
- [Rhee, 2009] Rhee, S. (2009). Fibroblasts in three dimensional matrices: cell migration and matrix remodeling. *Experimental & Molecular Medicine*, 41(12):858–865.
- [Riedel et al., 2001] Riedel, I., Czernobilsky, B., Lifschitz-Mercer, B., Roth, L. M., Wu, X. R., Sun, T. T., and Moll, R. (2001). Brenner tumors but not transitional cell carcinomas of the ovary show urothelial differentiation: Immunohistochemical staining of urothelial markers, including cytokeratins and uroplakins. *Virchows Archiv*, 438(2):181–191.
- [Rocca et al., 2018] Rocca, M., Fragasso, A., Liu, W., Heinrich, M. A., and Zhang, Y. S. (2018). Embedded Multimaterial Extrusion Bioprinting. *SLAS Technology*, 23(2):154–163.
- [Roth et al., 2004] Roth, E., Xu, T., Das, M., Gregory, C., Hickman, J., and Boland, T. (2004). Inkjet printing for high-throughput cell patterning. *Biomaterials*, 25(17):3707–3715.
- [Salet et al., 2017] Salet, T. A. M., Bos, F. P., Wolfs, R. J. M., and Ahmed, Z. Y. (2017). 3D concrete printing - A structural engineering perspective. *High Tech Concrete: Where Technology and Engineering Meet - Proceedings of the 2017 fib Symposium*, pages xliii–lvii.
- [Savina et al., 2016] Savina, I. N., Ingavle, G. C., Cundy, A. B., and Mikhalovsky, S. V. (2016). A simple method for the production of large volume 3D macroporous hydrogels for advanced biotechnological, medical and environmental applications. *Nature Publishing Group*, (February):1–9.

## Bibliography

- [Schneeberger et al., 2017] Schneeberger, K., Spee, B., Costa, P., Sachs, N., Clevers, H., and Malda, J. (2017). Converging biofabrication and organoid technologies: The next frontier in hepatic and intestinal tissue engineering? *Biofabrication*, 9(1).
- [Segur, 1953] Segur, J. (1953). Physical properties of glycerol and its solutions. *Aciscience.Org*, pages 1–27.
- [Serex et al., 2018a] Serex, L., Bertsch, A., and Renaud, P. (2018a). Microfluidics : A New Layer of Control for Extrusion- Based 3D Printing. *Micromachines*, 9(2):1–11.
- [Serex et al., 2018b] Serex, L., Braschler, T., Filippova, A., Rochat, A., Bédurier, A., Bertsch, A., and Renaud, P. (2018b). Pore Size Manipulation in 3D Printed Cryogels Enables Selective Cell Seeding. *Advanced Materials Technologies*, 1700340(3):1–8.
- [Serrano et al., 2004] Serrano, M. C., Pagani, R., Vallet-Regí, M., Peña, J., Rámila, A., Izquierdo, I., and Portolés, M. T. (2004). In vitro biocompatibility assessment of poly(caprolactone) films using L929 mouse fibroblasts. *Biomaterials*, 25(25):5603–5611.
- [Shang et al., 2017] Shang, W., Liu, Y., Wan, W., Hu, C., Liu, Z., Wong, C. T., Fukuda, T., and Shen, Y. (2017). Hybrid 3D printing and electrodeposition approach for controllable 3D alginate hydrogel formation. *Biofabrication*, 9(2).
- [Shelby et al., 2003] Shelby, J. P., White, J., Ganesan, K., Rathod, P. K., and Chiu, D. T. (2003). A microfluidic model for single-cell capillary obstruction by Plasmodium falciparum-infected erythrocytes. *Proceedings of the National Academy of Sciences*, 100(25):14618–14622.
- [Shi et al., 2008] Shi, J., Mao, X., Ahmed, D., Colletti, A., and Huang, T. J. (2008). Focusing microparticles in a microfluidic channel with standing surface acoustic waves (SSAW). *Lab Chip*, 8(2):221–223.
- [Shigeto Abr, Beat U. Steinmann, Larry M. Wahl, 1979] Shigeto Abr, Beat U. Steinmann, Larry M. Wahl, G. R. M. (1979). High cell density alters the ration of type III to I collagen synthesis by fibroblasts.
- [Sideridou et al., 2006] Sideridou, I. D., Achilias, D. S., and Karava, O. (2006). Reactivity of benzoyl peroxide/ amine system as an initiator for the free radical polymerization of dental and orthopaedic dimethacrylate monomers: Effect of the amine and monomer chemical structure. *Macromolecules*, 39(6):2072–2080.
- [Sigma Aldrich, 2019] Sigma Aldrich (2019). Adipic acid dihydrazide Product Page.
- [Skardal and Atala, 2014] Skardal, A. and Atala, A. (2014). Biomaterials for Integration with 3-D Bioprinting. *Annals of Biomedical Engineering*, 43(3):730–746.



- [Skardal et al., 2010] Skardal, A., Zhang, J., and Prestwich, G. D. (2010). Bioprinting vessel-like constructs using hyaluronan hydrogels crosslinked with tetrahedral polyethylene glycol tetracrylates. *Biomaterials*, 31(24):6173–6181.
- [Snyder et al., 2011] Snyder, J. E., Hamid, Q., Wang, C., Chang, R., Emami, K., Wu, H., and Sun, W. (2011). Bioprinting cell-laden matrigel for radioprotection study of liver by pro-drug conversion in a dual-tissue microfluidic chip. *Biofabrication*, 3(3).
- [Soman et al., 2013] Soman, P., Chung, P. H., Zhang, A. P., and Chen, S. (2013). Digital microfabrication of user-defined 3D microstructures in cell-laden hydrogels. *Biotechnology and Bioengineering*, 110(11):3038–3047.
- [Stauffer, 1979] Stauffer, D. (1979). Scaling theory of percolation clusters. *Physics Reports*, 54(1):1–74.
- [Stratsteffen et al., 2017] Stratsteffen, H., Köpf, M., Kreimendahl, F., Blaeser, A., Jockenhoevel, S., and Fischer, H. (2017). GelMA-collagen blends enable drop-on-demand 3D printability and promote angiogenesis. *Biofabrication*, 9(4).
- [Stroock et al., 2002] Stroock, A. D., Dertinger, S. K. W., Ajdari, A., Mezic, I., Stone, H. a., and Whitesides, G. M. (2002). Chaotic mixer for microchannels. *Science (New York, N.Y.)*, 295(January):647–651.
- [Sun et al., 1996] Sun, T. T., Zhao, H., Provet, J., Aebi, U., and Wu, X. R. (1996). Formation of asymmetric unit membrane during urothelial differentiation. *Molecular Biology Reports*, 23(1):3–11.
- [Sverzut et al., 2012] Sverzut, A. T., Crippa, G. E., Morra, M., De Oliveira, P. T., Beloti, M. M., and Rosa, A. L. (2012). Effects of type I collagen coating on titanium osseointegration: Histomorphometric, cellular and molecular analyses. *Biomedical Materials*, 7(3).
- [Sydney Gladman et al., 2016] Sydney Gladman, A., Matsumoto, E. A., Nuzzo, R. G., Mahadevan, L., and Lewis, J. A. (2016). Biomimetic 4D printing. *Nature materials*, 15(4):413–8.
- [Tan et al., 2017] Tan, X. P., Tan, Y. J., Chow, C. S., Tor, S. B., and Yeong, W. Y. (2017). Metallic powder-bed based 3D printing of cellular scaffolds for orthopaedic implants: A state-of-the-art review on manufacturing, topological design, mechanical properties and biocompatibility. *Materials Science and Engineering C*, 76:1328–1343.
- [Tobergte and Curtis, 2013] Tobergte, D. R. and Curtis, S. (2013). *The Physics of Phase Transitions*, volume 53.
- [Todd, 2018] Todd, I. (2018). Metallurgy: Printing steels. *Nature Publishing Group*, 17(1):13–14.



## Bibliography

- [Torabi et al., 2015] Torabi, K., Farjood, E., and Hamedani, S. (2015). Rapid Prototyping Technologies and their Applications in Prosthodontics, a Review of Literature. *Journal of dentistry (Shīrāz, Iran)*, 16(1):1–9.
- [Trampe et al., 2018] Trampe, E., Koren, K., Akkineni, A. R., Senwitz, C., Krujatz, F., Lode, A., Gelinsky, M., and Köhl, M. (2018). Functionalized Bioink with Optical Sensor Nanoparticles for O<sub>2</sub> Imaging in 3D-Bioprinted Constructs. *Advanced Functional Materials*, 1804411:1804411.
- [Uygun et al., 2015] Uygun, M., Akduman, B., Uygun, D. A., Akgol, S., and Denizli, A. (2015). Dye functionalized cryogel columns for reversible lysozyme adsorption. *J Biomater Sci Polym Ed*, 5063(January):1–13.
- [Vaezi et al., 2013] Vaezi, M., Seitz, H., and Yang, S. (2013). A review on 3D micro-additive manufacturing technologies. *International Journal of Advanced Manufacturing Technology*, 67(5-8):1721–1754.
- [Vajanto et al., 2002] Vajanto, I., Rissanen, T. T., Rutanen, J., Hiltunen, M. O., Tuomisto, T. T., Arve, K., Närvänen, O., Manninen, H., Räsänen, H., Hippeläinen, M., Alhava, E., and Ylä-Herttua, S. (2002). Evaluation of angiogenesis and side effects in ischemic rabbit hindlimbs after intramuscular injection of adenoviral vectors encoding VEGF and LacZ. *Journal of Gene Medicine*, 4(4):371–380.
- [Valero et al., 2010] Valero, A., Braschler, T., Demierre, N., and Renaud, P. (2010). A miniaturized continuous dielectrophoretic cell sorter and its applications. *Biomicrofluidics*, 4(2).
- [Vijayavenkataraman et al., 2017] Vijayavenkataraman, S., Lu, W. F., Fuh, J. Y. H., Bulysheva, A. A., Burcus, N., Lundberg, C., Arslan-Yildiz, A., Assal, R. E., Chen, P., Hodgkinson, T., Bayat, A., Gu, J., Liu, N., Yang, X., Dai, X., Ma, C., Lan, Q., Mosadegh, B., Xiong, G., Dunham, S., Marga, F., Jakab, K., Khatiwala, C., Lu, H., Oh, H. H., Kawazoe, N., Cubo, N., Garcia, M., Del Cañizo, J. F., Velasco, D., and Jorcano, J. L. (2017). 3D bioprinting of functional human skin: production and in vivo analysis. *Biofabrication*, 9.
- [Vijayavenkataraman et al., 2018] Vijayavenkataraman, S., Yan, W. C., Lu, W. F., Wang, C. H., and Fuh, J. Y. H. (2018). 3D bioprinting of tissues and organs for regenerative medicine. *Advanced Drug Delivery Reviews*.
- [Wang et al., 2017a] Wang, S., Gao, D., and Chen, Y. (2017a). The potential of organoids in urological cancer research. *Nature Reviews Urology*, 14(7):401–414.
- [Wang et al., 2017b] Wang, X., Jiang, M., Zhou, Z., Gou, J., and Hui, D. (2017b). 3D printing of polymer matrix composites: A review and prospective. *Composites Part B: Engineering*, 110:442–458.

- [Weaver et al., 1997] Weaver, V., Petersen, O., Wang, F., Larabell, C., Briand, P., Damsky, C., and Bissell, M. (1997). Reversion of the Malignant Phenotype of Human Breast Cells in Three-Dimensional Culture and In Vivo by Integrin Blocking Antibodies. *The Journal of Cell Biology*, 137(1):231–245.
- [Williamson et al., 2018] Williamson, I. A., Arnold, J. W., Samsa, L. A., Gaynor, L., DiSalvo, M., Cocchiaro, J. L., Carroll, I., Azcarate-Peril, M. A., Rawls, J. F., Allbritton, N. L., and Magness, S. T. (2018). A High-Throughput Organoid Microinjection Platform to Study Gastrointestinal Microbiota and Luminal Physiology. *Cmgh*, 6(3):301–319.
- [Wilson et al., 1999] Wilson, P. W., Arthur, J. W., and Haymet, A. D. (1999). Ice premelting during differential scanning calorimetry. *Biophysical Journal*, 77(5):2850–2855.
- [Wu et al., 2016] Wu, Z., Su, X., Xu, Y., Kong, B., Sun, W., and Mi, S. (2016). Bioprinting three-dimensional cell-laden tissue constructs with controllable degradation. *Scientific Reports*, 6(1):24474.
- [Xiang et al., 2018] Xiang, N., Ni, Z., and Yi, H. (2018). Concentration-controlled particle focusing in spiral elasto-inertial microfluidic devices. *Electrophoresis*, 39(2):417–424.
- [Xing et al., 2011] Xing, Y., Cheng, E., Yang, Y., Chen, P., Zhang, T., Sun, Y., Yang, Z., and Liu, D. (2011). Self-assembled DNA hydrogels with designable thermal and enzymatic responsiveness. *Advanced Materials*, 23(9):1117–1121.
- [Xu et al., 2005] Xu, T., Jin, J., Gregory, C., Hickman, J. J., and Boland, T. (2005). Inkjet printing of viable mammalian cells. *Biomaterials*, 26(1):93–99.
- [Xu et al., 2018] Xu, Y., Hu, Y., Liu, C., Hongyi, Y., Boxun, L., and Shengli, M. (2018). A Novel Strategy for Creating Tissue-Engineered Biomimetic Blood Vessels Using 3D. *Materials*, 11(1581):1–15.
- [Xuan et al., 2010] Xuan, X., Zhu, J., and Church, C. (2010). Particle focusing in microfluidic devices. *Microfluidics and Nanofluidics*, 9(1):1–16.
- [Yamada and Seki, 2005] Yamada, M. and Seki, M. (2005). Hydrodynamic filtration for on-chip particle concentration and classification utilizing microfluidics. *Lab Chip*, 5(11):1233–1239.
- [Yamada and Seki, 2006] Yamada, M. and Seki, M. (2006). Microfluidic particle sorter employing flow splitting and recombining. *Analytical Chemistry*, 78(4):1357–1362.
- [Yang et al., 2018] Yang, X., Lu, Z., Wu, H., Li, W., Zheng, L., and Zhao, J. (2018). Collagen-alginate as bioink for three-dimensional (3D) cell printing based cartilage tissue engineering. *Materials Science and Engineering C*, 83(June 2017):195–201.

## Bibliography

- [Ye et al., 2014] Ye, K., Felimban, R., Traianedes, K., Moulton, S. E., Wallace, G. G., Chung, J., Quigley, A., Choong, P. F. M., and Myers, D. E. (2014). Chondrogenesis of infrapatellar fat pad derived adipose stem cells in 3D printed chitosan scaffold. *PLoS ONE*, 9(6).
- [Yu et al., 2016] Yu, Y., Moncal, K. K., Li, J., Peng, W., Rivero, I., Martin, J. A., and Ozbolat, I. T. (2016). Three-dimensional bioprinting using self-Assembling scalable scaffold-free "tissue strands" as a new bioink. *Scientific Reports*, 6(February):1–11.
- [Zadpoor and Malda, 2017] Zadpoor, A. A. and Malda, J. (2017). Additive Manufacturing of Biomaterials, Tissues, and Organs. *Annals of Biomedical Engineering*, 45(1):1–11.
- [Zeng et al., 2005] Zeng, L., Balachandar, S., and Fischer, P. (2005). Wall-induced forces on a rigid sphere at finite Reynolds number. *Journal of Fluid Mechanics*, 536:1–25.
- [Zhang et al., 2017] Zhang, Y. S., Yue, K., Aleman, J., Mollazadeh-Moghaddam, K., Bakht, S. M., Yang, J., Jia, W., Dell'Erba, V., Assawes, P., Shin, S. R., Dokmeci, M. R., Oklu, R., and Khademhosseini, A. (2017). 3D Bioprinting for Tissue and Organ Fabrication. *Annals of Biomedical Engineering*, 45(1):148–163.
- [Zhao et al., 2007] Zhao, Y., Fujimoto, B. S., Jeffries, G. D. M., Schiro, P. G., and Chiu, D. T. (2007). Optical gradient flow focusing. *Optics Express*, 15(10):6167.
- [Zhu and Xuan, 2009] Zhu, J. and Xuan, X. (2009). Dielectrophoretic focusing of particles in a microchannel constriction using DC-biased AC electric fields. *Electrophoresis*, 30(15):2668–2675.
- [Zhu et al., 2018] Zhu, K., Chen, N., Liu, X., Mu, X., Zhang, W., Wang, C., and Zhang, Y. S. (2018). A General Strategy for Extrusion Bioprinting of Bio-Macromolecular Bioinks through Alginate-Templated Dual-Stage Crosslinking. *Macromolecular Bioscience*, 1800127:1800127.



Mr. Ludovic Serex

Micro-engineer

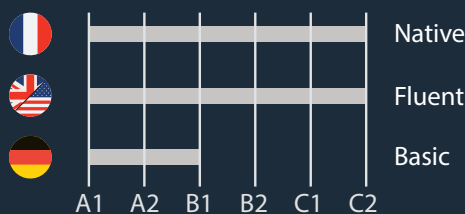
PROFILE

My formation as an engineer gave me outstanding analytical skills. I pay great attention to details which allows me to find elegant and creative solutions to problems. My core skills are microfabrication, microfluidic and bioengineering however thanks to my formation I am able to learn quickly and adapt to new situations. Moreover by working in parallel of my studies at Cmi in a cleanroom facility as well as for the CERN gave me a sense of responsibility as well as the opportunity to work in team toward a common goal. I also participated in multiple contests with friends that gave us the opportunity to present our ideas before peoples in foreign countries which gave me confidence and pitching skills.

PERSONAL

- +41 78.854.63.99
ludovic.serex@gmail.com
Ludovic Serex
Av. Menthon 14, 1005 Lausanne, CH
Nationality: Swiss
13th April 1989

LANGUAGES



SOFT SKILLS

Through contests done with friends, I obtained great team work skills as well as presenting and pitching skills. Furthermore, thanks to continuing training I also acquired experience in constructive feedback, verbal communication and team management.

HOBBIES

Climbing, Trekking, Traveling, Music

EDUCATION

Table with 3 columns: Year, Degree, Institution. Rows include PhD - Microsystems and Microelectronics (EPF Lausanne), Master of Science - Micro and Nano Systems (EPF Lausanne), Bachelor of Science - Microengineering (EPF Lausanne).

WORK EXPERIENCE

Table with 3 columns: Year, Position, Location. Rows include European Organization for Nuclear Research (Geneva-CH) and Center of MicroNanoTechnology (CMI) (Lausanne-CH).

PROFESSIONAL SKILLS

Technical Skills

Advanced knowledge in microsystems, CAD design, mechanics, materials, micor-bio-engineering and micro-fabrication processes. Accreditation to work in class ISO 5 cleanroom. Good knowledge in Simulation (FEM), Matlab, programming and electronic. Good knowledge in project management with a Prince2 foundation certification.

Main Projects

- 1. Micro-bioengineering: Developement of advanced printing heads for extrusion bioprinter
2. Bioengineering: Weaving blood vessels from living threads
3. Microengineering: Development and testing of microfluidic scintillators. for particle detection.
4. Engineering: Conception of an electronic assisted stethoscope for educational purposes.

MAIN PUBLICATIONS AND AWARDS

Main publications

- Serex & al., "Pore Size Manipulation in 3D Printed Cryogels Enables Selective Cell Seeding", Advanced material technologies, 2018
Serex & al., "Microfluidics: A New Layer of Control for Extrusion-Based 3D Printing", Micromachines, 2018
Serex & al., "Microfluidic bioprinting head for controlled high cell concentration tissue printing.", Under review, 2019

Patent

Ludovic Serex, "Micro-fluidic particle concentrator and filtering device", 2017

Creativity and Innovation

Design, construction and programming of an electronic device controller by arm movement detection for the 2011 International Contest of Applications in Nano-Micro Technologies.
Participation to Start Lausanne 2012 contest for startup creation and entrepreneurship.
Participation to Kick-off Acceleration Program Series La Forge 2.0.
Global winners of the "Imagine IF!" contest for innovation.